

# Modelling Properties of Cement Paste from Microstructure: Porosity, Mechanical Properties, Creep and Shrinkage

THÈSE N° 5881 (2013)

PRÉSENTÉE LE 9 AOUT 2013

À LA FACULTÉ DES SCIENCES ET TECHNIQUES DE L'INGÉNIEUR  
LABORATOIRE DES MATÉRIAUX DE CONSTRUCTION  
PROGRAMME DOCTORAL EN STRUCTURES

ÉCOLE POLYTECHNIQUE FÉDÉRALE DE LAUSANNE

POUR L'OBTENTION DU GRADE DE DOCTEUR ÈS SCIENCES

PAR

Quang Huy DO

acceptée sur proposition du jury:

Prof. N. Geroliminis, président du jury  
Prof. K. Scrivener, Prof. S. Bishnoi, directeurs de thèse  
Dr G. Chanvillard, rapporteur  
Prof. P. Lura, rapporteur  
Prof. B. Pichler, rapporteur



ÉCOLE POLYTECHNIQUE  
FÉDÉRALE DE LAUSANNE

Suisse  
2013



## Foreword

The doctoral thesis of Dr. Do Quang Huy is an apt culmination of almost two decades of work in microstructural modelling of cements at EPFL. This work holistically tackles the phenomenon of autogeneous shrinkage through microstructural modelling. In a first such attempt, the author has used the same microstructural model to simulate the microstructural development, elastic properties, creep and autogeneous shrinkage. The task of putting these models together was not simple. The author has successfully handled several problems at each step in an elegant manner. For example, although several earlier studies have pointed out that discrete models are unable to capture the late setting times of cements due to mesh effects, this study offers the most effective solution yet on the problem. It is also the first time that creep has been modelled on a young evolving microstructure that is subjected to a time-variable load. Furthermore, each of these issues has been treated to a great depth and not just superficially.

Despite the thoroughness of the models, the minimal variation of fit parameters required to reproduce experimental results demonstrates the tremendous development in our understanding of the hydration of cement. Throughout the work, it can be consistently seen that the introduction of microstructural effects such as flocculation and diffuse growth of C-S-H improves the quality of results. It has also been seen that without introducing these effects, it is difficult to obtain the experimentally observed trends.

At the same time, the results, especially on pore-structure, show that there are still large parts of hydration and microstructural development that we do not understand. As is often said, a good piece of research throws open many more questions than it answers. As models play an increasingly important role in the construction industry, continued efforts to understand these concepts will contribute much beyond mere satisfaction of academic curiosity.

At the end, I would like to congratulate Dr. Do Quang Huy for his hard work and his stubborn perseverance against the challenges he faced during this work.



# Acknowledgements

I would like to thank all the people who helped me over the last four years in the work leading to this dissertation. I would like to acknowledge the Doctoral school at EPFL for accepting me as a PhD student and Swiss National Science Foundation for providing financial support for this research.

I wish firstly to address my great gratitude to Karen, my thesis director, for giving me the opportunity to work at LMC, for her precious advices, stimulating discussions, insightful comments and constructive criticisms, without which this work could not have been successfully carried out. Discussions with Karen not only brought new understandings but also opened new challenges that I needed to face with. She has given me the chance to learn from world leading scientists and approach advanced knowledge.

The second person who has made impacts on my work is Shashank. He was a first person to welcome me to LMC and my thesis co-director. I gratefully acknowledge him for his inspiring guidance, fruitful discussions, invaluable help and support and for his persistent encouragement and for also being my great friend. My research would not be running well without Shashank's supervision. Looking back to the early stage of my doctoral study, I deeply appreciate how enormously patient Shashank was in teaching me. I would not have such patience to teach a student with almost zero knowledge in cement science like me at that time. I have learnt a lot from Shashank when I was working with him despite our geographical distance.

I would like to thank Amor, my thesis co-director, for his enthusiastic guidance and support and for sharing his expertise and knowledge from which my understandings of poro-mechanics have been enriched. The productive discussions with him equipped me to implement mechanical simulations and earned me wonderful results.

I am grateful to Cyrille for his enthusiastic and continuous support and for carefully reading through every line in my thesis and giving me extremely valuable feedback. I consider him as my thesis adviser and the encyclopaedia of all useful information.

I offer my sincere thanks to Matthieu (at Navier, Université Paris Est) who lets me know the philosophy of his experimental data on the creep properties. I enjoyed our short-lasting but very interesting and informative meetings.

I would like to thank my thesis jury members, Gilles from Lafarge, Bernhard from TU Wien and Pietro from Empa, for their reviewing and correcting this research, which helped me to considerably improve this dissertation.

I thank Sandra, Anna-Sandra, Maude, Marie-Alix, Christine for their administrative support, much more beyond their helping me with various logistic issues related to my conference travels and project meetings. I also thank Isabelle, Martina and Nikolas for helping me to submit this thesis in time. Thanks to Frédéric for his enthusiastic help related to human resource administration.

Thanks to all my LMC colleagues, my friends. Thanks to Ruzena for sharing her FE code and giving me a complete training. Thanks to Hui for letting me steal her hard-earned experimental results. Thanks to the geeks: Alain, Adytia, John for their computer tricks, and Olga, Arnaud, Théo, Trinh, Aude, Simone, Silke, Alexandra, 2 Philippe, Amélie, Cheng, Pawel, Berta, Aslam, Jaskanwal, Mohamad, Cedric, Christophe, Lionel, Elise, 2 Julien, Mathieu, Ruben, Mohammadhadi, Yaobo, Nicola, Mohsen, Patrick, Vanessa and Carolina for offering plenty of help, support and enthusiastic collaboration with cheerful attitude, and for all the good moments spent together outside the lab: Satellite, ski seminar, hiking, barbecues...

I am thankful to my former classmates, special friends: Suresh, Raja, Dinesh and Deepak for chat, encouragement, both academic and more practical discussions, and for their kind help with this PhD application.

To my Vietnamese group: Xin cảm ơn anh chị em cộng đồng người Việt Nam, những người bạn tuyệt vời của tôi, vì những giúp đỡ trong cuộc sống, nguồn động viên chia sẻ và sự cảm thông sâu sắc của những người con Việt xa quê hương.

To my family: Tình yêu và sự dạy dỗ của bố mẹ đã là cái nôi nuôi dưỡng cho con tri thức, niềm đam mê khoa học. Dù ở xa nhưng bố mẹ luôn là chỗ dựa tinh thần nguồn động lực vô cùng to lớn tiếp con sức mạnh vượt qua những khó khăn trong học tập nghiên cứu cũng như trong cuộc sống mà nhiều lúc tưởng chừng con không thể vượt qua. Em cảm ơn anh chị Quỳnh Thủy, cháu cảm ơn bà ngoại, các cô, bác, chú, thím, gì, cậu, mợ và các anh chị em từ hai bên nội ngoại đã luôn cổ vũ động viên trong suốt thời gian qua.

Und zum Schluss auch besonderen Dank an meine Freundin, Almut, für ihre Liebe, Fürsorge und Geduld in stressigen Zeiten, dass sie mit mir durch alle Hochs und Tiefs geht, immer zu mir steht, egal, was passiert und auch meine beste Freundin ist.

## Abstract

Autogeneous shrinkage can be important in high-performance concrete characterized by low water to cement (w/c) ratios. The occurrence of this phenomenon during the first few days of hardening may result in early-age cracking in concrete structures. Although the scientific community has reached a fair level of agreement on the basic mechanisms and standard test methods, the prediction of autogeneous shrinkage is still a very challenging task. Good prediction of autogeneous shrinkage is necessary to achieve better understanding of the mechanisms and the deployment of effective measures to prevent early-age cracking.

The aim of this thesis was to develop a numerical, micromechanical model to predict the evolution of autogeneous shrinkage of hydrating cement paste at early age. The model was based on the three-dimensional hydration model *μic* of microstructure and the mechanism of capillary tension to simulate macroscopic autogeneous shrinkage. Pore-size distribution and Mercury Intrusion Porosimetry (MIP) were simulated. Elastic and creep properties of the digital microstructure were calculated by means of numerical homogenization based on the Finite Element Method (FEM). Autogeneous shrinkage was computed by the average strain resulting from the capillary stress globally applied on the simulated microstructure.

It was found that bulk density of C-S-H has to be assumed low at early age and gradually increased at later age to obtain an agreement between the experimentally measured and simulated total porosity. It was found that the experimentally observed break-through diameter from MIP is much lower than the values obtained by applying a numerical algorithm of MIP to the digital microstructure. The effect of some of the most important input parameters on the pore-sizes in the simulated microstructure was explored. The reason which seems best able to explain this discrepancy is that C-S-H is not in fact a phase with a smooth surface as represented in microstructural models, but a phase which grows as needles into the pore space, leading to the formation of very small water filled capillary pores from early ages. This result indicates it will be extremely challenging to reproduce the pore structure of real microstructures in microstructural models on the scale of hundreds of microns necessary to study macroscopic transport. Consequently, it was necessary to use some experimental inputs in the later simulation of the autogeneous shrinkage.

The first approach to determining elastic properties for the modelled microstructure gave values at early ages much higher than experimental ones, due to the connections formed in the microstructure as an artefact of the meshing procedure. Furthermore the percolation of the solids was found to occur even before hydration started. A procedure to remove these artefacts, on the basis of the information available in the vector microstructures was developed. Thanks to this improved procedure, a better agreement of the calculated and experimental results was obtained. More realistic estimates of percolation threshold were obtained if either flocculation of initial placing of particles or a densification of C-S-H with hydration is assumed in the model.

The basic creep of a simulated Portland cement microstructure is computed using Finite Elements. A generalized Maxwell model is used to describe the intrinsic C-S-H viscoelasticity as obtained by nano-indentation tests. It is found that if C-S-H is assumed to be homogenous with bulk density  $\rho = 2.0 \text{ g/cm}^3$  (i.e. with a packing density  $\eta = 0.7$ ), the numerical creep results of cement paste are in good agreements with experimental values for loading from 24 and 30 hours. However, the simulated creep for age of loading 18 hours appeared lower than the measured values: the input bulk density is much higher than its actual value at that time. In a refined model, C-S-H is assumed to have a creep response depending on  $\eta$  that varies with time. This latter model provides better predictions of early age cement paste ageing creep.

Autogeneous shrinkage was modelled using poro-elasticity and creep-superposition methods. It was found that the creep-superposition method provides a much better estimate of shrinkage than does the poro-elasticity method. The simulated results according to the creep-superposition method clearly show the effect of w/c ratio. This also suggested that the contribution of creep to shrinkage is considerable and should not be neglected. Considering C-S-H densification in the simulations provides better predictions of autogeneous shrinkage in early age cement paste.

Keywords: Autogeneous shrinkage, Modelling, Cement hydration, Cement microstructure, Mechanical properties, FEM, Homogenization methods, Ageing basic creep, Porosity analysis, C-S-H densification, Hydration model *μic*.



## Résumé

Le retrait endogène est important dans les bétons à haute performance caractérisés par un faible rapport eau sur ciment ( $e/c$ ). L'apparition de ce phénomène pendant les premiers jours de la prise peuvent conduire à une fissuration au jeune âge des structures en béton. Même si les mécanismes de base et les méthodes de test sont maintenant bien établis au sein de la communauté scientifique, sa prédiction reste une tâche difficile, et nécessaire pour mieux en comprendre les mécanismes et ainsi développer des mesures de prévention.

Le but de cette thèse est le développement d'un modèle numérique et micromécanique pour prédire l'évolution du retrait endogène d'une pâte de ciment au cours de son hydratation. La simulation du retrait endogène à l'échelle macroscopique est basée sur *μic*, une plateforme de modélisation, en trois dimensions de l'hydratation du ciment, et sur les mécanismes de tension capillaire qui interviennent au niveau de la microstructure. La distribution des tailles de pores ainsi que le porosimétrie par intrusion de mercure (MIP) sont simulés. Les propriétés élastiques et de fluage de la microstructure digitale sont calculées par homogénéisation numérique basée sur la méthode des éléments finis (MEF). Le retrait endogène est calculé comme le déplacement moyen résultant des contraintes capillaires globales appliquées à la microstructure simulée.

Afin de reproduire les mesures expérimentales de porosité, la densité des C-S-H doit être faible au jeune âge, et progressivement augmentée durant l'avancement de l'hydratation. Cependant, le rayon critique mesuré par MIP est significativement plus faible que les valeurs obtenues par l'application d'un algorithme numérique de MIP sur la microstructure digitale. L'effet des paramètres les plus importants sur les tailles de pore est exploré. La principale raison de cette différence est que les C-S-H ne présentent pas de surface lisse comme dans le modèle microstructurel, mais se forme en tant qu'aiguilles qui remplissent l'espace poreux, ce qui crée une fine porosité capillaire dès le jeune âge. Cet résultat indique qu'il est très difficile de reproduire la structure poreuse réelle dans les modèles microstructurels sur les échelles nécessaires pour l'étude du transport macroscopique. Ainsi, il est nécessaire d'utiliser certains résultats expérimentaux comme paramètres pour la simulation du retrait endogène.

Les premières tentatives pour déterminer les propriétés élastiques des microstructures modélisées donnèrent des valeurs largement supérieures à celles mesurées, à cause de

connections artificielles induites dans la microstructure par la procédure de maillage. De plus, la precolation de la phase solide apparaissait avant même que l'hydratation ne commence. Une procédure pour supprimer ces artefacts a été développée grâce aux informations contenues dans les microstructures vectorielles. Grâce à cette procédure, une meilleure concordance entre les résultats expérimentaux et numériques a été obtenue. L'estimation du seuil de percolation est améliorée si le modèle inclut la flocculation lors du placement initial des particules ou une densification des C-S-H.

Le fluage de base de la microstructure est simulé avec la FEM. Le modèle de Maxwell généralisé est utilisé pour décrire la visco-élasticité intrinsèque des C-S-H, mesurée expérimentalement par nano-indentation. Si les C-S-H sont supposés homogènes avec une densité constante  $\rho$  de  $2.0 \text{ g/cm}^3$  (ce qui correspond à une densité d'arrangement  $\eta$  de 0.7), le fluage calculé numériquement reproduit avec précision les mesures expérimentales pour des âges de chargement de 24 et 30 heures. Cependant, le fluage simulé pour un chargement de 18 heures est inférieur au fluage expérimental puisque la densité du C-S-H utilisée dans la simulation est supérieure à sa valeur réelle. Des résultats plus proches de la réalité sont obtenus si le fluage des C-S-H dépend de leur densité  $\eta$ , laquelle dépend également du temps.

Le retrait endogène est modélisé en prenant par des méthodes de poro-élasticité et de superposition du fluage. La méthode de superposition du fluage conduit à des estimations plus réalistes que la méthode de poro-élasticité, et est capable de reproduire clairement les effets de rapport e/c. La contribution du fluage au retrait est donc considérable et ne devrait pas être négligée.

Mots-clés : Retrait endogène, Modélisation, Hydratation du ciment, Microstructure du ciment, Propriétés mécaniques, MEF, Méthodes d'homogénéisation, Fluage de base vieillissant, Analyse de la porosité, Densification des C-S-H, Modèle d'hydratation *mic*.

# Zusammenfassung

Autogenes Schwinden kann für Hochleistungsbeton, der sich durch ein niedriges Wasser-Zement-Verhältnis auszeichnet, eine wichtige Rolle spielen. Das Auftreten dieses Phänomens während der ersten Tage des Aushärtens kann zu frühzeitiger Rissbildung im Beton führen. Obwohl sich die Wissenschaft über die Grundmechanismen und Standard-Testmethoden halbwegs einig ist, ist die Vorhersage von autogenem Schwinden immer noch eine sehr große Herausforderung. Eine gute Vorhersage des autogenen Schwindens ist notwendig, um ein besseres Verständnis über die Vorgänge zu erlangen und um effektive Maßnahmen ergreifen zu können, die frühzeitiger Rißbildung vorbeugen.

Das Ziel dieser Doktorarbeit war es, ein numerisches, mikromechanisches Modell zu entwickeln, um die Entstehung des autogenen Schwindens von hydratisiertem Zementleim im frühen Stadium vorherzusagen. Das Modell basiert auf dem dreidimensionalen Hydrationsmodell  $\mu ic$  des Mikrogefüges und dem Mechanismus der Kapillarspannung, um makroskopisches, autogenes Schwinden zu prognostizieren. Die Porengrößenverteilung sowie die Quecksilber-Intrusionsporosimetrie (MIP) wurden simuliert. Elastische Eigenschaften und Kriecheigenschaften des digitalen Mikrogefüges wurden mit Hilfe der numerischen Homogenisierung, basierend auf der "Finite Element Method" (FEM), kalkuliert. Das autogene Schwinden wurde mit der durchschnittlichen Deformation errechnet, die aus der allgemein angewendeten kapillaren Beanspruchung des simulierten Mikrogefüges resultiert.

Es wurde festgestellt, dass die Schüttdichte von C-S-H im frühen Stadium niedrig einzuschätzen ist und sich im fortschreitenden Stadium schrittweise erhöht, um eine Übereinstimmung zwischen der experimentell gemessenen und der simulierten Gesamtporosität zu erreichen. Es stellte sich heraus, dass die im Experiment beobachteten Durchbruch-Durchmesser der MIP weitaus niedriger sind, als die Werte, die sich durch die Anwendung eines numerischen MIP-Algorithmus auf das digitale Mikrogefüge ergaben. Es wurde der Effekt einiger der wichtigsten Eingabe-Parameter der Porengröße im simulierten Mikrogefüge erforscht. Der Grund, der diese Diskrepanz am besten zu erklären scheint, ist, dass C-S-H Phasen tatsächlich gar keine glatte Oberfläche, wie in mikrostrukturellen Modellen dargestellt, haben, sondern wie Nadeln in den Porenraum eindringen, was zu sehr kleinen wassergefüllten Kapillarporen in frühen Stadien führt. Dieses Ergebnis lässt darauf schließen, dass es äußerst anspruchsvoll sein wird, die Porenstruktur von realen Mikrogefügen in mikrostrukturellen Modellen in einer Skala von hunderten von Mikronen zu reproduzieren, um den makroskopischen Transport zu analysieren. Daher war es erforderlich, experimentellen Input für die spätere Simulation von autogenem Schwinden zu nutzen.

Ein erster Ansatz, die elastischen Eigenschaften für die modellierte Mikrostruktur zu bestimmen, ergab weit höhere Werte im frühen Stadium, als in den experimentellen Werten, was auf die Verbindungen zurückzuführen ist, die im der Mikrogefüge als Artefakte während des vernetzungsprozesses gebildet werden. Außerdem stellte sich heraus, dass die Versickerung der Feststoffe schon vor der Hydratation eintrat. Es wurde ein Verfahren, basierend auf den vorhandenen Informationen aus dem Vektor-Mikrogefüge entwickelt, um diese Artefakte zu beseitigen. Dank dieses verbesserten Verfahrens konnte eine bessere Übereinstimmung der kalkulierten und der experimentellen Ergebnisse erreicht werden. Noch realistischere Schätzungen können erzielt werden, wenn im Modell entweder die Ausflockung von erstmalig platzierten Partikeln oder eine Verdichtung von C-S-H mit Hydratation als gegeben angenommen wird.

Das grundlegende Kriechverhalten des simulierten Mikrogefüges wurde unter Anwendung der Finite Element Method (FEM) simuliert. Das "Generalized Maxwell Model" wurde benutzt, um die intrinsische C-S-H Viskoelastizität, die durch Nanoindentationsprüfungen erhalten wird, zu beschreiben. Es wurde festgestellt, dass, solange angenommen wird, dass C-S-H homogen ist, mit einer konstanten Schüttdichte  $\rho$  von  $2.0 \text{ g/cm}^3$  (korrespondierend zu seiner Packungsdichte  $\eta$  von 0.7), die numerischen Ergebnisse des Kriechverhaltens von Zementleim in ausgezeichneter Übereinstimmung mit den gemessenen Werten bei einer Beladung nach 24 und 30 Stunden sind. Das simulierte Kriechverhalten für eine Beladung nach 18 Stunden Lebensdauer erschien jedoch niedriger als die gemessenen Werte, da die angenommene vorgegebene Schüttdichte weit höher war, als ihr aktueller Wert bei 18 Stunden. Das Modell liefert bessere, wirklichkeitsnähere Vorhersagen für den Alterungsprozess von Zementleim in frühen Stadien, wenn angenommen wird, dass C-S-H in seinem Kriechverhalten reagiert, welches abhängig von seiner Packdichte  $\eta$  ist, die mit der Zeit variiert.

Autogenes Schwinden wurde unter der Anwendung des Poroelastizitäts- und Kriechverhalten-Superpositions-Verfahrens dargestellt. Es wurde festgestellt, dass das Kriechverhalten-Superpositions-Verfahren eine sehr viel bessere Schätzung des Schwindens liefert, als das Poroelastizitätsverfahren. Die simulierten Ergebnisse nach dem Kriechverhalten-Superpositions-Verfahren zeigen eindeutig den Effekt des Wasser-Zement-Verhältnisses. Dies deutet auch darauf hin, dass der Einfluss des Kriechverhaltens auf das Schwinden erheblich ist und nicht vernachlässigt werden sollte.

Schlüsselwörter: Autogenes Schwinden, Modellierung, Zementhydratation, Zementmikrogefüge, mechanische Eigenschaften, FEM, Homogenisierungsverfahren, Alterung bei allgemeinem Kriechen, Porositätsanalyse, C-S-H Verdichtung, Hydrationsmodell *µic*.

## Tổng kết

Hiện tượng co ngót tự sinh đóng vai trò quan trọng trong bê tông hiệu suất cao được đặc trưng bởi tỷ lệ nước với xi măng thấp. Sự xuất hiện của hiện tượng này trong những ngày đầu tiên của quá trình hóa rắn có thể dẫn đến sự rạn nứt ngay ở tuổi sớm trong các kết cấu bê tông. Tuy rằng cộng đồng khoa học đã nhất trí ở mức độ vừa phải về cơ chế cơ bản và phương pháp đo lường tiêu chuẩn cho hiện tượng này, nhưng sự dự đoán co ngót tự sinh vẫn còn là một vấn đề rất nan giải. Việc phỏng đoán chính xác co ngót tự sinh là cần thiết để giúp chúng ta hiểu biết rõ hơn về các cơ chế phát sinh của hiện tượng và việc triển khai các phương pháp đo lường hữu hiệu cũng như để ngăn ngừa rạn nứt ở tuổi sớm.

Mục đích của luận án này là phát triển số mô hình mô phỏng vi cấu trúc để dự đoán sự quá trình phát triển của co ngót tự sinh của hồ xi măng đang thủy hợp ở độ tuổi sớm. Mô hình này được dựa trên mô hình ba chiều vi cấu trúc *mic* của quá trình thủy hóa xi măng và cơ chế của áp lực căng mao dẫn để mô phỏng vĩ mô co ngót tự sinh. Sự phân bố kích thước lỗ rỗng và quá trình đo lường xâm nhập lỗ rỗng bằng thủy ngân được mô phỏng. Tính chất đàn hồi và sự đảo môi của vi cấu trúc vật liệu số hóa được tính toán bằng phương pháp đồng nhất vật liệu dựa trên phương pháp phần tử hữu hạn. Co ngót tự sinh được tính toán bởi biến dạng trung bình bởi kết quả của áp lực căng mao dẫn tác dụng ở phạm vi toàn cục lên vi cấu trúc được mô phỏng.

Độ đặc chắc của sản phẩm thủy phân Canxi Silicat Hydrat (C-S-H), đã được nhận thấy rằng, phải được giả định thấp hơn ở tuổi sớm và tăng dần ở độ tuổi trưởng thành để đạt được sự nhất quán về tổng độ xốp rút ra từ thực nghiệm đo lường và từ mô phỏng số. Đường kính "ngưỡng cửa" từ kết quả quan sát thực nghiệm thấp hơn so với giá trị thu được từ áp dụng thuật toán số mô phỏng thí nghiệm trên vi kết cấu được số hóa. Sự ảnh hưởng của một số các thông số đầu vào quan trọng của thuật toán này lên kết quả tính toán của kích thước lỗ rỗng trong mô hình vi cấu trúc mô phỏng đã được xét đến. Lý do mà dường như tốt nhất có thể giải thích sự khác biệt này đó là vật chất C-S-H không phải trên thực tế là một vật liệu với bề mặt trơn nhẵn như đang được mô phỏng trong các mô hình, mà là một vật liệu phát triển như hình kim trong không gian trống, dẫn đến các lỗ rỗng rất nhỏ chứa nước từ tuổi sớm vật liệu. Kết quả này cho thấy rằng sẽ là vô cùng khó khăn để tạo lại cấu trúc lỗ rỗng của các vi cấu trúc thực tế bằng mô hình số vi cấu trúc trên phạm vi hàng trăm micron cần thiết cho nghiên cứu tính giao vận trong vật liệu. Do đó, việc sử dụng một số yếu tố đầu vào từ kết quả thí nghiệm là cần thiết cho các mô phỏng tiếp theo của sự co ngót tự sinh.

Phương pháp ban đầu để xác định độ cứng đàn hồi của mô hình vi cấu trúc đưa ra giá trị ở tuổi sớm cao hơn nhiều so với những giá trị thực nghiệm, điều này là do các kết nối "giả tạo" hình thành trong vi cấu trúc của thủ tục chia lưới trong phương pháp phần tử hữu hạn. Hơn nữa hiện tượng kết nối của các vật chất rắn ở mức toàn cục đã được hình thành xảy ra ngay cả trước khi thủy hóa bắt đầu. Một thủ tục để loại bỏ các kết nối "giả tạo" dựa trên những thông tin vector cơ sở có sẵn trong các vi cấu trúc số đã được thực hiện. Thủ tục cải tiến này đem đến sự nhất quán tốt hơn cho các kết quả giữa tính toán và thực nghiệm. Xét đến sự gieo rắc các hạt xi măng cho tạo kết bông của hoặc kể đến sự lớn dần theo tuổi của mật độ đặc chắc của vật chất C-S-H dẫn đến phỏng đoán tốt hơn đối với ngưỡng kết nối toàn cục của các vật chất rắn trong vi cấu trúc.

Tính dẻo mỗi của vi cấu trúc số hóa được mô phỏng bằng cách áp dụng phương pháp phần tử hữu hạn. Mô hình tổng quát của Maxwell đã được sử dụng để mô tả bản chất đàn nhớt của vật chất C-S-H mà đã thu được từ thực nghiệm bởi phương pháp bám nano. Có thể thấy rằng, nếu vật chất C-S-H được giả định là đồng nhất với một mật độ khối lượng không đổi  $\rho$  2,0 g/cm<sup>3</sup> (tương ứng với mật độ đặc chắc  $\eta$  0,7), kết quả tính toán về độ dẻo mỗi của vữa xi măng là nhất quán cao với giá trị thu được từ thí nghiệm đo lường cho tuổi chất tải từ 24 và 30 giờ. Tuy nhiên, độ dẻo mỗi được mô phỏng cho tuổi chất tải tại 18 giờ là thấp hơn so với giá trị từ thí nghiệm đo lường bởi vì mật độ đặc chắc của vật chất C-S-H đã được giả định là cao hơn nhiều so với giá trị trên thực tế của nó vào lúc 18 giờ. Thực tế hơn, nếu C-S-H được giả định là có một ứng xử dẻo mỗi tùy thuộc vào mức độ đặc chắc của nó  $\eta$  thay đổi theo thời gian, mô hình cung cấp dự đoán tốt hơn tính dẻo mỗi trong hồ xi măng đang trưởng thành.

Tính co ngót tự sinh được mô phỏng số dựa trên phương pháp vật liệu xếp đàn hồi và phương pháp chồng chất dẻo mỗi. Phương pháp chồng chất dẻo mỗi được nhận thấy rằng đưa ra một ước tính co ngót tự sinh tốt hơn nhiều so với phương pháp xếp đàn hồi. Kết quả mô phỏng theo phương pháp chồng chất dẻo mỗi cho thấy rõ ràng hiệu ứng của tỷ lệ nước/xi măng. Điều này cũng cho thấy sự ảnh hưởng của ứng xử dẻo mỗi đến độ co ngót của vật liệu là đáng kể và không nên bỏ qua. Sự kể đến sự lớn dần theo tuổi của mật độ đặc chắc của vật chất C-S-H dẫn đến phỏng đoán tốt hơn mức độ co ngót trong hồ xi măng ở tuổi sớm.

Các từ khóa: Co ngót tự sinh, mô hình, hydrat hóa xi măng, vi cấu trúc xi măng, tính chất cơ học, phương pháp phần tử hữu hạn, các phương pháp đồng nhất, dẻo mỗi cơ bản, phân tích độ xếp, độ đặc chắc của C-S-H, mô hình hydrat  *$\mu ic$* .

# Table of Contents

Acknowledgements .....	iii
Abstract .....	v
Résumé .....	vii
Zusammenfassung .....	ix
Tổng Kết.....	xi
Table of Content .....	xiii
Glossary.....	xvii

## **CHAPTER 1 - INTRODUCTION**

1.1 Overview.....	1
1.2 Research Motivation .....	1
1.3 Research Objectives .....	3
1.4 Research Strategy.....	3
1.5 Layout of the Thesis .....	5

## **CHAPTER 2 - LITERATURE REVIEW**

2.1 Portland Cement: Composition and Hydration .....	7
2.2 Porosity and Water of Microstructural Cement Paste .....	9
2.3 Chemical Shrinkage.....	11
2.4 Autogenous shrinkage and its Mechanisms .....	13
2.4.1 Definition.....	13
2.4.2 Capillary Tension .....	15
2.4.3 Surface Tension .....	17
2.4.4 Disjoin Pressure.....	18
2.5 Factors influencing Autogenous Shrinkage .....	19
2.6 Expansion during Autogenous Deformation.....	20
2.7 Shrinkage, Creep and Cracking .....	22
2.8 Measurement Methods of Autogenous Deformation .....	23
2.9 Numerical Models for Cement Microstructure .....	25
2.10 Modelling Shrinkage in Cement Paste .....	32
2.10.1 Semi-empirical model based on surface tension.....	32
2.10.2 Experiment based model- capillary depression from MIP test .....	34

2.10.3	Experiment based model -capillary depression from change in RH.....	36
2.10.4	Multiscale micromechanics model .....	38
2.10.5	Mathematical/empirical based model .....	40
2.10.6	The previous modelling of autogeneous shrinkage in our laboratory.....	41
<b>2.11</b>	<b>Limitations of Currently available Models of Shrinkage .....</b>	<b>42</b>
<b>2.12</b>	<b>Modelling in the Current Study .....</b>	<b>44</b>

### ***CHAPTER 3 - MATERIAL NUMERICAL SIMULATION OF POROSITY IN CEMENT***

<b>3.1</b>	<b>Introduction .....</b>	<b>45</b>
<b>3.2</b>	<b>Numerical Modelling.....</b>	<b>47</b>
3.2.1	Method to model pore sizes.....	47
3.2.2	Method to model mercury intrusion porosimetry .....	48
<b>3.3</b>	<b>Simulations.....</b>	<b>51</b>
3.3.1	Matching total porosity with simulation results.....	52
3.3.2	Impact of simulation parameters .....	55
<b>3.4</b>	<b>Discussion of results and the “nature of C-S-H” .....</b>	<b>64</b>
<b>3.5</b>	<b>Conclusions .....</b>	<b>66</b>

### ***CHAPTER 4 - SIMULATING THE SETTING TIME AND THE EARLY AGE MECHANICAL PROPERTIES OF TRICALCIUM SILICATE PASTES: EFFECT OF FLOCCULATION AND DENSIFICATION OF CALCIUM SILICATE HYDRATE***

<b>4.1</b>	<b>Introduction .....</b>	<b>67</b>
<b>4.2</b>	<b>Microstructural model.....</b>	<b>70</b>
<b>4.3</b>	<b>Simulations.....</b>	<b>71</b>
4.3.1	Intrinsic elastic properties of chemical phases.....	71
4.3.2	Self consistent scheme(SCS) .....	72
4.3.3	Finite element method(FEM) .....	73
<b>4.4</b>	<b>Mechanical properties.....</b>	<b>73</b>
4.4.1	Comparison with experiments .....	73
4.4.2	Double burning algorithm.....	75
4.4.3	Effect of flocculation of C <sub>3</sub> S particles .....	78
4.4.4	Effect of C-S-H densification .....	79
4.4.5	Combination effect of C-S-H densification and flocculation of C <sub>3</sub> S particles.....	82
<b>4.5</b>	<b>Conclusions .....</b>	<b>82</b>



## **CHAPTER 5 - MICROSTRUCTURAL MODELLING OF AGEING CREEP IN EARLY AGE CEMENT PASTE**

<b>5.1 Introduction</b> .....	<b>85</b>
<b>5.2 Homogenization based on Finite Element Method (FEM)</b> .....	<b>86</b>
5.2.1 Formalize governing equations for linear viscoelastic boundary value problems .....	87
5.2.2 Numerical approach.....	87
5.2.2.1 Constitutive linear viscoelasticity based on internal variables.....	87
5.2.2.2 Linear viscoelastic material model of generalized Maxwell for the uniaxial case.....	88
5.2.2.3 Expansion of the model to a 3D multi-axial isotropic material .....	90
5.2.2.4 Finite element simulation .....	91
<b>5.3 Intrinsic short-term C-S-H Creep Function</b> .....	<b>92</b>
5.3.1 Experiment data .....	92
5.3.2 Generalized Maxwell model fitting for C-S-H constant density $\rho=2.0 \text{ g/cm}^3$ .....	93
5.3.3 Multi generalized Maxwell model fitting for C-S-H densification creep functions .....	94
<b>5.4 Materials and Hydration Simulation</b> .....	<b>98</b>
<b>5.5 Simulation Method for Ageing Creep in Hydrating Cement Paste</b> .....	<b>100</b>
<b>5.6 Results and Discussion</b> .....	<b>101</b>
5.6.1 Assuming C-S-H constant density $\rho =2.0 \text{ g/cm}^3$ .....	101
5.6.1 Assuming C-S-H densification .....	103
<b>5.7 Conclusions</b> .....	<b>104</b>

## **CHAPTER 6 - MODELLING OF AUTOGENEOUS SHRINKAGE IN PORTLAND CEMENT PASTE AT EARLY AGE**

<b>6.1 Introduction</b> .....	<b>107</b>
<b>6.2 Materials and Hydration Simulation</b> .....	<b>108</b>
<b>6.3 Results and Discussion</b> .....	<b>109</b>
6.3.1 Elastic and creep properties.....	109
6.3.2 Calculation of capillary tension.....	113
6.3.3 Autogeneous deformation from experiments.....	115
6.3.4 Modelling autogeneous shrinkage based on poro-elasticity approach.....	117
6.3.5 Modelling autogeneous shrinkage based on creep-superposition approach .....	119
<b>6.4 Conclusions</b> .....	<b>123</b>

## **CHAPTER 7 - CONCLUSIONS AND PERSPECTIVES**

<b>7.1 On the Study of Pore Structure Modelling</b> .....	<b>125</b>
<b>7.2 On the Study of Elasticity Modelling</b> .....	<b>126</b>
<b>7.3 On the Study of Creep Modelling</b> .....	<b>127</b>
<b>7.4 On the Study of Autogeneous Shrinkage Modelling</b> .....	<b>128</b>
<b>7.5 Limitations and Suggestions for Future Research</b> .....	<b>129</b>

***APPENDIX***

**A Modelling of Cement Microstructure in  $\mu\text{ic}$  ..... 133**  
**B Calculation of Cement Fineness ..... 136**  
**C Numerical Homogenization Based on FEM..... 137**  
**D Elastic Properties of Microstructural Portland cement..... 139**  
**E Finite Element Implementation..... 142**

***REFERENCES***

**References ..... 145**  
**Curriculum vitae ..... 161**

# Glossary

## Abbreviations

CV: Computational Volume

DoH: Degree of Hydration

FEM: Finite Element Method

HPC: High-Performance Concrete

MIP: Mercury Intrusion Porosimetry

psd: Particles Size Distribution

RH: Relative Humidity

REV: Representative Element Volume

SCS: Self Consistent Scheme

XRD: X-Ray Diffraction

w/c: Water to Cement ratio by weight

## Cement chemistry notation

C: CaO (lime)

S: SiO<sub>2</sub> (silica)

H: H<sub>2</sub>O (water)

A: Al<sub>2</sub>O<sub>3</sub> (alumina)

F: Fe<sub>2</sub>O<sub>3</sub> (ferric oxide)

\$: SO<sub>3</sub> (sulfate)

C<sub>3</sub>S: Tricalcium Silicate (alite)

C<sub>2</sub>S: Dicalcium Silicate (belite)

C<sub>3</sub>A: Tricalcium Aluminate (aluminate)

C<sub>2</sub>(A,F): Calcium Aluminoferrite (ferrite)

C-S-H: Calcium Silicate Hydrate

CH: Calcium Hydroxide (Portlandite)



# Chapter 1: Introduction

## 1.1 Overview

Recent years have seen the increasing use of high-performance concrete (HPC) which can bring exceptional benefits both technical and economical. HPC is being regularly used in many applications including bridge decks, buildings, offshore structures, pavements and other infrastructures. Compared to traditional concrete, HPC typically possesses many advantageous properties such as, high strength, high elastic stiffness, low permeability, high abrasion and corrosion resistance. However, these types of concretes have a higher risk of early-cracking than traditional concretes [RILEM TC 181-EAS (2002)], due to the use of low water/cement ratios and, in some cases, addition of silica fume. Early age cracking will have a detrimental impact on the long term performance of HPC if it is not properly cured.

Autogeneous shrinkage is one of major causes of cracking of HPC. Autogeneous shrinkage arises due to self desiccation of the concrete as water is consumed by the hydration process. After setting, the chemical shrinkage on hydration results in the formation of voids in the pastes. Menisci at the interface between the gas filled voids and the pore solution exert capillary forces. Cracking will occur if the strains from autogeneous shrinkage and aggregate restraint, exceed the tensile strength of the concrete. This is most likely at early age when the concrete has a low tensile strength.

## 1.2 Research Motivation

The long-term performance of cementitious materials is strongly dependent on their property development at early ages. Controlling early-shrinkage is of paramount importance to ensure long-term durability. Apart from thermal strains, early-age deformation includes two similar phenomena: autogeneous shrinkage and drying shrinkage. Autogeneous shrinkage is caused by chemical shrinkage as the volume of hydration products is less than the sum of the volume of the hydrated and the water consumed. Drying shrinkage is caused by the loss of water due to evaporation from the cement surface to the environment. Autogeneous shrinkage occurs even when there is no exchange of moisture with the environment, due to self desiccation through the consumption of water by the hydration process. While drying shrinkage can be

avoided or mitigated by appropriate curing, autogeneous shrinkage is difficult to overcome and occurs simultaneously in the first days of hydration.

Although the autogeneous shrinkage phenomenon and its impact on performance of cementitious materials have long been realized, the mechanism behind it has not been fully understood. While a fair level of agreement by the scientific community on standard test methods and the basic mechanisms has been reached [Lura 2003], the prediction of shrinkage is still very challenging [van Breugel 2001].

The extraordinary improvement of computer science in the last two decades has brought a great progress of computer based scientific research. Availability and good performance of computers provide the possibility of intensive simulations to numerically describe complex mechanism of early-shrinkage that is influenced by many factors, both internal and external, including environment conditions, mixture characteristics, and curing practices. Computer based numerical simulations offer a distinct approach to study material properties by comparison to values computed from a model to those experimentally observed. One of the major problems in studying cementitious materials at early ages is the large number of interactions amongst chemical and physical mechanisms. The advantage of numerical models is that they are effective to treat separately modelled mechanisms, while experimental techniques are generally difficult to isolate the effects caused by individual mechanism. For example, under realistic conditions, the hydration process of cement at early ages generates heat and causes temperature rise and accelerates hydration rate. The behaviour of autogeneous shrinkage during variable temperatures therefore is complicated by the fact that the measured deformation is the coupling of autogeneous shrinkage and thermal dilation. Another example is the presence of creep effects which are widely acknowledged to play a role in autogeneous shrinkage. The total measured shrinkage is the sum of elastic and creep deformations. It has been found that the creep makes a significant contribution to the total deformation and therefore its effect has to be taken into account [Hua *et al.* 1995, Lura *et al.* 2003, Jaouadi 2008]. The quantification of creep effect during early hydration is very complex due to continuous changes of cement microstructure.

Another advantage of modelling approaches is that numerical models are versatile in multi-scale applications. For an example, a standard FEM framework can be an effective tool for scale bridging of intrinsic C-S-H viscoelasticity at the nano-level to creep behaviour of

cement paste and possibly concrete at the macro-level. The model, therefore, could be used not only to achieve better understanding of creep mechanism but also to provide practical prediction of creep for the cement and concrete industry.

### 1.3 Research Objectives

The overall objective of this research is to develop a micromechanical model to predict the evolution of autogeneous shrinkage of hardening cement paste at early age. The aim of the model is to go directly from an existing hydration model of microstructure through the mechanisms to the macroscopic result of autogeneous shrinkage. The modelling approach is guided by the following research objectives:

- Study the impact of degree of hydration for isothermal hydration temperature of 20° C and the influences of mixture characteristics (e.g. the chemical compositions, w/c ratio and fineness) on the microstructural porosity.
- Develop numerical methods to characterize modelled microstructural porosity by pore size and MIP simulations.
- Develop FEM and SCS homogenization models on the modelled microstructure to calculate effective elastic properties of cement paste.
- Develop FEM model on the modelled microstructure to predict creep of cement paste based on C-S-H creep properties available in the literature.
- Study autogeneous shrinkage mechanisms and assess the prediction of autogeneous shrinkage by different modelling approaches.

### 1.4 Research Strategy

Various mechanisms have been proposed to explain autogeneous shrinkage, such as surface tension of colloidal particles, disjoining pressure and capillary tension. Among these mechanisms, the capillary tension is widely accepted by most authors [Hua *et al.* 1995, Tazawa and Miyazawa 1995a, Bentz and Jensen 2004, Lura *et al.* 2003, Coussy *et al.* 2004, Gawin D. *et al.* 2008]. The current study is therefore, based on the capillary tension mechanism to predict autogeneous deformation.

The microstructural modelling platform *μic* [Bishnoi and Scrivener 2009] has been developed to model the development of hydrating cement pastes. *μic* uses the vector approach to represent the geometry of the microstructure. Due to its flexible design, the users of the

platform can define custom materials, particles and reactions, and control the development of the microstructure by defining laws that define the mechanisms of the reactions.  $\mu ic$  is constantly updated to our recent improvements in our understanding of cement hydration in ability to model these mechanisms. For these reasons,  $\mu ic$  is chosen as the model to simulate cement hydration microstructure, porosity, mechanical properties and shrink deformation.

Overall, the modelling approach in this study goes directly from  $\mu ic$  microstructure through the capillary tension mechanism to obtain the macroscopic result of autogenous shrinkage. The flowchart of the modelling process is sketched in figure 1.1.

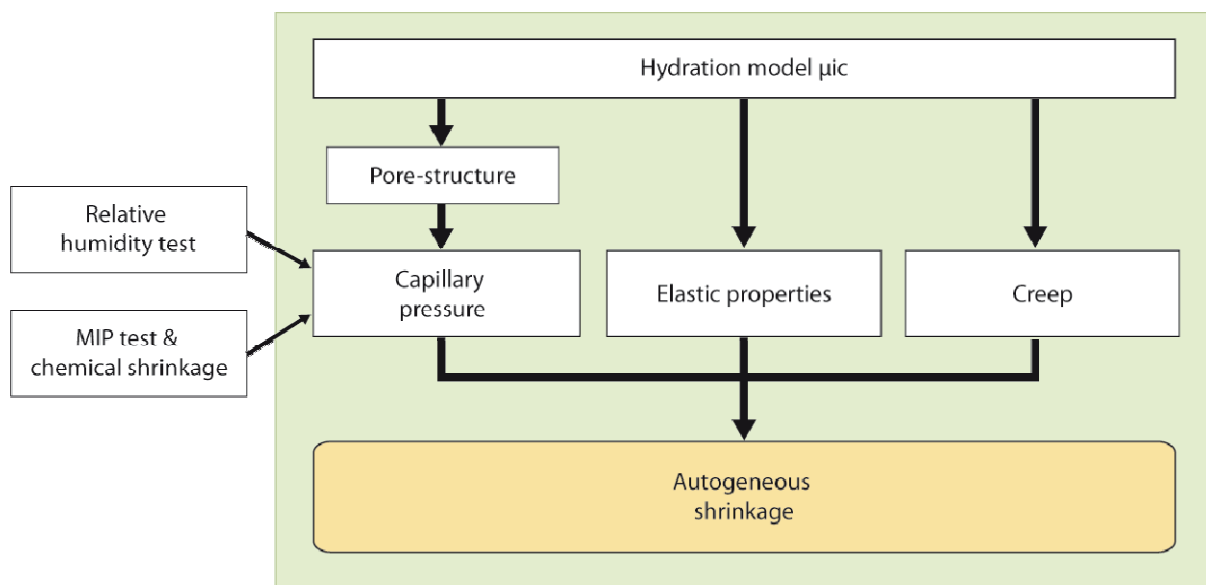


Figure 1.1: The flowchart of the modelling approach of autogenous shrinkage. At the outset of this thesis, it was planned to simulate autogenous shrinkage based purely on numerical approaches. However, the exploration of the simulated pore structure in chapter 3 indicated that simulation does not well capture the real pore structure due to the rough, “diffuse” nature of C-S-H. Therefore, the experimental input was used to estimate the capillary tension.



## 1.5 Layout of the Thesis

The following chapters discuss numerical modelling of porosity, mechanical properties and autogenous shrinkage on cement microstructures simulated by *μic*.

Chapter 2 reviews the literature. It provides a brief introduction on chemical compositions and hydration of Portland cement and microstructural models and modelling approaches of shrinkage. The advantages and drawbacks of currently available models are also discussed.

Chapter 3 discusses our study on porosity simulations. The two numerical methods of pore size and MIP simulations pore size to characterize porosity in the modelled microstructure are presented. Various microstructural model parameters that impact calculated results also are discussed. The chapter is closely based on a paper accepted for publication.

Chapter 4 discusses our study on microstructural modelling of elasticity properties of C<sub>3</sub>S paste at early ages. FEM and SCS homogenization approaches on microstructural models are presented. The microstructural model parameters that influence the setting time are discussed. A paper based on this chapter has been submitted for publication.

Chapter 5 presents a microstructural model based on FEM to predict basic creep in hydrating pastes at early ages. The densification of C-S-H and the development of microstructure during creep simulations are taken into account. The method demonstrates that the numerical model can serve as an effective tool for bridging of mechanical properties of cement paste from the nano-level to the macroscopic level.

Chapter 6 presents analytical and numerical approaches based on the capillary tension mechanism to assess autogenous shrinkage. It is demonstrated that application of the creep superposition approach on the modelled microstructure with C-S-H densification can explain high shrinkage of cement pastes at low w/c ratios.

Chapter 7 presents the conclusions of the study and proposes the perspectives for further numerical and experimental studies on autogenous shrinkage.



## Chapter 2 Literature Review

### 2.1 Portland Cement: Composition and Hydration

Portland cement was invented in early 19<sup>th</sup> century and is now the most used material in the world. It is notably used in buildings and infrastructures. Portland cement is produced by firing a mixture of raw materials containing limestone, clay, silicious sand and iron oxide in a rotary kiln at a calcining temperature (around 1450 ° C for modern cements [Taylor 1997]). The minerals fuse and form clinker nodules after cooling. Portland cement clinker is primarily composed of calcium oxide, silicon dioxide, aluminium oxide and ferric oxide. The nodular clinker is then mixed with a small amount of gypsum (typically about 5% in order to archive the desired setting qualities of the final product) and is finely ground to form the final cement powder.

The phases in Portland cement are tricalcium silicate ( $C_3S$ ), dicalcium silicate ( $C_2S$ ), tricalcium aluminate ( $C_3A$ ) and calcium aluminoferrite ( $C_2(A,F)$ ), and their typical percentages by mass are listed in tables 2.1. In Portland cement these actual phases are present in their impure forms with ionic substitutions in their crystalline structures. These impure phases are named by cement chemists as alite, belite, aluminate and ferrite.

Table 2.1 Contents of Portland cement

Compound	Phase Name	Abbreviation	Typical Amount
Tricalcium Silicate	Alite	$C_3S$	50-70%
Dicalcium Silicate	Belite	$C_2S$	10-30%
Tricalcium Aluminate	Aluminate	$C_3A$	5-10%
Calcium Aluminoferrite	Ferrite	$C_2(A,F)$	5-15%
Calcium Sulfate	Gypsum	$CSH_2$	2-10%

Cement reacts with water in a process called hydration. Hydration consumes the clinker phases and forms product phases. The total volume of solid phases (the clinker plus the product) increases while the volume of water decreases. During hydration, the mixture of cement and water, commonly called cement paste, decreases its overall volume and converts

it into a stiff solid. A simplified evolution of volume fractions of cement phases in a typical cement paste of w/c ratio 0.5 is illustrated in figure 2.1.

The hydration of cement is a complex exothermic process. The reaction rate of the individual clinker phases differs from one to another. Though aluminate is the most reactive phase among the four clinker phases, alite controls the hydration kinetics at early age in well-sulfated systems. While alite and aluminate phases react rapidly, belite and ferrite react slowly and for longer durations. The overall progress of hydration is traditionally measured using the heat flow as measured by differential scanning calorimetry (DSC). The typical heat evolution profile during approximately the first 3 days of hydration of ordinary Portland cement is sketched in figure 2.2.

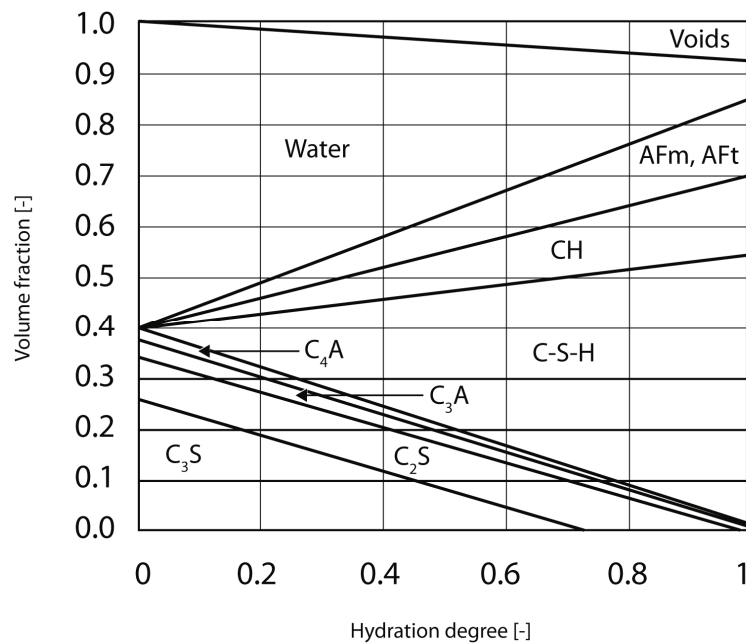


Figure 2.1: A simplified evolution of volume fractions of cement phases in a typical cement paste at w/c ratio 0.5 [Bernard *et al.* 2003]

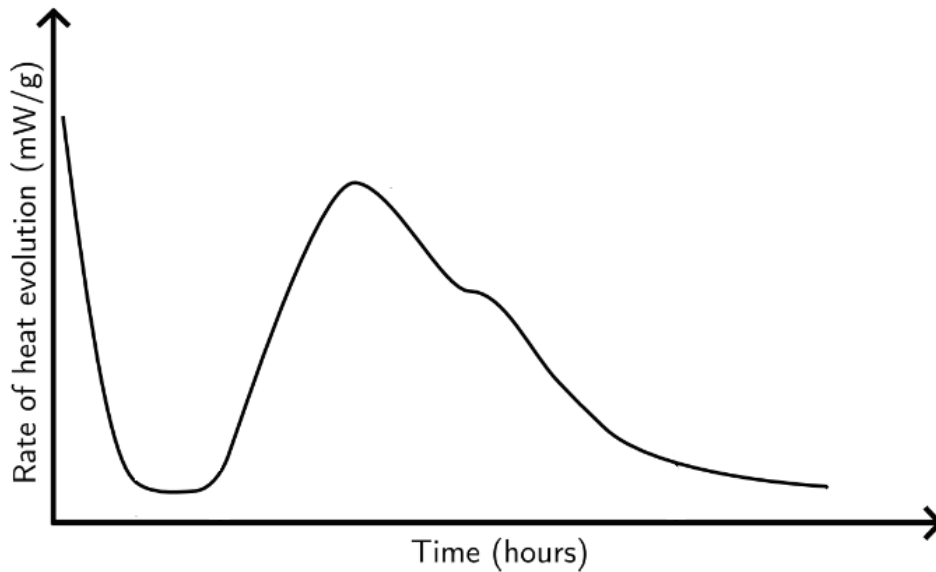


Figure 2.2: Typical heat evolution curve of Portland cement [Bishnoi 2008]

## 2.2 Porosity and Water of Microstructural Cement Paste

As a result of hydration, hydrates bind cement particles and a solid skeleton of the hardening cement paste is formed. The microstructure of cement paste develops from solid particles isolated in the liquid phase to a partially saturated porous solid. The capillary porosity of the cement paste gradually reduces. The pore structure is the crucial factor controlling most engineering properties of cementitious materials including strength, elastic modulus, durability, transport and shrinkage.

The term “pore structure” covers the pore size distribution, the connectivity of the pore system and the volume of pores. The geometry of pores is very complex, and their classification is not strictly established either by size or shape. Two main types of pores in cement paste can be classified: *gel pores* and *capillary pores* as sketched in figure 2.3. The gel pores are an intrinsic part of C-S-H and their sizes are too small to induce menisci in them at practically observed relative humidity. During hydration, the gel pores increase in their total volume but their size may remain constant. On the contrary, the capillary pore sizes as well as the overall capillary porosity volume decrease during hydration. The capillary pores are partially or completely filled with water as a function of the environmental humidity, which can take part in the continuous hydration of cement clinkers. Despite their differing

origins, there is no sharp size cut-off between capillary pores and gel pores. The capillary pores are considered to have a size of ranging from tens of micrometers down to tens of nanometers, with the lower end of their size range overlapped by the upper end of the C-S-H gel pore-size distribution.

The classification of the states of water in a microstructural cement paste is important to understand the volume changes that are associated with water kept within pores. In a hydrating cement paste, water can be present in many states, and these may be classified by the degree of ease or difficulty with which water can be evacuated. As water is continuously consumed and internal relative humidity of cement paste is gradually reduced with hydration, then the drying process of the pore network starts from big pores to small pores (discussed in detail in section 2.4.2) the dividing thresholds between the different forms of water are not rigid. Figure 2.4 shows the total NMR intensity at 20 MHz as a function of sample mass during controlled drying of an underwater cured white cement paste at w/c ratio of 0.4 [Muller *et al.* 2013]. From the NMR signal it is possible to identify the water in the different types of pore space as a function of relative humidity. As the RH decreases, the capillary pores empty first and contain no more water by 80% RH, then the gel pore progressively empty down to about 20% RH.

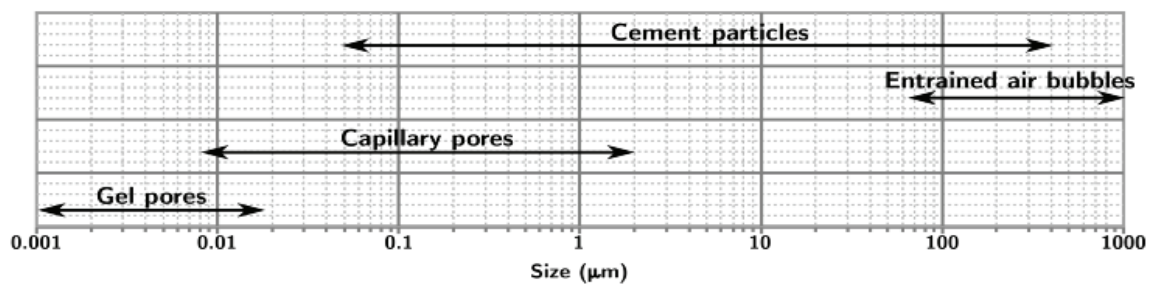


Figure 2.3: Dimensional ranges of solids and pores in hydrated cement paste [Mehta and Monteiro 2006]

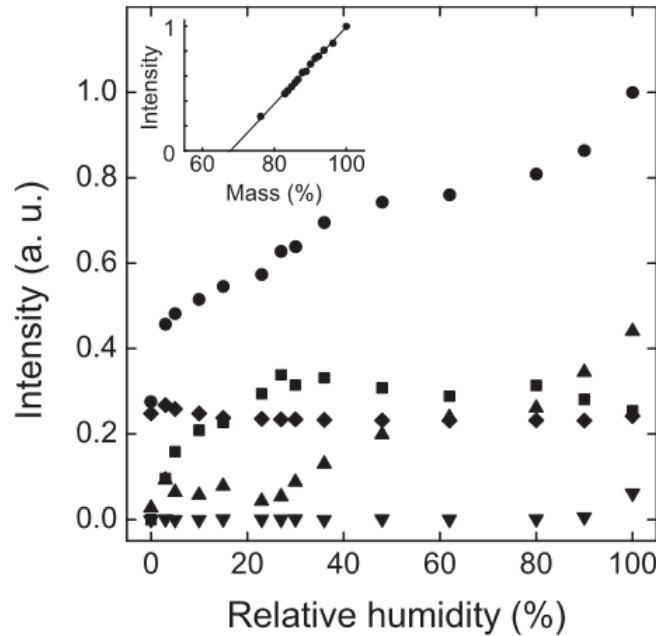


Figure 2.4: Inset: The total normalised NMR signal against relative sample mass in progressively dried white cement paste. Main: The total signal plotted against relative humidity (circles) and de-composed into chemically combined water (diamonds), and water in C-S-H interlayer spaces (squares), gel pores (triangles) and capillary pores (inverted triangles): the pore-specific desorption-isotherm. Notice that, as gel pores empty, so residual water on the C-S-H surface appears similarly to the interlayer space one. Hence this signal increases [Muller *et al.* 2013]

### 2.3 Chemical Shrinkage

The overall volume of the hydration products is smaller than the combined volume of the reacted cement and consumed water. This reduction in volume is called the chemical shrinkage of cement paste, and also known as Le Châtelier contraction [Le Châtelier 1900]. Experimental assessments of chemical shrinkage usually give a value of chemical shrinkage in the range of 6-8% of initial volume at full hydration [Powers and Brownyard 1948].

Chemical shrinkage increases with the degree of hydration and after setting, this is accommodated as empty pore volume in the hardening paste. Figure 2.5 [Neville 1996] illustrates the volumetric proportions in a cement paste with w/c of 0.475 in a sealed condition

at three different degrees\* of hydration. It is assumed that the initial volumes were 60 ml of water and 40 ml of cement. At 100% degree of hydration, the 40 ml of cement produces 61.6 ml of solid hydration products that are the solid part of the cement gel. The volume of the total reaction products including the solid products, gel water and capillary water is 92.6 ml, which is 7.4 ml less than the initial volume of 100 ml. This volume of 7.4 ml of the capillary pores is empty and represents the ultimate chemical shrinkage.

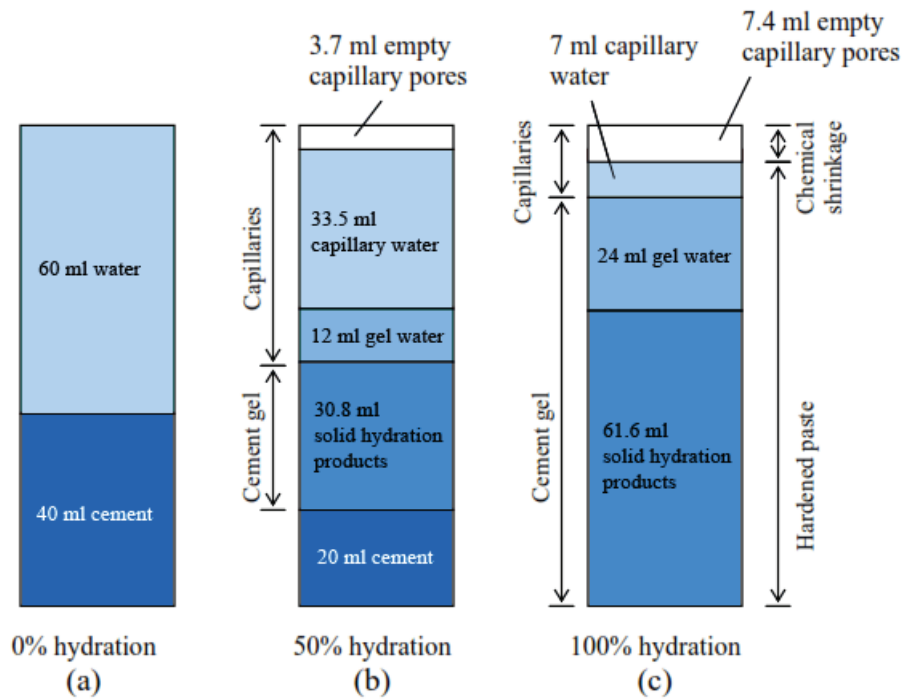


Figure 2.5: Schematic representation of the volumetric proportions of sealed cement paste of  $w/c = 0.475$  at different stages of hydration [Neville 1996]

Table 2.2: Net volume of  $C_3S$  hydration

	$C_3S$	+	5.3 H	→	$C_{1.7}SH_4$	+	1.3 CH
Number of molecule	1		5.3		1		1.3
Mole mass (g/mol)	228		18		227.4		74
Mass of reaction (g)	228		95.4		227.4		96.2
Density ( $g/cm^3$ )	3.15		1		2		2.24
Volume of reaction ( $cm^3$ )	72.4		95.4		113.7		42.9
	$V_{\text{reactants}} = 167.8$				$V_{\text{products}} = 156.6$		

\* The degree of hydration is defined as the amount of cement reacted divided by original amount of cement



The chemical shrinkage depends not only on the cement type, but also on cement content and degree of hydration. As it is impossible to exactly quantify all cement hydration reactions, the ultimate chemical shrinkage cannot be calculated precisely even if the initial mineral composition of the cement is known. This is because C-S-H compounds are poorly defined in terms of their chemical composition and crystallization. Values are given for C-S-H density range from 1.85 to 2.1 g/cm<sup>3</sup>. [2002]. The ultimate chemical shrinkage of C<sub>3</sub>S hydration can therefore vary from 2% to 10%. Table 2.2 shows the calculation using C-S-H density of 2.0 g/cm<sup>3</sup>, which leads to about 6.7% of the ultimate chemical shrinkage. In this thesis, the calculation of chemical shrinkage in model  $\mu$ ic takes into account the total change in solid and liquid volumes from the chemical reactions.

## **2.4 Autogeneous Shrinkage and Its Mechanisms**

### **2.4.1 Definition**

Chemical shrinkage is the reduction in volume at the molecular level of cement paste and it is the underlying driving force for the macroscopic bulk deformation. Chemical shrinkage is identical to the bulk deformation while the cement paste is fluid. When the hydrates percolate, forming the first interconnected solid paths, partially saturated pores start to form and menisci cause hydrostatic tensile stresses in the pore fluid. These stresses cause the bulk deformation, also known as autogeneous deformation. The transition time of hardening paste into a solid is defined as the setting time. The setting shrinkage is much smaller than the ultimate chemical shrinkage (see figure 2.6).

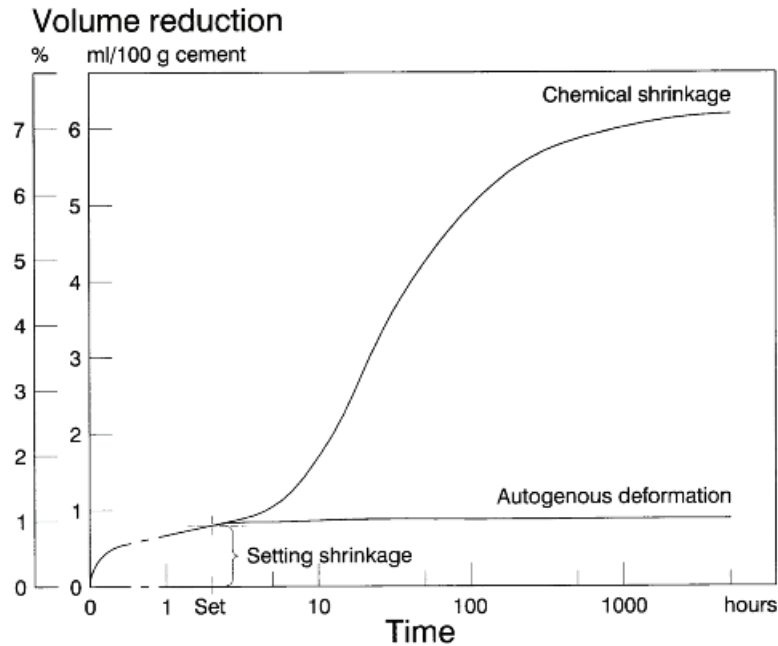


Figure 2.6: Chemical shrinkage and autogenous shrinkage of cement paste [Jensen and Hansen 2001]. Shrinkage is plotted as positive

The following terminologies related to autogenous shrinkage are adopted from the literature [Jensen and Hansen 2001b].

**Autogeneous deformation:** The bulk deformation of a closed, isothermal, cementitious material system not subject to external forces.

**Autogeneous relative humidity change:** The change of internal relative humidity in a closed, isothermal, cementitious material system not subject to external forces.

**Self-desiccation:** Autogeneous relative humidity change of a cementitious material system after setting, caused by chemical shrinkage.

**Self-desiccation shrinkage:** Autogeneous deformation of a cementitious material system after setting, caused by chemical shrinkage.

Note that “*closed*” means no exchange of water occurs between the cementitious material and the surroundings; “*isothermal*” requires that the temperature be kept constant.

Autogeneous deformation might be divided into autogenous shrinkage and possible short-term autogenous expansion that may be attributed to the formation of crystalline hydration products at the early stage of cement hydration. This thesis focuses on autogenous shrinkage.

Commonly, three mechanisms have been proposed to explain autogeneous shrinkage, namely surface tension of the solid gel particles, disjoining pressure and changes in tension in capillary water [Lura *et al.* 2003]. The following subsections will present a basic review of each mechanism.

#### 2.4.2 Capillary Tension:

The chemical shrinkage creates internal empty pores within cement paste as soon as the solid skeleton is formed and gas filled voids, bounded by liquid-gas menisci, start to nucleate and grow in the unsaturated pores that have the largest radii. The capillary tension in pore liquid is identical to the pressure difference across the liquid-air interface of the menisci. This capillary tension is related to the radius of menisci by the Laplace (also known as Young- Laplace) equation:

$$p_c = -\frac{2 \sigma \cos\theta}{r} \quad (2.1)$$

Where  $p_c$  [N/m<sup>2</sup>] is the capillary tension in the pore liquid,  $r$  [m] is radius of the menisci (also known as Kelvin radius),  $\sigma$  [N/m] is the surface tension of the fluid,  $\theta$  is wetting angle between the liquid and solid.

The relation between capillary pressure and internal relative humidity is given by the Kelvin equation:

$$p_c = \frac{R T \ln(RH)}{V_m} \quad (2.2)$$

Where:  $R$  is the gas constant (8.314 J/mol K);  $T$  is the absolute temperature [K];  $V_m$  [m<sup>3</sup>/mol] is the molar volume of liquid and  $RH$  is the internal relative humidity [-].

The Kelvin and Laplace equations can be combined into the Kelvin-Laplace equation:

$$\ln(RH) = \ln\left(\frac{p}{p_o}\right) = -\frac{2 \sigma \cos\theta V_m}{r R T} \quad (2.3)$$

Where  $p$  is vapour pressure over the liquid [N/m<sup>2</sup>],  $p_o$  is the saturation vapour pressure [N/m<sup>2</sup>]

During hydration water is continuously consumed and internal relative humidity of cement paste is gradually reduced, then the drying process of the pore network starts from big pores to small pores. As the consequence, all pores with radius smaller than the meniscus radius are liquid filled, whereas all pores with radius bigger than the meniscus radius are empty (see figure 2.7).

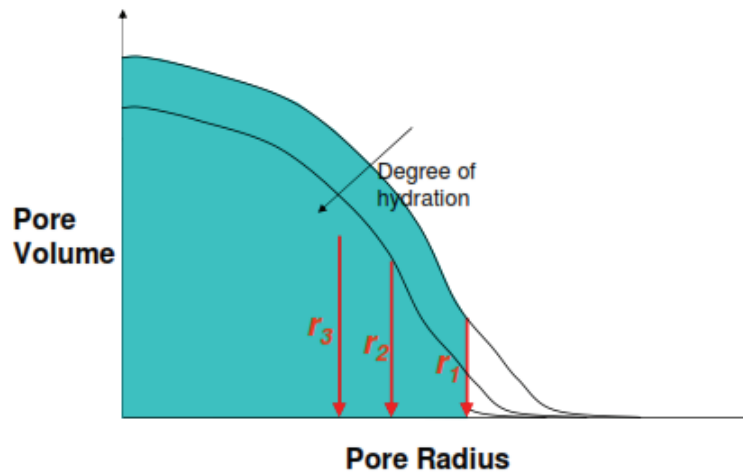


Figure 2.7: Self desiccation process from bigger pores to smaller pores in sealed cement paste  
[Bentz and Jensen 2004]

As deduced from the Laplace equation, the liquid in the capillary pores is under tensile stress that is balanced with the compressive stress in the solid skeleton [Powers 1965]. The compressive stress causes a decrease in the bulk volume, also known as shrinkage, of the cement paste. Both the tensile stress in liquid and shrinkage in cement paste increase with the development of the chemical shrinkage and the degree of hydration.

It is important to note that capillary menisci become unstable if the internal relative humidity drops below around 45% [Soroka 1979, Mindess and Young 1981]. For this reason, this mechanism is valid only for the upper range of relative humidity, certainly above 45% and probably much higher. However, as the relative humidity due to self-desiccation alone varies in the range of 100-75% [Jensen 1995] (hydration stops at lower relative humidities); this nevertheless supports the idea that capillary tension is the main mechanism to cause autogenous shrinkage.

Derived from the Kelvin-Laplace equation (2.3), figure 2.8 depicts the relations and the evolution ranges of internal relative humidity, Kelvin radius and capillary tension in cement paste.

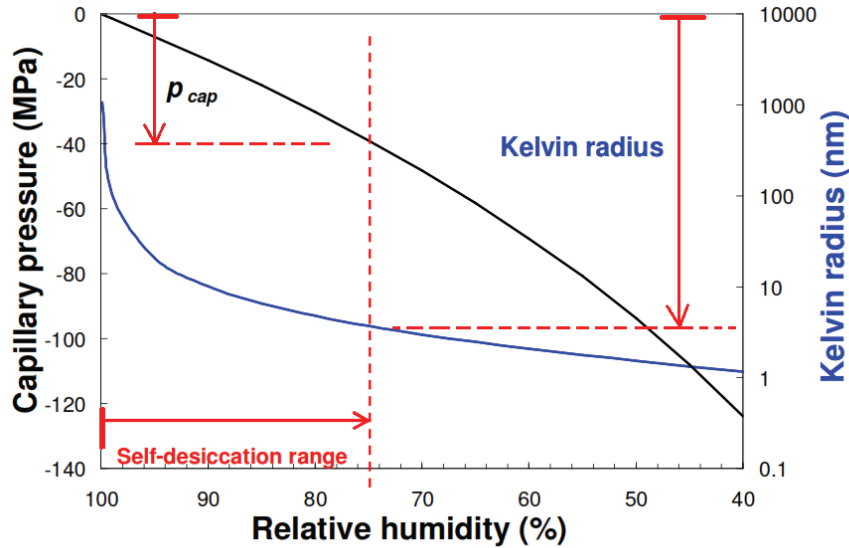


Figure 2.8: The relations and the evolution ranges of internal relative humidity, Kelvin radius and capillary tension in cement paste [Lura 2009]

### 2.4.3 Surface Tension

The surface tension approach postulates that changes in the surface tension of the solid gel particles may causes bulk shrinkage and expansion of the cement paste. Adsorption of water layers decreases the surface tension of the cement gel hydrates and leads to expansion, whereas desorption of water layers leads to shrinkage [Powers 1968]. The magnitude of the bulk expansion/shrinkage is dependant on the thickness of adsorbed/ desorbed the layers of water.

An equation proposed by Bangham and Fakhoury [1930] to relate swelling of coal to changes in the surface tension is:

$$\frac{\Delta l}{l} = \lambda \Delta \sigma \quad (2.4)$$

Where  $l$  [m] is the length,  $\Delta l$  [m] is the length change,  $\Delta \sigma$  [N/m] is the change in surface tension of the solid gel particles, and  $\lambda$  [s<sup>2</sup>/kg] is a coefficient of proportionality.

The coefficient depends on the internal surface of the porous body, on the density of the solid and on the elastic modulus of the porous material [Hiller 1964]:

$$\lambda = \frac{\Sigma \rho_s}{3 E} \quad (2.5)$$

Where  $\Sigma$  [m<sup>2</sup>/kg] is pore wall area of empty pores,  $\rho_s$  [kg/m<sup>3</sup>] is the density of the solid and  $E$  [MPa] is the elastic modulus of the porous material.

Because only adsorbed (or physically bound) water impacts surface tension, this mechanism is valid only at low humidity [Powers 1965], when variation in water content of the cement paste are mainly due to variation in only the first two or three adsorbed water layers. Later, it was suggested that this mechanism is valid in the range of the humidity of 5-50 % [Wittmann 1968, Wittmann 1982].

On the other hand, self-desiccation only caused a drop in the internal relative humidity from 100% to about 75%. Hydration ceases at lower values [Jensen 1995]. The mechanism, therefore, should not play a major role in autogeneous deformation [Lura *et al.* 2003].

#### 2.4.4 Disjoining Pressure:

This mechanism, derived from van der Waals's force, concerns the interaction between two solid surfaces (e.g. C-S-H sheets) whose distance is smaller than twice the thickness of the free adsorbed water layer. At a given temperature, the thickness of the adsorbed water layer is related to the relative humidity. However, the layer of adsorbed water can no longer develop freely up to a certain relative humidity as the distance between the two solid surfaces is too small. If the relative humidity continues to rise, the adsorption induces the “disjoining pressure” to separate the two solid surfaces in order to increase the thickness of the adsorbed layer. A simplified sketch to describe disjoining pressure mechanism is depicted in figure 2.9.

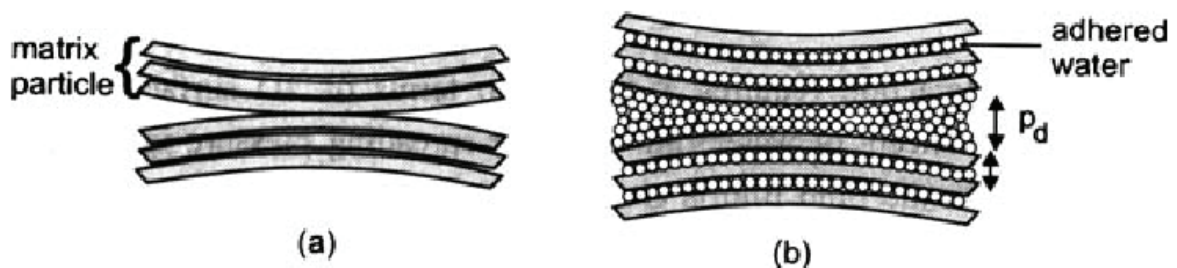


Figure 2.9: Disjoining pressure  $p_d$ : (a) dry matrix material and (b) matrix material with adhered water [Visser 1998]

Due to the progress of hydration, self-desiccation in cement paste lowers the relative humidity and the disjoining pressure decreases. Shrinkage, therefore, occurs since the two surfaces move close to each other.

The disjoining pressure is practically constant when the relative humidity varies from 80 % to 100 % [Ferraris 1986]. Moreover, when the relative humidity remains high in this range, its variation does not impact much adsorbed/desorbed water molecules, and hence the change of disjoining pressure should not be the driving force of autogenous shrinkage.

## 2.5 Factors Influencing Autogenous Shrinkage

### *Water cement ratio:*

Water to cement ratio (w/c) has been considered as the major parameter that impacts the autogenous shrinkage of cementitious material. Lower w/c ratio pastes show higher autogenous shrinkage. This is because pastes with a lower w/c ratio promote self-desiccation and more significant drops in internal relative humidity. In pastes with low w/c ratios, capillary stresses are induced in finer pores due to a lower total porosity in these pastes and the increase in the bulk stiffness is not sufficient to counteract the higher stresses, which leads to an increase in the observed shrinkage (see figure 2.10).

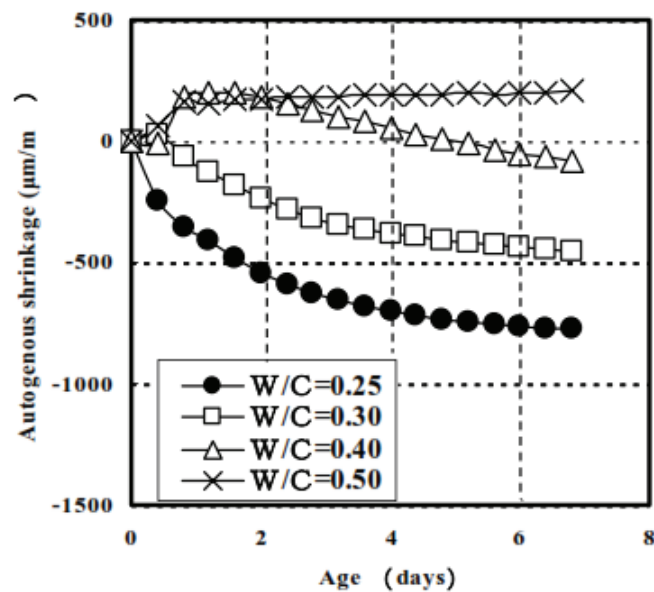


Figure 2.10: Influence of w/c ratio on autogenous shrinkage of cement paste [Nawa and Horita 2004]

### *Mixture characteristics:*

Characteristics of the mixture, both fineness and mineral composition influence the evolution of autogenous shrinkage [Tazawa and Miyazawa 1995, Jensen 2000]. Cement with finer

particle size accelerates hydration rate, increases the rate of internal relative humidity drop, and results in higher shrinkage (see figure 2.11). The cement paste with added silica fume was found to have higher self-desiccation and autogenous shrinkage than the traditional Portland cement paste [Jensen and Hansen 1996].

According to literature [Tazawa and Miyazawa 1995, Baroghel and Kheiberk 2001] early shrinkage depends primarily on the content of aluminate ( $C_3A$ ), and in fact, the reaction of  $C_3A$  with water has higher chemical shrinkage than reactions of other cement phases. According to other reports [Jensen 2000] however, it was also proposed that  $C_3A$  may mitigate autogenous shrinkage by microscopic expansion due to formation of ettringite. This contradiction indicates that the influence of the cement composition on autogenous deformation is still not well understood.

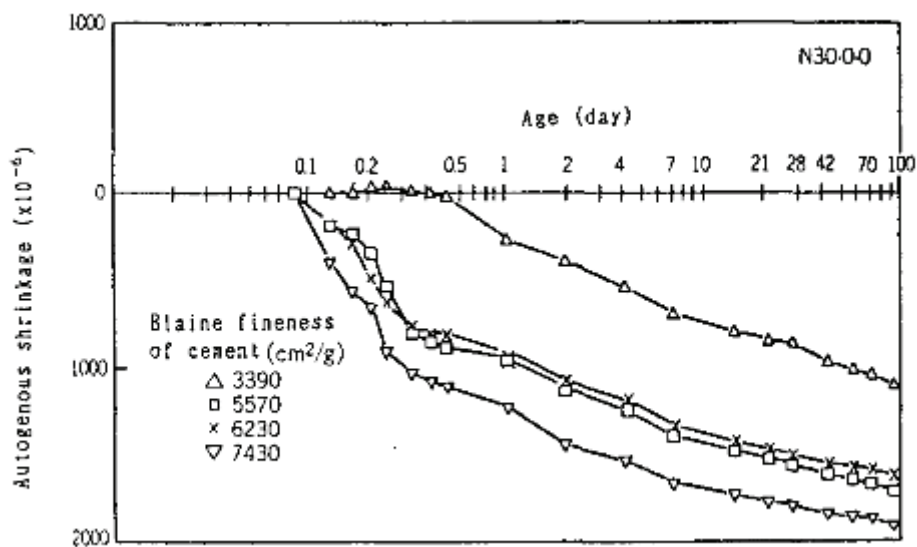


Figure 2.11: Influence of fineness on autogenous shrinkage of Portland cement paste [Tazawa and Miyazawa 1995]

## 2.6 Expansion during Autogenous Deformation

Expansion of concrete under natural conditions occurs at early age due to re-absorption of bleeding water [Bjøntegaard 1999]. If the bleeding water is removed, the expansion was considerably reduced. On the contrary, if extra water is added in a bleeding sample, the expansion is larger and lasts longer.



While the actual mechanisms leading to bulk expansion in isothermal conditions are still under discussion, it has been believed that a crystallization pressure [Scherer 1999], e.g. induced by formation of ettringite [Scherer 2004] or Portlandite [Sant 2011, Sant *et al.* 2011], develops inside pore spaces and may cause moderate swelling of the paste.

It must be pointed out that the driving force for shrinkage is different from the expansion phenomenon, and therefore both expansion and shrinkage take place simultaneously in bulk autogeneous deformation. The expansion typically initiates shortly after setting time when the self-desiccation and the shrinkage are very low, and stiffness of pastes is not yet strongly developed. The expansion continues and lasts for several hours [Chen 2013, Nawa and Horita 2004] (see figure 2.9) until the autogeneous deformation is dominated by the shrinkage. For this reason, the pastes having less self-desiccation, e.g. cast with shrinkage reducing admixtures, show more expansion at young age which compensates the total subsequent shrinkage later on [Sant 2011, Chen 2013].

Experimentally observed deformations are in general caused by many driving forces from complex interactions of different origins during hydration. For instance, microcracking and viscous behaviours also play important roles in measured deformations [Hua *et al.* 1995, Wittmann 2001].

Nevertheless, for various engineering applications, since volumetric expansion generally leads to compressive stresses, it is usually not considered as problem with respect to the risk of cracking, and even lengthening the period of expansion can provide considerable benefits in shrinkage mitigation at later ages [Barcelo *et al.* 2005, Weiss *et al.* 2008, Cusson 2008].

## 2.7 Shrinkage, Creep and Cracking

Cement-based materials show both elastic and inelastic strains under self-desiccation/drying or external loading. If restrained, the strains due to shrinkage result in complex stresses that may lead to cracking. The viscoelastic response of materials may reduce stresses and lead to a redistribution of these stresses caused by shrinkage. In practice, shrinkage and viscoelastic phenomena usually take place simultaneously. The impact of the viscoelastic response on the shrinkage strain cannot be ignored in most cementitious materials.

If the shrinkage strain in an elastic material is completely restrained, it results in an elastic tensile stress, and the magnitude of the induced stress  $\sigma$  is determined by the product of the strain  $\epsilon$  and the elastic modulus  $E$  of the material ( $\sigma = E \epsilon$ ). The material is expected to crack when the stress level exceeds its tensile strength (see figure 2.12, curve a). Given the low tensile strength of concrete, this should happen frequently in practice but, fortunately, the magnitude of the stress is not as high as predicted by the elastic assumption.

To explain why the cementitious material may not crack at all or may crack but much later after exposure to the environment, it needs to be known how concrete responds to sustained stress or to sustained strain. The phenomenon of a gradual increase in strain with time caused by a given level of sustained stress is called creep. The phenomenon of gradual decrease in stress with time caused by a given level of sustained strain is called stress relaxation. Both phenomena are typical properties of viscoelastic materials. If a cement-based material is restrained, it will respond with a progressive decrease in stress with time (see figure 2.12, curve b). Therefore, under the restraining conditions occurring in cement-based materials, the interaction between the elastic tensile stresses due to shrinkage strains and the stress relaxation due to viscoelastic behaviour plays a vital role in controlling deformations and cracking in most structures.

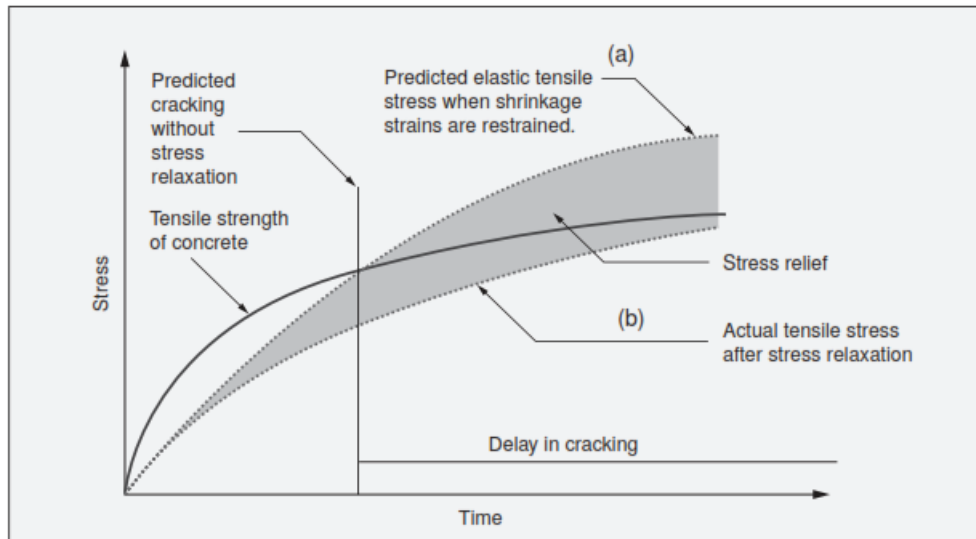


Figure 2.12: Influence of shrinkage and creep on concrete (also on cement paste) cracking  
[Troxell *et al.* 1968]

## 2.8 Measurement Methods of Autogenous Shrinkage

In chapter 6, the results of simulated autogenous shrinkage are compared with the experimentally measured data from a companion study in our laboratory [Chen 2013] for the validation of the numerical approaches. Therefore, measurement methods of autogenous deformation are discussed below for the sake of completeness.

Autogenous deformation has usually been measured by two methods: volumetric measurement and linear measurement methods. For both methods, the sample is kept in a constant temperature and cured in sealed conditions to avoid exchange of moisture with the environment.

### *The volumetric method:*

The volumetric measurements are usually carried out by casting a fresh cement paste inside a tight membrane that is immersed in a liquid (e.g. water or paraffin oil) as shown in figure 2.13 a [Lura and Jensen 2007]. The volume change of the cement paste is measured by monitoring the weight (i.e., buoyancy change) of the immersed sample [Yamazaki 1976].

The advantage of the volumetric method is the availability of measurements soon after casting. But the lack of a stable contact between the membrane and the cement sample is a considerable shortcoming. A very thin layer of liquid, due to bleeding or entrapped air at the surface of the cement sample may obstruct this contact significantly. During the hydration process the liquid or entrapped air may be absorbed back into the cement paste as a result of chemical shrinkage. Hereby, the internal volume reduction may be mistakenly measured as bulk shrinkage. Additionally, it was reported that pressure that occurs from the tight elastic membrane could damage the weak structure around setting [Buil 1979].

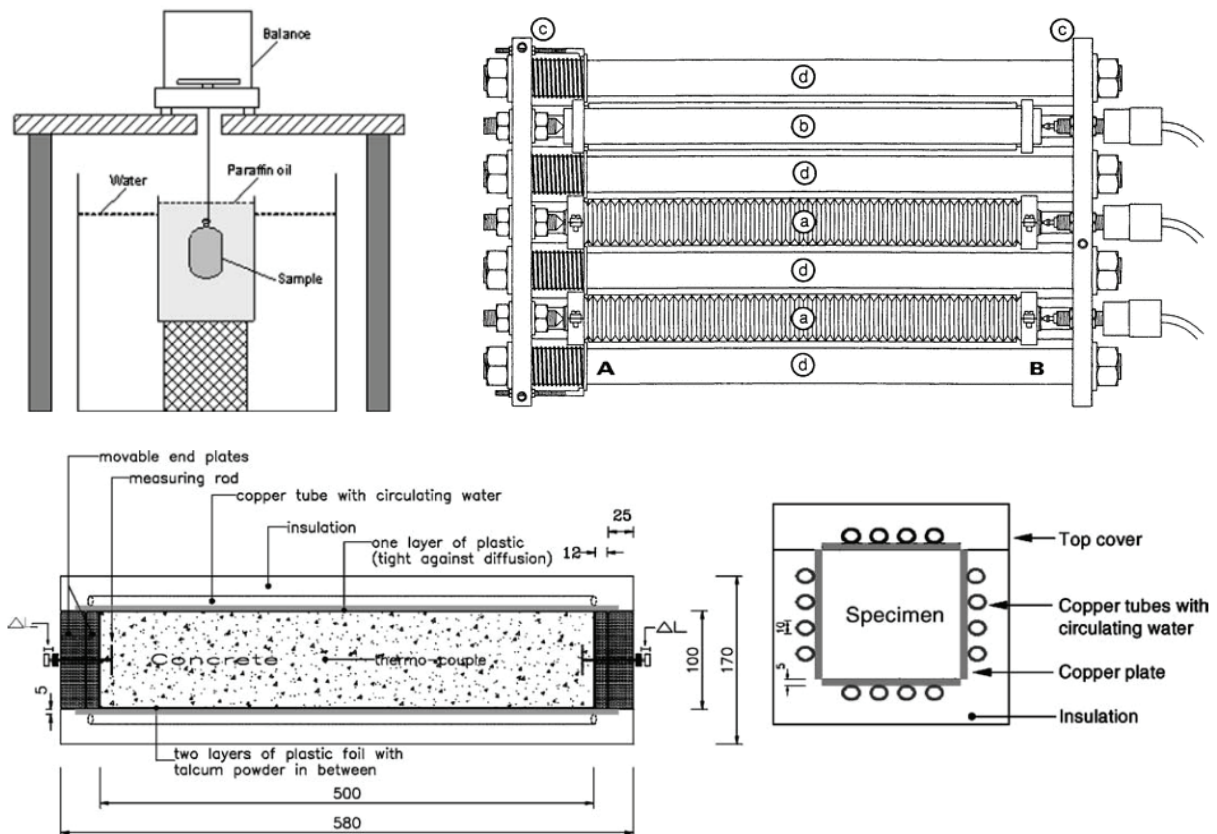


Figure 2.13: An illustration of experimental methods to measure autogenous shrinkage: a) Buoyancy method (left) [Lura and Jensen 2007], b) Corrugated tube method (right) [Jensen and Hansen 1995] and c) free deformation rig with its cross section of 100 x100 mm (down) [Bjøntegaard *et al.* 2004]

### ***The linear method:***

The linear measurements are usually carried out using free deformation rig (see figure 2.13 b) and corrugated tube method (see figure 2.13 c). In the free deformation rig method [Bjøntegaard *et al.* 2004], the length change of a sample is measured using inductive displacement transducers or linear variable differential transformers. The rig allows recording

of free length change with time for hardening samples of 500 mm length and a 100x100 mm cross section. The length change is measured at both sides of samples. The transducers are connected by an invar steel rod to minimize the sensitivity to variations in the surrounding air temperature. The signals are recorded separately and added to obtain the total length change.

The corrugated tube method is presented in the standard test [ASTM C1698]. In this standard protocol corrugated polyethylene moulds have length of  $420 \pm 5$  mm and outer diameter of  $29 \pm 0.5$  mm. Due to a higher stiffness in the radial direction than in the longitudinal direction of the corrugated moulds, this method allows transformation of volumetric deformations into linear deformations. The method is designed to minimize restraint of the fresh paste, and hereby it enables measurements to start at final setting time.

A disadvantage of linear methods is the risk of restraining the cement paste, mostly in the very first hours after setting time. At young ages the cement paste may be too soft to overcome the friction with the rigid mould, however, this problem could be mitigated by lubricating the mould [Jensen and Hansen 1995, Lura 2003]. The bleeding problem may also affect the linear measurements of autogenous deformation [Bjøntegaard *et al.* 2004, Jaouadi 2008]. Upon setting, the bleed water may be reabsorbed by the cement sample and reduce autogenous shrinkage or even induce microscopic expansion [Boivin *et al.* 1998]. This problem can be eliminated by rotating samples about their longitudinal axis.

These above are the most widely used techniques to measure autogenous shrinkage. Further information about other techniques and the details on their protocol can be found in literature [Hammer *et al.* 2002, Bjøntegaard *et al.* 2004, Lura 2003, Chen 2013]. Due to advantages of the linear methods, the corrugated tube method was chosen for the companion study in our laboratory [Chen 2013].

## **2.9 Numerical Models for Cement Microstructure**

Microstructure-property relationships are of paramount importance in modern cement science. Hydrating cement microstructure develops through complex processes in which several chemical and physical mechanisms interact with each other. Therefore, it is difficult to produce realistic numerical models for cement microstructure, from which the behaviour of

the material can be reliably predicted. Recently, the advances in computing technology have provided an impetus to computer based scientific research. Computer based numerical models provide a distinct methodology to study the macroscopic effects of microscopic mechanisms. In the past decades significant progress has been made towards the development of microstructural models [Jennings and Johnson 1986, Bentz and Garboczi 1991, Breugel 1995b, Navi and Pignat 1996, Maekawa *et al.* 2003, Bullard 2007, Bishnoi and Scrivener 2009a] to simulate hydration of cement-based systems. Some of currently available microstructural models are discussed below. The summaries include capabilities of the models, their applications and the mechanisms used to simulate the hydration process. The assumptions made in the models are emphasized along with their strengths and limitations.

### ***HymoStruc model***

The HymoStruc model [van Breugel 1995 a, b] is based on the vector approach using spheres to represent cement particles. Spherical particles of cement paste are randomly placed in a three dimensional virtual cube filled by water. The hydration process of cement and water are simulated according to the volumetric balance of chemical reactions. During hydration, a single hydrate precipitates as concentric layers on the surface of the shrinking anhydrous particles (see figure 2.14). In this model, the degree of hydration is reproduced as a function of the particle size distribution and of the chemical composition of the cement, the w/c ratio and the reaction temperature. Semi-empirical relationships are then used to relate the modelled microstructure and shrinkage [Konenders and van Breugel 1997]. Simplified techniques to estimate the permeability from the digitized microstructure are also presented [Ye *et al.* 2006].

The major shortcoming of this model lies in the assumption that only a single hydrate is produced, which does not account for nucleation products in the porous space. Because of this and the lack of intrinsic kinetics, the model does not consider many important microstructural features including morphology, phase-assemblage, and densification and their impact on the overall hydration kinetics. Another limitation of the model is that only a statistical scale to reaction rates is modeled with oversimplification that the reaction rates of the particles depend only on size, not on interacting from overlaps amongst particles. Furthermore, the influences of impingements of solid phases, pore-connectivity and solid-connectivity are not computed explicitly.

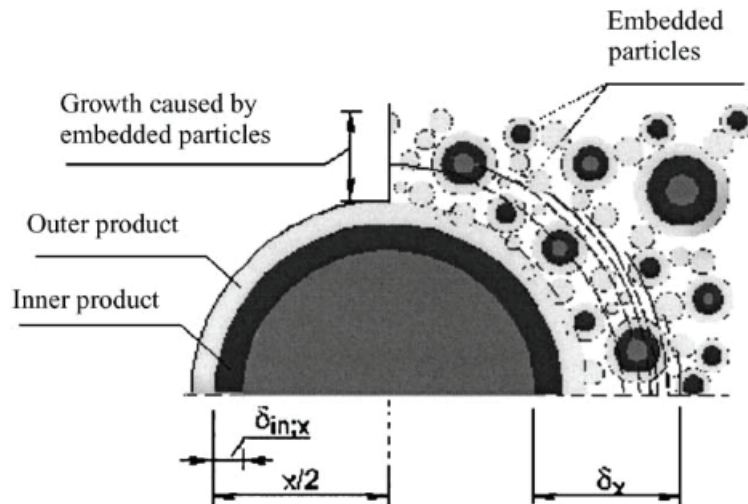


Figure 2.14: Schematic representation of growth of products in hardening cement paste in the HymoStruc model [van Breugel 1995 b]

### ***CemHyd3D model***

The CemHyd3D model [Bentz 1997] is based on the discrete (or pixel, or voxel) approach, in which microstructure of cement paste is digitally meshed onto a three-dimensional uniform grid (see figure 2.15). Each volume element (or a voxel) of the grid represents an anhydrous or hydrate or porosity. Properties such as particle shapes, distribution of phases and reactions are reproduced statistically according to extensive data sets from analyses of various types of real cements. The hydration process of the digital microstructure is simulated using a list of rules that are defined on the scale of individual voxels with dependencies on participating phases, mixture characteristics, impingements between phases and their neighbourhood. The evolution of the microstructure is modelled through elapse cycles underlying controlling mechanisms consisting of dissolution, diffusion (reaction), nucleation and growth.

CemHyd3D has been widely used over years to simulate the development of cement microstructures. The discrete approach implemented in the CemHyd3D model possesses many advantages. The spatial distribution of different phases and arbitrary shapes of particles could be well reproduced digitally in the model. The output of this model, combined with empirical relationships and experimental measurements, was used to study the development of mechanical properties [Haecker *et al.* 2005].

Despite various advantages, the CemHyD3D model also presents some disadvantages. The serious shortcoming of the model stems from its inherent voxel resolution limit of 1  $\mu\text{m}$ , which comes from the discrete approach which necessitates enormous computation over a large set of volume elements of the grid. Consequently, the model is not capable of representing particles or species that are less than 1  $\mu\text{m}$  in size, whereas many features in real cement microstructures such as a large part of small capillary pores, small clinker cement particles and small nuclei of products are only a fraction of a micron in size. Although some studies have used other voxel sizes in this model, it must be noted that the reaction of phases through the “voxel diffusion” method fails to work due to locking of voxels at finer resolutions.

Another drawback of this model is the highly empirical dependencies on experimental data. The lack of the description on reaction controlling kinetics is compensated by an extensive set of empirical rules. A specified calibration, e.g. the time scale, is a prerequisite for every modelled cement mixture. The model, therefore, is in lack of generality and limited to serve as a predictive tool that is expected to replace experiments.

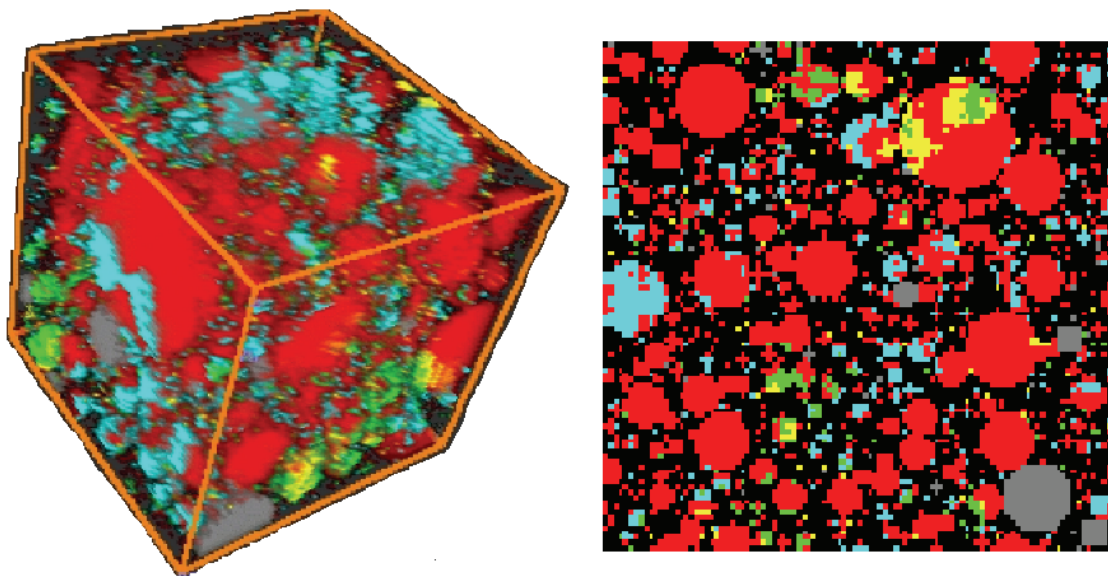


Figure 2.15: Schematic representation in the CemHyD3D model for a three-dimensional microstructure (left image) and two-dimensional slices for cement paste at the initial state for  $w/c=0.30$  (right image). Color assignments are black- porosity, red-  $C_3S$ , aqua- $C_2S$ , green-  $C_3A$ , yellow  $C_4AF$ , and grey- gypsum [Bentz 2000]



### ***Integrated particle kinetics model (IPKM)***

IPKM [Navi and Pignat 1996, Pignat 2003 and Pignat *et al.* 2005] was developed using the vector approach to simulate the hydration of spherical C<sub>3</sub>S particles in a three-dimensional microstructural cube. During hydration, C-S-H products grow outwards as depositing concentric layers and inwards as shrinking from the original boundary of C<sub>3</sub>S grains (see figure 2.16 a. The CH products expand at new spherical nuclei formed in the pore space at an exponentially reducing rate with time.

The reaction kinetics implemented in the model are nucleation and growth, phase-boundary and diffusion as shown in figure 2.16 b. In the first stage, the Avrami type was used to simulate the nucleation and growth regime of the reaction. The Avrami equation here was adapted to describe the change rate of particle radii as a function time and particles size for individual particles. In the second stage, phase-boundary kinetics was modeled, where the rate of reaction controlled by the surface area available of the individual reactant particles. In the third stage, the reaction rate of the cement grains is inversely proportional to the thickness of the hydrates layers deposited on their surface. All the hydration kinetics were modeled taking explicitly into account individual particles along with their neighborhood interactions, development of the exposed surface area and pore space in the surroundings. Furthermore, the formation of clusters of products that do not grow on cement particles, e.g. CH, could be simulated in this approach.

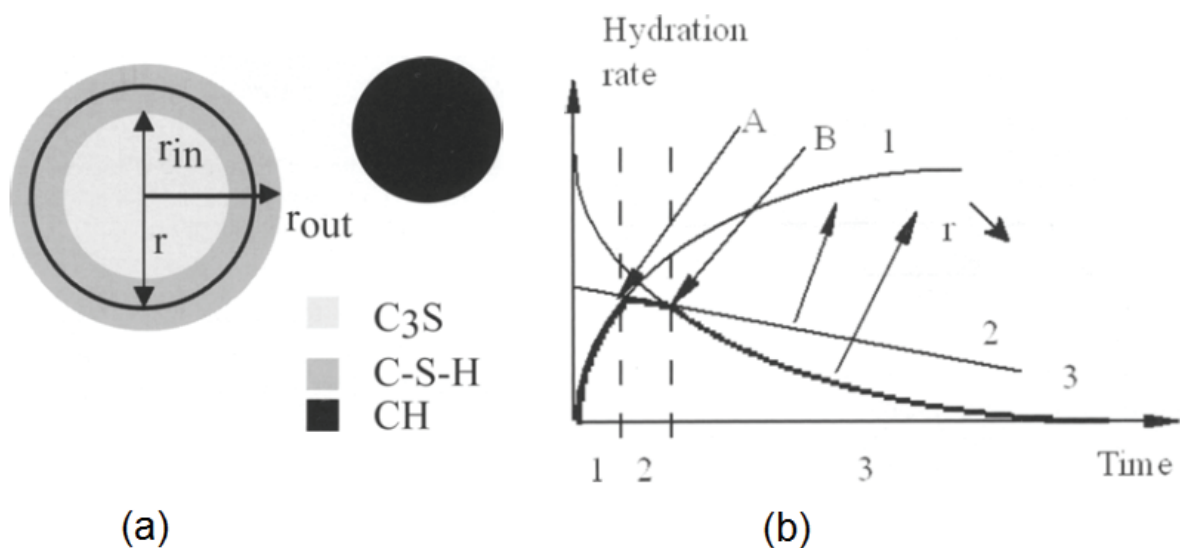


Figure 2.16: (a) Schematic representation of growth of products in the IPKM; (b) reaction controlled kinetics the IPKM [Pignat *et al.* 2005]

Based on the obtained digital microstructure, simulations were implemented further to characterize pore-sizes, pore-connectivity and permeability [Pignat *et al.* 2005]. The limitation of the model was the lack of efficient data-structure algorithms to overcome the computational complexity. This was a serious problem because the number of particles in simulations was limited to around twenty thousands [Pignat *et al.* 2005], while a real cement sample having a size of  $100 \mu\text{m}^3$  contains millions of particles. This limitation perhaps leads to overestimate model derived values of permeability [Pignat *et al.* 2005].

Because of these shortcomings, IPKM was not widely used. However it was a base for the development of the sophisticated modelling platform  $\mu\text{ic}$ , which inherits the basic principles and implementations from IPKM.

### ***$\mu\text{ic}$ modelling platform***

The modelling platform  $\mu\text{ic}$  [Bishnoi and Scrivener 2009a] is based on the vector approach to simulate hydration of spherical particles, new nucleation and concentric growth of products in cement systems. Inheriting all advantages from IPKM,  $\mu\text{ic}$  uses several efficient implementations of data-structure algorithms that allow the model to simulate reacting particles with a realistic representation of a particle size distribution similar to that of commercial cement. The benchmark simulation for a realistic cement paste having about 3 millions grains takes just a few hours on a personal computer. The key algorithms which improve considerably the performance of the model are grid subdivisions and point sampling techniques in order to efficiently calculate overlap and impingement of spherical grains [Bishnoi 2008 and Bishnoi and Scrivener 2009a].

The model has been developed with an objective to offer flexibility to its users because of the limitations in our current understanding of the driving mechanisms of cement hydration. The model primarily aims to aid rather than replace experiments. The platform is designed as a user-oriented fashion to minimize hard-wired (or core) elements and maximize customizable elements for the users (see figure 2.17). Indeed, the core of model serves as a stand-alone programming module that provides the user interfaces, calculates reactions and creates “vector” microstructure. Customizable elements can be classified into two levels. At the first level, a user can add and customize the properties of the materials, particles and reactions in the simulations. At the second level, the user is capable of customizing the models for

processes that control microstructural development using plugins<sup>1</sup>. In  $\mu ic$ , plugins are used to describe customized mechanisms and rules in the expression of mathematical equations that define the reaction kinetics, mechanism and morphology of product formation. Various sets of plugins and their detailed descriptions can be found online [Bishnoi 2012].

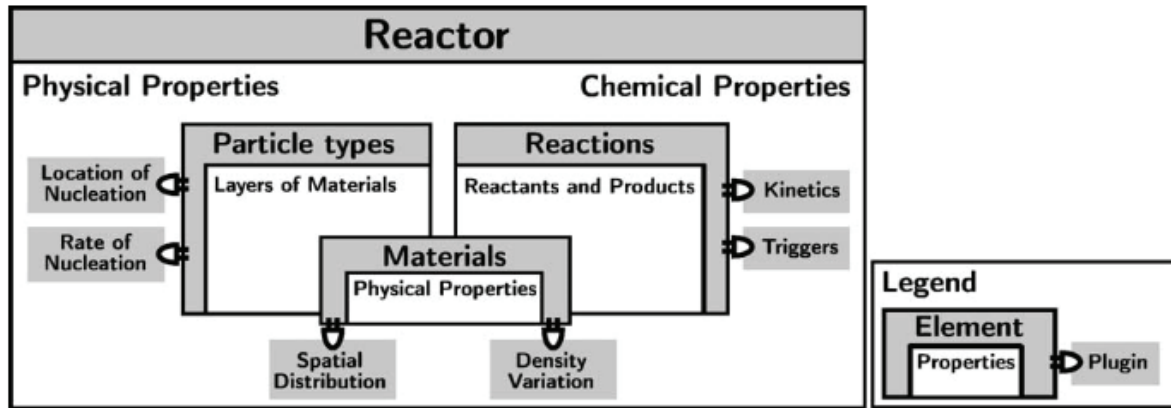


Figure 2.17: Elements in  $\mu ic$  with examples of customizable properties and plugins [Bishnoi and Scrivener 2009a]

$\mu ic$  provides application for wide range study on various relationships linking mixture characteristics, its developing microstructure and its outcome properties, such as clinker fineness, mix compound, w/c ratio and filler addition.  $\mu ic$  provides, both visually and quantitatively, detailed outputs including 3D microstructural images, heat evolution profile, phase information, chemical shrinkage, pore-structure, pore-connectivity etc.

In this study,  $\mu ic$  has been used to generate microstructures simulating the development of properties of alite and Portland cement pastes for different w/c ratios. Using the flexibility of the model several customizable parameters such as densification of C-S-H, flocculation of initial parking of particles, and number of CH nuclei formation are tested for their effects on porosity, elastic modulus, creep and shrinkage.

The major drawback of the model is the representation of C-S-H product by smooth surfaces. The simplification of smooth surface is a problem because, in reality, products may grow unevenly into the pore-space and build a fine pore network even at quite young ages. This

<sup>1</sup> A plugin is a program that can be compiled independently from the platform and introduced as input to the main program during run-time

affects evaluation of the Kelvin radius (see equation 2.3), consequently, calculation of shrinkage as discussed in section 2.4.4.

The above is only a brief review of numerical models simulating cement microstructure; further discussion on this topic can be found in literature [Thomas *et al.* 2011, Bullard *et al.* 2011].

## 2.10 Modelling of Shrinkage of Cement Paste

### 2.10.1 Semi-empirical model based on surface tension

Koenders and van Breugel [1997] developed a model that uses a thermodynamic approach to predict autogeneous of hardening cement paste. In this model, variation in surface tension is considered as the major driving force of autogeneous shrinkage. As hydration proceeds, self-desiccation causes reduction of internal relative humidity and, at the same time, desorption of water layers in the pore wall (see figure 2.18 right). As discussed in section 2.4.3, this desorption of water layers increases the surface tension of the cement gel hydrates and may lead to shrinkage [Koenders and van Breugel 1997].

The authors used the HymoStruc model (see section 2.9) [Breugel 1995 a, b] to simulate the hydrating cement paste in order to get the pore size distribution and the degree of hydration. In this approach, the real pore volume is not considered. The cumulative pore volume is empirically described by a logarithmic distribution whose parameters can be evaluated from the hydraulic radius of the microstructure generated in the HymoStruc model.

Thermodynamic equilibrium in the pore space to describe the development of the surface tension during hydration reads (see Gibbs theory [Defay *et al.* 1966]):

$$\sigma = RT \int \Gamma d \ln(p) \quad (2.6)$$

Where  $\sigma$  [N/m] is the surface tension,  $p$  [N/m<sup>2</sup>] is the pore pressure,  $R$  (8.314 J/mol K) is the gas constant,  $T$  [K] is the absolute temperature,  $\Gamma$  [mol/m<sup>2</sup>] is the number of moles per unit area adsorbed to the pore wall.

Autogeneous shrinkage of hardening cement paste then was evaluated according to Bangham and Fakhoury [1930] (see equations 2.4 and 2.5). The number of adsorption layers in terms of the internal relative humidity was derived from literature (see figure 2.18 left) while the elastic modulus was derived from a lattice model. This modelling approach is closer to a phenomenological model, with empirical fitting than a true simulation since there is no real mechanical response of the microstructure to the driving force. The microstructure generated by the hydration model was rather used as tool to calculate the basic parameters for equations rather than a computational volume to predict the physical and mechanical behaviours of the same paste.

The authors found that model derived results are in good agreement with experiment results. However, the validity of the Bangham's equations in this model for autogeneous shrinkage seems to be questionable. As was discussed in section 2.4.3, in practical cements even with high self-desiccation, the internal relative humidity does not drop below 75%, whereas application of the Bangham's equations of the surface tension mechanisms is valid only at an internal relative humidity below around 50%.

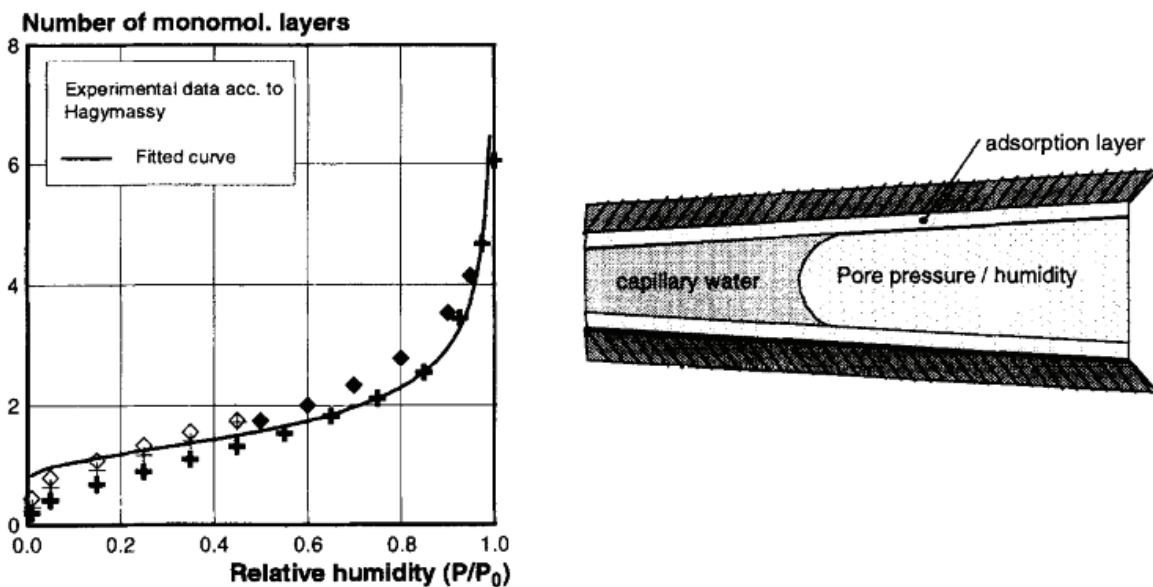


Figure 2.18: Number of adsorption layers (roughly between 2 and 6 layers of  $3\text{\AA}$  each) vs. relative humidity in the pore-structure (left). Schematic view of the state of water in the pore-structure (right) [Koenders and van Breugel 1997]

### 2.10.2 Experiment based model- capillary depression from MIP test

An important model of autogeneous based on the capillary tension approach was developed by Hua *et al.* [1995]. The authors considered that at the size of the representation volume element of cement paste, the liquid phase is continuous. At the macro-scale, in the equilibrium state, the capillary tension is therefore uniform. The cement paste was assumed to be macroscopically homogeneous and isotropic, and the capillary tension produces therefore a hydrostatic macroscopic stress equal to the product of the capillary tension and the total porosity. In this model, the capillary tension is regarded as a time dependent function of hydration, and it is estimated using experimental MIP (Mercury Intrusion Porosimetry).

According to the Laplace and Kelvin laws discussed in section 2.4.4, there exists, for a given unsaturated state of the microstructure, a threshold radius  $r_0$  such that all the pores with access radius smaller than  $r_0$  are fully filled by liquid and all the pores with access radius bigger than  $r_0$  are empty. The radius is  $r_0$  precisely the radius of the meniscus formed in the microstructure. The capillary pressure  $p_c$ , therefore, is a function of the total volume of the empty pores  $p_c(\Delta V)$  produced by the chemical shrinkage.

Suppose that the hydration is stopped at certain time  $t_0$ , to which a chemical shrinkage of  $\Delta V(t_0)$  corresponds, and the cement microstructure is completely dried out, the microstructural solid skeleton then is identical to that shown in figure 2.19 a. As shown in the figure 2.19 b and c, the same volume of mercury  $\Delta V(t_0)$  is penetrated under a pressure of  $p_{hg}(\Delta V(t_0))$  in the experimental MIP. Because both the pressure  $p_{hg}(\Delta V(t_0))$  and the capillary pressure  $p_c(\Delta V(t_0))$  correspond to the same volume  $\Delta V(t_0)$  and the microstructural solid skeleton in the two cases (figure 2.19 (a) and (b)) is assumed to be identical, the equivalence of the access radius  $r_0(t_0)$  leads to:

$$p_c(V(t_0)) = \frac{\sigma_w \cos\theta_w}{\sigma_{hg} \cos\theta_{hg}} p_{hg}(V(t_0)) \quad (2.7)$$

Where  $\sigma_w$ ,  $\sigma_{hg}$  are surface tensions of water/water vapor and mercury/vacuum, respectively, and  $\theta_w$ ,  $\theta_{hg}$  are wetting angles of water and mercury on the solid skeleton, respectively.

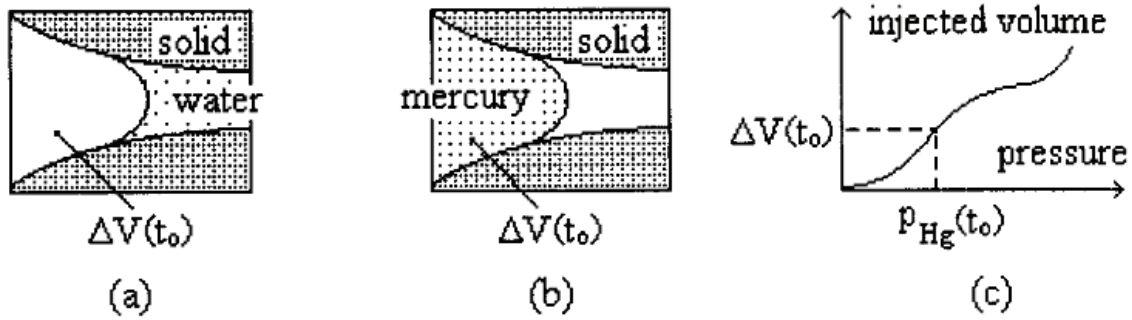


Figure 2.19: (a) Diagram of water evacuation under capillary pressure; (b) and (c) diagram of mercury intrusion under pressure [Hua *et al.* 1995]

The chemical shrinkage  $\Delta V(t)$  as function of time can be derived from the degree hydration. Based on the assumption that the cement paste is homogenous and isotropic, its viscoelastic behaviour can be separated into volumetric and deviatoric creep components, and only the former is responsible for the volume change under compression of the capillary pressure. For the sake of simplicity, the Poisson ratio was considered a constant, therefore the ageing of the cement paste could be described by a single creep function and the linear autogenous shrinkage was estimated rather than the volumetric one.

Based on the Boltzmann's principle of the creep-superposition, the linear autogenous shrinkage of the cement paste can be defined as:

$$\varepsilon(t) = \int_{t_0}^t (1 - 2\nu) J(t, t') d\Sigma(t') \quad (2.8)$$

Where:  $J(t, t')$  [ $\text{MPa}^{-1}$ ] is the one-dimensional creep function.

$\Sigma(t')$  [ $\text{MPa}$ ] is the macroscopic compression on the solid skeleton.

$\nu$  [-] is the Poisson ratio.

$t$  [day] and  $t_0$  [day] are the current time and the reference time, respectively.

In the equation 2.8, authors used empirical creep functions found in the literature [Aker 1987]; the degree of hydration through the quantification of chemically bonded water, and the compression was considered a product of the capillary pressure  $p_c$  [ $\text{MPa}$ ] and the total porosity  $\varphi$  [-]:

$$\Sigma(t') = p_c(t') \varphi(t') \quad (2.9)$$

This approach showed calculated results in a relatively good agreement with experiments. It confirmed that the mechanism of capillary tension is able to explain autogeneous shrinkage. Furthermore, the calculated results indicated that viscous behaviour of cement paste is considerable and this cannot be ignored. However, it should be noted here that the model still strongly relies upon the experimental data such as the pore size distribution, mechanical and creep properties and degree of hydration.

### 2.10.3 Experiment based model – capillary depression from change in RH

According to the Kelvin-Laplace equation (2.1-2.3), the capillary tension in the pore fluid related to the menisci in the partly empty pores of microstructure of hardening cement paste can be determined from either MIP test or parameters of internal state of water, such as internal relative humidity, water sorption isotherm, saturation degree.

MIP measurements are based on the assumptions that the porous network is built by connected cylindrical pores accessible from the outer surfaces of the specimen and pore sizes decreases gradually from outer surface to inner core of the sample. MIP tests provide a function of cumulative pore volume versus intruded pressure levels that are converted into equivalent pore radii. There are some major drawbacks of this technique. First, large internal pores that are accessible only through small entries are identified as smaller ones-the so called entry-pore effect. Second, the modification of pore structure may occur before the drying of the sample and/or during the mercury pressured intrusion, especially at the young ages. For these reasons, the accuracy of the MIP analyses is frequently questioned [Diamond 2000].

Considered the more advanced and direct approach, some models used measurement values of the internal relative humidity to estimate the capillary tension [Jensen 1993 and Lura *et al.* 2003]. In a model proposed by Lura *et al.* [2003], the capillary pressure is a function of the relative humidity due to menisci  $RH_k$  according to the Kelvin equation 2.4:

$$p_c = \frac{RT \ln (RH_k)}{V_m} \quad (2.10)$$

$RH_k$  can be derived from the total measured internal relative humidity (RH) and relative humidity drop ( $RH_s$  about 2%) due to dissolved salts [Lura *et al.* 2003]:

$$RH_k = \frac{RH}{RH_s} \quad (2.11)$$



For the dimensional change, Mackenzie [1950] proposed an analytical solution for a fully-saturated porous medium under a capillary pressure  $p_c$  in the pore fluid. This solution is only exact when the solid skeleton is linearly elastic, and the pores are fully saturated:

$$\varepsilon_{linear} = \frac{p_c}{3} \left( \frac{1}{K} - \frac{1}{K_s} \right) \quad (2.12)$$

Where  $\varepsilon_{linear}$  is the linear autogeneous deformation,  $K$  is the bulk modulus of the porous solid, and  $K_s$  is the bulk modulus of the material making up the solid frame of the porous solid.

The value of  $K$  in the equation (2.12) is for empty pores, which assumes that the bulk modulus of the pore fluid has no effect and the flow of the pore fluid is neglected during volume change of the porous material. Under a compressive pressure (hydrostatic tension), the deformation  $\varepsilon_{linear}$  is negative, implying shrinkage. In practice with a partially saturated porous solid, the average of the capillary pressure over the pore space can be used instead of capillary pressures  $p_c$ , which involves in the saturation fraction  $S$ . The resulting approximate shrinkage equation for partially saturated porous solids reads:

$$\varepsilon_{linear} = \frac{S p_c}{3} \left( \frac{1}{K} - \frac{1}{K_s} \right) \quad (2.13)$$

The saturation fraction  $S$  can be calculated as the ratio between the evaporable water content in the sealed hardening paste and the total pore volume of the paste, which are both functions of the  $w/c$  ratio and the degree of hydration [Powers and Brownyard 1948].

Lura *et al.* [2003] based on equation (2.13) to calculate autogeneous shrinkage calculated for cement paste with 5.2% silica-fume (SF) replacement at  $w/c$  ratio of 0.37. The measurements of shrinkage were based on the linear method with corrugated tubes in a dilatometer [Jensen and Hansen 2001b]. The calculated values were in good agreement with experimental values down to relative humidity of 97% (see figure 2.20). The authors concluded that the underestimation of the simulations may stem from two sources that the model does not take into account. Firstly, the pozzolanic reaction of silica fume consumes the calcium hydroxide crystals, inducing additional shrinkage in the paste. Secondly, the creep effect becomes significant at lower relative humidity. Although this is truly an experiment-based model on the macroscopic scale, the approach shows a good evaluation of basic mechanisms of autogeneous shrinkage.

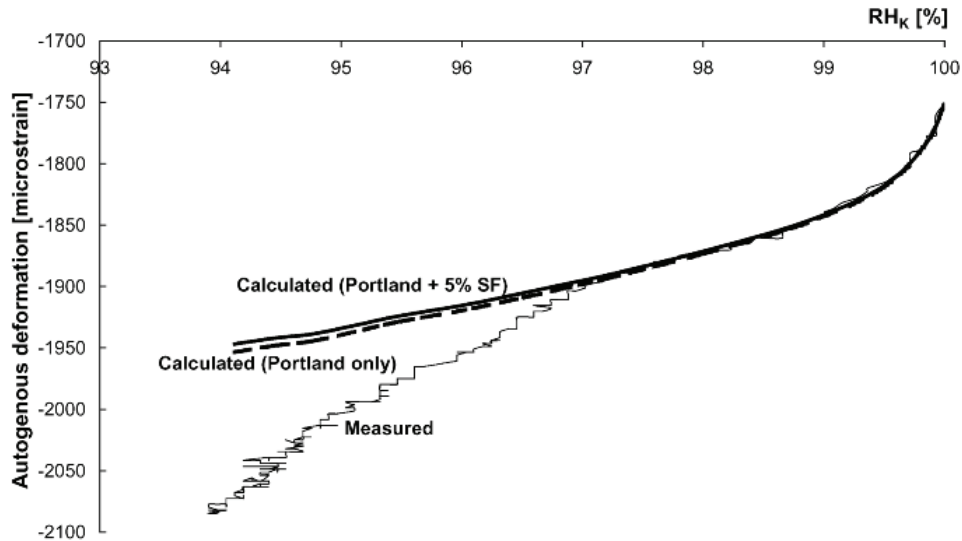


Figure 2.20: Measured and calculated autogeneous deformations plotted vs. relative humidity due to menisci formation ( $RH_k$ ) [Lura *et al.* 2003]

#### 2.10.4 Multiscale micromechanics model

Pichler *et al.* [2007] based on a multi-scale material model [Bernard *et al.* 2003] to develop a micromechanics model for prediction of macroscopic autogeneous deformation of early-age cement-based materials (see figure 2.21). A description of cement hydration, based on the affinity concept [Ulm and Coussy 1996], was modified by introducing reaction extents for the four main clinker phases. This refined hydration model provided the information of the volume fraction of phases at the cement paste level.

In this model, the internal loading applying on the microstructure (a representative volume element) for each hydration degree consists of the capillary pressure in the liquid and the swelling induced pressure by crystallization of ettringite formation. The evolution of the Kelvin radius was derived from empirical fitting pore size distribution data that obtained experimentally by MIP tests and image analyses of scanning-electron-microscopy (SEM) on various cement pastes at different hydration degrees and w/c ratios. The development of the capillary pressure with hydration was then calculated from the Kelvin radius via the Laplace equation. Finally, the macroscopic elastic and autogeneous deformation were calculated using analytical homogenization upscaling from the cement paste.

The simulated values of autogeneous deformation are in reasonable agreement to measured data and they can nicely capture the effects of w/c ratio and cement fineness. However, it can be seen that there are some drawbacks of this approach. Firstly, again, the approach relies on empirical hydration kinetics, experimental data of pore size distribution. Secondly, the analytical homogenization techniques (the Mori-Tanaka and Self-Consistent Scheme used in this model), based on only individual fraction and stiffness of phases, cannot take into account the arrangement of phases. Those techniques also do not provide explicitly information of stress and strain fields in the representative volume element, and hence they may be very difficult to go further to simulate other effects e.g. cracking. Thirdly, the viscous behavior of C-S-H was not properly considered in the model. As mentioned by the authors on their future work, the C-S-H-creep compliance should be deduced from indentation experiments.

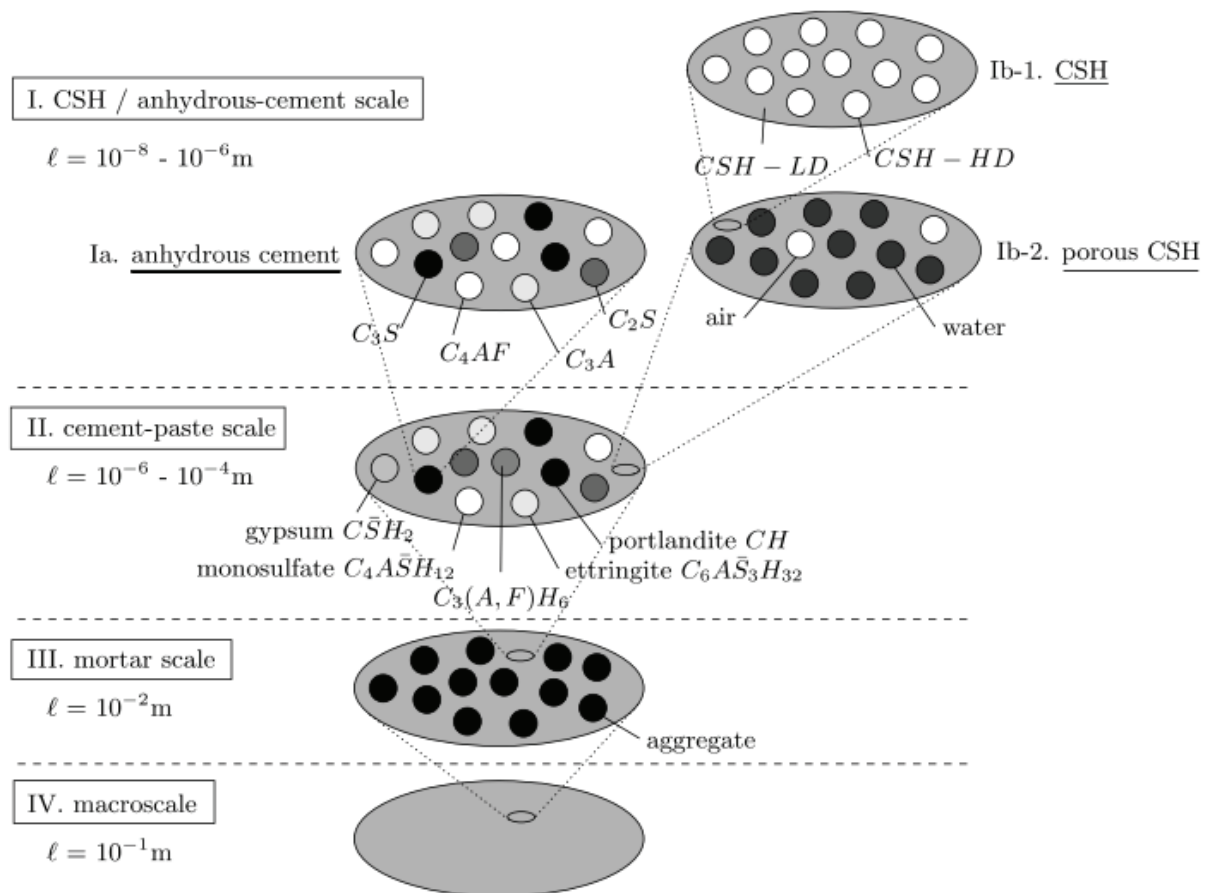


Figure 2.21: Scales of observation for upscaling of properties of cement-based materials ( $\ell$  is size of the representative volume element) [Pichler *et al.* 2007]

### 2.10.5 Mathematical/empirical based model

Gawin *et al.* [2006 a, b] reproduced the shrinkage phenomena of hardening cement-based materials based on poromechanical approach, which were utilized by applications of a mathematical/numerical model. This model is based on the mechanistic-type approach, meaning that the phenomena observed macroscopically are directly described in terms of their intrinsic physical origins and not according to a phenomenological approach. The couplings between hygral, thermal, chemical and mechanical phenomena, and along with the development of material properties during hydration such as porosity, density, permeability, and strength are considered.

Based on the hybrid mixture theory [Hassanizadeh and Gray 1979 a, b, Hassanizadeh and Gray 1980], the balance equations for phases and their interfaces are described at the micro-scale, and then averaged to obtain macroscopic balance equations. The constitutive laws of the mechanistic approach are directly introduced at the macroscopic level, at which materials are treated as homogenous. The final equations including mass, energy and momentum balance equations, are written in terms of the chosen primary state variables consisting of gas pressure, capillary pressure, temperature and displacement. The evolution of the hydration rate are derived from the chemical affinity concept [Ulm and Coussy 1996], and modified for the effect of the relative humidity on the process by considering in addition to the existing models in other literature.

The analytical model equations are rewritten as the discretization expression of the Finite Element and Finite Difference techniques for finding the numerical solution of state variables in space and time. It was found that the model is an effective tool to study chemo-physical maturing processes in realistic/curing conditions, in which there are couplings of several phenomena e.g. self-desiccation, heating, temperature exchange with the surrounding. Furthermore, the generalized capillary pressure used as a state variable in the model was able to describe the hygral state of the porous medium in a wide range of capillary moisture. The advantage of such approach, therefore, is that it is able to model both external drying and self-desiccation.

However, the authors noted that the spatial analysis by the Finite Element technique is not required to simulate the autogeneous deformation in the curing conditions (i.e., no external

load, isothermal conditions and no moisture exchange with the environment). In such the conditions, theoretically there are no gradients of physical quantities at the macroscopic level, and every point in the computational volume is assumed to behave in the same way. The major drawback of this model is that the approach strongly relies upon empirical fitting parameters e.g. the sorption isotherms, reaction kinetics.

### **2.10.6 The previous modelling of autogenous shrinkage in our laboratory**

A full modelling approach to simulate autogenous shrinkage of cement paste was studied by Jaouadi [2008]. Based on the capillary tension mechanism, autogenous shrinkage of the modelled microstructure generated by the *μic* platform was calculated using equation (2.12). In this equation, the capillary tension was deduced the calculated chemical shrinkage and the pore size distribution simulated by a voxel erosion algorithm proposed by Bishnoi and Scrivener [2009a]. The elastic properties in (2.12) were taken from the calculated results that were the output of the numerical homogenization based on FEM [Chamrová 2010] applying on the modelled microstructure.

This approach was able to reasonably capture the effect of cement fineness. However, simulated values were considerably lower than experimentally measured values (see figure 2.22). The author noted that the difficulties in numerical characterization of the pore structure were not overcome. The resolution limit in the pore analysis could not fully capture the extent of pores available in the modelled microstructure, which results in underestimation of the capillary pressure.

The creep effect on autogenous shrinkage was taken into account by considering an additional term of viscous deformation in the total deformation. The two parameters of the exponential creep function were fit to the experimental data found in other literature [Tamtsia 2004]. It was found that consideration of creep leads to an increase of 15% in calculated autogenous shrinkage that is in better agreement with the measured values.

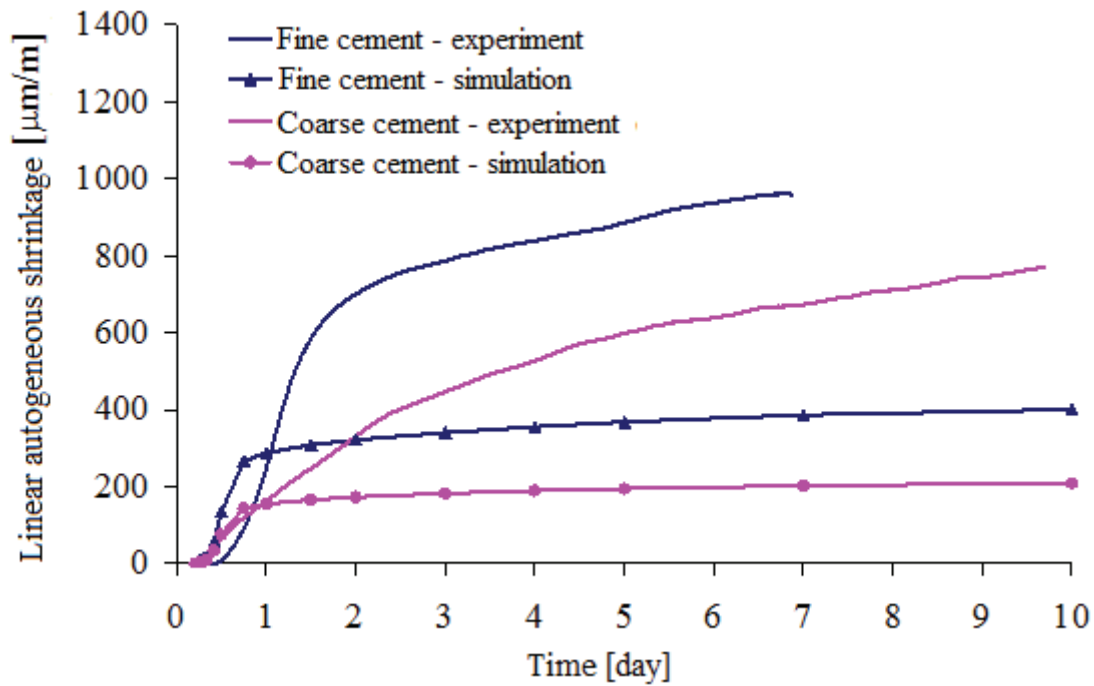


Figure 2.22: Measured and calculated autogeneous deformations [Jaouadi 2008]

The above list of models is not exhaustive and this only broadly represents the recent and notable approaches used by various researchers to model autogeneous deformation of cementitious materials. Other models/approaches simulating autogeneous/drying shrinkage can be found in literature [Hua *et al.* 1997, Ishida 1998, Bentz *et al.* 1998, Coussy *et al.* 2004, Valahilic *et al.* 2009]

## 2.11 Limitations of Currently available Models of Shrinkage

It can be seen from the discussion above that researchers are agreed that in any case, the internal state of water and interaction between water and solid phases in pore structure place the key role in the development of shrinkage. In the view of numerical modelling shrinkage, the numerical modelling of hydrating cement microstructure and the corresponding pore structure should be considered as high priority.

However, the currently available approaches are often carried out based on macroscopic phenomenology or empirical fitting of microscopic investigations. As such direct links between mixture characteristics, microstructure and autogeneous deformation have been addressed poorly. In addition, capabilities to represent realistic pore structures in the available numerical models and efficient methods to numerically characterize pore structures have been

not tackled. While this study does not offer improved numerical techniques to represent porosity, results show that it is important to consider realistic pore-properties in simulations.

Another serious limitation of the current models is their assessment of the mechanical properties. On one hand, it is apparent that in the macroscopic approaches, there is no possibility to obtain mechanical properties without using experimental or empirical values, and hence the models are certainly limited to serve as a predictive tool. On the other hand, in the approaches based on empirically analytical microstructures, the simulations of elastic response of materials by means of analytical homogenization micromechanics present some limitations. This is because, analytical homogenizations cannot consider the effect of arrangement of inclusions and they are found not suitable for high porosity ranges at young ages when microstructures have evolving morphologies.

Although the presence of creep during autogeneous shrinkage had been confirmed by many authors, and that its impact on shrinkage is considerable, the current models either do not take into account this effect or adopt it from experimental creep properties or just numerically treat it with oversimplification. In fact, the C-S-H phase is considered as the main source causing viscoelastic behaviour in cementitious materials, and the lack of considering intrinsic viscoelastic properties of nano-indentation C-S-H in numerical models will limit their generic predictions. Moreover, the strains due to creep tend to augment the autogeneous deformation, but these strains are important components to mitigate cracking through stress relief. The available approaches may have a certain limitation on modelling this effect since they either do not simulate at the microstructure scale or consider the effect of spatial distribution of heterogeneous phases in the computational volume. Indeed, this effect is the crucial importance, especially when modellers want to simulate developing cementitious properties at very young ages. When a developing microstructure is subjected to sustained stress i.e., let us say, hydrostatic pressure, this microstructure will deform elastically and will, thereafter, deform due to creep. In the early stage of hydration, when the microstructure still has a loose spatial structure, characterized by a sparse distribution of solids and a low packing C-S-H density, the solid skeleton may deform (including creep) relatively easily. During the continuing hydration process, the new hydrates will progressively be filled-up in the spatial structure and, as the same time, previously formed hydrates (mostly the C-S-H phase) will increase their density, stiffening the microstructure and restraining the total deformations (elastic shrinkage and creep). Once hydrates have been formed, the creep deformations will

result in a redistribution of stresses between hydrates formed at different times, and consequently this will influence mutually the total shrinkage. Thereby, from the modelling point of view at the microscopic level, modelling the evolution of hydrating microstructure to identify the geometrical properties is necessary.

## 2.12 Modelling in the Current Study

The current study presents a new approach (see figure 1.1) to simulate autogeneous shrinkage at the scale of microstructural cement paste. The simulation starts directly from hydration modelling of three-dimensional cement microstructure using the *μic* platform (see section 2.9 and appendix A).

Two numerical methods (see chapter 3) to characterize the modelled pore structure are improved to obtain the finer resolution. However, it is found that the Kelvin radii are not able to obtain from the modelled microstructure due to its representation of C-S-H morphology. It is, therefore, necessary to use some experimental inputs in the later simulation of the autogeneous shrinkage.

The elastic properties of the modelled microstructure are calculated using homogenization based on FEM (see chapter 4). The so-called “burning” algorithms that take into account the solid percolation are implemented to improve the results at very early ages.

A new approach based on FEM to simulate ageing basic creep of Portland cement pastes of its modelled microstructure is presented (see chapter 5). The intrinsic creep properties of C-S-H are taken from the literature (obtained from the nano-indentation test) [Vandamme 2008], and then numerically represented by a Generalized Maxwell model.

Based on the calculated properties above and the experimental data of capillary tension, the autogeneous shrinkage of the simulated microstructure is estimated using the poro-elasticity method and the creep-superposition method (see chapter 6).



## Chapter 3: Numerical Simulation of Porosity in Cements

### 3.1 Introduction

The transport of fluids through the capillary pore network is known to control the durability of concrete. This network is formed during the hydration of cement, when unhydrated phases react with water to form hydrates which increase the solid volume, filling the originally water-filled space between the cement particles. This leads to a refinement in the capillary porosity and hence a reduction in the permeability of the material. Two main approaches have been developed to model the transport properties of hydrating cement pastes. In the first approach, transport is calculated by homogenising the microstructure using experimentally measured or calculated global values [e.g. Marchand *et al.* 2002]. In the other approach, microstructural models are used to recreate the complex capillary pore-network in cement pastes [Garboczi and Bentz 1991, Navi and Pignat 1996, Munch and Holzer 2008, Zhou *et al.* 2010]. This study examines the ability of such microstructural models to accurately reproduce the capillary pore network of cementitious materials. This chapter is based on an article recently published [Do *et al.* 2013]

Microstructural models numerically simulate microstructural development and generate three-dimensional images of the microstructure at various stages of hydration. The images can then be used to predict macroscopically measurable properties such as elastic moduli [Haecker *et al.* 2005, Sanahuja *et al.* 2007, Pichler *et al.* 2009], rates of hydration [Bishnoi and Scrivener 2009b, Kumar *et al.* 2012], autogenous shrinkage [Koenders and van Breugel 1997] and permeability of cement pastes [Bentz *et al.* 1999]. Microstructural models can themselves be classified into two main types according to the approach used to represent the microstructural information in the computer memory. In the discrete approach the computational volume is divided into smaller finite-sized “voxels” containing phase information that can evolve with hydration. The vector approach uses simple geometric shapes such as spheres and shells to represent the elements in the microstructure. The size of the smallest element in a discrete model is limited by the voxel size, but no such limitation exists in the vector approach. However, the characterisation of the pore-space using the vector approach has been found to be computationally complex [Pignat *et al.* 2005, Bryant *et al.* 1993], so vector microstructures are typically converted to a discrete format to analyse their porosity.

To examine the accuracy of simulated microstructures they must be compared to experimental results. This is made difficult by the fact that all experimental techniques to determine the capillary pore structure of cementitious materials have limitations. Mercury intrusion porosimetry (MIP) continues to be the most widely used and has been shown to provide good comparisons between different systems. The main limitation of MIP is that it does not really measure pore “size”, but the volume of porosity which can be accessed through a given size of pore entry [Abell *et al.* 1999, Diamond 2010]. In cementitious materials the necks connecting pores are generally very small and a large volume (including much “larger” pores) is accessed through small pore entries. (The term “ink bottle effect”, commonly used to describe this phenomenon, is misleading as it implies that it concerns only dead end pores). For this reason it is really not useful to consider the derivative MIP curve (a so called pore size distribution). The cumulative curve does, however, provide useful information on the threshold pore entry size, below which the majority of the porosity becomes accessible, and the total intrudable porosity. Other criticisms of MIP are: that the technique requires prior removal of water, which may change the microstructure; that the high pressures used damage the microstructure (particularly at young ages) and that the mercury does not intrude all the porosity (particularly at late ages). Despite these drawbacks, we consider the technique as the best available to make quantitative comparisons with the output of microstructural models of capillary porosity, due the relative ease of measurement, its reproducibility and the fact that the physics behind the intrusion process are well understood.

The calculation of pore-sizes from the numerical microstructures is also far from straightforward. Lin and Cohen [Lin and Cohen 1982] first applied a method called morphological thinning, which is similar to skeletisation often used in image analysis, to quantify the geometry of microporous systems or models thereof. This technique is useful to describe the topology of digitised three-dimensional images. Later, Baldwin *et al.* [Baldwin *et al.* 1996] modified the method to characterise pore-structures. Navi and Pignat [Navi and Pignat 1999a] applied this method to determine the pore-size distribution of cement pastes and to simulate MIP on such systems.

It has been reported that, due to the limited resolution in the discrete approach, simulations of mercury intrusion appear to show the microstructures to be much less connected than real measurements [Bentz and Martys 1994, Garboczi and Bentz 2001]. On the other hand, previous work with the vector approach could not deal with the larger number of fine particles

in real PSDs of anhydrous cements, which led to higher connectivity in the simulated microstructures than in reality [Pignat *et al.* 2005, Ye *et al.* 2003]. With developments in computational capacities and methods both these limitations can now be reduced.

In this chapter the *μic* microstructural modelling platform [Bishnoi and Scrivener 2009a], which uses the vector approach to generate three-dimensional microstructures, has been used to study the effect of various input parameters on the pore-structures of simulated microstructures. Pore-networks in the microstructures obtained from *μic* are discretised and analysed to calculate the total porosity and pore size distributions. An algorithm is also applied to simulate the process of mercury intrusion. First the total porosity in the simulations is compared with the porosity obtained from MIP measurements, and then parameters such as the resolution of the microstructures, the roughness and shape of particles and the numbers of particles are then varied to study their effect on the break-through diameter.

We would like to stress that in this study, the simulations only represent explicitly, so called, capillary pores, which are the spaces not occupied by hydration products. In the type of simulated microstructure considered here, with volumes of dimension around 100 μm, it is not possible to explicitly represent the, so called, “gel” pores with dimensions of a few nanometres, which are an intrinsic part of the C-S-H. However, as discussed later, the amount of these gel pores will affect the “bulk” density of the C-S-H.

## 3.2 Numerical modelling

### 3.2.1 Method to model pore sizes

In this chapter the pore-sizes are calculated using a slightly modified version of the method published earlier by Bishnoi and Scrivener [Bishnoi and Scrivener 2009a]. This method uses the technique of three-dimensional erosion of pore-space to locate pore-centres and then the extent of each pore is calculated by walking back to the pore surfaces from each of the pore-centres. Computationally the speed of this method was increased by the introduction of lists that help in the erosion process. A parallel version of the programme was also developed, in which the volume is divided into smaller sub-volumes, each of which can be separately analysed on different processors and averaged to calculate the overall pore size distribution. The accuracy of the subdivision technique is presented later in this study. This technique

allowed calculation of pore-sizes down to 10 nm in microstructures with 100  $\mu\text{m}$  dimension, using a total of one trillion ( $10^{12}$ ) voxels within a few days of computational time.

Figure 3.1 shows performance of the three versions of the algorithm for pore simulations of a Portland cement microstructure volume of size 100  $\mu\text{m}$  at 20% total porosity. In the figure,  $O(n^x)$  means that computational time is proportional to the  $x^{\text{th}}$  power of the size of the problem ( $n$ ), i.e. the number of voxels in the computational volume. It can be seen in the figure that an improvement in the order of the problem was achieved through the single-processor optimisation described above, while a linear reduction in the computational time was achieved by parallelising over 10 nodes.

### **3.2.2 Method to model mercury intrusion porosimetry**

The MIP curves of the simulated computational volume were calculated by mimicking the flow of mercury through the volume under pressure, automatically accounting for the pore-connectivity and the “pore-entry effect”. Using the voxel-erosion method [Bishnoi and Scrivener 2009a], all pore voxels are first marked with their distance from the closest solid boundary (figure 3.2). In order to simulate the dependence of the intrusion diameter on the applied pressure, the process is simulated in several steps. In the first step it is assumed that mercury flows only into the pores that are at least as large as the largest pore on the boundary of the computational volume. The pore-sizes are identified using the distances obtained by erosion described in section 3.2.1 and in [Bishnoi and Scrivener 2009a]. Following the walk-back technique discussed above, the extent of the intruded pores is then identified. Flow into a voxel of a given pore-size is allowed only if the voxel is either located on the boundary of the computational volume or if it shares a face with a voxel which has already been intruded. The iterative process of intrusion continues until all connected pores of at least the size being intruded have been filled. In each subsequent step flow is allowed into pores that are one size smaller than those intruded in the previous step. The number of voxels intruded in any step is measured as the apparent volume for the respective pore-size as obtained experimentally from MIP. The above process is also illustrated in figure 3.3 and the pore-entry size measured using this technique is shown in figure 3.4.

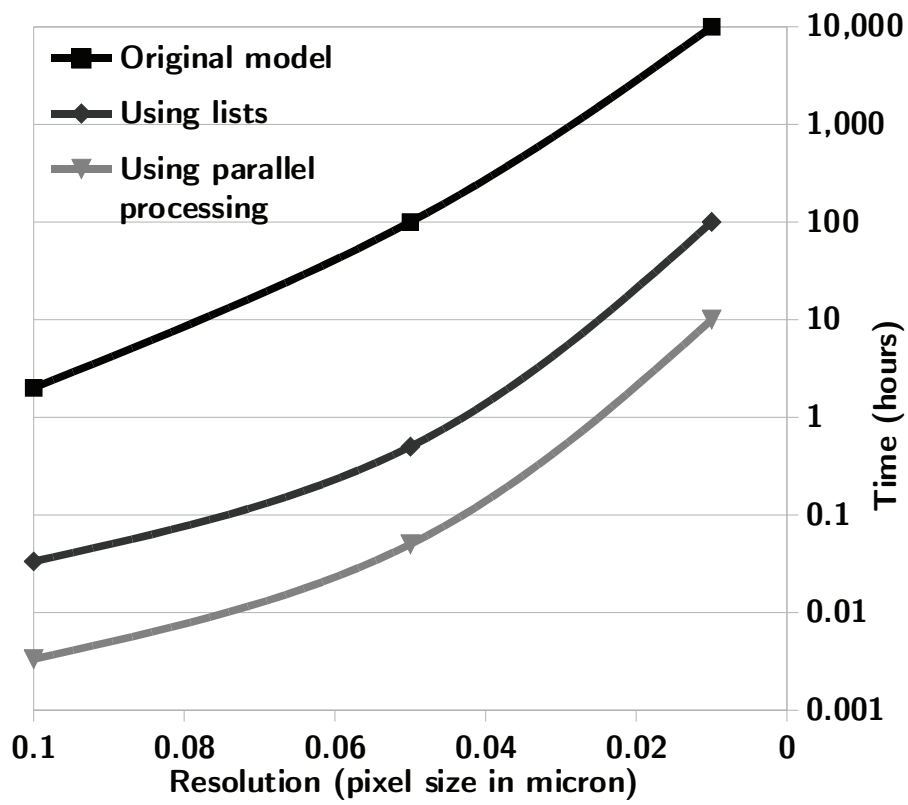


Figure 3.1: Improvement in computational times using the improved approach. The order of the Original model was  $O(n^{2.33})$  and for the other two versions is  $O(n^{1.67})$

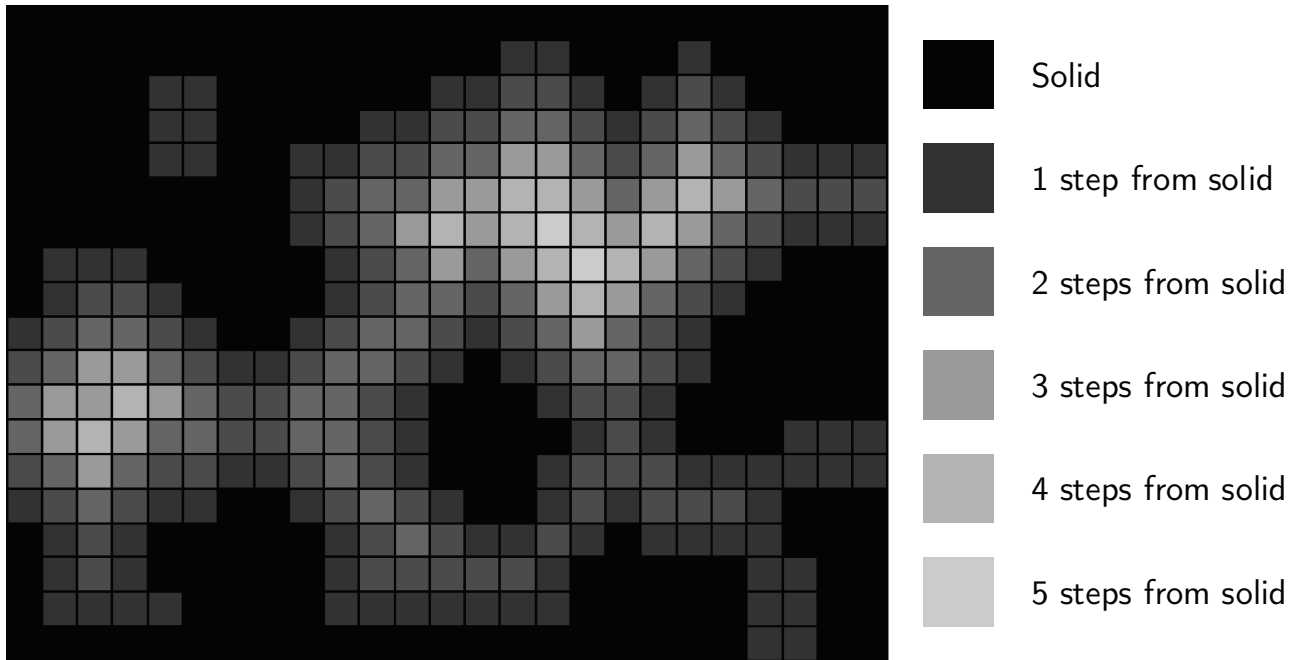


Figure 3.2 : Voxel erosion from the solid wall to find the pore centres. The grey region represents the solids and the white regions the pores. The numbers represent the number of steps required to reach a cell from the solid boundary.

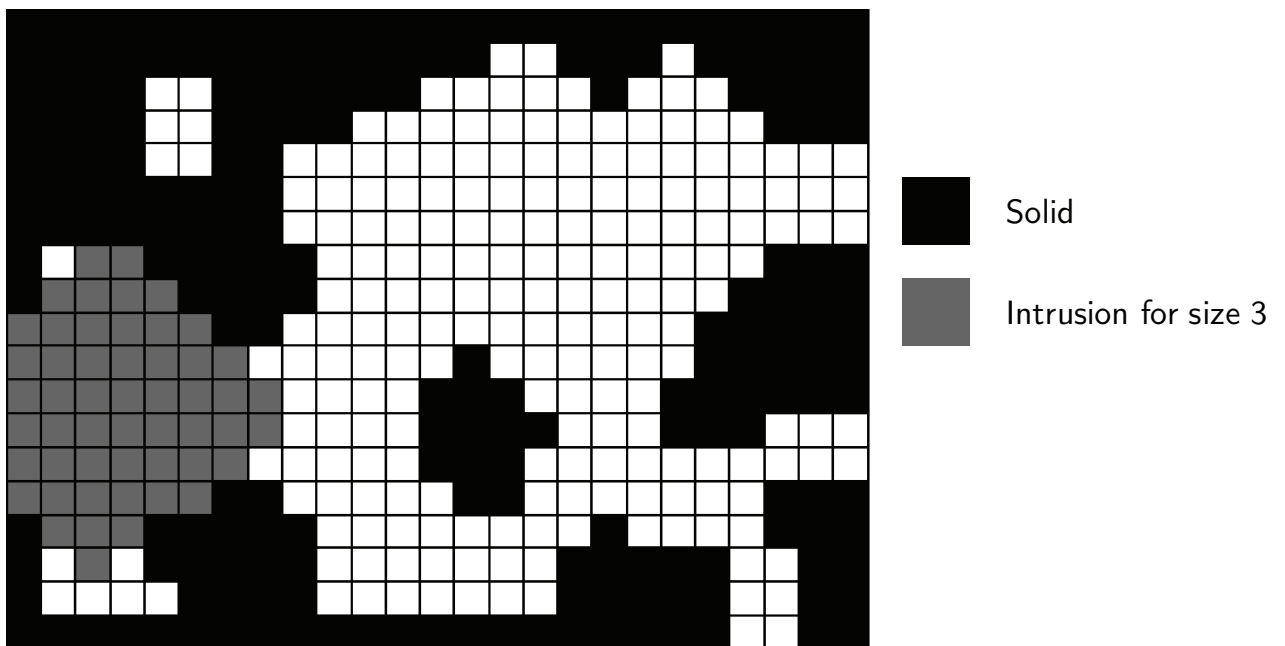


Figure 3.3: Mercury fills the porosity after the first step of the liquid intrusion process. The grey cells represent the region that has been intruded by mercury in the first step of the MIP simulation.

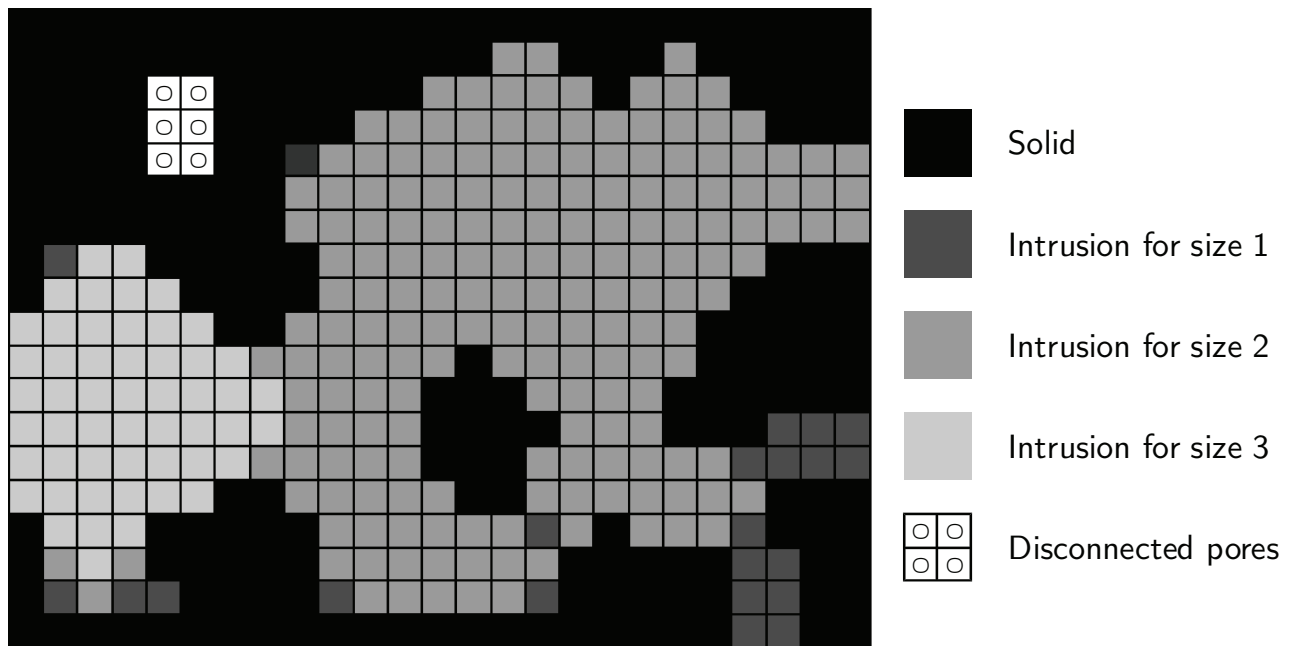


Figure 3.4: The result from MIP simulation. All connected pores appear to be of sizes 1, 2 or 3 despite larger pores being present.

### 3.3 Simulations

The composition of the Portland cement simulated in this chapter is listed in table 1 and its particle size distribution is shown in figure 3.5. A water-cement ratio of 0.35 was used for all simulations. The hydration kinetics of the cement were measured using isothermal calorimetry at 20°C. MIP measurements were made on pastes hydrated for 6 hours, 12 hours and 3 days, corresponding to 8%, 23% and 60% hydration respectively based on the calorimetry measurements.

Hydration was simulated on a cubic computational volume of 100  $\mu\text{m}$  on each side. The size of the computational volume was chosen to be about 2.5 times larger than the largest cement grain. This size was found to be sufficient for simulating hydration and porosity [Bishnoi and Scrivener 2009a]. A total of 1,193,100 cement particles were generated using the known PSD of the cement. A description of the methodology used to generate and pack the particles and the implementation of the microstructural development model is discussed elsewhere [Bishnoi

and Scrivener 2009a]. Some of the hydration products, e.g. calcium silicate hydrate (C-S-H) and ettringite are deposited around the hydrating cement particles and some others such as calcium hydroxide, also known as portlandite or CH, nucleates in the pores. Microstructures were simulated corresponding to the measured degrees of hydration identified above. The hydration was carried out in 30 steps and the calculation took under 2 hours on a desktop computer. The microstructures generated from the model were used to calculate pore-sizes using the methods discussed earlier.

Table 1: Main compositions of the Portland cement

	Alite	Belite	Aluminate	Ferrite	Gypsum
Composition (%)	73.25	8.21	4.75	9.81	3.98

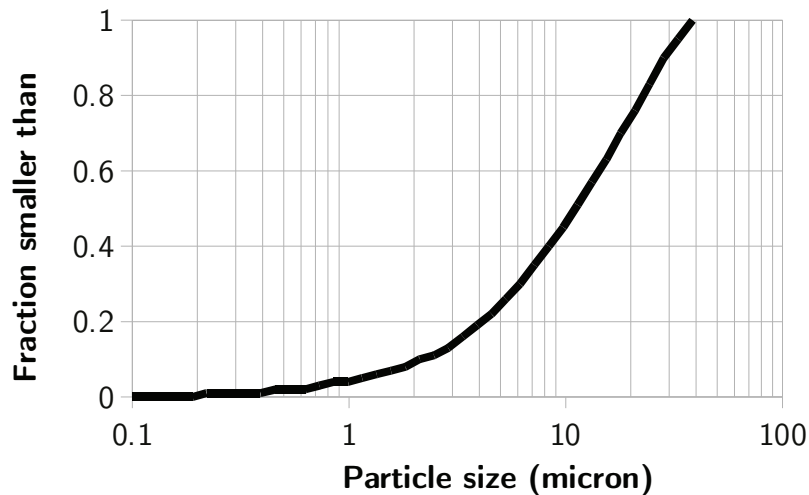


Figure 3.5: Particle size distribution used in the hydration model

### 3.3.1 Matching total porosity with simulation results

Initial results from *mic* showed that if the bulk density of C-S-H is assumed to be a constant value of  $2.0 \text{ g/cm}^3$ , which is the typical value reported in the literature [Jennings 2006], the total porosity calculated from the simulations was significantly higher than the MIP measurements at early ages. At early ages, when the pore structure is still well connected, it is reasonable to assume that all capillary pores are intruded in the MIP measurements and therefore the total volume of mercury intruded at the maximum pressure gives a good measure of the total volume of capillary pores in the system. In fact, at young ages it could be possible that the pressure of mercury damages the solid phases so, if anything, might over



estimate the total porosity. It was found that in order to obtain the same porosities as the experiments, the bulk density of C-S-H had to be adjusted to  $0.97 \text{ g/cm}^3$ ,  $1.38 \text{ g/cm}^3$  and  $1.97 \text{ g/cm}^3$  respectively for degrees of hydration of 8%, 23% and 60% (figure 3.6). The possibility of a variable density of C-S-H was conjectured earlier [Jennings 2004]. Bishnoi and Scrivener also postulated the idea of C-S-H densification during the course of hydration to explain the observed hydration kinetics [Bishnoi and Scrivener 2009b]. Recently direct measurements of undried samples by proton NMR have confirmed that the “bulk” density of C-S-H (including gel porosity) does increase during the course of hydration and the values obtained agree well with the values found here.

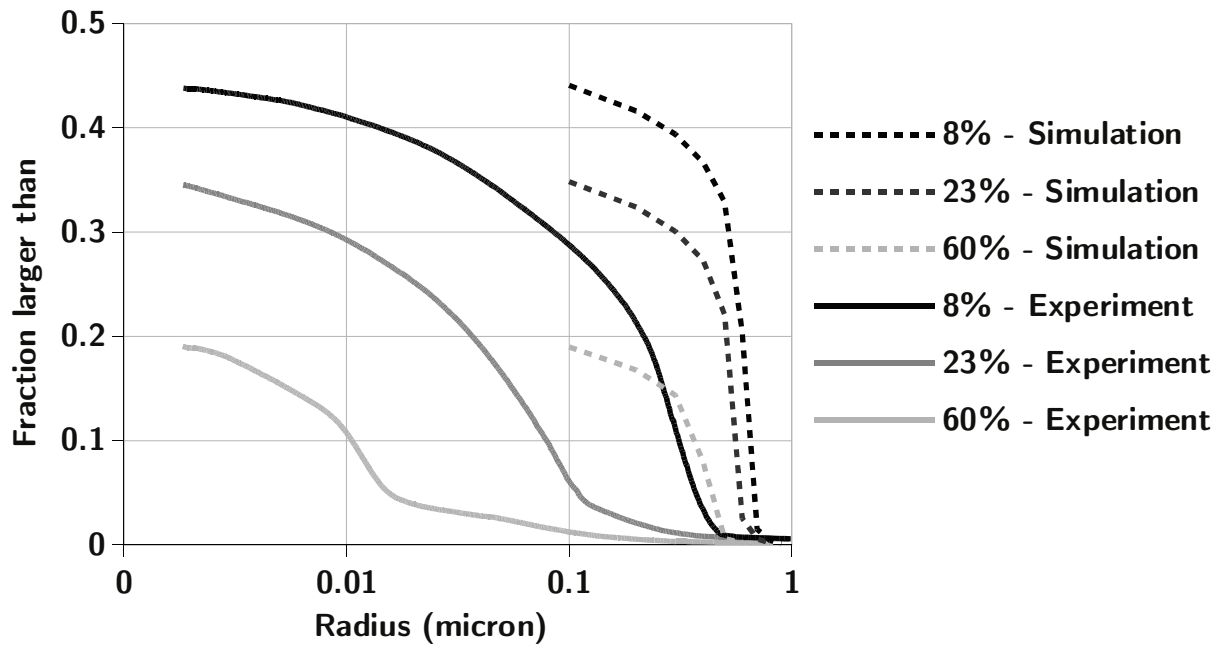


Figure 3.6: Comparison of MIP simulations with experimental simulations at 6 hours (8% hydration), 12 hours (23% hydration) and 3 days (60% hydration). The C-S-H density was set to  $0.97 \text{ g/cm}^3$  at 6 hours,  $1.38 \text{ g/cm}^3$  at 12 hours and  $1.97 \text{ g/cm}^3$  at 3 days.

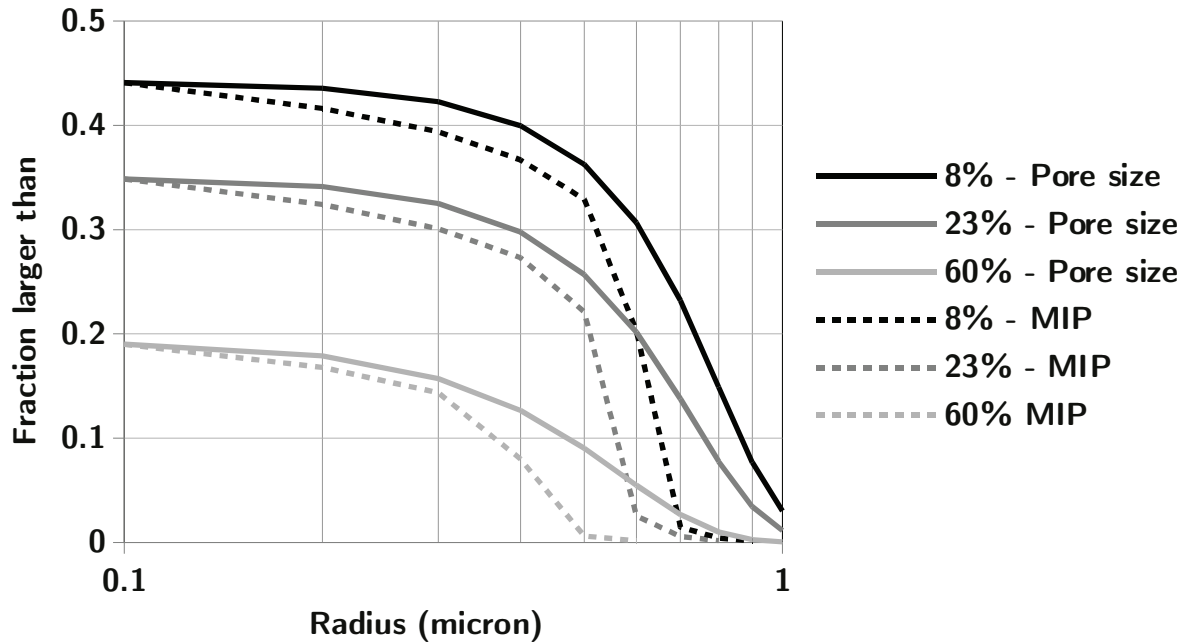


Figure 3.7: Comparison of simulated pore-size distributions and MIPs for 8%, 23% and 60% hydration shows that the entire pore network is percolated until 60% hydration

A comparison between the pore size distribution and the mercury intrusion curves for the three microstructures (figure 7) shows that the entire pore network is connected at least until 60% hydration. Even so the distribution of pore entry sizes in the simulated mercury intrusion curves, shift to smaller sizes compared to the pore sizes. However, the breakthrough diameter in the mercury intrusion simulations was significantly higher than the experimental results. The reduction in the density of C-S-H did not significantly reduce the breakthrough diameter. The discrepancy between measured and simulated breakthrough diameters was found to increase as hydration progressed, with the experimental values decreasing by nearly one and a half orders of magnitude, while the simulated values were only halved.

The results above can interpreted to mean that either experimental MIP shows too low values of porosity and the breakthrough diameter or that the simulations give too high values compared to real microstructures. However, most artefacts which can be imagined for mercury intrusion experiments – for example the high pressures applied to the specimen leading to a collapse of the fine pores in C-S-H – would be expected to increase the experimental determination of breakthrough diameter and total porosity rather than to decrease them. Only incomplete penetration of mercury into all the porosity could lead to the

experimental volumes being too low, but incomplete penetration would be expected to be greater at high degrees of hydration, when the pores are more disconnected – which is not compatible with the observations. Therefore, we are led to the conclusion that the mercury intrusion results, do in fact, give a reasonable picture of the true pore structure (which is supported by the results of proton NMR published elsewhere [Muller *et al.* 2013]) and so that the *simulated* microstructures *do not* well represent the pore structure of real materials.

In order to understand the aspects of the microstructure which may be responsible for this discrepancy between the simulation and the reality; we investigated various parameters in the simulations, which might be expected to have a significant effect on the breakthrough diameter and therefore should potentially be changed to obtain a more realistic microstructure. Since the effect of density of C-S-H and generally the hydration products has already been seen, the value of the density of C-S-H was subsequently set to its expected long-term value of 2.0 g/cm<sup>3</sup>. The results from these simulations are presented in the following sections.

### **3.3.2 Impact of simulation parameters**

#### ***Effect of resolution:***

As discussed above, the method used to characterise the pore sizes relies on a mesh of voxels superimposed on the vector microstructure. Since it is possible to include smaller and a larger number of features in them, finer meshes tend to give better representations of the reality. However, this comes at the cost of higher computational memory and time requirements and practical limitations generally limit the maximum possible resolution in simulations. First, simulations were carried out on the same microstructure with using different resolutions in order to study the effect of resolution on the threshold diameter and the pore size distribution.

The resolution does not affect the total porosity due to the method of converting the vectorial simulations into digitised microstructures for analysis of the pore structure. The hydration and the resulting solid phases are generated by the vector approach which has no lower resolution. This vectorial representation is converted to a voxel representation, by sampling the phase at the centroid of that voxel. This sampling method is analogous to point counting, which gives a rigorously unbiased estimate of the volume fractions of different phase in a microstructure.

The higher resolutions (5 and 10 nm) require calculations using the parallelisation. Therefore, the accuracy of this method was first tested on simulations using a relatively low resolution of 0.1  $\mu\text{m}$  by the single-processor and by the parallel versions of the programme. The calculations were carried out on microstructures having approximately 74% degree of hydration. The average of results from 1000 parallel computations is compared with those obtained without sub-dividing the volume in figure 3.8. The results show the excellent accuracy of the method and confirm that it can be used to obtain pore-size calculations at higher resolutions.

Figure 3.9 shows the pore-size distributions calculated from the microstructure using voxel sizes of 200 nm, 100 nm, 10 nm and 5 nm. The simulations for the first two resolutions used the single-processor version of the code and the parallel version was used for the other two resolutions. The results, shown in figure 3.9, confirm that the resolution does not affect the total calculated porosity. The pore-size distributions become finer when finer resolutions are used, but converge at a voxel size of around 10 nm. Although MIP simulations could not be carried out on the higher resolution microstructures due to computational limitations, the reduction in the pore-sizes does not appear to be high enough to lead to an appreciable change in the MIP simulation results.

These results indicate that the observed increase in the threshold diameter is not due to the limited resolution of the microstructures.

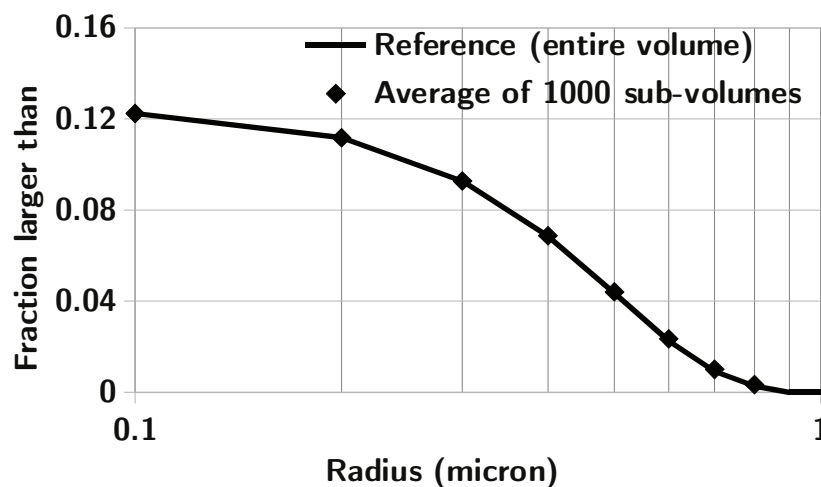


Figure 3.8: Accuracy test for the subdivision technique

***Effect of size of computational volume on MIP simulations:***

In the MIP simulations, the intrusion is simulated from the boundary of the computational volume. However, since the computational volume represents only a small portion of a larger material, it is expected that the connectivity of pores will be reduced when larger computational volumes are used [Pignat 2003]. This is because a larger number of the bigger pores are expected to be farther from the boundary, and so only accessible through finer pores, in the case of larger computational volumes. To study the effect of the size of the computational volume on the mercury intrusion curves the computational volumes were placed next to each other to create larger cubes two and three times the size of the original volume. Due to the periodic boundary conditions used in *μic*, this yields a seamless and continuous microstructure.

A relatively higher voxel size of 0.2 μm had to be used in these simulations since the number of voxels was too large when smaller voxel sizes were used with the computational volume that was 3 times the original volume. This increase in the voxel size is expected to reduce the degree of connectivity of pores and to further increase the pore-entry effect. A degree of hydration of 74% was chosen for the simulations since lower degrees of hydration would lead to microstructures with little pore entry effect and higher degrees of hydration would lead to pore-structures that are too disconnected at the resolution used.

Results from MIP simulations on these 'multiplied' microstructures are shown in figure 3.10. The results show that the pores appear to be finer when larger microstructures are simulated even though the entire pore-network is still connects at this above this resolution of 0.2 μm. However, no effect was observed on the breakthrough diameter, indicating that the deviation from the experimental results is not a result of the finite size of the computational volume being used.

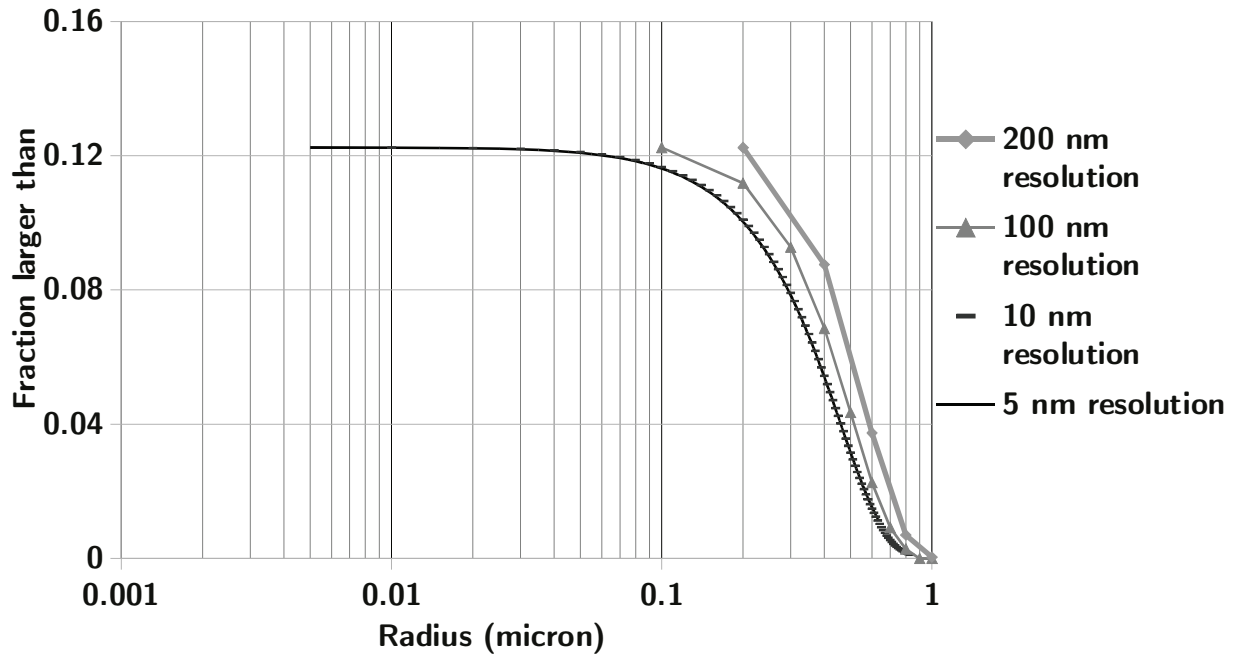


Figure 3.9: Effect of resolution on pores size distribution

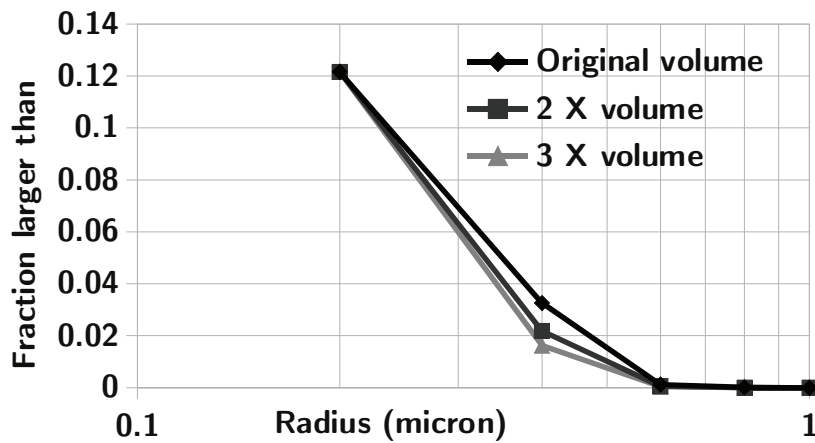


Figure 3.10: Effect of computational volume size on the MIP simulation

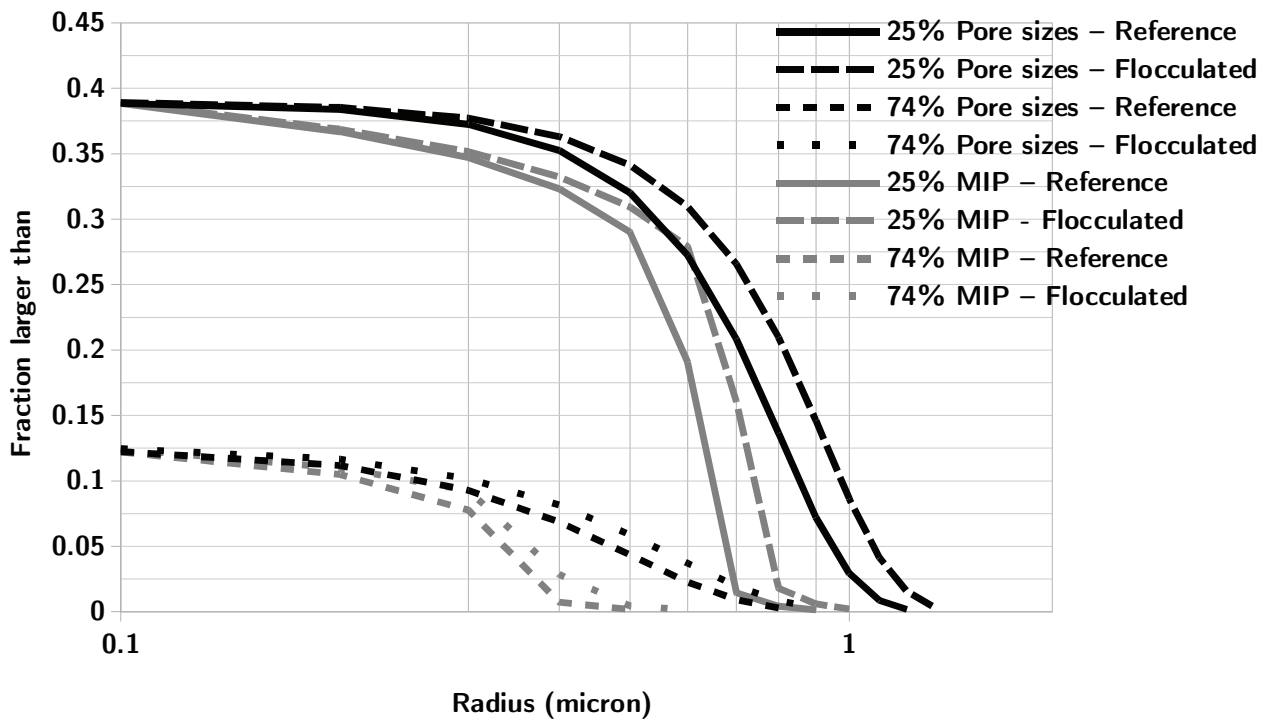


Figure 3.11: Effect of flocculation on pore size and MIP simulations

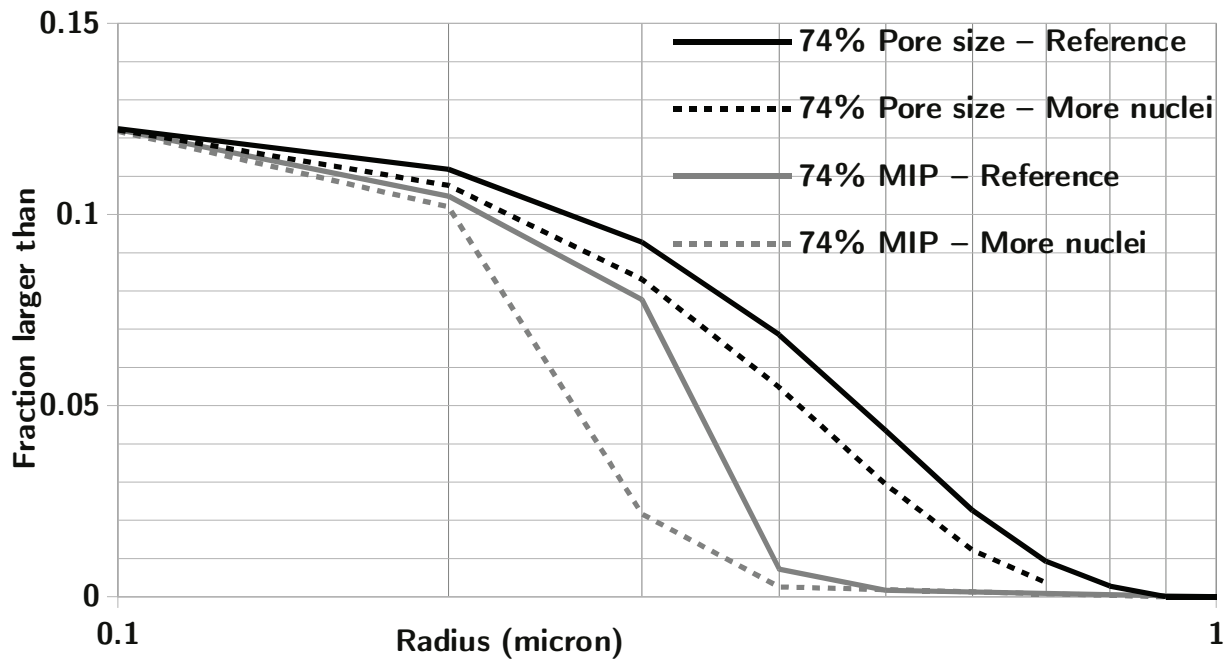


Figure 3.12: Effect of number of new clusters nucleating on pore size and MIP simulations

***Effect of flocculation:***

It is generally considered that the flocculation of cement particles has a considerable effect on the properties of cement paste [Scherer *et al.* 2012a]. Since the default simulations in  $\mu ic$  utilise a random parking algorithm for packing the initial particles in the computational volume, the effect of rearrangement of particles into chains on the pore-size distribution and MIP simulations was studied. Flocculated microstructures were obtained by following a two-step procedure where all particles in the system were first moved closer to the particle closest to them by half the original distance between them and were then rotated around the other particle either for a fixed number of steps in random directions or until they collided with a third particle. Although this method does not attempt to replicate any physical laws of particulate suspensions, it is observed that chains of particles are formed if the above steps are repeated 3 to 5 times. This technique had been originally developed in  $\mu ic$  to allow a high density packing of particles [Bishnoi 2008]. While other techniques for flocculation could lead to different results, the order of the difference measured is expected to be similar.

The effect of flocculation on pore size and MIP simulations at approximately 25% and 74% hydration are shown in figure 3.11. The results show that flocculation leads to an apparent increase in the pore entry size. This is because the rearrangement of particles into chains leads to slightly larger spaces between the chains. The results also show that the magnitude of the effect of flocculation reduces with hydration, as the extra space created due to flocculation is filled by the hydration products.

***Effect of number of nucleating clusters:***

Here the effect of the number of nuclei of hydration products that create new particles in the pore-space was studied. In the simulation of hydration, while most of the hydration products are assumed to grow concentrically over the surface of the cement particles, some of the products, e.g. Portlandite (CH) form new particles in the pores. Since few studies have attempted to study the factors that control the precipitation and growth of these clusters [Gallucci and Scrivener 2007], the choice of the number of CH particles produced during hydration is often arbitrary [Navi and Pignat 1996] or based on empirical measurements with limited reliability [Jennings and Parrott 1986]. Often, these particles are completely ignored and all hydration products are assumed to grow around the cement particles [van Breugel



1995a]. In order to test the sensitivity of the pore size distribution and the threshold diameter to this parameter, the number of CH clusters in the simulation was increased from 5,000 to 400,000. The results in figure 3.12 show that there is a small reduction in the pore sizes and breakthrough diameter when a larger number of CH clusters are assumed. The number of clusters did not affect the total porosity in the microstructure as this is fixed by the relative volumes of reactants and products. The results demonstrate that the higher breakthrough diameter is not a result of the choice of the number of nucleating clusters.

### ***Effect of particle shape:***

One of the limitations of the vector approach is that due to computational restrictions it is difficult to represent the elements in the microstructure using shapes other than spheres. This is mainly due to the fact that it is easy to find the distance and detect overlaps between spheres. The accuracy of the vector microstructures has, therefore, been questioned and models that can consider more realistic shapes of particles have been developed [Bullard and Garboczi 2006, He *et al.* 2010]. Simulations were carried out to study if the relatively higher breakthrough diameters simulated were a result of the spherical shape of the particles.

For these simulations a microstructure generated from *mic*, having a degree of hydration of 74%, was converted by replacing all spherical hydrated cement particles with cylinders. The cylindrical shape was chosen since its length to diameter ratio can be varied and it has sharp edges. We do not propose that cement grains are in fact cylinders. No hydration was carried out on the cylindrical particles. The centres of the cylinders were made to coincide with the centre of the spheres in the original microstructure and the cylinders were randomly oriented. The outer radius of the cylinder was chosen to be the same as the outer radius of the original sphere. Although, theoretically, in order to have the same volume of the cylinder as the original sphere, the length of the cylinder should be  $4/3^{\text{rd}}$  its radius, it was found that since the pattern of overlap for cylinders is not the same as for spheres, the length of the cylinders had to be reduced by 7.5% in order to keep the total porosity the same as the original volume. During this process, the aspect ratio was kept constant for all cylinders. This modified microstructure was then meshed and pore-size and MIP simulations similar to those above were carried out. A comparison of the microstructures using spheres and cylinders is shown in figure 3.13. It can be seen in the figure that since the length of the cylinders is smaller than the diameter of the original sphere, larger pores may exist on the surface of some of the cylinders.

This is an artefact of the conversion of the microstructure from spheres to cylinders and is not expected to occur if the growth of cylinders was simulated.

The comparison of results from cylindrical particles with those from spherical particles is shown in figure 3.14. The results show that a wider range of pore sizes are obtained when cylindrical particles are used and the breakthrough diameter appears to be higher. The results indicate that although the particle shape can have an effect on the pore-sizes, the observed change is too small to account for the deviation from the experiments.

***Effect of surface roughness:***

Another limitation of the vector approach is that the surface of all pores is smooth. In real systems, it is expected that since the growth of hydration products will take place in a more random fashion, more rough surfaces will form and parts of the hydrates will extend into the pore-space leading to a reduction in the effective pore size. In order to quantify this effect, a roughening algorithm was applied on the microstructures obtained from  $\mu\text{ic}$ . This process was carried out in steps, where some of the pore-voxels adjacent to solid-voxels were converted to solid-voxel in each step. The choice of the voxels to be converted is made by generating a pseudo-random number and comparing it with a pre-defined probability of conversion of 25% for each voxel. A similar process of randomly converting solid-voxels to pore-voxels was then carried out to obtain the same total porosity as the initial microstructure (see figure 3.15). Again this “roughening” process is rather arbitrary and just intended to get an idea of the effect it can have, rather than to be an accurate representation of a real microstructure.

A relatively lower degree of hydration of 35% was used in these simulations since the finer pore sizes at higher degrees of hydration did not allow sufficient number of steps of roughening to be carried out and the effect of roughening could not be seen clearly. The pore sizes and MIP simulations from the reference microstructure with no roughening are compared with microstructures with 5 and 10 steps of roughening in figure 3.16. It can be seen that the effect of roughness on pore-sizes is the most significant of all the parameters considered and as expected rougher microstructures appear to have finer pore-sizes.

It must be noted that in the case where 10 steps of roughening using voxels of  $0.1\ \mu\text{m}$  were carried out, the maximum possible movement of the surface of the pore is  $1\ \mu\text{m}$ , which is

close to the largest pore size. The average movement of the surface will be around  $0.25\mu\text{m}$  in both directions due to a 25% possibility of conversion, making the pores smaller by approximately  $0.5\mu\text{m}$ . This change is reflected both in the largest pore size and the breakthrough diameter. This means that so as to reduce the breakthrough diameter by the order of magnitude needed to achieve agreement between experimental and simulation results, a roughness equivalent to over 90% the size of the largest pore would have to be introduced.

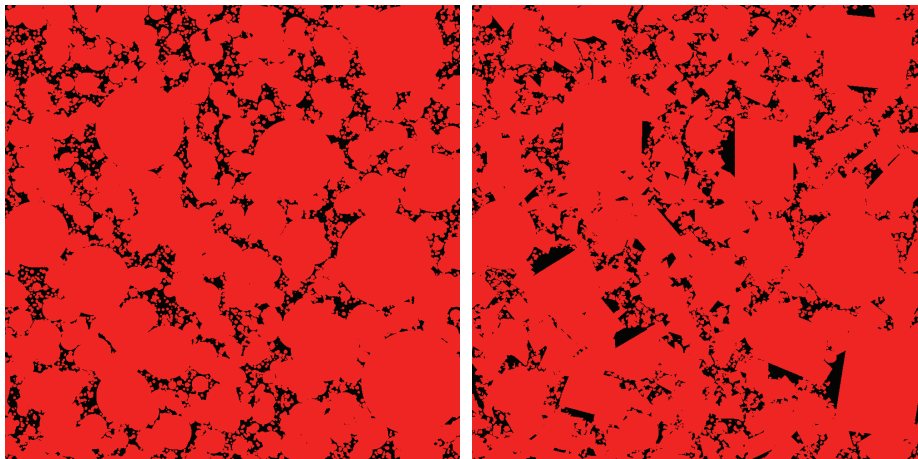


Figure 3.13: Conversion of spherical particles to cylindrical particles (image at 75% hydration, dimension  $100\mu\text{m}$ ). All solid phases are shown in black and the pores are shown in white.

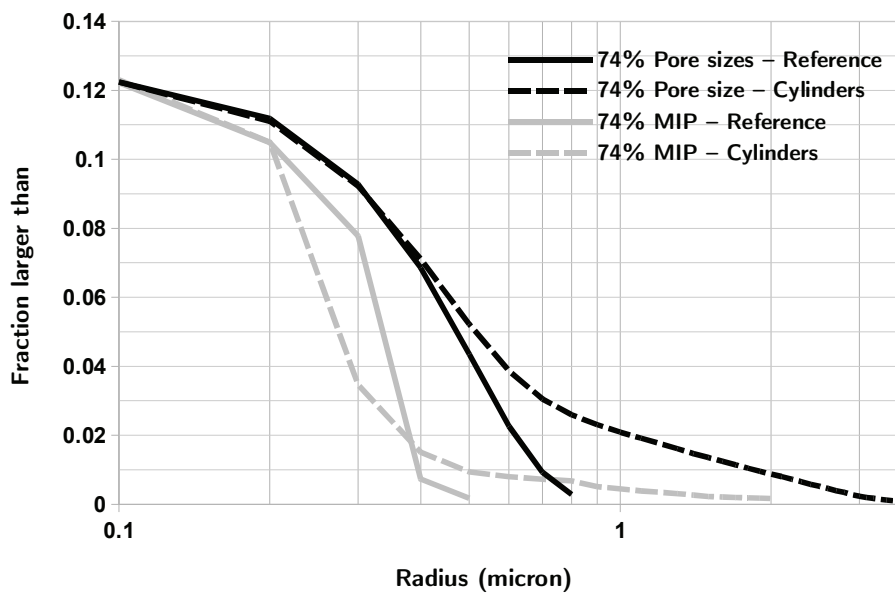


Figure 3.14: Effect of particle shape on pore size and MIP simulations

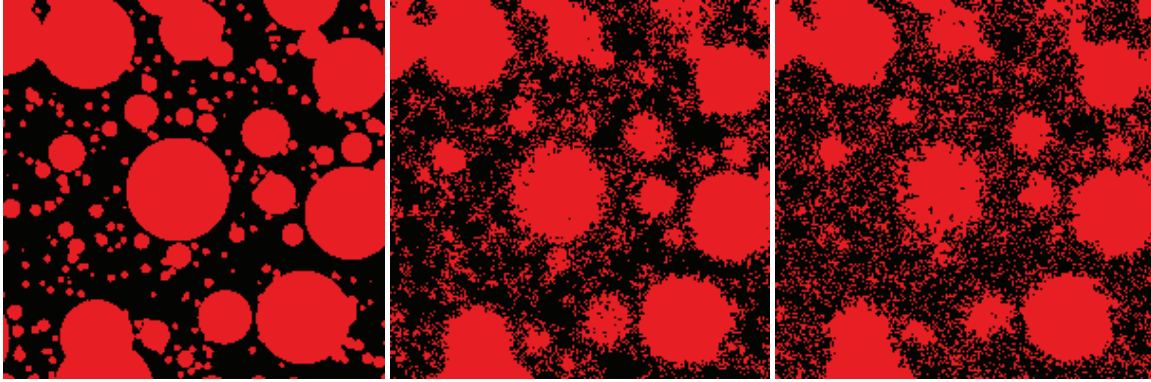


Figure 3.15: The same region of the microstructure before and after 5 and 10 steps of roughening respectively (from left to right, dimension  $20\mu\text{m}$ ). All solid phases are shown in red and the pores are shown in black.

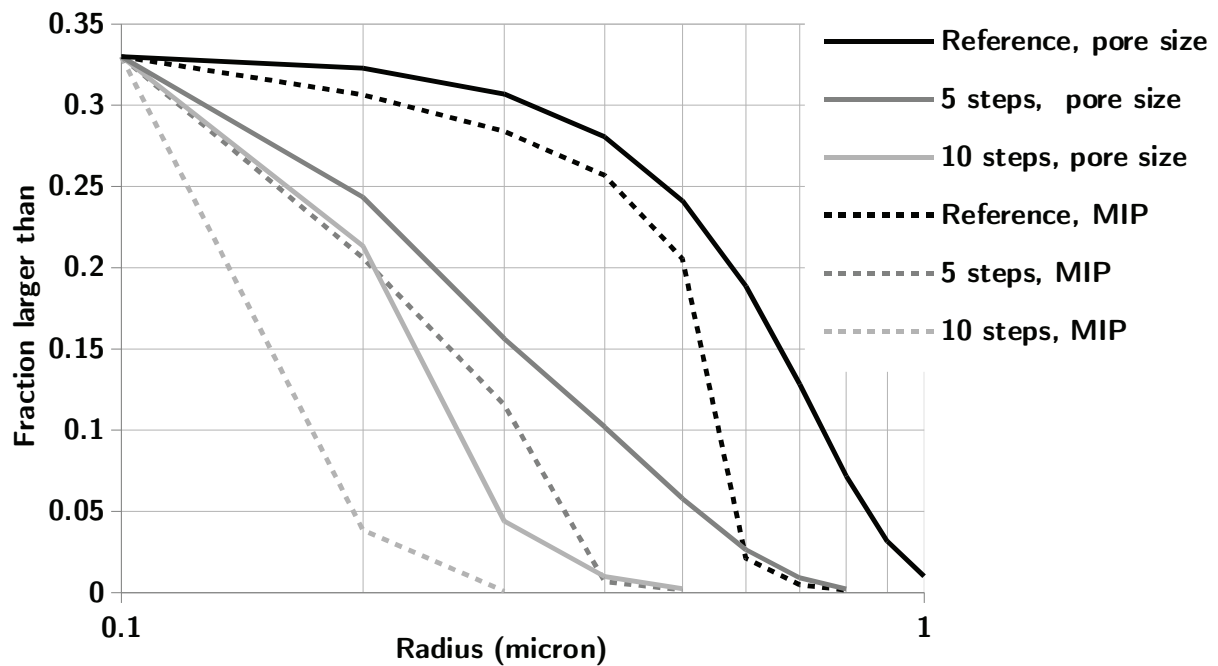


Figure 3.16: Effect of surface roughness on pore size and MIP simulations

### 3.4 Discussion of results and the “nature of C-S-H”

The results in this study demonstrate that while the pore size distributions and MIP simulations on numerically generated microstructures are sensitive to parameters such as the density of the product, the number of particles and the roughness of the surface, the pore

network in the microstructures simulated using numerical models is significantly different from the reality. The biggest difference between the two appears to be the much smaller breakthrough diameter in real systems.

Although most of the parameters considered in this study have some effect on the simulations, the only parameter that appeared to have an effect large enough on the breakthrough diameter to bring it close to the real values is the surface roughness. This indicates that the hydration product would have to extend into the pores by at least 90% of their size even at low degrees of hydrations. This result is in line with the observation, that in order to match the total porosities measured using MIP, the density of C-S-H during early ages has to be assumed to be less than half of its final value. Several studies have postulated a variable packing density of C-S-H [Jennings 2004, Masoero *et al.* 2012] and conclusions similar to those in this study were earlier drawn during a study of the hydration kinetics of alite [Bishnoi and Scrivener 2009b]. These results were independently confirmed later in other studies [Thomas *et al.* 2009, Scherer *et al.* 2012a, Scherer *et al.* 2012b]. Recent results measuring the pore sizes on hydrating cement pastes that have never been dried [Muller *et al.* 2013] confirm the absence of pores larger than a few tens of nanometres and therefore spread of the hydration products throughout a large part of the microstructure after 24 hours of hydration. Similar results, although without quantification, have been reported earlier [Fratini *et al.* 2003, McDonald *et al.* 2007]. It must be noted that although this C-S-H is often referred to as a ‘loosely packed product’ at least some of this product has to be strong enough to withstand the pressures applied during MIP measurements in order to explain the results in this study. Furthermore, the apparent bulk density of C-S-H in this study may be higher than the real values due to a partial collapse of the loose product.

The results also demonstrate that in order to obtain more a realistic representation of the microstructural development in cement pastes, a proper treatment of this product is required in the microstructural models. It is expected that a better understanding of this ‘diffuse’ growth of C-S-H through experiments and simulations will significantly affect our current understanding of the way the properties of concrete develop.

### 3.5 Conclusions

A new simulation algorithms based on the voxel method was proposed to simulate mercury intrusion curves of numerical microstructures of cementitious systems at higher resolutions than previously possible. It was also shown that through parallelisation and the use of sufficiently small voxels, an accurate characterisation of numerical microstructures can be carried out.

The sensitivity of the calculated pore-size distributions to various parameters used in microstructural simulations was studied. Most importantly, it was seen that a more diffuse growth of C-S-H has to be considered in order to obtain better agreement between the experiments and the simulations. First a lower bulk density of C-S-H has to be assumed at early age to obtain an agreement between the experimentally measured and simulated total porosity. Then, even at early ages, C-S-H must be distributed throughout a major portion of the capillary pores, with “rough” edges – for example needles projecting into the empty pores – in order to obtain better estimates of the breakthrough diameter.

While it is admitted that the approach used to quantify pore-sizes is approximate, the errors due to the simplified approach used are expected to be much smaller than the difference between computed and experimental curves. It can finally be concluded that the currently available microstructural simulations, in which C-S-H is assumed to have compact growth with a smooth interface with the porosity, give unrealistic representations of the pore structure of cement paste.

## **Chapter 4: Simulating the setting time and the early age mechanical properties of tricalcium silicate pastes: Effect of flocculation and densification of calcium silicate hydrate**

### **4.1 Introduction**

This chapter is mainly based on an article submitted to “Modelling and Simulation in Materials Science and Engineering” [Do *et al.* 2013b].

The mechanical properties of cementitious materials, such as their compressive strength and elasticity are important parameters in material and structural design. The strength of the material determines the maximum load that can be safely carried by the structure and the elasticity governs deformations and the serviceability. In this chapter, the elastic properties of C<sub>3</sub>S paste are calculated by applying various techniques on numerically simulated hydrating microstructures. Although easier to measure, compressive strength is difficult to calculate as it requires complex fracture mechanics. Most available models of compressive strength are empirical and relate it to factors that govern the porosity and its evolution with hydration [Feret 1892, Abrams 1918, Bolomey 1935, Powers 1958]. However, the utility of these relationships is limited as they do not take the microstructural features into account. Compressive strength can also be indirectly calculated using empirical relationships with elastic modulus [e.g. ACI committee 318:2008, EN 1992-1-1:2004], which is relatively easier to simulate numerically.

Several approaches exist for the calculation of homogenised mechanical properties, such as the elastic modulus and poisson's ratio, of composite materials. Early work in micromechanics used assumptions of uniform strains [Voigt 1887] or uniform stresses [Reuss 1929] to calculate moduli of crystal aggregates. Such assumptions, however, were approximate since in the former approach the forces between grains were not in equilibrium, while in the latter the deformations are not compatible. Still, it was shown that these approaches gave the lower and upper limits for the possible real values of the elastic modulus [Hill 1952]. Later work by Eshelby [1957,1959] modelling the stress field in an elastic medium with an ellipsoidal

inclusion, led to the development of various schemes, e.g. the self-consistent scheme (SCS) for the evaluation of multi-inclusion systems [Hill 1965, Mori and Tanaka 1973]. These approaches have also been applied to hydrating cement pastes with encouraging results [Bernard *et al.* 2003, Sanahuja *et al.* 2007]. Although these approaches can take the mechanical properties of individual phases and their overall volume fraction into account, their arrangement is not considered. Although approaches that can take the spatial distribution of inclusions into account have been developed [e.g. Castaneda and Willis 1995], the large number of phases in cements and their complex distribution cannot be analytically modelled.

The arrangement of phases in the microstructure can be explicitly considered through microstructural models that simulate the evolution of cement microstructure with hydration [e.g. Bentz 1995, Bishnoi and Scrivener 2009a]. These models can be classified into two main types: discrete and vector. In the former the volume is divided into smaller cubic elements called voxels, each containing one phase that may change with hydration. In the latter approach, the microstructural development is simulated through the growth of layers of products on spherical cement particles and the production of new nuclei in the pores. The discrete approach is computationally less expensive but suffers from a resolution limit that restricts the size of the smallest feature that can be represented in a microstructure. The vector approach is resolution free but is computationally more expensive and is generally limited to spherical particles.

For the calculation of elastic properties, numerical techniques such as the finite element method (FEM) [Hrennikoff 1940, Courant 1943] can be applied directly to the discrete microstructures and to discretised versions of vector microstructures. In FEM, the microstructure is built by joining small elements with uniform properties and the response of the composite material to applied boundary conditions is calculated [Haecker *et al.* 2005]. Good estimates of mechanical properties can be obtained at later ages using FEM, however, it has been reported that due to the relatively low resolution meshes required due to computational limitations, higher elastic moduli are predicted at early ages as artificial connections between voxels are induced (see figure 4.1) [Haecker *et al.* 2005]. It has been shown that the additional connectivity induced due to the limited resolution can be corrected through separation of elements using heuristic rules [Šmilauer and Bittnar 2006]. These rules can often be simplistic and it can be difficult to correctly distinguish between the real and artificial connections. Although another method known as the Fast Fourier Transform (FFT)



[Suquet 1990, Moulinec and Suquet 1994] method has also been applied to cements [Šmilauer and Bittnar 2006], large contrasts between the elastic properties of phases, e.g. cementitious phases and water, can lead to inaccuracies in the results [Dunant *et al.* 2013].

*μic* was used to generate three-dimensional hydrating  $C_3S$  microstructures that were discretised and analysed using some of the methods discussed above. All artificial connections due to meshing were removed by explicitly calculating overlaps between the particles in the resolution-free vector microstructure before the final meshing. The mechanical properties of the corrected microstructure were calculated using FEM and SCS and were compared with results in the literature [Boumiz *et al.* 2000]. Two different approaches are then explored to reduce the time of onset of mechanical properties. In the first approach, the  $C_3S$  particles were assumed to be flocculated in the initial microstructure and in the second approach the packing density of C-S-H was assumed to increase with hydration.

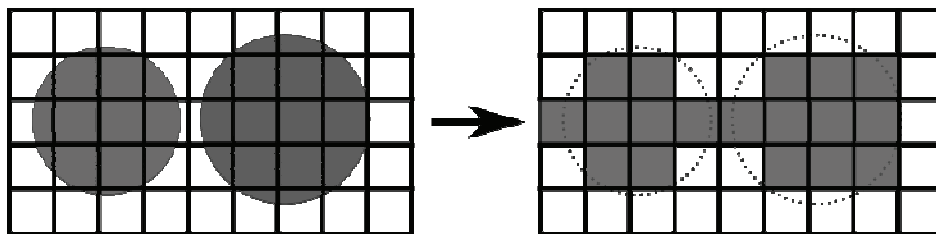


Figure 4.1: Artificial connections may be induced due to meshing when distances are smaller than mesh size

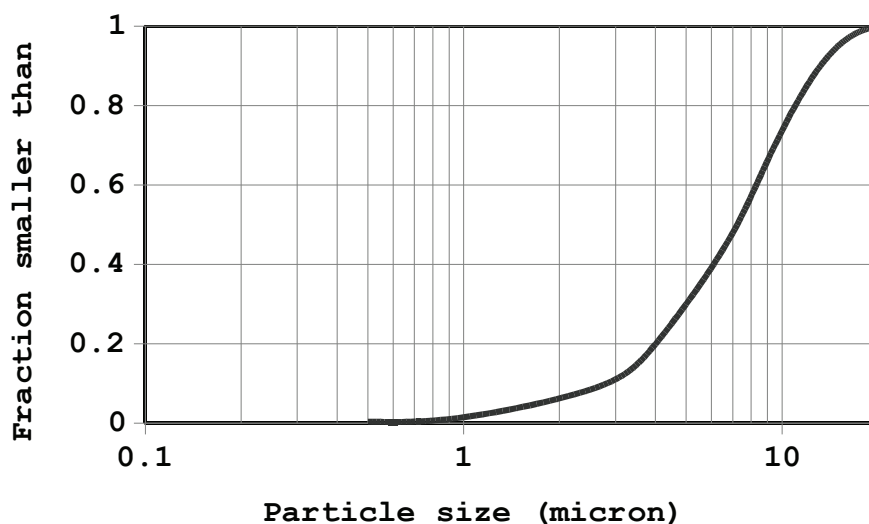


Figure 4.2: Particle size distribution of  $C_3S$  used in the simulations

## 4.2 Microstructural model

The modelling platform *μic* was used to model the hydration of tricalcium silicate ( $3\text{CaO}\cdot\text{SiO}_2$  or  $\text{C}_3\text{S}$  in cement chemistry notation\*) pastes – the main phase of portland cements and the resulting three-dimensional microstructure. The advantage of using microstructures from *μic* is that rather generating random spatial distribution of phases, it simulates the processes that lead to microstructural development, generating more realistic representations of microstructures. Additionally, as *μic* uses the vector approach, the generated microstructures do not suffer from a resolution limit. Although the output of such simulations is often discretised to calculate mechanical properties using FEM, the original vector microstructure can be easily used to obtain additional information. In the simulations, spherical particles of  $\text{C}_3\text{S}$  were placed in a computational volume (CV) with  $50\ \mu\text{m}$  side having periodic boundaries, using random parking. The effect of flocculation on the development of properties was also studied. The particle size distribution used for  $\text{C}_3\text{S}$  is shown in figure 4.2. This distribution was generated using the median diameter of  $8.7\ \mu\text{m}$  and the Blaine's fineness of  $400\ \text{m}^2/\text{kg}$  reported for the powder with which the mechanical results will be compared [Boumiz *et al.* 2000]. In order to obtain a representative volume element (RVE) both for hydration and mechanical simulations, the largest unhydrated particle of  $\text{C}_3\text{S}$  was chosen to be 2.5 times smaller than the CV. The diameter of the smallest particle was  $0.1\ \mu\text{m}$  (one-fifth of the voxel size of  $0.5\ \mu\text{m}$ ). Approximately 43,000 particles of  $\text{C}_3\text{S}$  were placed in the  $50\ \mu\text{m}$  CV. The hydration of  $\text{C}_3\text{S}$  was simulated by its consumption and the production of calcium silicate hydrate (C-S-H) and calcium hydroxide (CH or portlandite). For each unit volume of  $\text{C}_3\text{S}$  reacting, 1.569 unit volumes of C-S-H and 0.593 unit volumes of CH were assumed to be produced. These numbers are based on specific gravities of 3.15, 2.0 and 2.24 for  $\text{C}_3\text{S}$ , C-S-H and CH respectively and the formula  $\text{C}_{1.7}\text{SH}_4$  for C-S-H. The density of C-S-H of  $2.0\ \text{g}/\text{cm}^3$  is a typically accepted value including the intrinsic “gel” porosity. As will be discussed below, in some simulations this value was varied. The C-S-H was assumed to grow around the reacting  $\text{C}_3\text{S}$  grains and new particles of CH were created in the pores. The CH particles were produced throughout the first 20 hours of hydration to give a final number of 8,000, which is approximately one-fifth the number of  $\text{C}_3\text{S}$  particles in the system, based on the results published by Jennings and Parrott [1986].

---

\*Cement chemistry notation:  $\text{CaO} - \text{C}$ ;  $\text{SiO}_2 - \text{S}$ ;  $\text{H}_2\text{O} - \text{H}$ .  $\text{C}_3\text{S}$  is the main phase in portland cements.

A time-stepping scheme for the simulations was manually entered using trial and error in order to achieve no more than 3% of hydration in each step. Microstructures were produced at various degrees of hydration and discretised using a mesh size of 0.5  $\mu\text{m}$  giving a total of one million voxels in the CV. Discretisation was carried out by marking all voxels whose centres are contained inside one of the layers of the cement or hydrate particles as the phase contained in that layer. When multiple particles overlap over the centre of a voxel, the particle that reaches the point earlier in hydration decides the phase of the voxel. When the centre of a voxel does not lie inside any particle, it is considered to be a water-filled pore.

Table 1: Intrinsic elastic properties of chemical phases in the homogenization as measured by nanoindentation or mechanical tests

Phase	Young's modulus [GPa]	Poisson's ratio[-]	References
C <sub>3</sub> S	135	0.3	[Velez <i>et al.</i> 2001]
Portlandite	38	0.305	[Constantinides and Ulm 2004]
C-S-H average (1Low:1High)	25.55	0.24	[Constantinides and Ulm 2004]
Water-filled porosity	0.001	0.499924	[Šmilauer and Bittnar 2006]

## 4.3 Simulations

### 4.3.1 Intrinsic elastic properties of chemical phases

The intrinsic elastic properties of the individual phases used in these simulations were taken from the literature [Velez *et al.* 2001, Constantinides and Ulm 2004] and are listed in table 1. Since a large variation exists in the reported elastic parameters of C-S-H, the average of the values of the elastic modulus reported by Constantinides and Ulm [2004] was assumed for a C-S-H having a density of 2.0  $\text{g}/\text{mm}^3$ . As discussed later in this chapter, in order to take the variable density of C-S-H into account, elastic modulus was calculated as a function of the bulk density of C-S-H using SCS. Isotropic linear elastic behaviour and perfect bond between all constituents was assumed.

Due to computational limitations, water was modelled to behave as an incompressible element with a low elastic modulus and a bulk modulus of 2.18 GPa and its flow and equalisation of pore pressures were neglected.

### 4.3.2 Self consistent scheme (SCS)

As discussed earlier, the SCS uses the elastic constitutive law for each phase, the volume fraction of phases and the average strain or strain concentration tensors of phases to represent the homogenised elasticity tensor. In the most widely used approach by Hill [1965], the strain concentration tensor is estimated by assuming uniform strain induced in an ellipsoidal inclusion in an infinite reference medium subjected to a uniform strain at its boundary, as proposed by Eshelby [1957,1959]. This approach gives good results even at lower volume fractions of the inclusions. In the current study, the inclusions are considered to be spherical and embedded in a medium having the same properties as the homogenised medium. The bulk modulus and shear modulus of the homogenised medium can then be calculated using equations 1-4 below.

$$\alpha_0^{est} = \frac{3k_0}{3k_0 + 4\mu_0} ; \beta_0^{est} = \frac{6(k_0 + 2\mu_0)}{5(3k_0 + 4\mu_0)} \quad (4.1)$$

$$k_{hom}^{est} = \sum_r f_r k_r (1 + \alpha_0^{est} (\frac{k_r}{k_0} - 1))^{-1} \left\langle \sum_r f_r (1 + \alpha_0^{est} (\frac{k_r}{k_0} - 1))^{-1} \right\rangle^{-1} \quad (4.2)$$

$$\mu_{hom}^{est} = \sum_r f_r \mu_r (1 + \beta_0^{est} (\frac{\mu_r}{\mu_0} - 1))^{-1} \left\langle \sum_r f_r (1 + \beta_0^{est} (\frac{\mu_r}{\mu_0} - 1))^{-1} \right\rangle^{-1} \quad (4.3)$$

$$k_0 \equiv k_{hom}^{est} ; \mu_0 \equiv \mu_{hom}^{est} \quad (4.4)$$

In the equations above,  $k_r$ ,  $\mu_r$ ,  $k_0$  and  $\mu_0$  are the bulk moduli and the shear moduli of phase  $r$  and of the reference medium, respectively. An iterative procedure using the Newton-Raphson method was implemented in order to estimate  $k_{hom}^{est}$  and  $\mu_{hom}^{est}$ . Although new approaches have been developed to take the shape of microstructural features into account [Sanahuja *et al.* 2007, Pichler and Hellmich 2009], in order to limit the number of fit parameters, the classical SCS approach has been used in this study. This approach is also consistent with that used in the microstructural model, of spherical inclusions in a soft matrix.

### 4.3.3 Finite element method (FEM)

FEM is a robust tool for micromechanical analysis that can be conveniently applied even to highly complex microstructures where a discrete mesh can be generated. Similar to the traditional FEM used in structural mechanics, here the stress and strain fields at each integration point in the CV are approximated after imposing kinematic or static uniform boundary conditions. In the kinematic boundary conditions, a uniform deformation is applied to two opposite faces of the CV. In the static boundary condition, a uniform force is applied to one of the faces and the opposite face is held fixed. The Young's modulus and Poisson's ratio can be extracted using the averages of stress and strain fields over the whole CV. A tri-linear shape function for brick elements was found appropriate to approximate the displacement field [Haecker *et al.* 2005, Šmilauer and Bittnar 2006, Chamrová 2010]. Further details of the FEM implementation and the derivation to calculate the elastic properties can be found in Appendix B and D.

It has been shown that the true elastic properties of a composite material lie between the lower bound calculated using the static boundary condition and the upper bound calculated using the kinematic boundary condition and that the two values converge as the size of the CV tends towards a representative volume element (RVE) [Huet 1990]. It will be seen later that since similar results were obtained from both type of bounds, the CV of 50  $\mu\text{m}$  size can be assumed to be representative for the particle size distribution used in this study.

## 4.4 Mechanical properties

### 4.4.1 Comparison with experiments

As discussed earlier, the effective elastic properties were calculated by FEM homogenization using kinematic and static boundary conditions. The results for the kinematic and static boundary conditions are similar (figure 4.3), indicating that in the current case, the CV of 50  $\mu\text{m}$  size can be considered to be representative for the chosen particle sizes ( $<20 \mu\text{m}$ ) [Huet 1990]. Due to faster convergence, the kinematic boundary conditions were applied for calculations in the following sections.

In figure 4.4, the results are compared with experimental results measured by Boumiz *et al.* [2000] using ultrasonic pulse velocity. A comparison of the results shows that FEM and SCS methods give similar results throughout the range of degrees of hydration studied, even

though it has been demonstrated that the results from FEM are affected by the spatial distribution of phases and the results of SCS are not [Bary *et al.* 2009, Castaneda and Willis 1995]. Furthermore, it was found that both methods gave a finite elastic modulus even at the first step of the simulation at 2% degree of hydration. This occurs before set was experimentally observed. This is because the artificial connections discussed earlier have not been removed in these simulations, leading to a microstructure that appears to be much stiffer at early ages. It can be seen from the above results that the advantage gained from using microstructure-specific approaches like FEM is lost in comparison to more generalised analytical techniques due to meshing artefacts. The following sections present a technique developed to remove such artefacts before an FEM analysis is carried out.

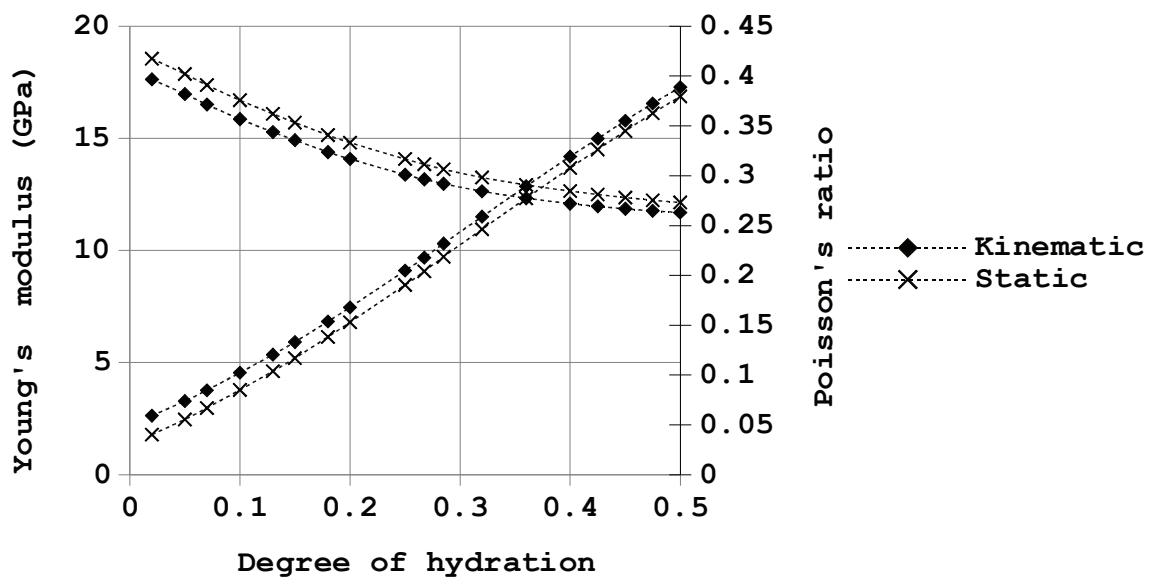


Figure 4.3: Comparison of Young's modulus and Poisson's ratio calculated using kinematic and static boundary conditions

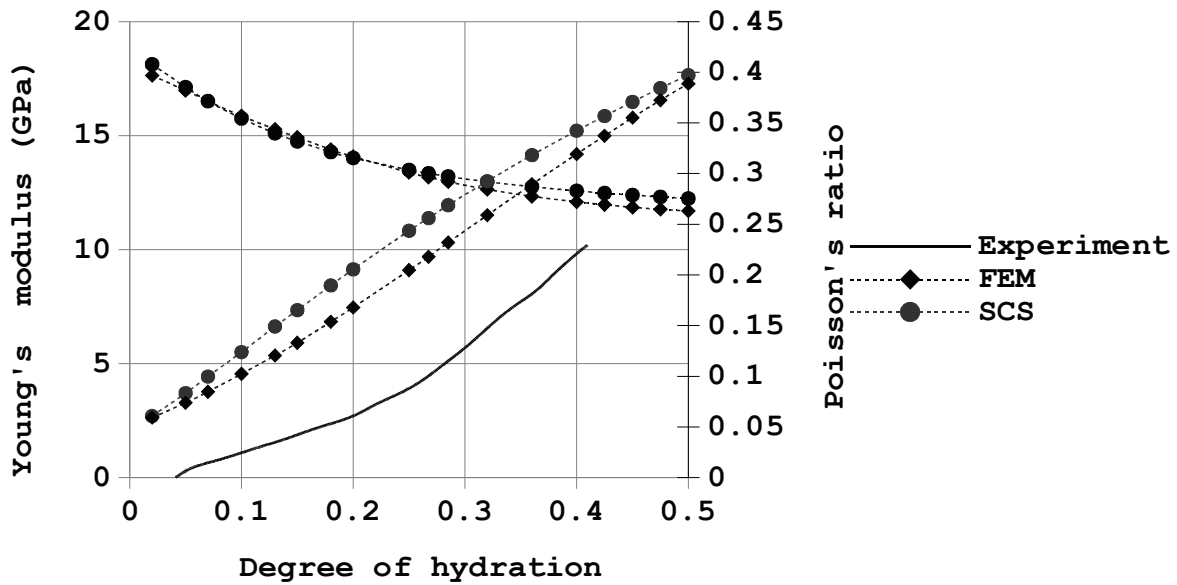


Figure 4.4: Elastic properties calculated using different homogenisation techniques

#### 4.4.2 Double-burning algorithm

A double burning algorithm was developed to remove the artificial connectivity induced in the microstructures due to the relatively coarse mesh size. This technique uses the vector information available from *mic* in the form of the centroids and radii of the particles in order to remove artificial connections in two steps. In the first step, known as global burning, all particles that are not connected to at least one of the faces of the CV where the boundary conditions are applied are removed from the microstructure to be discretised. This removes the possibility of disconnected particles appearing to be connecting in the mesh. The first point at which a connected chain of particles is found is known as the percolation threshold. This corresponds to the lowest degree of hydration where elastic properties can be measured. The voxel mesh is then generated using only the particles that have been identified as connected using the procedure discussed earlier. When the centre of a voxel does not lie within a connected particle, it is given the mechanical properties of a water filled pore.

After the generation of the initial mesh, artificial connections between the remaining particles that appear to be connected in the discretised mesh despite being disconnected in the vector microstructure are removed. In this step, known as local burning, for each solid voxel, it is verified that a connection exists between two faces of the voxel. This is done by starting from the sphere located at the centroid of the voxel and traversing through all spheres that are connected to this sphere directly or indirectly inside the voxel. If the connected spheres

provide a path to move from one face of the voxel to another, always staying within the voxel, the voxel is retained as solid, otherwise it is marked as a water-filled pore. This process is depicted in figure 4.5.

The effect of removing the artificially connected voxels on the microstructure is shown in figure 4.6 and the resulting change in the elastic modulus calculated using FEM is shown in figure 4.7. It is seen in the results that both steps in the double burning process play a role in removing the artificial connections and lower elastic moduli are observed at lower degrees of hydration. It was observed that for the water to cement ratio studied, the first step of burning had a larger effect on the percolation threshold and the second step has a bigger effect on values after percolation is reached.

It can be seen in figure 4.8 that, although a good agreement with the experiments was observed between 20% and 50% hydration. It was observed (see figure 4.8) that the values of elastic modulus calculated from SCS were lower than those calculated from FEM at degrees of hydration below 20%. This is because, although both methods consider similar phase compositions, since all particles that are not present in the percolated chain are removed at lower degrees of hydration, the distribution of the particles is no longer random as assumed in SCS.

In the simulations, percolation was found to occur at degrees of hydration higher than those in the experiments. The above result signifies that in real systems the particles get connected at a lower degree of hydration than in the microstructural model, pointing towards differences between the simulated and real  $C_3S$  microstructures, at least at lower degrees of hydration. In order to study the possible cause of these differences, the effect of flocculation of  $C_3S$  particles and a variation in the density of C-S-H is studied in the following sections.

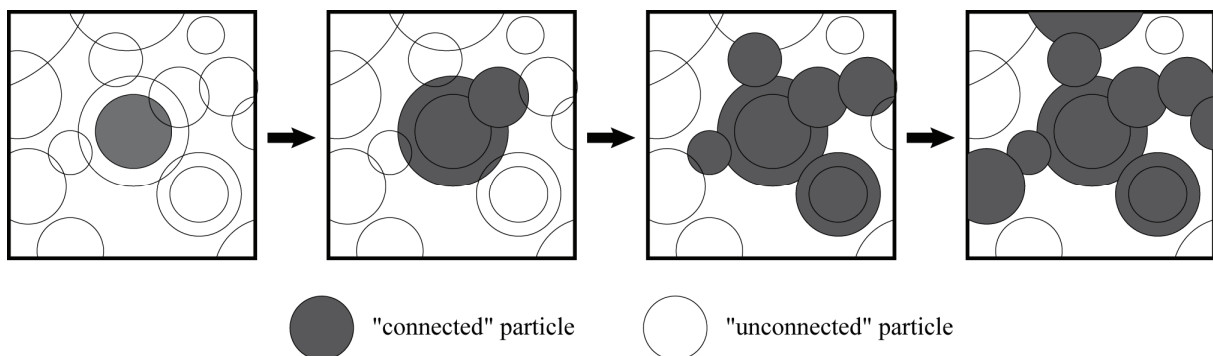


Figure 4.5: Second step of burning applied to a single voxel



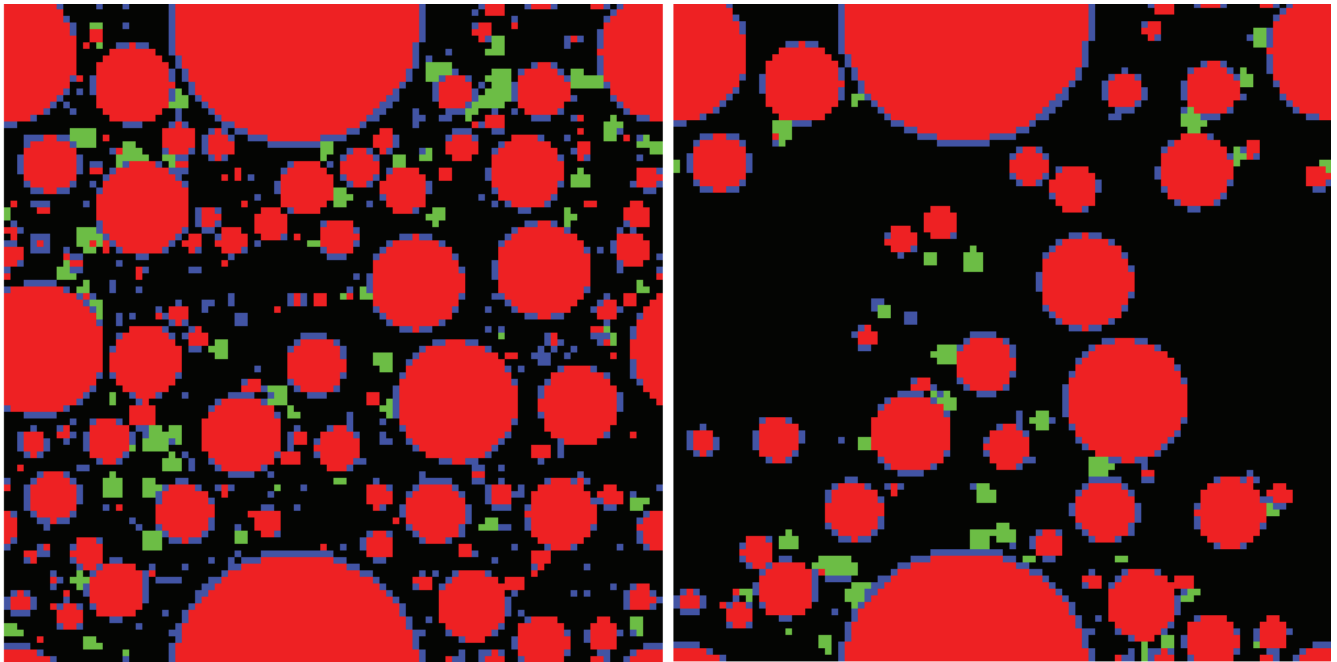


Figure 4.6: The meshed microstructure before (left) and after (right) burning

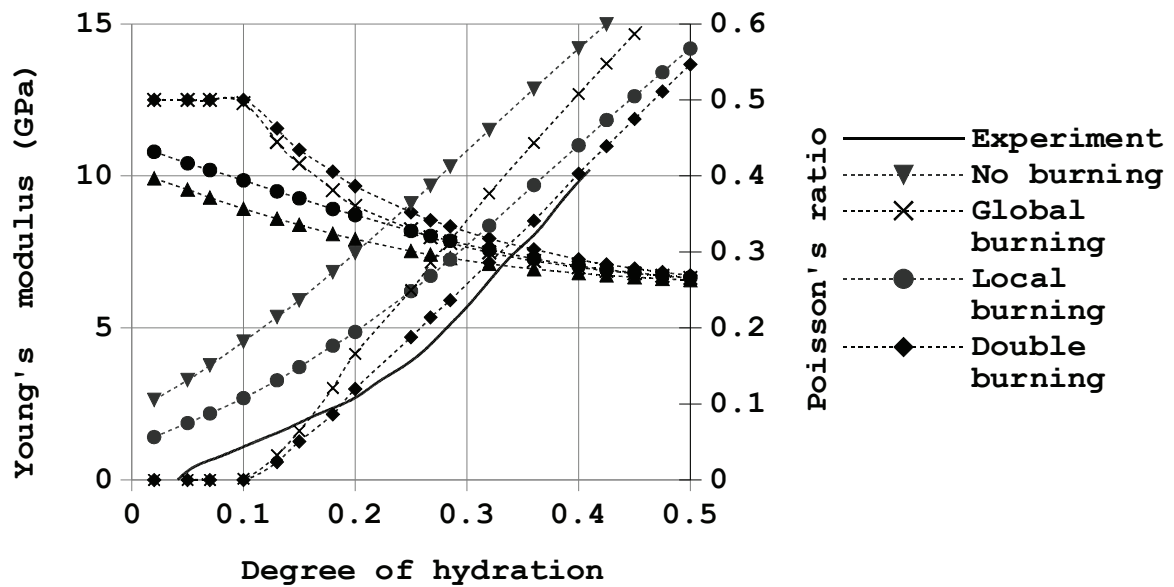


Figure 4.7: Effect of global burning, local burning and double burning on elastic modulus calculated using FEM

#### 4.4.3 Effect of flocculation of C<sub>3</sub>S particles

It has been suggested that setting time may be influenced by flocculation [Scherer *et al.* 2012]. As the average distance between closest particles in flocculated systems tends to be smaller than systems where particles have been randomly parked, a smaller volume of product and therefore a lower degree of hydration is required to create connections. It was found that the unhydrated cement particles in the simulations formed flocs when the following process was implemented on the microstructure before hydration.

1. Locate the nearest neighbour and find the distance between the surfaces of the two particles.
2. Move the first particle such that the distance between the surfaces of the two particles is halved.
3. Move the first particle in random steps, keeping the distance between the surface of the two particles fixed, for a fixed number of steps or until collision with a third particle occurs.
4. Repeat steps 1 to 3 for every particle in the microstructure.
5. Repeat steps 1 to 4 until a stable system is reached.

It was found that the above process has to be repeated 3 times to reach a stable microstructure for the particle size distribution used. Demonstrating the efficacy of the method discussed above, percolation was observed to occur at lower degrees of hydration after the above process was carried out. Simulations carried out at different water-cement ratios using FEM were compared with experimental results from Boumiz *et al.* [Boumiz *et al.* 2000], as shown in figure 4.9. Although it was found that the degree of hydration at percolation was still slightly higher than the experimentally observed values, flocculation was seen to have a significant effect on the degree of hydration at percolation. It must be noted that SCS cannot be used to study the effect of flocculation as it cannot consider the effect of arrangement of phases.

#### 4.4.4 Effect of C-S-H densification

It has been reported that the packing density of C-S-H is low at lower degrees of hydration and may increase as hydration progresses [Bishnoi S. and Scrivener 2009b, Thomas *et al.* 2009]. Since lower density products occupy larger volumes at similar degrees of hydration, it is expected that the degree of hydration required for percolation will be lowered as a result of a lower packing density. To study this effect, the variation in the density of C-S-H is modelled in the *mic* simulation platform by fitting an exponential curve to the average density of C-S-H calculated to match experimentally measured porosity with simulations (0.97 g/cm<sup>3</sup> at 6 hours, 1.38 g/cm<sup>3</sup> at 12 hours, 1.97 g/cm<sup>3</sup> at 3 days of hydration and 2.0 g/cm<sup>3</sup> at 100% hydration) [Do *et al.* 2013]. The function obtained using fitting is given in equation 5, where  $\rho(t)$  is the density of C-S-H at time  $t$ .

$$\rho(t) = 2.0 - (\exp(-0.207t) + \exp(-0.054t)) \quad (4.5)$$

SCS homogenisation of C-S-H with lower packing densities was carried out using the properties of the building block of C-S-H described by Jennings [2000] and their mechanical properties reported by Constantinides and Ulm [2004] and a relationship between the packing density of C-S-H and its elastic properties was obtained as shown in figure 4.10. A similar process for a smaller range of packing densities of C-S-H has been carried out by Vandamme [2008]. Elastic modulus and Poisson's ratio of C-S-H were varied with degree of hydration based on the relationship obtained above in order to calculate the mechanical properties of the paste. As seen in figure 4.11, a good agreement between the experimental results and the calculated elastic modulus could be obtained. Simulations at other water to cement ratios could not be carried out since data on the variation of density of C-S-H with hydration was not available.

The results show that both flocculation and a loosely packed C-S-H can be assumed to obtain a good correlation between experimentally measured and simulated elastic moduli.

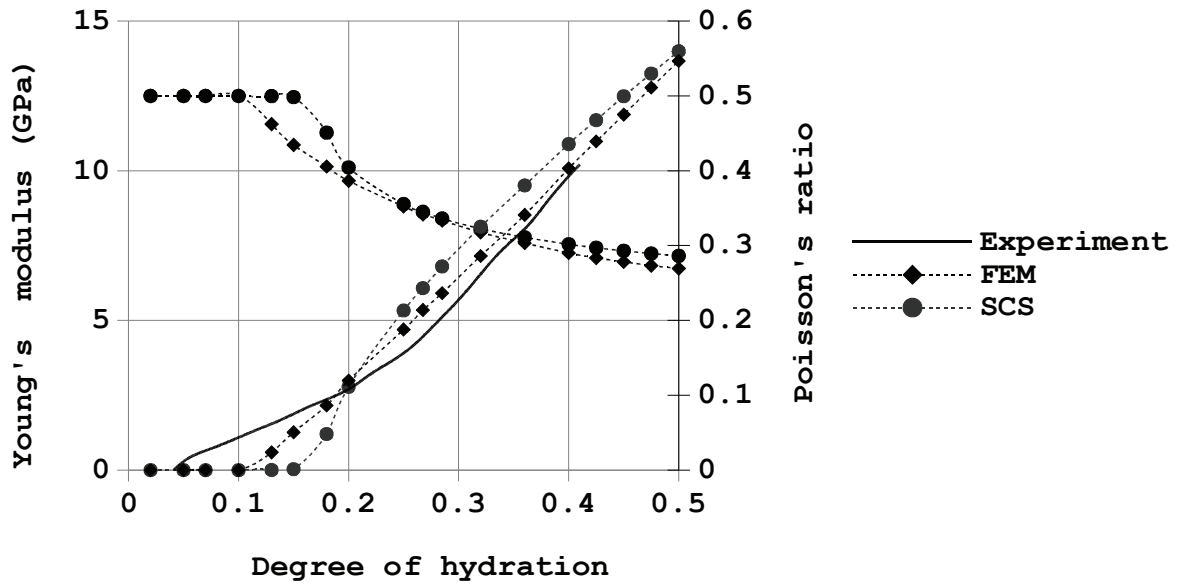


Figure 4.8: Elastic properties calculated using different homogenisation techniques after the application of the double-burning algorithm

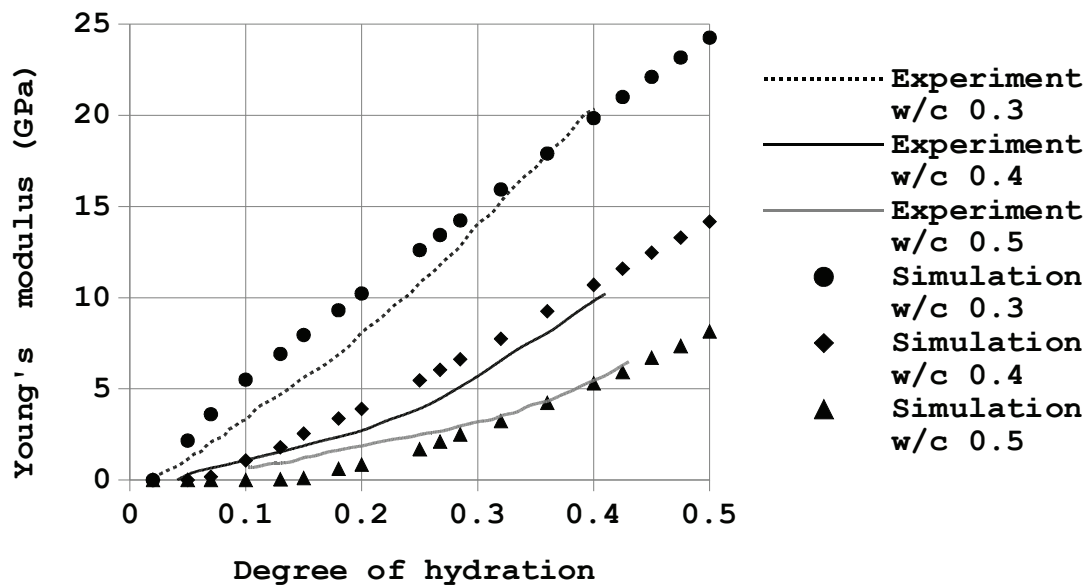


Figure 4.9: Effect of water to cement ratio on elastic properties

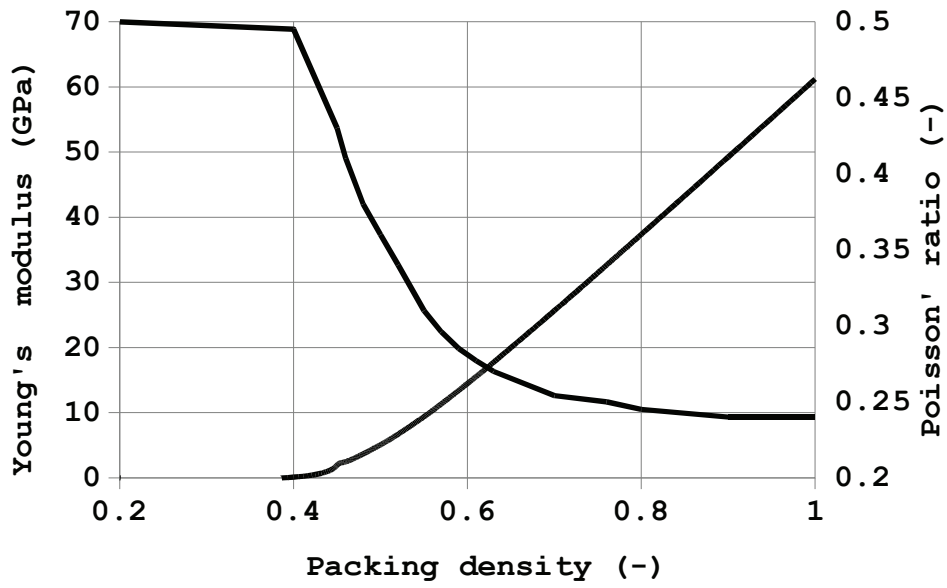


Figure 4.10: Effect of packing density of C-S-H on its elastic properties calculated using SCS

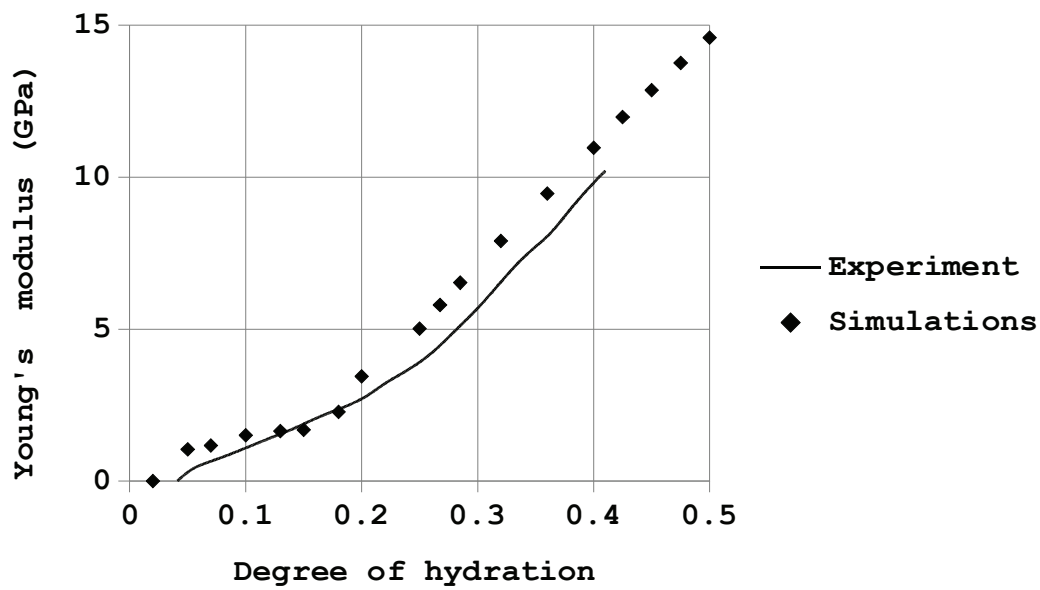


Figure 4.11: Comparison of experimental and simulated elastic modulus for microstructures with variable packing density of C-S-H

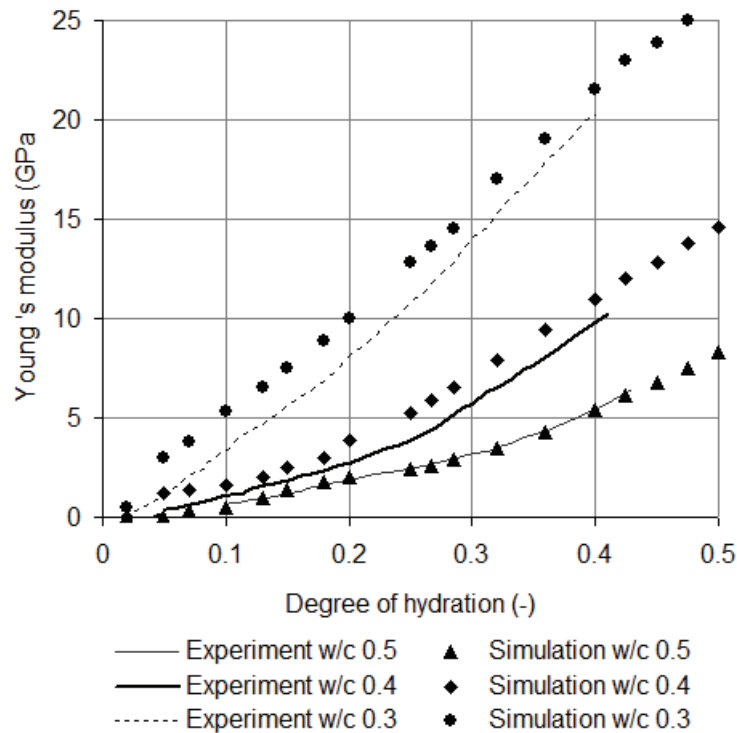


Figure 4.12: Comparison of experimental and simulated elastic modulus for microstructures with variable packing density of C-S-H and flocculation

#### 4.4.5 Combination effect of C-S-H densification and flocculation of $C_3S$ particles

The initial  $C_3S$  particles were placed in the system using the flocculation process discussed in section 4.4.3 and hydration and simulation of the elastic properties were carried out assuming C-S-H densification discussed in section 4.4.4. The calculated elastic moduli of the microstructures at different w/c ratios were again compared with measured results. As shown in figure 4.12. The simulations with considering both the effects of densification and flocculation still capture quite well experimental values. Due to larger volumes of C-S-H formed and the flocculation effect, the percolation thresholds of the microstructures were found at very early hydration and were in good agreement with experimental percolations for all w/c ratios.

## 4.5 Conclusions

The elastic properties of three-dimensional numerical microstructures of hydrating  $C_3S$  pastes were calculated at early ages by applying the finite element method on a discretised numerical microstructure. Higher than expected values of the elastic modulus were found at low degrees of hydration due to artificial connections in the relatively coarse mesh. A method was

developed to remove these artificial connections by using the information available in the resolution-free microstructures available from  $\mu ic$ . It was found that after this correction, although percolation takes place at higher than expected degrees of hydration, a good agreement with the experimental results could be obtained between 20% and 40% hydration. A better agreement with the experimental results at lower degrees of hydration could be obtained if the initial microstructure was considered to be flocculated or if a loosely packed C-S-H is assumed to fill a large part of the microstructure and then densify with hydration. The results also show the advantage of using the finite element method over analytical homogenisation techniques as it can more accurately account for the spatial arrangement of the phases.





## Chapter 5 Microstructural Modelling of Ageing Creep in Early Age Cement Paste

### 5.1 Introduction

The viscoelastic behaviour of cement-based materials is as an important factor in structural design since it significantly affects the stress evolution and time-dependent deformation of structures, notably pre-stressed and post-tensioned structures. In viscoelastic materials, the gradual increase in strain with time under a sustained stress is called creep. Creep in cement paste displays ageing effects: hydration significantly affects the microstructure and some phase properties notably at early age.

Despite its practical importance, there is very limited experimental data on the creep properties of cement paste at ages less than 72 hours in literature. This is because experiments on creep during this period are very sensitive and difficult to carry out as the microstructure of materials is changing rapidly, which interferes with in the interpretation of the experimental data and makes acquisition difficult.

Models to predict the creep of cement-based materials are usually based on mathematical functions that fit empirical data [Bažant and Baweja 2000, Grasley and Lange 2007] or based on simple analytical-micromechanics models [Pichler and Lackner 2008, Scheiner and Hellmich 2009]. Such models do not account for the detailed morphological arrangement of the different phases and they cannot explicitly track the phase geometries in the microstructure. More sophisticated, computer-based numerical models can represent more realistic microstructural configurations and offer the possibility of tracking the evolution of detailed stress and strain states at the microstructural level [Šmilauer and Bažant 2010, Sanahuja and Toulemonde 2011, Sedef *et al.* 2006]. These, however, must accurately represent the geometrical phase arrangement in the microstructure.

While it is generally agreed that creep of cement paste originates in C-S-H [Ulm *et al.* 1999, Velez *et al.* 2001, and Vandamme 2008], homogeneous C-S-H identical to the C-S-H in a hydrating cement paste seems impossible to prepare at scales suitable for mechanical testing. The identification of C-S-H properties therefore comes from one of two indirect approaches:

either (1) microstructural inverse analysis from creep data of cement paste or concrete [Šmilauer and Bažant 2010]; or (2) short-term nano-indentation measurements [Constantinides and Ulm 2007, Vandamme 2008, Vandamme and Ulm 2009] over some minutes at the scale of 1  $\mu\text{m}$ , at which the C-S-H is assumed to be homogenous. The latter is used in this study.

This chapter presents a new numerical approach for prediction the ageing creep in early-age cement paste. The simulations only need as input the mixture characteristics. The microstructure results from the hydration simulation and the mechanical simulations then use only the intrinsic properties of chemical phases. The creep behaviour at the paste scale of the digital microstructures generated by *mic* [Bishnoi and Scrivener 2009] is obtained by means of numerical homogenization using FE analysis using the burning algorithms discussed above. The linear viscous properties of C-S-H from measured nano-indentation [Vandamme 2008] are numerically represented using generalized Maxwell chains. The creep compliances of the digital microstructures for different ages of loading are calculated under a sustained constant stress. The novelty in this study is that the creep simulations for very young ages of loading take into account the rapidly changing microstructure due to continuing hydration. In the early stage of hydration, when the microstructure still has a loose spatial structure, characterized by a sparse distribution of solids and a low packing C-S-H density, the solid skeleton tends to deform relatively easily. During the continuing hydration process, the new hydrates are progressively filling up in the spatial microstructure and, as the same time, previously formed C-S-H elements gradually are hardened by increasing their density, which stiffen the microstructure and restrain the viscous deformations. Once new hydrates have been formed, the relaxation of existing C-S-H results in the internal loads that are then redistributed on hydrates formed at different times. Therefore, this approach considers both spatial solidification and C-S-H densification.

## 5.2 Homogenization based on Finite Element Method (FEM)

Elastic and viscoelastic responses of chemical phases in the cement paste microstructures are considered. The continuum FE formulation for elasticity boundary value problems can be found in elsewhere [Turner *et al.* 1956, Argyris *et al.* 1955]. Only the derivations here related to a viscoelastic material are described.

### 5.2.1 Formalized governing equations for linear viscoelastic boundary value problems

The displacement  $\mathbf{u}$  field, stress  $\boldsymbol{\sigma}$  and strain  $\boldsymbol{\varepsilon}$  tensors at each infinitesimal point at time  $t$  within a given spatial domain  $\Omega$  under the static condition are expressed by:

$$\text{Equilibrium:} \quad \nabla^T \boldsymbol{\sigma}(t) + \mathbf{b}(t) = 0 \quad (5.1)$$

$$\text{Kinematics:} \quad \boldsymbol{\varepsilon}(t) = \nabla \mathbf{u}(t) \quad (5.2)$$

$$\text{Constitutive linear viscoelasticity:} \quad \boldsymbol{\sigma}(t) = \mathbf{E} \cdot \boldsymbol{\varepsilon}(t) + \int_0^t \mathbf{R}(t, t') d\boldsymbol{\varepsilon}(t') \quad (5.3)$$

The boundary conditions prescribed on  $\Gamma$  read:

$$\text{Displacement boundary conditions } \Gamma_u: \quad \mathbf{u} = \hat{\mathbf{u}} \quad (5.4)$$

$$\text{Force boundary conditions } \Gamma_t: \quad \mathbf{n} \cdot \boldsymbol{\sigma} = \hat{\mathbf{t}} \quad (5.5)$$

Where:  $\nabla$  is the gradient operator;  $\mathbf{b}$  is the body force vector,  $\mathbf{E}$  is elastic modulus;  $\mathbf{R}$  is the relaxation function;  $\mathbf{n}$  is the unit normal vector;  $\hat{\mathbf{u}}$  is the prescribed displacement vector;  $\hat{\mathbf{t}}$  is the prescribed traction vector.

The boundary value problem above must be numerically solved due to the complexity of the microstructural geometry. As seen from governing equations (5.1-5.5), a viscoelastic boundary value problem differs from an elastic one in the constitutive equation (5.3) described by internal variables. This stress relaxation behaviour leads to the appearance of internal viscous forces in the left hand side of the FE balance equation as discussed in the following.

### 5.2.2 Numerical approach

#### 5.2.2.1 Constitutive linear viscoelasticity based on internal variables

The method of internal variables [Zienkiewicz *et al.* 1968, Taylor 1970, Huet 1993, Guidoum 1994] is used here to eliminate the dependency of the entire response history. Hence the response at a given discrete time requires only the stress-strain states and the internal variables from the previous time step, which are induced by the applied load history.

According to thermodynamics, the canonical system of governing equations describing the rheological behavior of viscoelasticity for any infinitesimal material point is:

$$\frac{\partial R}{\partial \dot{\boldsymbol{\varepsilon}}} + \frac{\partial \Phi}{\partial \boldsymbol{\varepsilon}} = \boldsymbol{\sigma} \quad (5.6)$$

$$\frac{\partial R}{\partial \dot{\boldsymbol{\beta}}} + \frac{\partial \Phi}{\partial \boldsymbol{\beta}} = 0 \quad (5.7)$$

Where:  $\Phi$  is the potential free energy function;  $R$  is the Rayleigh kinetic potential dissipation function;  $\sigma$  is the stress tensor;  $\epsilon$  is the total strain tensor; and  $\beta$  is the thermodynamic state variables tensor.

To describe the constitutive laws of linear viscoelastic materials<sup>1</sup> in detail, it is necessary to define explicitly the two functions  $\Phi$  and  $R$ . A generalized Maxwell model is used to describe numerically the material response. This model is a combination of several Maxwell elements that are assembled in parallel (see figure 5.1). It takes into account the material relaxation that does not occur at a single time, but over a set of periods: it functions as a piecewise linear approximation of the relaxation function in time. Individual segments correspond to different time periods, with shorter ones contributing less than longer ones, which allows the modelling of both short and long term viscoelastic responses given a large enough number of segments.

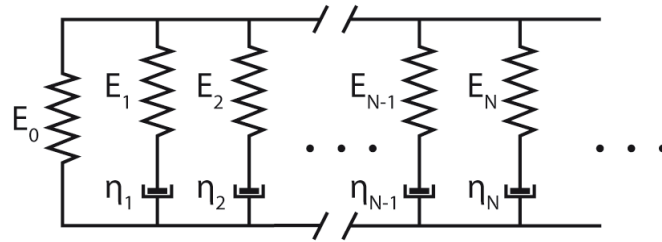


Figure 5.1: Generalized Maxwell model constituted by spring–dashpot Maxwell elements assembled in parallel

### 5.2.2.2 Linear viscoelastic material model of generalized Maxwell for the uniaxial case

The internal variables method with a generalized Maxwell model is formulated in the 1-dimensional case (1D), and then the extension to the 3-dimensional (3D) case is discussed.

The potential free energy function  $\Phi$  and the potential dissipation function  $R$  in the generalized Maxwell material (see figure 5.1) are expressed as:

$$\Phi = \frac{1}{2} \left[ E_0 \epsilon^2 + \sum_{\alpha=1}^N E_{\alpha} (\epsilon - \beta_{\alpha})^2 \right] \quad (5.8)$$

$$R = \frac{1}{2} \sum_{\alpha=1}^N \eta_{\alpha} \dot{\beta}_{\alpha}^2 \quad (5.9)$$

<sup>1</sup> For the sake of simplification, in this study the C-S-H and cement paste are assumed to be “linear” viscoelasticity, meaning that the creep compliance is independent of the stress level

Where:  $\beta_\alpha$  is the deformation of the damper in branch  $\alpha$ . It is called the internal variable as it cannot be measured macroscopically.

Substitution of functions  $\Phi$  and  $\mathbf{R}$  of (5.8-5.9) into (5.6-5.7) leads to the force equilibrium equations for the all branches and for each branch:

$$\sigma = E_o \varepsilon + \sum_{\alpha=1}^N E_\alpha (\varepsilon - \beta_\alpha) \quad (5.10)$$

$$0 = \eta_\alpha \dot{\beta}_\alpha - E_\alpha (\varepsilon - \beta_\alpha) \quad \alpha=1, N \quad (5.11)$$

The constitutive law is defined if all the internal variables  $\beta_\alpha$  are known. The solution can be obtained by integrating the differential equations system of (5.11).

$$\text{With the definition of the relaxation time } \tau_\alpha = \frac{\eta_\alpha}{E_\alpha} \quad (5.12)$$

$$\text{The equation (5.11) becomes } \dot{\beta}_\alpha + \frac{1}{\tau_\alpha} \beta_\alpha = \frac{1}{\tau_\alpha} \varepsilon \quad \alpha=1, N \quad (5.13)$$

The analytical solution of system (5.11) is written in a convolution integral:

$$\beta_\alpha = \int_0^t (1 - e^{-\frac{t-\tau}{\tau_\alpha}}) \dot{\varepsilon}(\tau) d\tau \quad \alpha=1, N \quad (5.14)$$

For the FE analysis, this equation requires integration over finite time intervals. In the numerical approach, the strain rate  $\dot{\varepsilon}$  is assumed to be constant within each time interval  $\Delta t_h$  but changes at steps  $t_h$ . This assumption allows us to obtain the internal variables  $\beta_\alpha$  at the time  $t_i$ , and they are expressed recursively as:

$$\beta_{\alpha_h} = e^{-\frac{\Delta t_h}{\tau_\alpha}} \beta_{\alpha_{h-1}} + \Delta \varepsilon_h \left[ 1 - \frac{\tau_\alpha}{\Delta t_h} (1 - e^{-\frac{\Delta t_h}{\tau_\alpha}}) \right] + \varepsilon_{i-1} (1 - e^{-\frac{\Delta t}{\tau_\alpha}}) \quad (5.15)$$

$$\text{Where: } \Delta t_h = t_h - t_{h-1} \text{ and } \Delta \varepsilon_h = \varepsilon_h - \varepsilon_{h-1} \quad (5.16)$$

Once the increment of internal variables are defined as:

$$\Delta \beta_{\alpha_h} = \beta_{\alpha_h} - \beta_{\alpha_{h-1}} \quad (5.17)$$

The solution then can be rewritten:

$$\Delta \beta_{\alpha_h} = \left[ 1 - e^{-\frac{\Delta t}{\tau_\alpha}} \right] (\varepsilon_{h-1} - \beta_{\alpha_{h-1}}) + (1 - \lambda_\alpha) \Delta \varepsilon_h \quad (5.18)$$

$$\text{Where: } \lambda_\alpha = \left[ 1 - e^{-\frac{\Delta t}{\tau_\alpha}} \right] \frac{\tau_\alpha}{\Delta t} \quad (5.19)$$

The increment of the total stress in (5.10) can also be written in an incremental form at time  $t_h$ :

$$\Delta\sigma_h = E_o\Delta\varepsilon_h + \sum_{\alpha=1}^N E_\alpha(\Delta\varepsilon_h - \Delta\beta_{\alpha_h}) \quad (5.20)$$

With the substitution of  $\Delta\beta_{\sigma_h}$  of (5.18) into (5.20), we obtain an explicit relation between stress and strain in an incremental form:

$$\Delta\sigma_h = (E_o + \sum_{\alpha=1}^N E_\alpha \lambda_\alpha)\Delta\varepsilon_h - \sum_{\alpha=1}^N E_\alpha (1 - e^{-\frac{\Delta t}{\tau_\alpha}})(\varepsilon_{h-1} - \beta_{\alpha_{h-1}}) \quad (5.21)$$

Finally it can be rewritten in tensorial notation for the FE implementation:

$$\Delta\sigma_h = \bar{E}\Delta\varepsilon_h + \Delta\bar{\sigma}_h \quad (\text{or } \Delta\sigma = \bar{E}\Delta\varepsilon + \Delta\bar{\sigma}) \quad (5.22)$$

$$\text{Where: } \bar{E} = E_o + \sum_{\alpha=1}^N E_\alpha \lambda_\alpha \quad \text{and} \quad \Delta\bar{\sigma}_h = -\sum_{\alpha=1}^N E_\alpha (1 - e^{-\frac{\Delta t}{\tau_\alpha}})(\varepsilon_{h-1} - \beta_{\alpha_{h-1}}) \quad (5.23)$$

### 5.2.2.3 Expansion of the model to a 3D multi-axial isotropic material

Based on the uni-axial case discussed above, the constitutive law in the multi-axial case can be described in a similar manner using the assumption that the viscoelastic material is isotropic. The stress and strain components of isotropic materials in the multi-axial case can be decomposed into volumetric and deviatoric parts:

$$\sigma_{ij} = \sigma_m \delta_{ij} + \sigma_{ij}^d \quad (5.24)$$

$$\varepsilon_{ij} = \varepsilon_m \delta_{ij} + \varepsilon_{ij}^d \quad (5.25)$$

$$\beta_{ij} = \beta_m \delta_{ij} + \beta_{ij}^d \quad (5.26)$$

Similar to (5.22), the volumetric component reads:

$$\Delta\sigma_m = 3(\bar{K}\Delta\varepsilon_m + \Delta\bar{\sigma}_m) \quad (5.27)$$

$$\text{Where: } \bar{K} = K_o + \sum_{\alpha=1}^N K_\alpha \lambda_\alpha \quad \text{and} \quad (5.28)$$

$$\Delta\bar{\sigma}_m = -\sum_{\alpha=1}^N K_\alpha (1 - e^{-\frac{\Delta t}{\tau_\alpha}})(\varepsilon_{m_{h-1}} - \beta_{\alpha_{m_{h-1}}}) \quad (5.29)$$

Similar to (5.22), the deviatoric component reads:

$$\Delta\sigma_{ij}^d = 2(\bar{G}\Delta\varepsilon_{ij}^d + \Delta\bar{\sigma}_{ij}^d) \quad (5.30)$$

$$\text{Where: } \bar{G} = G_o + \sum_{\alpha=1}^N G_\alpha \lambda_\alpha \quad \text{and} \quad (5.31)$$

$$\overline{\Delta\sigma_{ij}^d} = -\sum_{\alpha=1}^N G_{\alpha} (1 - e^{-\frac{\Delta t}{\tau_{\alpha}}}) (\varepsilon_{ij, h-1}^d - \beta_{\alpha ij, h-1}^d) \quad (5.32)$$

Similar to (5.24), the decomposition of the stress tensor in an increment form reads:

$$\Delta\sigma_{ij} = \Delta\sigma_m \delta_{ij} + \Delta\sigma_{ij}^d \quad (5.33)$$

Substitution (5.27-5.32) into (5.33) leads to the relation between the stress and strain tensors:

$$\Delta\sigma_{ij} = (3\overline{K} - 2\overline{G})\Delta\varepsilon_m \delta_{ij} + 2\overline{G}\Delta\varepsilon_{ij}^d + 3\Delta\overline{\sigma}_m \delta_{ij} + 2\Delta\overline{\sigma}_{ij}^d \quad (5.34)$$

This relation can be rewritten in a matrix notation for the FE implementation:

$$\Delta\boldsymbol{\sigma} = \overline{\mathbf{D}} \Delta\boldsymbol{\varepsilon} + \Delta\overline{\boldsymbol{\sigma}} \quad (5.35)$$

$$\text{Where: } \Delta\overline{\boldsymbol{\sigma}} = 3\Delta\overline{\sigma}_m \delta_{ij} + 2\Delta\overline{\sigma}_{ij}^d \quad (5.36)$$

and

$$\overline{\mathbf{D}} = \begin{bmatrix} \overline{K} + 4\overline{G}/3 & \overline{K} - 2\overline{G}/3 & \overline{K} - 2\overline{G}/3 & 0 & 0 & 0 \\ & \overline{K} + 4\overline{G}/3 & \overline{K} - 2\overline{G}/3 & 0 & 0 & 0 \\ & & \overline{K} + 4\overline{G}/3 & 0 & 0 & 0 \\ & & & \overline{G} & 0 & 0 \\ & \text{Sym} & & & \overline{G} & 0 \\ & & & & & \overline{G} \end{bmatrix} \quad (5.37)$$

#### 5.2.2.4 Finite element formulation

Derived from the equilibrium equation (5.1), the FE equilibrium in the incremental form to relate internal and external forces of an element in the domain  $\Omega$  for a viscoelastic material reads:

$$\int_{\Omega^e} \mathbf{B}^T \Delta\boldsymbol{\sigma} d\Omega = \Delta\mathbf{F}_{ex}^e \quad (5.38)$$

Where:  $\Delta\mathbf{F}_{ex}^e$  is the external node vector.  $\mathbf{B}$  is the strain displacement matrix.

The strain displacement matrix  $\mathbf{B}$  maps the element displacement vector  $\mathbf{d}$  onto the strain vector  $\boldsymbol{\varepsilon}$ . The incremental form of this relation reads:

$$\Delta\boldsymbol{\varepsilon} = \mathbf{B} \Delta\mathbf{d} \quad (5.39)$$

Substitution (5.35) into (5.38) leads to:

$$\int_{\Omega^e} \mathbf{B}^T (\overline{\mathbf{D}} \Delta\boldsymbol{\varepsilon} + \Delta\overline{\boldsymbol{\sigma}}) d\Omega = \Delta\mathbf{F}_{ex}^e \quad (5.40)$$

Substitution (5.39) into (5.40) reads:

$$\int_{\Omega^e} \mathbf{B}^T (\overline{\mathbf{D}} \mathbf{B} \Delta\mathbf{d} + \Delta\overline{\boldsymbol{\sigma}}) d\Omega = \Delta\mathbf{F}_{ex}^e \quad (5.41)$$

Rearrangement of (5.41) reads:

$$\int_{\Omega^e} (\mathbf{B}^T \overline{\mathbf{D}} \mathbf{B}) d\Omega \Delta \mathbf{d} = \Delta \mathbf{F}_{ex}^e - \int_{\Omega^e} \mathbf{B}^T \Delta \overline{\boldsymbol{\sigma}} d\Omega \quad (5.42)$$

The element stiffness matrix is defined as:

$$\mathbf{K}^e = \int_{\Omega^e} (\mathbf{B}^T \overline{\mathbf{D}} \mathbf{B}) d\Omega \quad (5.43)$$

By substitution (5.43) into (5.42), the canonical format for a FE procedure reads:

$$\mathbf{K}^e \Delta \mathbf{d} = \Delta \mathbf{F}_{ex}^e - \int_{\Omega^e} \mathbf{B}^T \Delta \overline{\boldsymbol{\sigma}} d\Omega \quad (5.44)$$

The global balance equations for the entire system corresponding to the boundary value problem are obtained by assembling equation (5.44) for all elements in the domain  $\Omega$ . In equation (5.44) the right hand side terms are known. Therefore, at each time step, the FE procedure solves for the incremental displacement at every node and incremental stress and strain at every integration point.

In the creep simulations in this study, a constant load with time is applied, the load increment  $\Delta \mathbf{F}_{ex}^e$  is set to zero tensor:  $\Delta \mathbf{F}_{ex}^e \equiv \mathbf{0}$ . For spatial discretisation, regular cubic elements with tri-linear shape functions are used. The detailed algorithm of the Finite Element implementation can be found in Appendix E.

It can be seen here that this incremental formulation using the 3D Finite Element Method with time discretization is an efficient recursive method to update the stress and strain fields, avoiding direct numerical integration of the convolution integral. As a consequence, the current internal variables which need to be updated depending only on their respective internal variables at the previous time step and therefore the method saves memory and is straightforward to implement.

### 5.3. Intrinsic Short-term C-S-H Creep Function

#### 5.3.1 Experimental data

The intrinsic creep properties of C-S-H are adopted from the experimental results of Vandamme and Ulm [2009] and Vandamme [2008]. In their work, the *in situ* creep behaviour of C-S-H, the nano-crystalline phase which forms the major part of hydrated cement paste was measured by means of a statistics on nano-indentation results.



According to Vandamme [2008], the creep compliance of any type of C-S-H can be presented as a logarithmic form:

$$L(t-t_0, t_0) = \frac{1}{M} + \frac{1}{C} \ln \left[ 1 + \frac{t-t_0}{\tau} \right] \quad (5.45)$$

Where:  $L(t-t_0, t_0)$  [GPa<sup>-1</sup>] is the contact creep compliance for loading from  $t_0$ ;  $M$  [GPa] is the elastic indentation module;  $C$  [GPa] is the contact creep module; and  $\tau$  [second] is the characteristic viscous time.

From the experimental results, Vandamme [2008] obtained the correlation between the contact creep modulus  $C$  and the packing density  $\eta$  of C-S-H as:

$$C = 1588.9 (\eta - 0.5)^{1.597} \quad (5.46)$$

Similar to the contact creep compliance in (5.45), the uniaxial creep compliance can be described as follow:

$$J(t-t_0, t_0) = \frac{1}{E} + \frac{1}{C_{uni}} \ln \left[ 1 + \frac{t-t_0}{\tau} \right] \quad (5.47)$$

Where  $J(t-t_0, t_0)$  [GPa<sup>-1</sup>] is the uniaxial creep compliance for loading from  $t_0$ ;  $E$  [GPa] is the elastic module of C-S-H; and  $C_{uni}$  [GPa] is the uniaxial creep modulus.

The relations between the contact and uniaxial parameters in (5.45) and (5.47) are:

$$\frac{E}{M} = \frac{C_{uni}}{C} = 1 - \nu^2 \quad (5.48)$$

Where:  $\nu$  [-] is the Poisson's ratio of C-S-H.

To numerically represent C-S-H behaviour in FE model described in section 5.2, generalized Maxwell chains are used to fit the experimental data. In this study, simulations are carried out assuming 2 cases of C-S-H density: a constant density  $\rho = 2.0 \text{ g/cm}^3$  and densification.

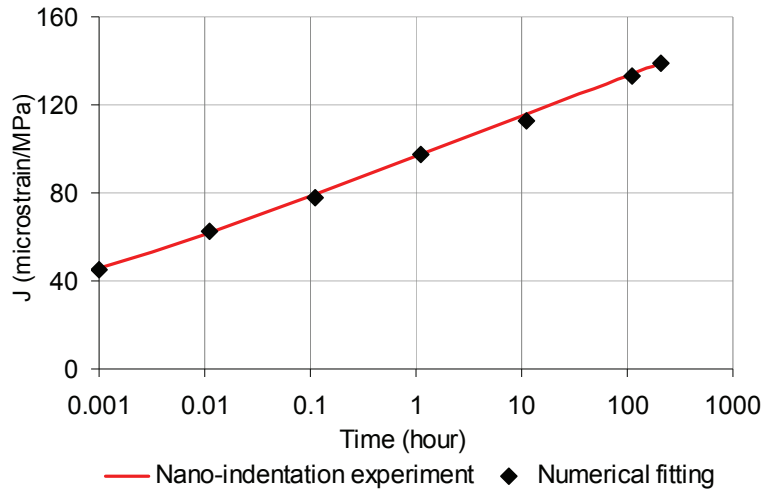
### 5.3.2 Generalized Maxwell model fitting for C-S-H constant density $\rho = 2.0 \text{ g/cm}^3$

C-S-H bulk density  $2.0 \text{ g/cm}^3$  is the typical value reported in the literature [Thomas and Jennings 2006]. The creep simulations for cement paste are performed using only one creep function of C-S-H that corresponds to its constant bulk density  $\rho = 2.0 \text{ g/cm}^3$ , its packing density  $\eta = 0.7$ , initial Young's modulus  $E$  of 25.55 GPa, and constant Poisson's ratio of 0.24. These parameters are used to calculate the uniaxial creep compliance of C-S-H using equation (5.47) whose parameters, in turn, are determined by equations (5.46) and (5.48).

In equation (5.47), one unknown parameter is the characteristic viscous time  $\tau$ . This coefficient was experimentally observed to have a weak correlation with the elastic indentation module  $M$  [Vandamme 2008]. The mean value  $\tau = 1.66$  seconds from the experiments [Vandamme 2008] is used in the simulations in this study. The intrinsic uniaxial creep function of C-S-H based on nano-indentation experiments is shown in figure 5.2. In the logarithmic time scale, C-S-H creep appears as linear. A generalized Maxwell chain with the parameters listed in table 5.1 is used to fit this function for C-S-H elements in the FE analysis of creep at the cement paste level. The Maxwell chain consisting of six branches shows an excellent fitting of the experimental data (see figure 5.2).

Table 5.1: Maxwell chain parameters

Young's modulus $E$ [MPa] ( $\sum E_i = 25550$ )	7629	5548	3773	1526	1526	5548
Relaxation time $\tau_i$ [hour]	0.001	0.01	0.7	40	700	$+\infty$

Figure 5.2: Input uniaxial creep function ( $J(t-t_0, t_0)$ ) of C-S-H derived from (5.47)

### 5.3.3 Multi generalized Maxwell model fitting for C-S-H densification creep functions

A number of authors reported that the packing density of C-S-H is low at a lower degree of hydration and increases with the hydration process [Bishnoi and Scrivener 2009, Thomas *et al.* 2009, Muller *et al.* 2012, Muller *et al.* 2013]. To study this effect on creep properties of cement paste, the simulations of the hydrating microstructure and the inputs of intrinsic compliance of C-S-H are considered with the densification of C-S-H. The development of C-

S-H bulk density  $\rho$  is assumed to be increased with time using the same function as in [Do *et al.* 2013]:

$$\rho(t) = 2.0 - (e^{-0.207t} + e^{-0.054t}) \quad (5.49)$$

If C-S-H is considered as a mixture of the C-S-H building blocks (pure C-S-H with 0% gel-porosity) and porosity, the packing density  $\eta$  of C-S-H will have a linear relation with the bulk C-S-H density. Consequently, all the mechanical properties of C-S-H vary as a function of time. Figure 5.3 shows the evolutions of the packing density (based on (5.47)) and contact creep modulus (calculated from (5.45)) of C-S-H. As seen in the figure, the contact creep modulus curve starts from around 12 hours when the packing density reaches the value of 0.5 (see (5.45)). This implies that the upscaling method of the spherical granular morphology on packing density is characterized by a percolation threshold of 50% solid inclusions below which the composite C-S-H has no stiffness [Vandamme 2008]. The intrinsic mechanical properties strongly develop up to 72 hours, and thereafter settle down to almost constant values.

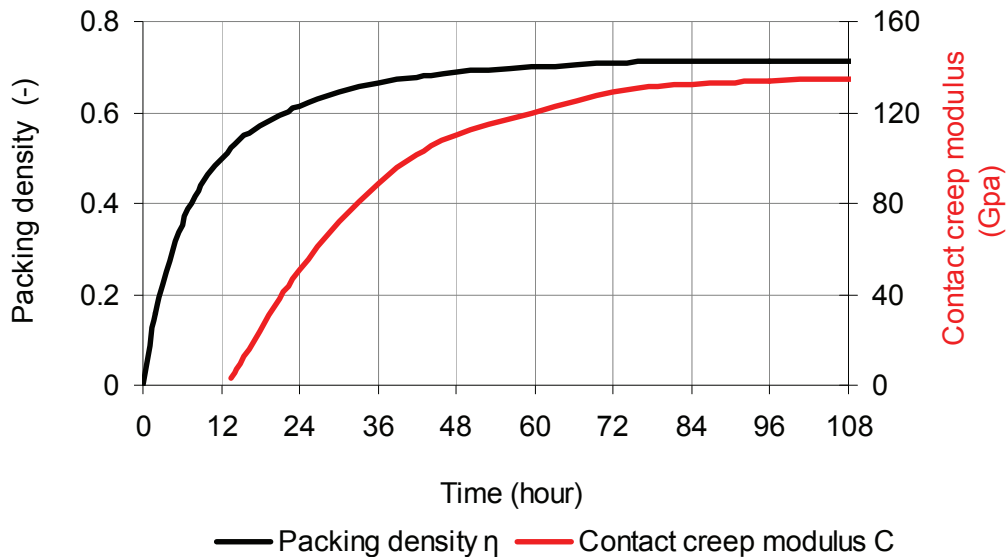


Figure 5.3: The developments of packing density and contact creep modulus of C-S-H

The uniaxial creep functions of C-S-H are determined using equation (5.47), but the major difference between this function and the one used in section 5.3.2 is that it is dependent on the age of loading and the C-S-H densification plays a role in reduction of the viscous component. A scheme to estimate C-S-H creep functions  $J(t, t')$  for loading from  $t'$  taking

into account their densification is sketched in figure 5.4. For the sake of illustrative simplification, in this figure, a C-S-H particle is assumed to grow with both size and densification. At the start of each time interval, a new C-S-H layer is deposited on the surface of this particle in the previous time step. Although this particle is assumed to be homogenous during hydration, its layers formed at different times have different load histories. Consequently, each layer is assumed to have its own viscoelastic response characterized by different creep functions. For loading from  $t' = t_0$ , figure 5.4 illustrates “effective” creep functions  $\mathbf{J}(t, t_0)$ ,  $\mathbf{J}(t, t_1)$ ,  $\mathbf{J}(t, t_2)$ ... corresponding to the responses of layers of C-S-H ( $L_0$ ,  $L_1$ ,  $L_2$  and  $L_3$  in the figure) from  $t_0$  as described below:

***$\mathbf{J}(t, t_0)$  for layer  $L_0$  formed at loading time  $t_0$ :***

The creep functions  $\mathbf{J}(t, t_0)$  (shown as the continuous lines) consists of one instantaneous part (the elastic deformation at loading  $t_0$ ) and segments of the viscous parts that are described by creep functions corresponding to the ageing of C-S-H. For the first viscous segment, the viscous deformation rate of  $\mathbf{J}(t, t_0)$  within the time interval  $[t_0, t_1]$  is derived from (5.47) with the C-S-H density at the time  $t_0$ . It is in the similar way for the second viscous segment, the rate of  $\mathbf{J}(t, t_0)$  within the time interval  $[t_1, t_2]$  is derived from (5.47) with the C-S-H density at the time  $t_1$ . Similarly, for the third and fourth segments of  $\mathbf{J}(t, t_0)$  within the time interval  $[t_2, t_3]$  and  $[t_3, t_4]$  are derived with densities at the time  $t_2$  and  $t_3$ , respectively. Due to densification, the slope of  $\mathbf{J}(t, t_0)$  decreases with each time step.

***$\mathbf{J}(t, t_i)$  for layer  $L_i$  formed at time  $t_{i>0}$  after loading time  $t_0$ :***

The creep functions  $\mathbf{J}(t, t_i)$  (shown as the continuous lines) consists of segments of the viscous deformation, which are described by creep functions from (5.47) corresponding to the C-S-H densities at  $t_i, t_{i+1}, t_{i+2}$ ... The rates of viscous deformation of  $\mathbf{J}(t, t_i)$  decreases with each time step.

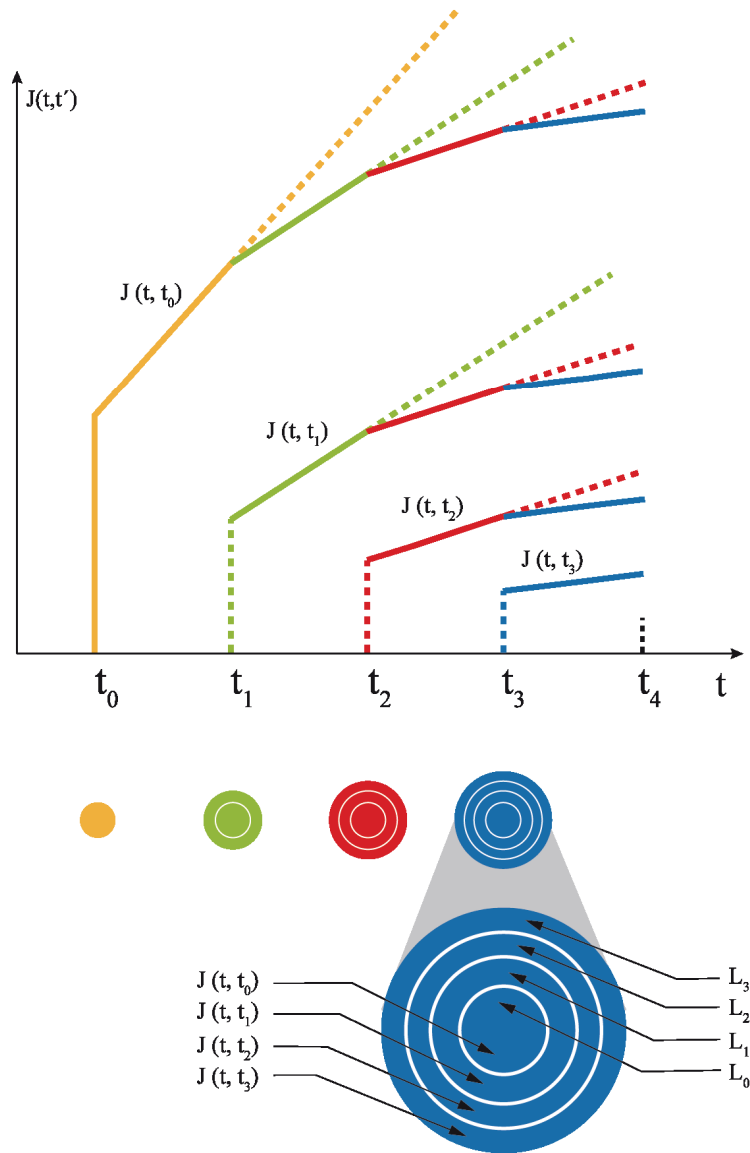


Figure 5.4: Scheme to estimate C-S-H creep functions  $J(t, t_i)$  for the creep simulation of cement paste for loading from  $t_0$  taking into account densification. Although this C-S-H particle is assumed to be homogenous during hydration, its layers formed at different times have different load histories. Consequently, each layer is assumed to have its own viscoelastic response characterized by different creep functions.

The solidification process during numerical creep testing is simulated taking into account 2 factors: the formation of hydrates and C-S-H densification. Due to this densification, the C-S-H phase is heterogeneous in term of creep response. For a creep simulation of cement paste for loading from  $t_0$ , apart from  $J(t, t_0)$ , all the densifying C-S-H phases characterized by creep functions  $J(t, t_1)$ ,  $J(t, t_2)$ ,  $J(t, t_3)$ ... etc also play roles. To account for this fact, several generalized Maxwell models are used in the simulation for a given initial age of loading. In

this multi generalized Maxwell model, each material model is to fit a C-S-H creep function corresponding to the time at which those new C-S-H elements were formed, and an index array is used in the simulation program to keep track of the age of all C-S-H elements. It should also be noted here again that in the FE procedure to simulate creep of cement paste for loading from  $t_0$ , only  $J(t, t_0)$  is assumed to affect for both the elastic and viscous parts, whereas  $J(t, t_1)$ ,  $J(t, t_2)$ ,  $J(t, t_3)$ ... etc are considered to affect only for the viscous part.

#### 5.4. Materials and Hydration Simulation

The hydration of a normal Portland cement at a w/c ratio of 0.5 is simulated using *mic*. The degree of hydration in the simulations are fit to the experimental data from Tamtsia *et al.* [2004] with which the computed elastic values and basic creep results will be compared. Based on the composition of the main minerals with the assumption of 5% gypsum content, the phase cement composition is calculated and is listed in table 5.2. The particle size distribution is obtained by fitting a Rosin-Rammler distribution [Taylor 1997] corresponding to a Blaine fineness of 3400 cm<sup>2</sup>/g (see figure 5.5). Hydration and creep properties are simulated on a cubic representative CV of 100 μm in size [Do *et al.* 2013]. The cement particles in the range from 0.1 μm to 40 μm in size are generated for the initial simulated microstructure.

The hydration kinetics in the model are chosen to fit the profiles of hydration degree (at a constant relative humidity of  $96 \pm 2\%$  and a constant temperature of  $22 \pm 2^\circ\text{C}$ ) as obtained by Tamtsia *et al.* [2004] from thermo-gravimetric analysis characterizing the state of water in the samples. In that paper Tamtsia *et al.* [2004] claimed that a sustained load for loading from 18 hours applied on cement samples during creep tests may accelerate the hydration rate which in turns influences on the microstructural development and the creep properties. However, it is shown from the results in that paper itself [Tamtsia *et al.* 2004] that the hydration degree profiles are very similar for the loaded and unloaded samples for both ages of loading at 24 and 30 hours, and hence creep loads seem have no effect at all on the hydration kinetics. Therefore, the hydration degree profile from the measurement for the case of loading at 24 hours is used in hydration model *mic* to obtain the evolution of the digital hydrating microstructures for the creep simulations of loading at both 18 and 24 hours. Figure 5.6 shows the profiles of hydration degree obtained by the experiments and simulations (using the fitting “ExternallyDefinedKinetics” kinetics, see Appendix A).

Table 5.2: Bogue cement composition of the Portland cement for simulations

Alite (%)	Belite (%)	Aluminate (%)	Ferrite (%)	Gypsum (%)	Total (%)
55	20	10.5	9.5	5	100

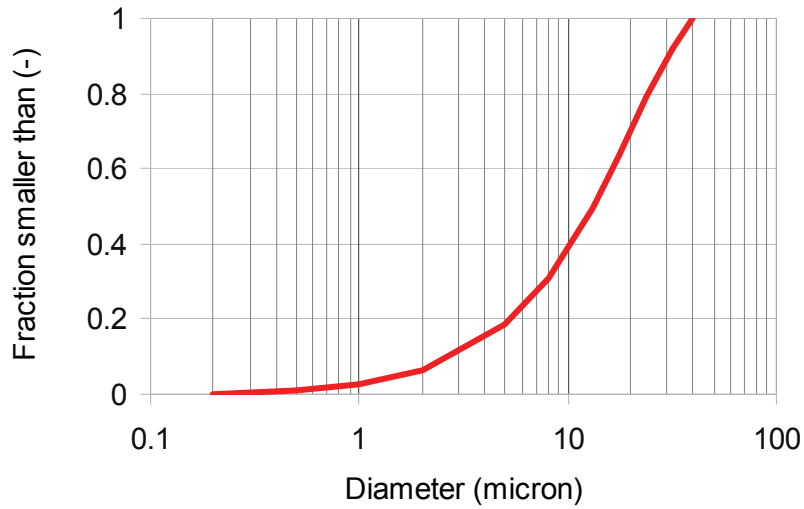


Figure 5.5: Particle size distribution for simulations corresponding to Blaine fineness of 3400  $\text{cm}^2/\text{g}$  from the experiment

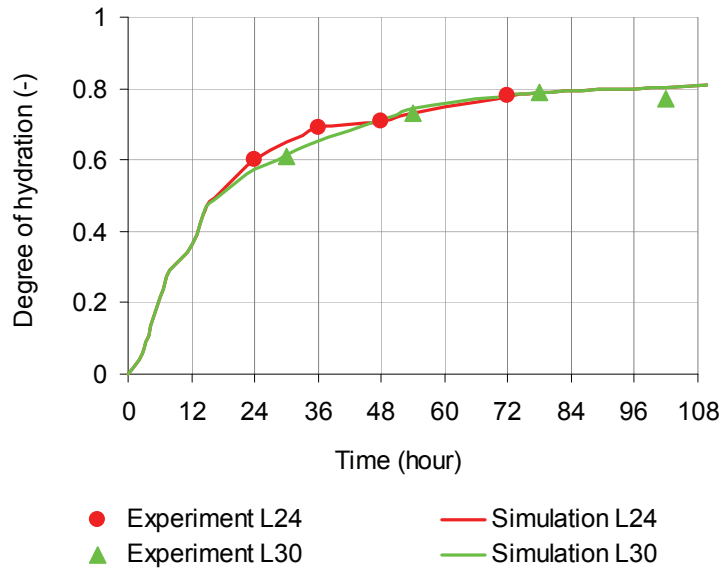


Figure 5.6: Degree of hydration for different ages of loading. L24 and L30 denote loading from 24 and 30 hours respectively. The hydration degree profile in the simulation for loading case at 18 hours is assumed to be the same one at 24 hours

## 5.5 Simulation Method of Ageing Creep in Hydrating Cement Paste

The microstructures are discretized on a regular cubic mesh (element size of  $1\mu\text{m}$ ) with the double burning algorithm (see chapter 4). The flowchart of the modelling procedure is sketched in figure 5.7. The effective strains developing with time of the modelled microstructure are calculated from the average strains over the CV that is under a uniaxial constant unit stress applied perpendicular to one surface and fixed zero displacement (normal direction to the surface) on the opposite surface. C-S-H is assumed be the only source of creep in cement paste and other phases are considered to have a purely elastic response. Intrinsic elastic properties of the phases and the source of the data are listed in table 5.3.

The microstructural development due to continuing hydration is taken into account during the simulation of the creep process. Solidification of the load-bearing microstructure under the simulated creep is modeled by an updating procedure for new states of the microstructure, which consists of gradual filling up by newly formed hydrates including C-S-H and other elastic phases (e.g. Portlandite). The total strain of the microstructure caused by the given external uniform stress (loading) applied on its boundary consists of 2 parts: elastic and viscous strains. The elastic part is an instantaneous deformation at the time of the externally applied loading, whereas the viscous part gradually increases with time due to the creep response of C-S-H present in the microstructure. During this viscoelastic behaviour of the cement paste it is reasonable to assume that the external stress loads only hydrate elements in the initial stage (at the loading time) of the microstructure and all the newly formed hydrates after the loading time are in a free stress state regarding to the applied external loading. For each simulation time step, once newly hydrated elements are formed, they take part in sustaining against the differential “internal loading” (i.e. the second term in the right hand side of equation (5.44)) that is transferred due to creep in the existing C-S-H elements within each time interval. The “internal loading” transferring from of each C-S-H element is characterized by the logarithmic function of time whose rate is inversely proportional to time (see equation (5.47) and the viscous component shown in figure 5.2). Due to the development of the simulated microstructure the formation of hydrates hinders the viscous deformation and thus the creep rate decreases. Although the overall average strain of the entire CV increases with time due to irrecoverable local strains (i.e.  $\Delta\varepsilon$  in equation (5.39)), the local elementary stresses are relieved (i.e.  $\Delta\sigma$  in equation (5.35)) as they are redistributed over a higher solid fraction for each time step.



The use of a constant FE mesh provides an easy updating procedure in which stress, strain states and internal variables in the same Gauss points can be reused without any requirement to project variables on the new mesh. The creep of the newly formed C-S-H elements is also easily simulated without any extra implementation effort.

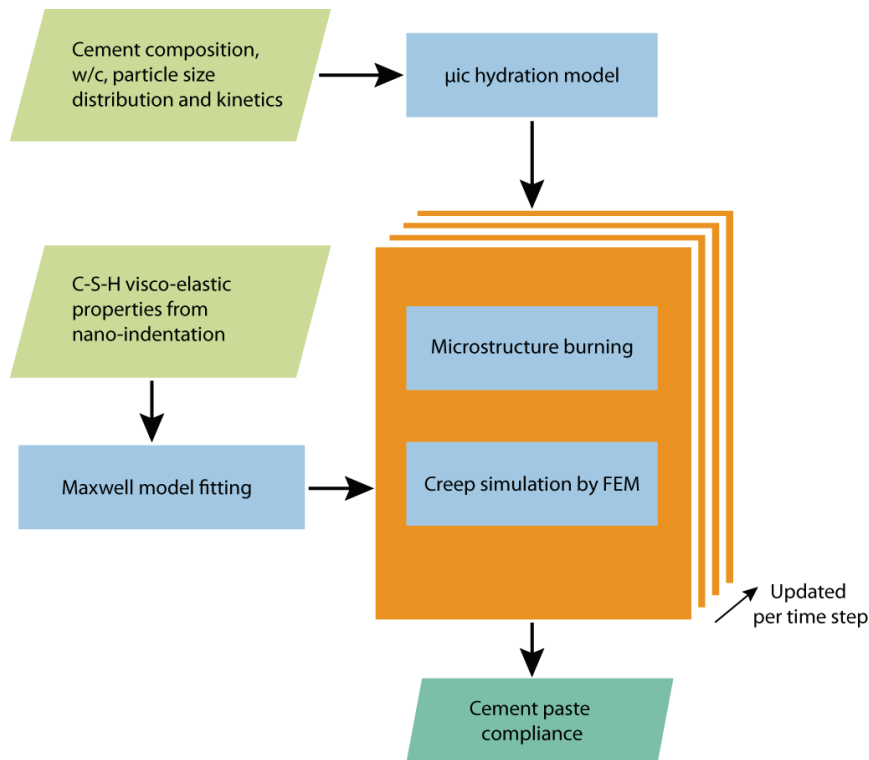


Figure 5.7: Flowchart of modelling of ageing creep in hardening cement paste for one given age of loading

## 5.6. Results and Discussion

### 5.6.1 Assuming C-S-H constant density $\rho = 2.0 \text{ g/cm}^3$

The creep results of the hardening cement pastes for loading from 18, 24 and 30 hours are shown in figure 5.8. The simulated compliances are in good agreement with measured values. The effect of age when loading on creep is well captured: the compliance of younger paste has a higher magnitude (of both the elastic and viscous components) due to a sparse spatial distribution of the solid phases at the early stages of hydration. It can be also seen that the simulated compliances are in good agreement with experiments for loading from 24 hours and 30 hours. However, the simulated creep is lower compared with the experimental creep for

loading from 18 hours. This is because the input creep function of C-S-H used in the simulation assumes a constant bulk density  $\rho$  of 2.0 g/cm<sup>3</sup>. In fact, this value is lower at very early ages [Muller *et al.* 2012]. The use of a higher C-S-H density leads to underestimating its creep function and consequently underestimates of the creep of the cement paste.

Table 5.3: Intrinsic elastic properties of chemical phases

The values are measured by nano-indentation or mechanical tests; \* Young's modulus of C-S-H assumed to be the mean value from the reference [Constantinides and Ulm 2004]

Phase	Young's modulus [GPa]	Poisson's ratio [-]	References
Water	0.001	0.499924	[Smilauer and Bazant 2010]
Alite	135	0.3	[Acker 2001]
Belite	130	0.3	[Velez <i>et al.</i> 2001]
Aluminate	145	0.3	[Velez <i>et al.</i> 2001]
Ferrite	125	0.3	[Velez <i>et al.</i> 2001]
Gypsum	30	0.3	[Bell 1994]
C-S-H	25.55*	0.24	[Constantinides and Ulm 2004]
Portlandite	38	0.305	[Constantinides and Ulm 2004]
Ettringite	22.4	0.25	[Kamali <i>et al.</i> 2004]
Monosulphate	42.3	0.324	[Kamali <i>et al.</i> 2004]
Hydrogarnet	22.4	0.25	[Kamali <i>et al.</i> 2004]
Iron Hydroxide	22.4	0.25	[Kamali <i>et al.</i> 2004]

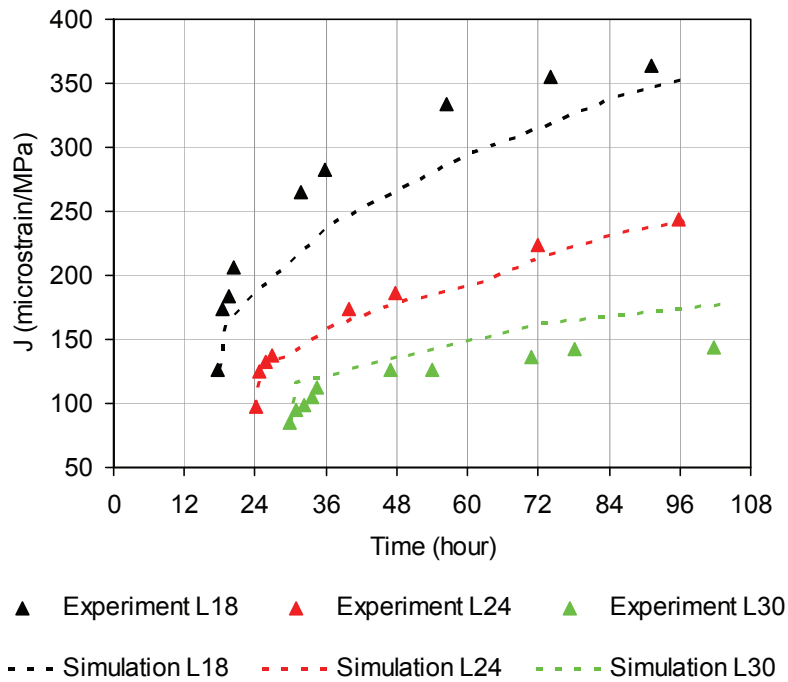


Figure 5.8: Results of creep compliance in the cement pastes at 3 different ages of loading. L18, L24 and L30 denote loading from 18, 24 and 30 hours respectively. The creep experiments [Tamstia *et al.* 2004] were performed using a compressive stress-strength ratio of 0.3 applied to the specimens at the age of loading. Regarding to this stress-strength ratio the linear viscoelasticity of cement paste can be assumed.

### 5.6.2 Assuming C-S-H densification

The creep results of the hardening cement pastes taking into account C-S-H densification for loading from 18, 24 and 30 hours are compared to ones with constant bulk C-S-H density of  $2.0 \text{ g/cm}^3$  and to experimental values as plotted in figure 5.9. The latter simulation compliances are in excellent agreement with measured values as the former simulation for loading from 24 and 30 hours. Interestingly, when loading from 18 hours, the creep compliance with C-S-H densification is higher than the one without, and it is now in excellent agreement with the measured data.

To explain these observations for the two later ages of loading at 24 and 30 hours, one should look back upon the calculations of elastic properties presented in [Do *et al.* 2013b]. It is shown that the densification has a very little effect on the effective elastic deformation of the CV after 15% degree of hydration. This means that the densifying microstructure having a larger amount in volume of less dense C-S-H with lower intrinsic stiffness exhibits an

“equivalent” effective elastic response comparable to the microstructure having a lesser amount in volume of the denser C-S-H with its higher intrinsic stiffness (25.55 GPa). Similarly, this “equivalence” on the effective viscoelastic deformations seems still to hold true for loading from 24 and 30 hours (figure 5.9): the densifying microstructure having a larger amount in volume of lower packing density C-S-H phases with their higher rates of intrinsic relaxation exhibits an “equivalent” effective viscoelastic behaviour comparable to the microstructure having a sparer amount of denser C-S-H with its lower rate of intrinsic relaxation.

On the contrary, for loading from 18 hours, the creep compliance curve of cement paste under the assumption of C-S-H densification is clearly higher than the one without it. This is an interesting result but not surprising. It is apparent in figure 5.9 that the slope of the curve with the densification is higher than the slope of the curve with the constant C-S-H density only within the range from 18 to 24 hours. This implies that in this particular time range, the densification assumption implies a higher rate of microstructure deformation. This time range coincides with the time interval when the densification process still developing very rapidly. It slows down after 24 hours (figure 5.3). The transient relaxation of a large amount of very low packing density C-S-H leads to the high rate of deformation from 18 to 24 hours and the higher irrecoverable deformation after 24 hours.

## 5.7. Conclusions

This chapter demonstrates the strength of microstructural models to model the effects of properties with spatial and temporal variation. It was demonstrated that the complicated processes of microstructural development and creep, which occur in parallel, can be captured and their combined effect simulated in these models.

The basic creep behaviour at young ages of three-dimensional numerical microstructures of hydrating cement pastes is simulated using FEM. The generalized Maxwell model is used to numerically describe intrinsic C-S-H viscoelasticity that is obtained by nano-indentation tests. It is found that, if the C-S-H phase is assumed to be homogenous with a constant bulk density  $\rho$  of 2.0 g/cm<sup>3</sup> (corresponding to its packing density  $\eta$  of 0.7) at all time, the numerical results on creep compliance of cement paste show excellent agreements with measured values for

loading from 24 and 30 hours. This model captures well the effect of age of loading that is observed in cementitious composites. However, under these assumptions, the simulated creep compliance for loading from 18 hours is lower than the experimental values as the input bulk density under the constant assumption is much higher than its actual value at 18 hours of hydration.

If C-S-H phases are assumed to have a creep response which depends upon their packing density itself varying with time, this densification has almost no effect on the effective deformation of the cement microstructure when loading from 24 and 30 hours. However, the densifying model predicts a higher viscous deformation rate of cement paste in the period of high densification rate and thus considerably higher overall deformation of cement paste in the case of loading at 18 hours. Taking into consideration the densification effect in the simulations provides markedly better predictions of ageing creep in early age cement paste.

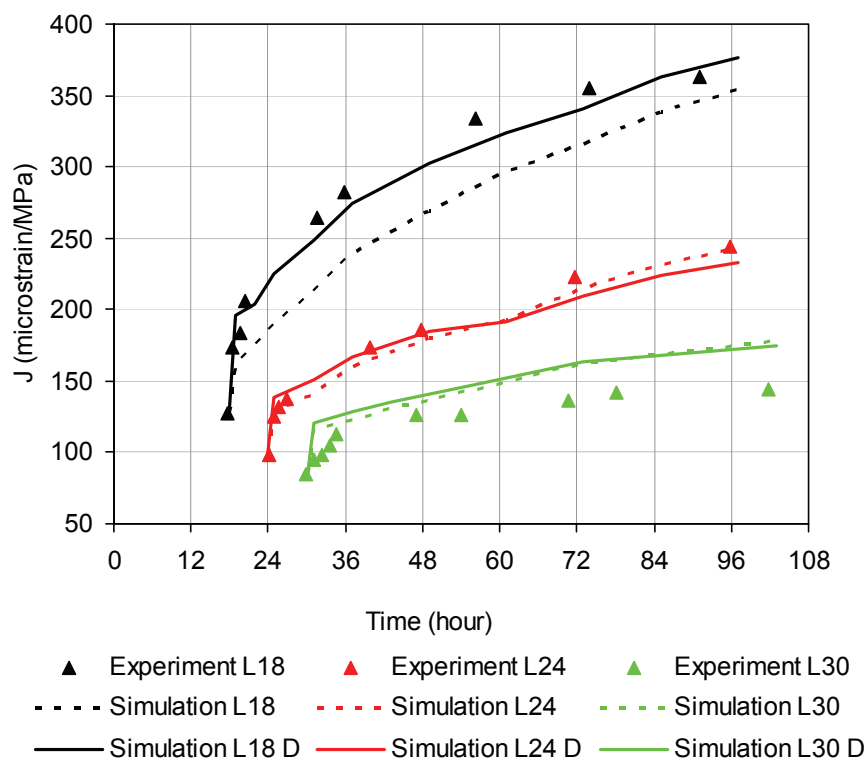


Figure 5.9: Results of creep compliance in the cement pastes taking into account the effect of C-S-H densification for 3 different ages of loading. L18, L24 and L30 denote loading from 18, 24 and 30 hours respectively with constant density of C-S-H, whereas L18 D, L24 D and L30 D denote loading from 18, 24 and 30 hours respectively considering the effect of C-S-H densification. The creep experiments [Tamtstia *et al.* 2004] were performed using the compressive stress-strength ratio of 0.3 applied to the specimens at the age of loading



## Chapter 6: Modelling of Autogenous Shrinkage in Portland cement Paste at Early Age

### 6.1 Introduction

In this chapter, the evolution of the autogenous shrinkage of hardening cement pastes at up to 7 days is simulated. The modelling approach at the microscopic level of cement paste is based on the mechanism of the development of capillary tension in the unsaturated pore-system (see also sections 1.4, 2.4.4 and 2.12). Figure 6.1 schematically shows the approach used. Initially, 3D digital microstructures at different w/c ratios are generated using the *μic* modelling platform. Elastic and creep properties of the digital microstructure then are computed using the methods discussed in chapters 4 and 5. Based on the Laplace-Kelvin equation, the capillary tension evolution is derived from the measured relative humidity or the pore size distribution measured by MIP tests and the chemical shrinkage. Finally, the autogenous shrinkage is computed as the average hydrostatic apparent strain using the poro-elastic and creep-superposition methods.

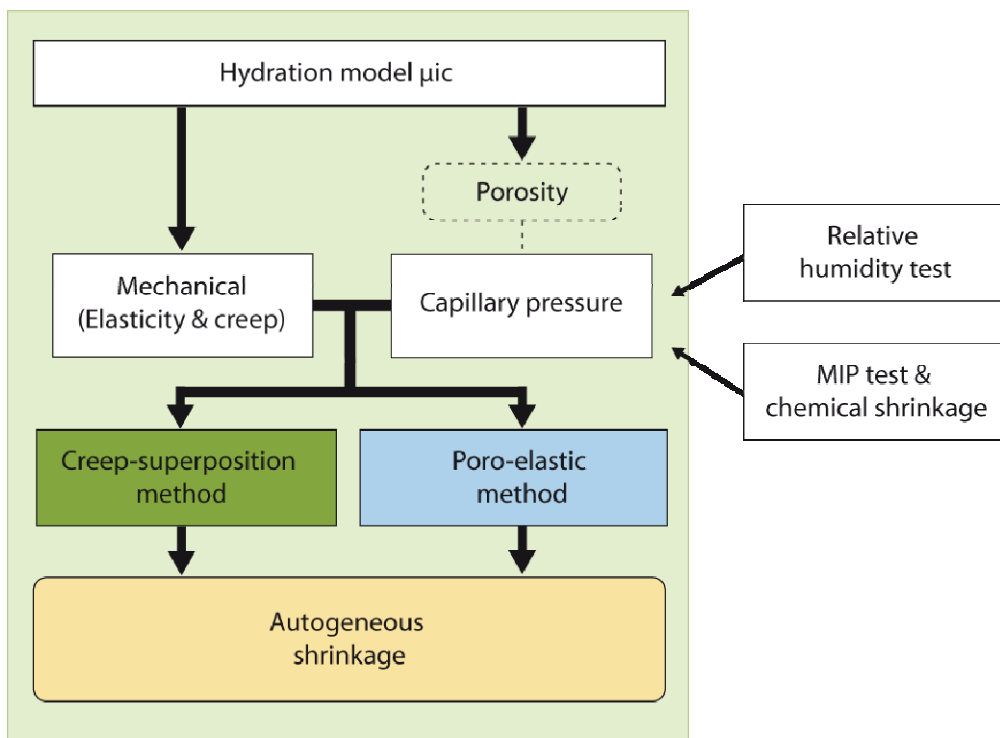


Figure 6.1: The overall flowchart of modelling of autogenous shrinkage in this study

## 6.2 Materials and Hydration Simulation

A rapid-hardening ordinary Portland cement (CEM I 52.5 R) was simulated at three different w/c ratios. The input parameters of the simulations were chosen to be similar to cements examined experimentally by Chen [2013] with which the computed elastic values and autogeneous shrinkage results will be compared. The cement phase composition determined by the XRD Rietveld is given in table 6.1. The particle size distribution was obtained by fitting a Rosin-Rammler distribution [Taylor 1997] corresponding to a Blaine fineness (see Appendix B) of  $4025 \text{ cm}^2/\text{g}$  with a maximum grain size of  $40 \text{ }\mu\text{m}$  (see figure 6.2).

Hydration and mechanical properties were simulated on a cubic computational volume of  $100 \text{ }\mu\text{m}$  in side that is about 2.5 times larger than the largest cement grain diameter; this volume size was found large enough to be a Representative Element Volume of the microstructure (see chapter 4). The cement grains were placed in the simulation volume and then “floculated” (as discussed in chapter 3) to give the best representation of the development of mechanical properties. The hydration kinetics in the model were chosen to match the same evolution of degree of hydration at  $20^\circ\text{C}$  as those measured by the isothermal calorimetry (see figure 6.3). The microstructures corresponding to three water-cement ratios of 0.3, 0.35 and 0.4 were simulated at various degrees of hydration.

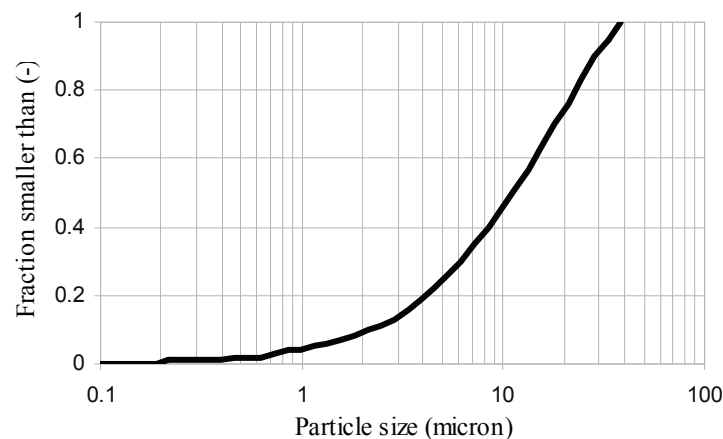


Figure 6.2: Particle size distribution for simulations corresponding to Blaine fineness of  $4025 \text{ cm}^2/\text{g}$  from the experiment



Table 6.1: Composition of Portland cement for simulations

Alite (%)	Belite (%)	Aluminate (%)	Ferrite (%)	Gypsum (%)	Total (%)
72.06	9.74	5.19	9.21	3.81	100

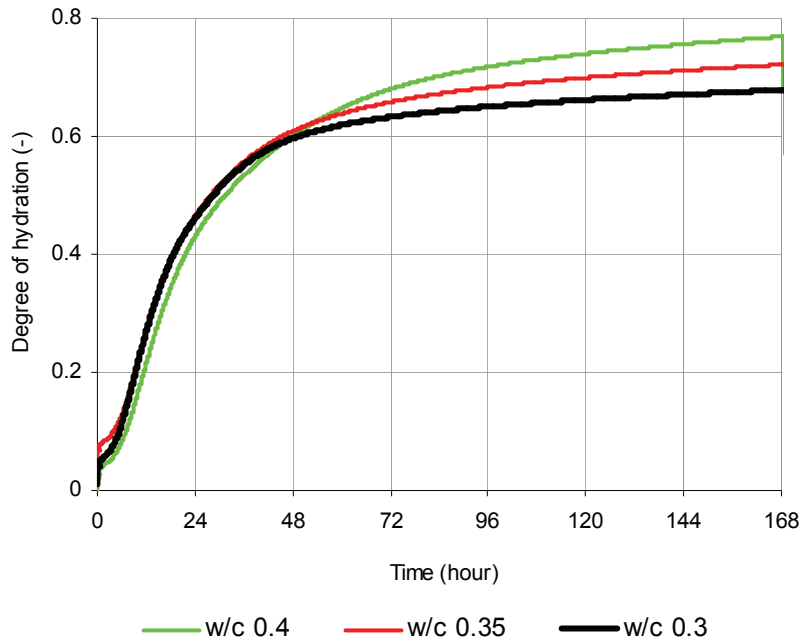


Figure 6.3: Degree of hydration at 20°C measured by the isothermal calorimetry [Chen 2013]

## 6.3 Results and Discussion

### 6.3.1 Elastic and creep properties

#### *Elastic properties*

The elastic properties of the microstructures with flocculation and assuming C-S-H density of  $2.0 \text{ g/cm}^3$  were calculated using FEM on a uniform mesh of  $1 \mu\text{m}$  element size with the double burning algorithm discussed in chapter 4. The simulation results are in excellent agreement with the experimental values measured by dynamic resonant frequency tests [Chen 2013], as presented in figure 6.4a and b.

***Creep properties based on assumption of C-S-H constant density  $\rho = 2.0 \text{ g/cm}^3$***

The creep simulations of cement pastes first were carried out using only one C-S-H creep function that corresponds to its bulk density of  $2.0 \text{ g/cm}^3$ , its packing density  $\eta$  of 0.7, an initial Young's modulus of 25.55 GPa, and a constant Poisson's ratio of 0.24. The creep compliances of the cement pastes at several ages of loading were simulated (figure 6.5 a, b and c). As expected, the effect of ageing on creep compliance was well captured for all w/c ratios. The compliance is higher for younger ages of loading due to low solid fractions of the microstructures at the early stages of hydration. It can be also seen from the comparison of the calculated curves at different w/c ratios that the cement paste at a lower w/c ratio has a lower instantaneous (elastic) deformation, but a higher ratio of creep/ elastic deformations. This is because the cement paste at a lower w/c ratio is stiffer due to a larger solid fraction, but it has more viscous sources from C-S-H produced in the microstructures.

***Creep properties based on assumption of C-S-H densification***

As discussed in chapter 3, 4 and 5, it is more realistic to assume in the simulation that C-S-H density increases with time. However, the variation of this parameter is not easy to obtain and is also influenced by w/c ratio [Muller *et al.* 2012]. The density variation for different w/c ratios can be calculated by matching the simulated total porosities with those obtained from MIP experiments (see section 3.3.1). For the sake of simplification, the hydration and creep simulations were carried out using the same densification function as calculated in chapter 3. The calculated creep compliances considering densification are compared to the ones assuming a constant density as shown in figure 6.5 a, b and c. As seen in the figure for three w/c ratios that the densification significant effects the calculated creep only for the young ages of loading (from 24 hours), which is very similar to the densification effect observed in chapter 5.

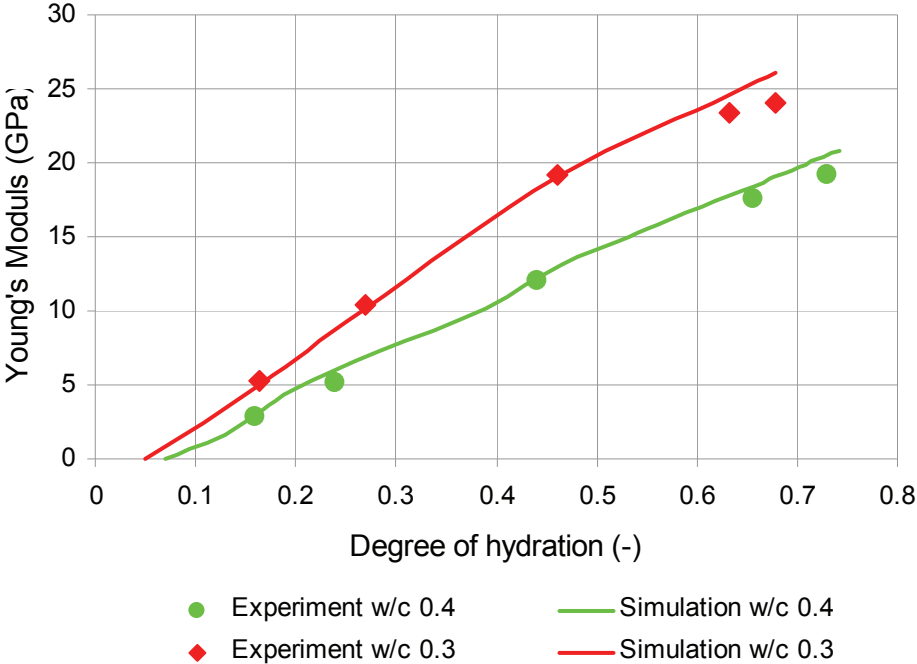


Figure 6.4a: Simulated Young's modulus

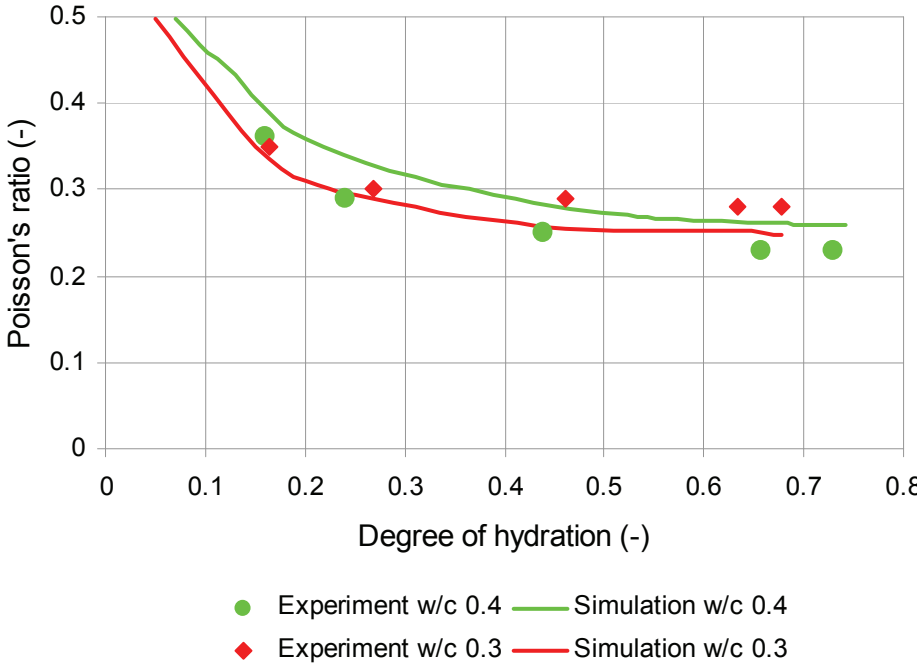


Figure 6.4b: Simulated Poisson's ratio

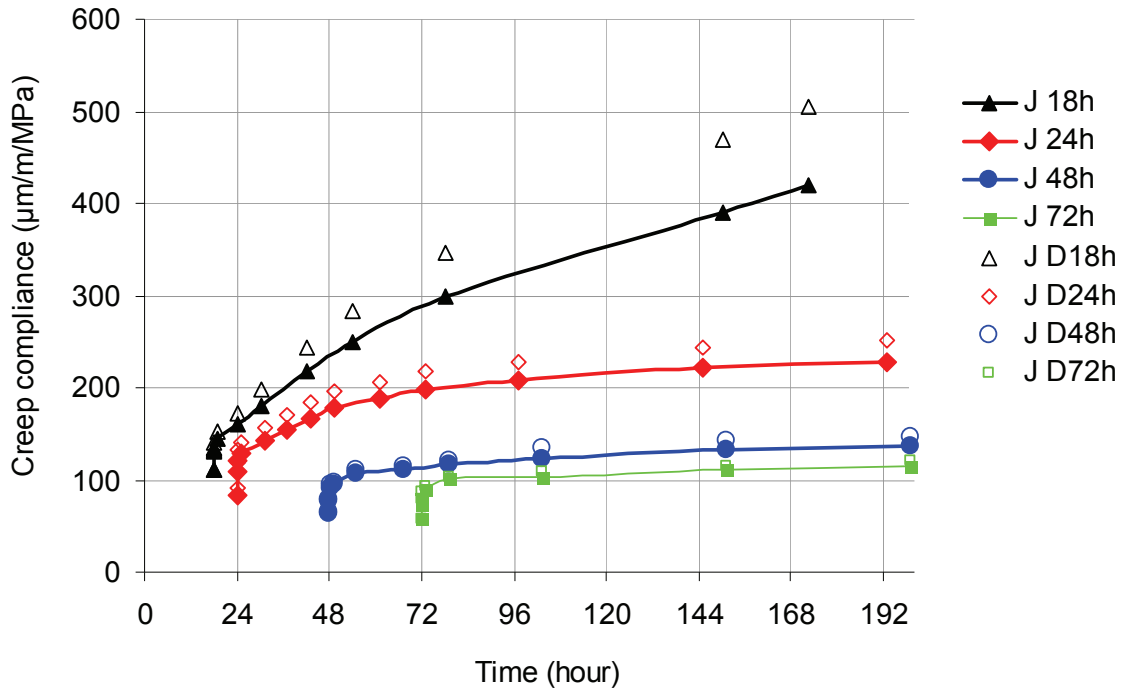


Figure 6.5a: Simulated creep compliances of cement paste at w/c ratio 0.4, for different ages of loading. J 18h, J 24h, J 48h, J 72h denote compliances of loading from 18, 24, 48 and 72 hours respectively, assuming constant density of C-S-H.

J D18h, J D24h, J D48h, J D72h denote compliances denote compliances of loading from 18, 24, 48 and 72 hours respectively, assuming C-S-H densification.

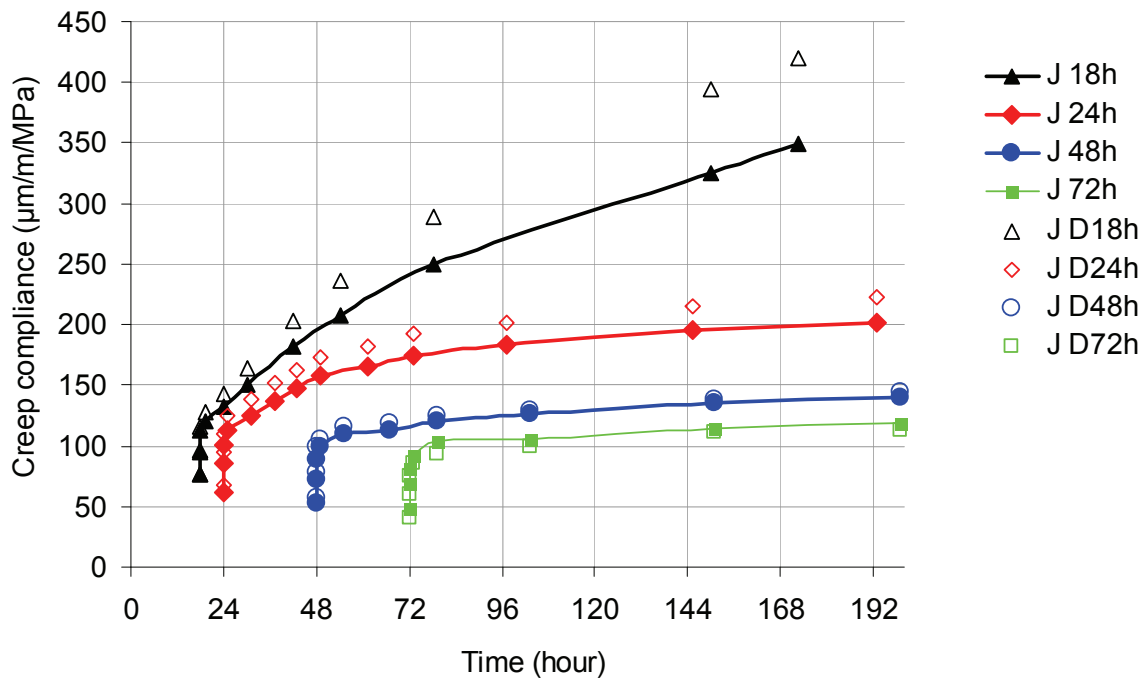


Figure 6.5b: Simulated creep compliances of cement paste at w/c ratio 0.35.

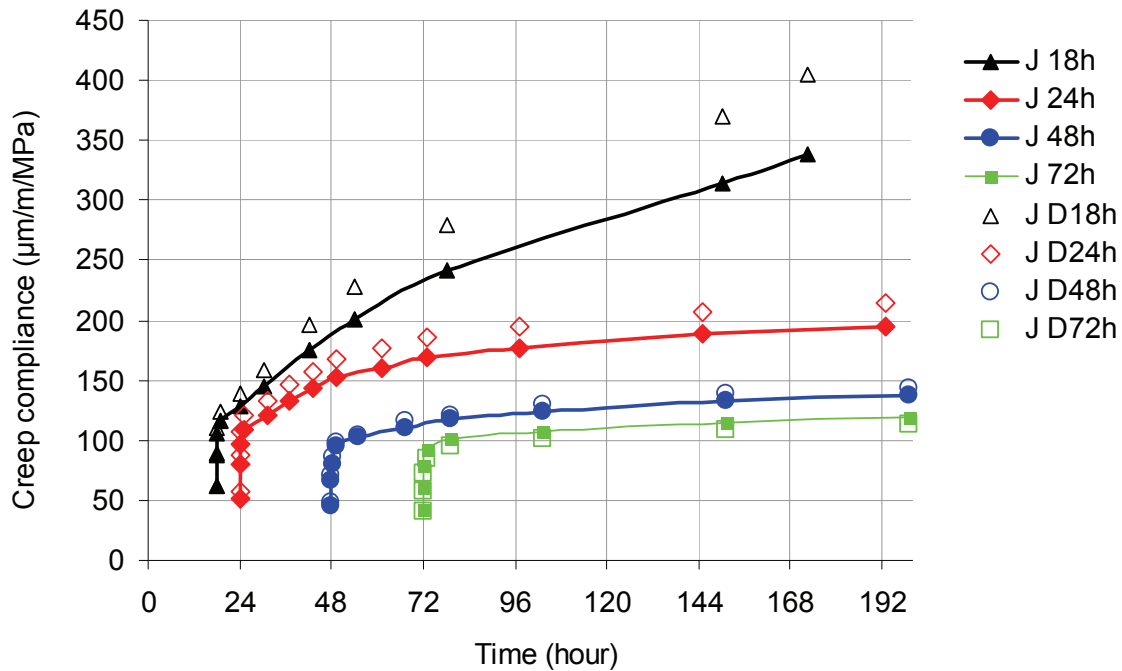


Figure 6.5c: Simulated creep compliances of cement paste at w/c ratio 0.3.

### 6.3.2 Calculation of capillary tension

At the outset of this thesis, it was planned to simulate autogenous shrinkage based purely on numerical approaches. However, the exploration of the simulated pore structure in chapter 3 indicated that simulation does not well capture the real pore structure due to the rough, “diffuse” nature of C-S-H. Therefore, the simulated pore-sizes could not be used to simulate the capillary tension. Therefore the experimental data of the internal relative humidity (RH) was used here to estimate the capillary tension.

The data is taken from Chen [2013], the development RH in the cement pastes was measured with two Rotronic hygroscope stations, equipped with high precision RH and temperature sensors with global nominal accuracy of  $\pm 0.8\%$  RH and  $\pm 0.1\text{ }^\circ\text{C}$ . The temperature of the measuring chambers was controlled using water circulating in the castings. This was to maintain the temperature in the measuring chambers at the level of  $20 \pm 0.07\text{ }^\circ\text{C}$ . About 20 hours after mixing, the cement paste samples were crushed into pieces of 5-10 mm sizes and then inserted into the sealed measuring chambers. The evolution of the internal relative humidity in the samples was continuously measured at 1 min intervals up to the age of 1

week. The sensors were calibrated using saturated salt solutions in the range 81 to 98% before and after each measurement. This procedure allowed a measuring accuracy of about  $\pm 1\%$  RH.

Due to technical difficulties, the measurements of RH could be performed only from 24 hours. The RH values before 24 hours were linearly interpolated from the RH calculated values at 8 hours using the measured chemical shrinkage and the MIP measured pore-size distribution [Chen 2013 and Chen *et al.* 2013]. The developments of RH up to 7 days in the cement pastes at w/c ratios of 0.3, 0.35 and 0.4 are plotted in figure 6.6.

Once the RH was known, the development of the capillary pressure was calculated according to the Kelvin equation (see also equation 2.4), with the assumption that the salts in the pore solution decrease RH by about 2% [Chen *et al.* 2013]:

$$p_c = \frac{RT \ln (RH_K)}{V_m} = \frac{RT\rho \ln (RH_K)}{M_m} \quad (6.1)$$

Where: R is the gas constant (8.314 J/mol K); T is the absolute temperature 293.15 [K];  $V_m$  [ $m^3/mol$ ] is the molar volume of liquid;  $RH_K$  [-] is the relative humidity due to menisci formation =  $RH_{measured} + 2\%$ ;  $\rho$  is the density of pore solution (or water)  $1000 kg/m^3$  and  $M_m$  is the molar mass of pore solution (or water) 0.01802 kg/mol.

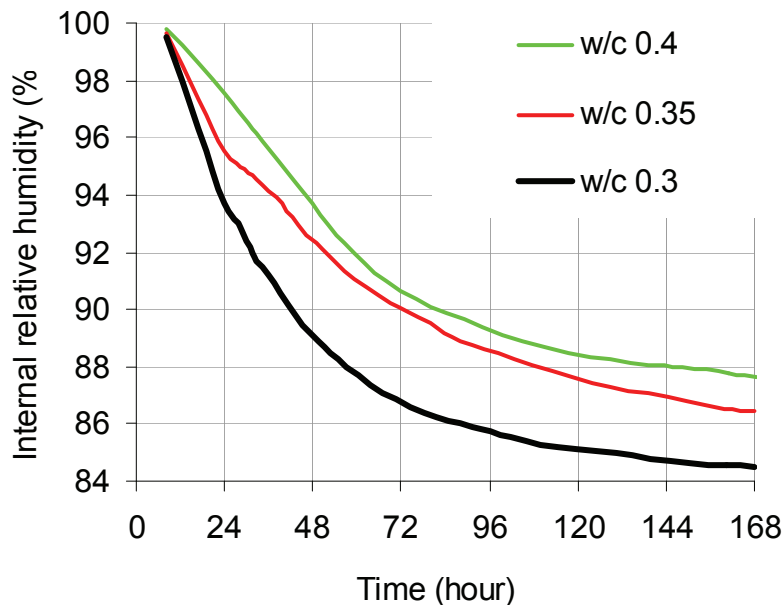


Figure 6.6: Internal relative humidity measured [Chen 2013]

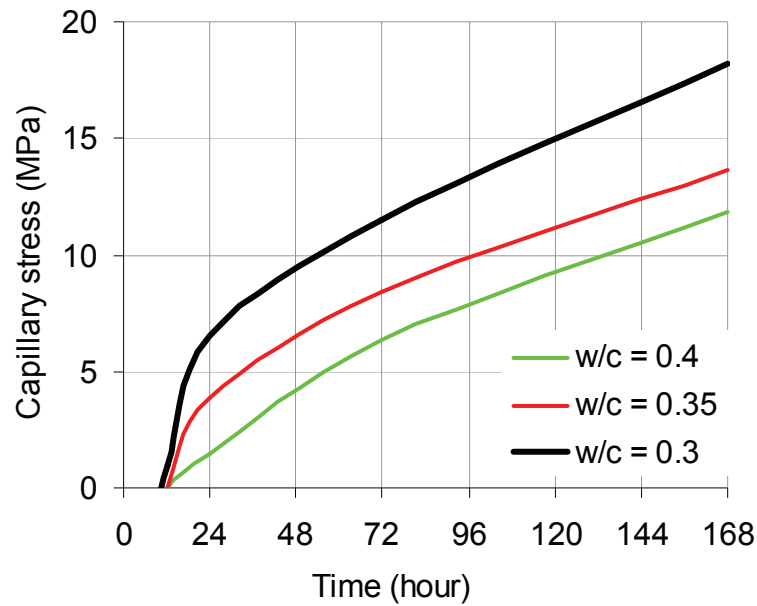


Figure 6.7: Capillary stress calculated from experimental internal relative humidity

The evolution of capillary pressure of cement pastes at different w/c ratios, plotted in figure 6.7, demonstrate that the capillary pressure significantly increases with the decrease of w/c ratio.

### 6.3.3 Autogeneous deformation from experiments

The autogeneous deformation (the results from Chen [2013]) of the cement pastes at different w/c ratios cured at 20°C and measured by the corrugated tube method [ASTM C1698] (see also section 2.8) are shown in figure 6.8. For each cement mix, the autogeneous deformation curve was the average of 3 parallel measurements. All the measured results were set to zero at the final setting time (see table 6.2) measured by automatic Vicat needle apparatus.

Table 6.2: Setting times of the cement pastes at different w/c ratios [Chen *et al.* 2013]

	w/c = 0.30	w/c = 0.35	w/c = 0.4
Initial set (min)	124	185	246
Final set (min)	211	260	395

The lower w/c ratio paste shows a higher autogeneous deformation, as expected. This is because a low w/c ratio is associated with a strong self-desiccation (rapid drop of RH) in a finer pore network, which consequently results in a higher capillary tension and finally in a higher shrinkage.

At all w/c ratios, the deformation shows a period in which a deceleration of shrinkage or even a swelling (at w/c ratio of 0.4) occurs. The period initiates shortly after the setting time and continues over several hours. In this period, the expansion appears to be superimposed on an underlying shrinkage attributable to self-desiccation. The reason for this expansion is may stem from the development of crystallization pressures induced by the formation of ettringite or Portlandite [Scherer 1999, Scherer 2004, and Sant *et al.* 2011] (see also section 2.6).

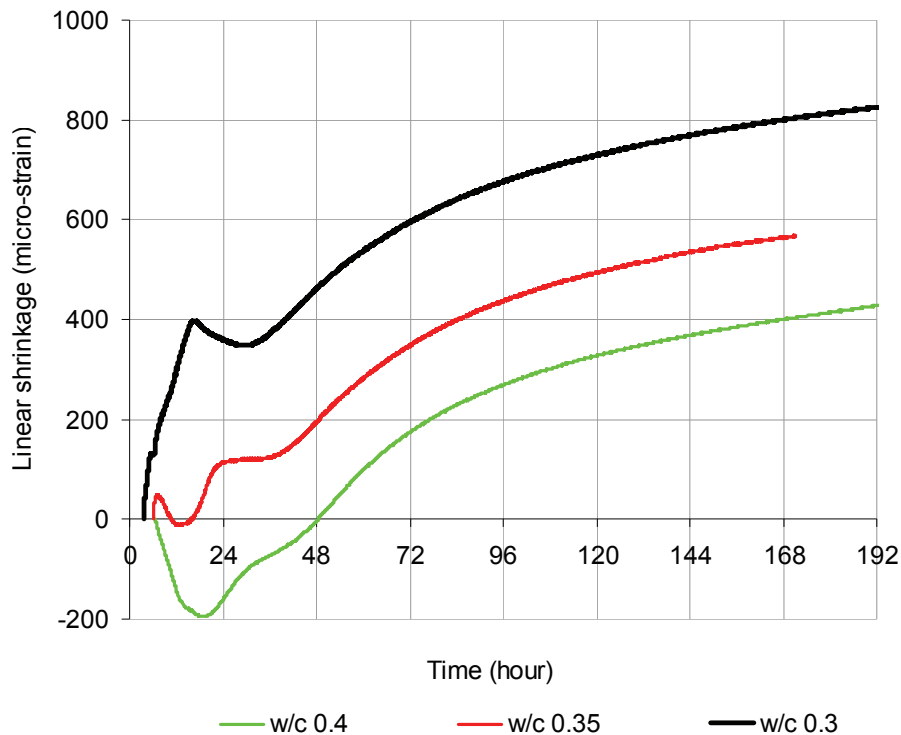


Figure 6.8: Autogeneous deformation measured by the corrugated tube method from Chen [2013]



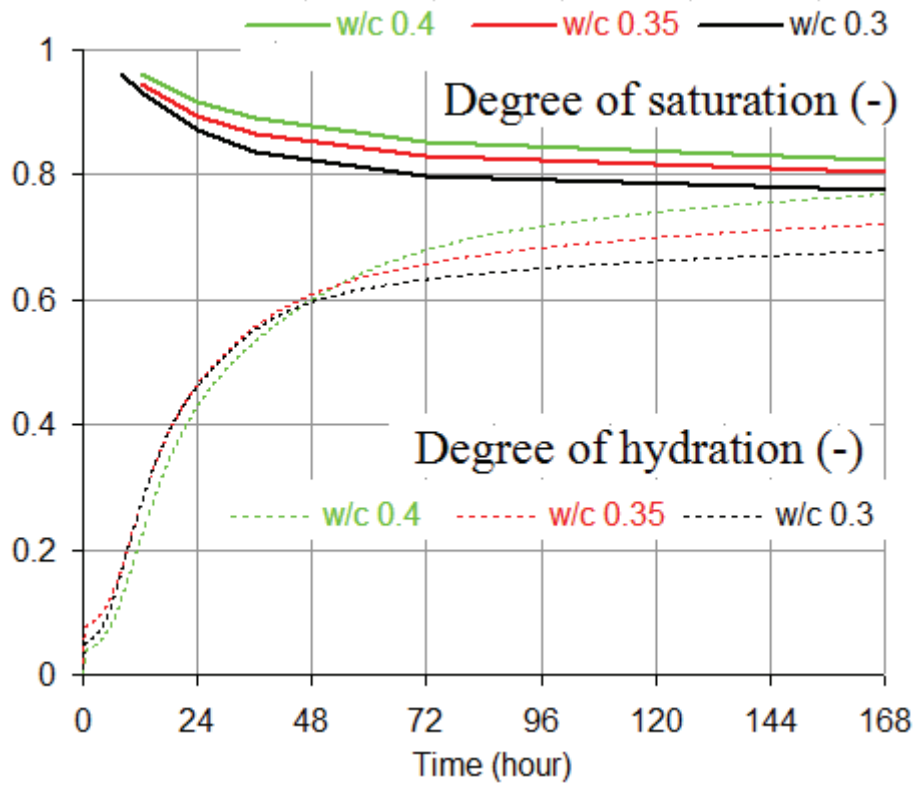


Figure 6.9: Degree of saturation calculated according to Powers' model [1965]

### 6.3.4 Modelling autogeneous shrinkage based on poro-elasticity approach

The shrinkage caused by the internal capillary stress was first calculated using the self-consistent method on the porous materials [Mackenzie 1950, Bentz *et al.* 1998 and Lura *et al.* 2003] (see also section 2.10.3). It was assumed that isolated, saturated, spherical pores under internal capillary stress are distributed at random throughout the volume of solid material that has homogenous and isotropic elastic properties. It was assumed also that the volume of all the capillary pores are small compared with the total volume and pores are distributed statistically within the total volume. Using the self-consistent scheme, the shrinkage resulting from capillary stress can be expressed as follows (see 2.13):

$$\varepsilon_{linear} = \frac{S p_c}{3} \left( \frac{1}{K} - \frac{1}{K_s} \right) \quad (6.2)$$

Where  $\varepsilon_{linear}$  is the linear autogeneous deformation;  $p_c$  is the internal capillary stress;  $S$  is the degree of saturation;  $K$  is the bulk modulus of the porous material; and  $K_s$  (44 GPa) is the bulk modulus of the material making up the solid frame of the porous material.

The bulk modulus  $K$  of the porous material can be calculated from its elastic modulus  $E$  and Poisson's ratio  $\nu$  as:

$$K = \frac{E}{3(1-2\nu)} \quad (6.3)$$

Based on this approach, Jaouadi [2008] calculated the autogeneous shrinkage using all the parameters from experimental data and assuming degrees of saturation of 100%. Although the calculated results captured well the effect of cement fineness, they were much lower compared with the measured autogeneous deformation.

The degree of saturation is a function of degree of hydration and w/c ratio and is calculated here according Powers's model [1965] as shown in figure 6.9. The developments of autogeneous shrinkage were calculated using the calculated elastic values in equations (6.2) and (6.3) and capillary pressure in equation (6.1).

The simulated results of shrinkage were compared with the experimental data as shown in figure 6.10. It can be clearly seen in the figure that the simulation much underestimates the autogeneous shrinkage, with the amount of underestimation increasing from one day onwards. More seriously, the simulation does not clearly capture the effect of w/c ratio on shrinkage, the deformation at low w/c ratio is a bit higher than the one at high w/c ratio up to 3 days and then three curves go almost horizontally and converge to an almost same value at 7 days, and this is unlikely observed in practice. The reason of this problem is that the elastic modulus at lower w/c ratio develops rapidly and restrains the autogeneous deformation caused by the capillary stress in the pore solution. The poro-elastic approach according to equation (6.2) considers only the instantaneous strain, and ignores the influence of the historical evolution of strain due to the developing capillary stress. The drawback of this approach is that it does not take into account the creep effects that may be crucial at low w/c ratio.

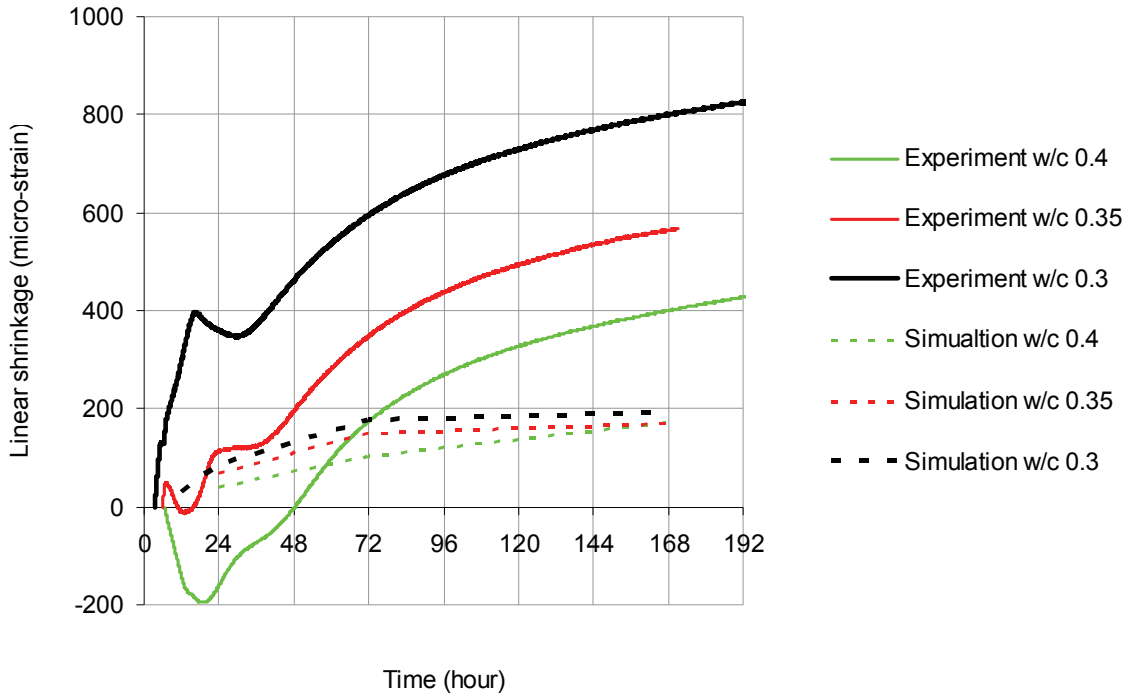


Figure 6.10: Autogeneous shrinkage in the Portland cement pastes simulated based on the poro-elastic approach. Shrinkage is plotted as positive

### 6.3.5 Modelling autogeneous shrinkage based on creep-superposition approach

In the second approach, the linear autogeneous shrinkage  $\varepsilon$  [-] was derived using the Boltzmann's principle of the creep-superposition [Bažant 1982] (see also section 2.10.2), as follows:

$$\varepsilon(t) = \int_{t_0}^t J(t, t') d\sigma(t') \quad (6.4)$$

Where:

$J(t, t')$  [ $\text{MPa}^{-1}$ ] is the one-dimensional creep function for loading from  $t'$ .

$t$  [hour] and  $t_0$  [hour] are the current time and the reference time, respectively.

$\sigma(t')$  [MPa] is the macroscopic compression load causing the volumetric deformation and this is a function of the applied capillary tension  $p_c$  [MPa], porosity  $\phi$  [-] and Poisson ratio  $\nu$  [-] of the microstructure:

$$\sigma(t') = (1 - 2\nu) p_c \phi \quad (6.5)$$

To compute the deformation due to the history of capillary tension, the right hand side of equation (6.4) was estimated by a summation of a set of time discrete products (for various ages of loading  $t' = t_0, t_1, t_2, t_3, \dots$ ) of the creep functions  $J(t, t')$  and differentials of volumetric capillary stress  $\Delta\sigma(t')$ :

$$\varepsilon(t) = J(t, t_0)\sigma_0 + J(t-t_1, t_1)\Delta\sigma(t_1) + J(t-t_2, t_2)\Delta\sigma(t_2) + J(t-t_3, t_3)\Delta\sigma(t_3) + \dots \quad (6.6)$$

Time step discretization of equation (6.6), differentials of volumetric capillary stress  $\Delta\sigma(t_i)$  and their corresponding creep compliance  $J(t-t_i, t_i)$  are simply illustrated in figure 6.11.

### ***Autogeneous shrinkage based on assumption of constant C-S-H density $\rho = 2.0 \text{ g/cm}^3$***

Based on equation (6.6) according to this creep-superposition approach, the computed results of autogeneous shrinkage of the Portland cement pastes using assumption of a constant C-S-H density of  $2.0 \text{ g/cm}^3$  are presented in figure 6.12. It is clearly seen in the figure that the calculated autogeneous shrinkage agrees better with the experimental values in terms of shrinkage magnitude compared with the ones computed by the poro-elasticity approach. Interestingly, the simulations are now able to show the effect of w/c ratio on shrinkage, which is that the shrinkage increases with the decrease of w/c ratio. Two main reasons that can explain this effect are the development of capillary tension and creep deformation. Firstly, the cement paste at a lower w/c ratio has stronger self-desiccation and its internal relative humidity is drops rapidly. The capillary stress in the finer pore network of the microstructure at lower w/c ratio paste develops much faster than the one at higher w/c ratio (see figure 6.7). Secondly, the cement paste at a lower w/c ratio has a higher ratio of viscous/elastic deformations (see figure 6.5 a, b and c), which leads high multiple factors of capillary stresses by high total deformations at very early age.

As seen in figures 6.5 of creep compliance for all w/c ratios, the viscous components are major parts of the total deformations. Due to the ageing effect, creep magnifies strongly the deformation resulted from capillary tension, particularly in young ages. Compared with the results based on the pore-elasticity approach, the autogeneous shrinkage based on the creep-superposition approach is much higher for low w/c ratio paste and not only an increase 15% as was supported by Jaouadi [2008]. With the confirmation of experimental data, the numerical results suggest that the contribution of creep on autogeneous shrinkage is considerable especially at very early age.

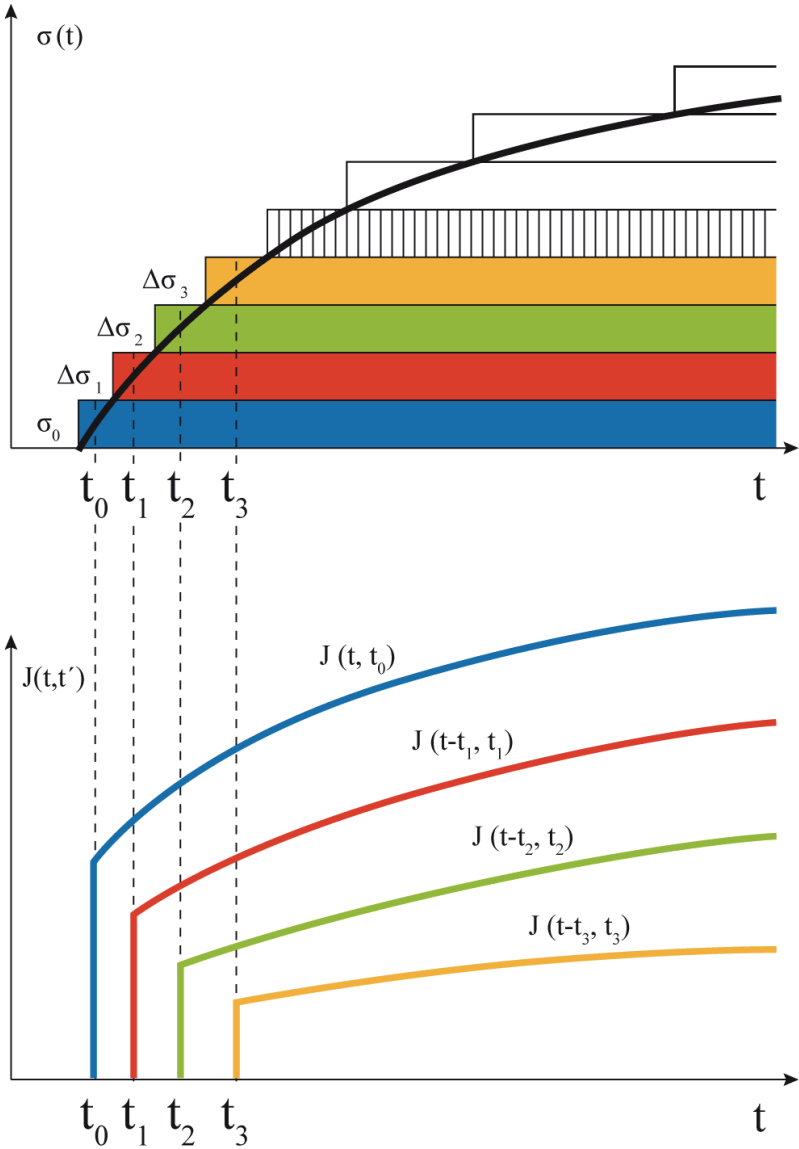


Figure 6.11: Decomposition of history of volumetric capillary stress into differential terms and their corresponding creep compliance plotted in the same colours

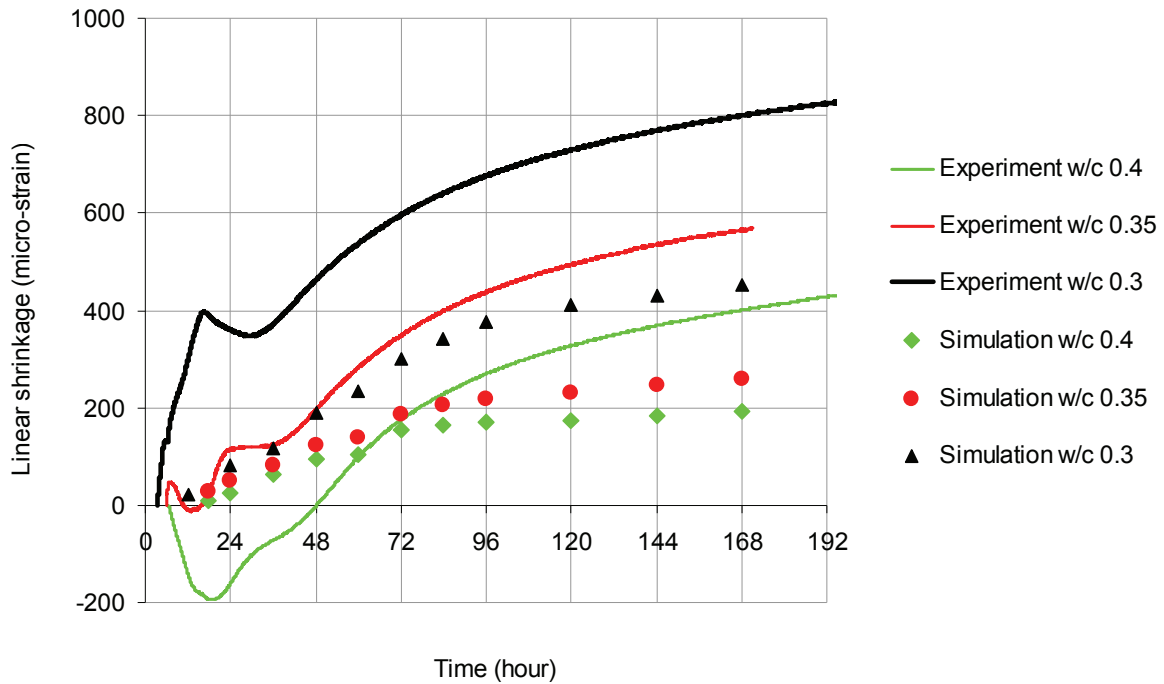


Figure 6.12: Simulated autogenous shrinkage based on the creep-superposition approach with assumption of a constant C-S-H density  $\rho = 2.0 \text{ g/cm}^3$

#### ***Autogenous shrinkage based on assumption of C-S-H densification***

The autogenous shrinkage was calculated using equation (6.6) in which creep compliances of pastes were simulated considering the C-S-H densification effect. The calculated shrinkages considering densification are compared to the ones assuming a constant density and experimental values as shown in figure 6.13. It is clearly seen that simulations with the densification effect give higher shrinkage and better agree with experiments for the pastes at 0.3 and 0.35 w/c ratios. Account for the densification makes clearer the impact of w/c ratio on the calculated autogenous shrinkage. This is because the capillary stresses in the low w/c pastes are already developed even at the early ages (before 24 hours, see figure 6.7) at which the creep deformations are very high due to the low packing densities of C-S-H.

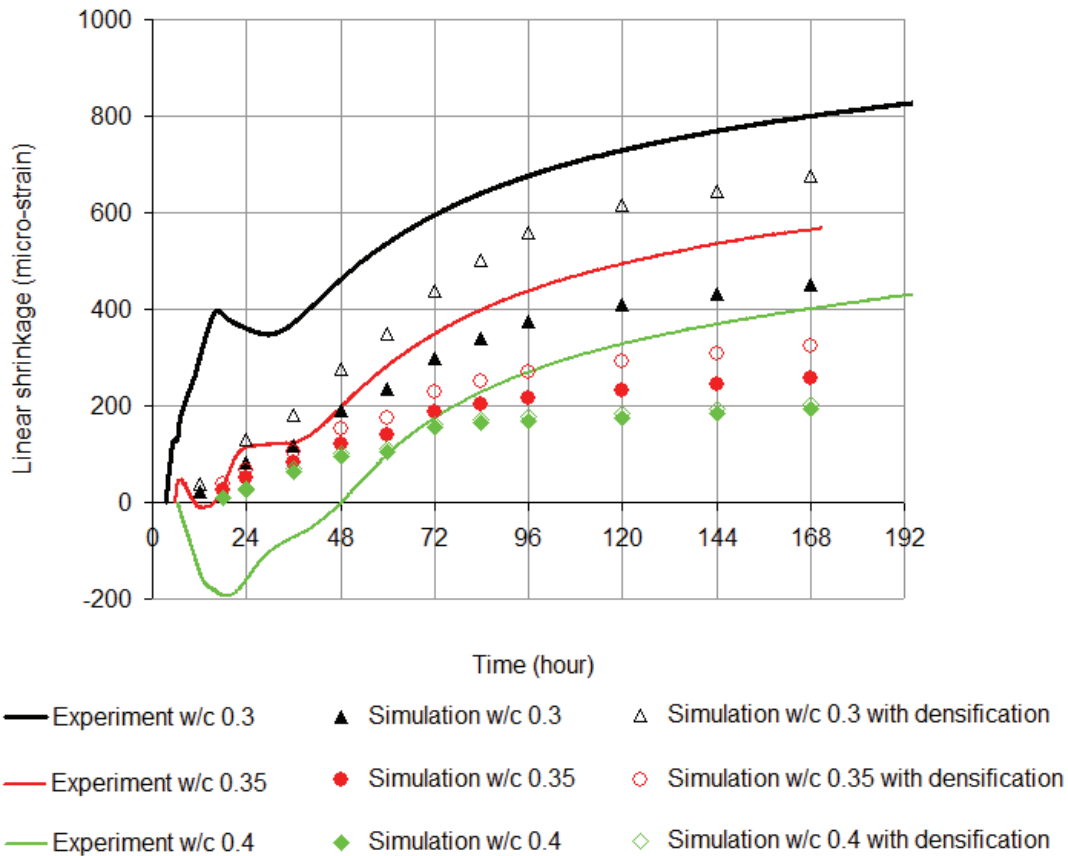


Figure 6.13: Simulated autogeneous shrinkage based on the creep-superposition approach with assumption of C-S-H densification

## 6.4 Conclusions

Autogeneous shrinkage in Portland cement pastes was modelled using two approaches, namely poro-elasticity and creep-superposition. The simulation results were compared with the experimental data from a companion study in our laboratory [Chen 2013]. The principal difference between these two modelling methods stems from the microstructural homogenization techniques on mechanical properties. On the one hand, the poro-elasticity method using the Self-Consistent Scheme estimates the effective elastic response of the microstructure. On the other hand, the creep-superposition method applying numerical homogenization from Finite Element analysis evaluates the effective visco-elastic response of the microstructure. It was found that the creep-superposition method provides more accurate assessments of shrinkage than the poro-elasticity method does. The simulations according to the creep-superposition approach reproduce clearly the effects of w/c ratio on autogeneous shrinkage. It was clearly seen that the low w/c ratio leads to a significant drop of internal

relative humidity, a raise of the capillary tension and hence a promotion of autogeneous shrinkage in cement paste during sealed hydration. It could be also concluded that the contribution of viscous deformation on shrinkage is considerable and should not be neglected.

Based on creep superposition method, the calculated shrinkage with assumption of densification is higher than the one with a constant density of  $2.0 \text{ g/cm}^3$  and simulated results with the densification effect are in better agreement with experimental values. The rapidly developed capillary stresses in low w/c pastes and their strong impact on the high creep deformations of low packing densities of C-S-H at very first hours of hydration can explain better the w/c ratio effect on autogeneous shrinkage.



## Chapter 7 Conclusions and Perspectives

The current work aimed to simulate the evolution of autogenous shrinkage in hardening cement paste at young age (up to 7 days). Digital microstructures were produced numerically using the modelling platform *μic*. Based on the mechanism of capillary tension in the gas-fluid-solid media, autogenous shrinkage was simulated on the modelled microstructure was performed in four steps: (1) modelling of the pore structure, (2) modelling of the elastic properties, (3) modelling of the creep effect and (4) calculation of the autogenous shrinkage. It was seen that significant development of the numerical model for pore structure is needed to provide pertinent predictions of autogenous shrinkage. It was also found that the models can help in better understanding of the shrinkage phenomenon and the factors influencing it. In the following, some of the principal numerical and scientific findings in this study are described. Future directions for research are then suggested.

### 7.1 On the Study of Pore Structure Modelling

A modelling algorithm based on a voxel method was proposed to simulate MIP testing on the digital microstructures. It was seen that despite having a resolution for the capillary pores very close to reality, the experimentally observed breakthrough diameter from mercury intrusion is much lower than the values obtained by the MIP simulation. The effect of several input parameters on the pore-sizes of the simulated microstructure was examined. The phenomenon which seems best able to explain this discrepancy is that C-S-H is not in fact a phase with a smooth surface as represented in simple microstructural models, but a phase which grows as needles into the pore space, leading to very small water filled capillary pores from quite young ages. This indicates that it will be very difficult to represent the porosity of real microstructures in model volumes on the scale of hundreds of microns, such as are necessary to study macroscopic transport. Some specific findings on the study of pore-structure modelling are listed below:

- The C-S-H product forms in a diffuse manner and fills a large part of the microstructure from the early hours of hydration.
- A parallel computation algorithm for pore-size analysis was implemented, which allows the high resolution to be obtained (voxels measuring a few nanometres).

- In the pore structure analysis of the typical digital microstructure of  $100 \mu\text{m}^3$  in size, the voxel resolution, in the range of 5-200 nm, does not much affect the total calculated porosity and the pore-size distributions become only slightly finer when finer resolutions are used. Convergence is obtained at a voxel size of around 10 nm.
- The similarity between the total porosity determined by the two numerical algorithms indicates that the entire pore-network of the digital microstructure is connected even at high degree of hydration.
- The MIP simulation algorithm exhibits minor effect of the computational volume size due to the good connectivity of the modelled microstructure.
- The distribution of pore entry sizes in the simulated mercury intrusion curves shifts to smaller sizes compared to the one in the simulated pore sizes curves. However, the breakthrough diameter in the mercury intrusion simulations was much higher than the experimental results.
- Flocculation in initial particle packing leads to a slight increase in the pore entry size; this effect reduces with hydration.
- The variation of the number of CH clusters results in only a small reduction in the pore sizes and breakthrough diameter and does not affect the total porosity in the microstructure.
- If spherical particles are replaced by cylindrical particles, the microstructure has a wider range of pore sizes and the breakthrough diameter is higher but these changes are not sufficient to account for the deviation from the experimental values.
- The effect of the roughness of the C-S-H product on the pore-sizes is the most significant of all numerical parameters as rougher microstructures appear to have finer pore sizes and the breakthrough diameter shifts close to the measured one when the degree of “diffuse” growth of C-S-H in the pore-space is high enough.

## **7.2 On the Study of Elasticity Modelling**

The development of elastic properties of the simulated microstructures was calculated by means of numerical homogenization based on FEM using a regular mesh of brick elements. Due to the connections formed in the microstructure as an artefact of the meshing procedure, the simulated Young's modulus were found to be considerably higher than the experimentally measured results. Furthermore, the percolation of the solid phases was found to happen even

before hydration started. A procedure to remove these artefacts, on the basis of the information available in the vector microstructures was developed. After this correction, a better agreement of the experimental results with calculations was obtained. However, the percolation threshold was found to be delayed significantly. More realistic estimates of percolation threshold were obtained if either flocculation of the initial packing of particles or a densification of C-S-H with hydration is assumed. Some specific findings on the study of elastic property modelling are listed below:

- The consistency of the elastic property results calculated by the FEM applying the static and kinematic boundary conditions suggests that the computational volume of the microstructure is representative. This means that for a typical particle size distribution of real cement, the computational volume size can be obtained at about 2.5 times larger than the maximum particle size.
- The FEM calculations on the original digital microstructure highly overestimated its elastic modulus which was more than 2 GPa at a zero hydration degree. This problem originates from the artificial connectivity between particles that occurs when the particles are too close to each other when using an insufficiently refined mesh. To resolve this problem, two burning algorithms at both local and global levels were used. It was shown that the FEM convergence could be obtained when the mesh of  $100^3$  voxels was used to represent a microstructure of  $100 \mu\text{m}^3$  in size.
- The simulated results of alite and Portland cement pastes at various w/c ratios using the double burning procedure were in good agreement with measured values for the entire range of hydration. The percolation threshold of the modelled microstructure was best predicted if C-S-H densification or particle flocculation is assumed.

### **7.3 On the Study of Creep Modelling**

The creep behaviour of the digital microstructure was simulated using homogenization using FEM. The C-S-H compliance taken from nano-indentation tests was numerically reproduced by the generalized Maxwell chain. It was shown that the models were able to simulate the ageing creep behaviour of cement paste. The current study also demonstrates that numerical models can be effective tools for upscale bridging of mechanical properties from the nano-

level of C-S-H to the macroscopic level of cement paste. This could potentially bring a significant benefit for predicting the macroscopic creep of cement paste and concrete.

Some specific findings on the study of creep modelling are listed below:

- It was observed that the approach of a generalized Maxwell material chain integrated in a Finite Element model has many advantages such as simplicity of implementation, low processor and memory consumptions, stability and fast convergence of numerical solutions.
- The simulation results for basic creep of cement paste at w/c ratio of 0.5 for three ages of loading (18, 24 and 30 hours) show excellent agreements with experimental results. The effect of the age of loading on the creep compliance was well captured.
- The modelled cement paste at a lower w/c exhibits less elastic deformation but a higher rate of viscous deformation. This is because the lower w/c ratio cement paste has a larger solid fraction, which gives a higher elastic stiffness. As the same time, the cement paste has a larger amount of viscosity from C-S-H, which results in a higher viscous strain, particularly at young ages. It would be interesting to examine this prediction experimentally.
- If the C-S-H density is assumed to vary with time, the simulated creep compliance is considerably higher than the one which assumes a constant bulk density of  $2.0 \text{ g/cm}^3$  only for ages of loading before 24 hours, after which point the densification process develops strongly.
- It is interesting to note that although the microstructure modelled can be used to explain the observed variation in the mechanical properties, an agreement with the pore properties could not be obtained. This is because, although the simulation of the pore network requires much finer detail in the microstructure, the representation of the rough, loosely packed C-S-H was made in a crude way in the simulation of the pore network. However, for the description of the mechanical properties, it was sufficient to include the homogenised effect of the loosely packed C-S-H.

#### **7.4 On the Study of Autogeneous Shrinkage Modelling**

Autogeneous shrinkage was calculated using poro-elasticity and creep-superposition methods. It was found that the simulated autogeneous shrinkage based on the latter method is much higher and is in better agreement with experimentally measured values than the one based on the former method. More importantly, the latter method reproduced the w/c ratio effect on

autogeneous shrinkage which could not be clearly obtained from the former method. The phenomenon which is best able to explain this observation is that cement paste is not in fact a material with only an elastic response as assumed in the poro-elastic method, but a material which is characterized by viscoelastic behaviour with a large viscous flow at early age. While in the poro-elastic method the deformation is considered as the elastic (instantaneous) part caused by the capillary stress only, in the creep-superposition the total deformation at a given time is assumed to be sum of cumulative deformations (both elastic and viscoelastic components) resulted from the entire history of the capillary stress from the setting time to the time being considered.

When the C-S-H density is assumed to vary with time, the model gives higher values of the calculated creep function for the young ages of loading (notably before 24 hours). Consequently, the calculated autogeneous shrinkage with the densification effect is in better agreement with experimentally measured values. This means that considering the densification effect in the simulations provides better predictions of autogeneous shrinkage in early age cement paste.

## **7.5 Limitations and Suggestions for Future Research**

While the good predictions of some cement paste properties from the microstructure at early age were obtained, the current models have several limitations that are needed to overcome in the future. Firstly, the limitation of pore-structure representation is not only from lack understanding of C-S-H structure but also from the computational complexity. Secondly, the models do not consider early-age expansion that usually happens in practice and appears to be superimposed on an underlying shrinkage as observed in experiments. Thirdly, the simplified assumptions for mechanical simulation do not accurately reflect the solid- liquid interactions in the real partially saturated system, e.g. the globally applying capillary stress on the boundary of the microstructure to find the effective deformation, neglecting water flow and the pore pressure. Last but not least, the models, due to the computational complexities, use many simplifications such as finite element approximation, mechanical phase properties, creep statistical data...etc.

Some suggestions for the future work are proposed as follows:

***Modelling of pore structure:***

At the outset of this thesis the aim was to implement an autogenous shrinkage model that would be purely numerical. This means that, apart from the mechanical properties of chemical phases determined by nano-indentation techniques, the numerical model should not rely upon any other experiment data. The ideal modelling pipeline should be: mix composition, hydration kinetics, microstructure formation, pore-structure evolution, self-desiccation, mechanical properties and autogenous shrinkage. In this work the critical problem that remains unsolved is the representation of pore structure in the microstructural model. Although methods for characterising the pore structure were improved, an accurate representation of pore structure is necessary for accurate modelling of autogenous shrinkage. A possible solution can be a multiscale approach in which a coupling model incorporates the pore structure of capillary pores along with the pore structure of C-S-H gel pores. This requires a better understanding of the structure of C-S-H. Once the pore structure is properly reproduced, the pertinence of different driving forces with regard to autogenous shrinkage can also be tested. This will require modelling of:

- The capillary pressure, evaluated by the drying process of the porosity starting from the wide pores to fine pores.
- The adsorption-desorption process with regard to the relationship between the number of adsorbed water layers and the autogenous relative humidity.
- The estimation of the disjoining pressure as a function the hygral state in the porous material.

***Modelling the effect of microcracking on autogenous shrinkage:***

A factor to be considered during the study of volume changes is the possible occurrence of microcracking. The presence of microcracks presupposes, or even requires, that strains and tensile stresses are present prior to the moment of cracking. The formation of microcracks leads to expansion and thus a reduction of shrinkage. Numerical modelling of the contribution of microcracks to the volumetric deformation requires modelling of the fracture behaviour and hence of the crack propagation process. The fracture mechanics of viscoelastic materials should be used to describe the failure criteria. Although this can be relatively straightforwardly implemented in the 2-dimensional case, it is still a difficult problem to solve in the 3-dimensional case. As an alternative solution, a continuum damage model to estimate the effect of crack opening or a smeared crack model can be used.

***Modelling the effect of temperature on autogenous shrinkage:***

Early age volume changes of cementitious materials are mainly attributed to thermal expansion, autogenous shrinkage and drying shrinkage. While drying shrinkage can be avoided or mitigated by proper curing, the first two phenomena are difficult to overcome and occur simultaneously in the first days of hardening under natural conditions. To understand the individual contributions of each phenomenon and their interactions, a study of isothermal autogenous shrinkage at different constant temperatures and the evolution the thermal dilatation coefficients as a function of the hydration degree in natural conditions is required. The superimposition of the two deformations (isothermal autogenous shrinkage and thermal expansion/shrinkage) will then be compared against the total deformation (under the real temperature history) at equivalent ages. A proper understanding of shrinkage in high performance concrete at young ages of hydration under complex conditions would enable a good prediction of volume changes and risk of cracking, which ultimately contributes to improve durability of concrete structures.





## Appendix

### A. Modelling of Cement Microstructure in $\mu ic$

This appendix presents a typical microstructural simulation of cement hydration in  $\mu ic$  model. The amounts of cement clinkers corresponding to the input compositions at given w/c ratios are calculated by converting into volume terms, assuming the density of each phase and only C-S-H density may be varied with time (controlled by user plugins). Spherical particles having sizes to match the input particle size distribution are placed at random locations in the initial microstructure within the computation volume.

Hydration and mechanical properties are simulated on a cubic computational volume of 100  $\mu m$  in size. Commonly, a total of more than one million cement particles are initially generated. Cement particles can contain many different phases interspersed together into a single grain and during hydration layers of other phases may deposit over these particles (see figure A1) [Bishnoi and Scrivener 2009a]

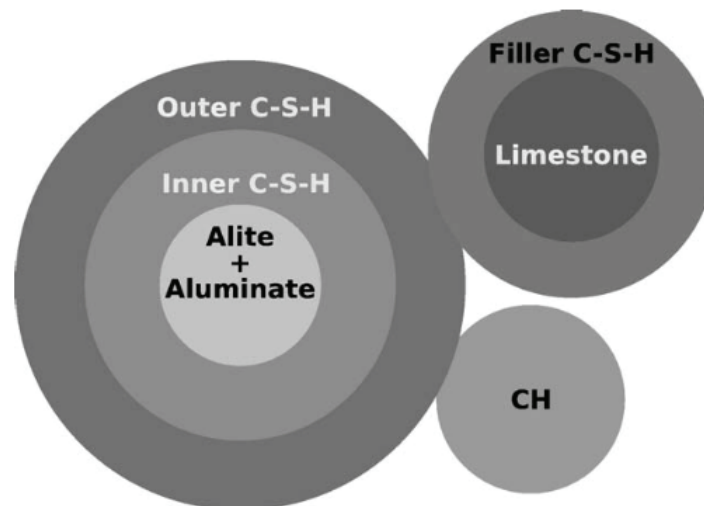


Figure A1: Example of different materials and particle types defined in a simulation [Bishnoi and Scrivener 2009a]

The densities of phases are assumed as listed in table A.1. The reactions of cement clinkers are calculated in volumetric terms in the equations from (A.1) to (A.8). Some of the hydration products, e.g. C-S-H and ettringite are deposited around the hydrating cement particles and others e.g. Portlandite nucleates in the pores. Portlandite particles are produced throughout the first 24 hours of hydration to give a final number around 20% of the number of  $C_3S$  particles in the system.

Alite and aluminate contribute the main reaction at early hydration whereas belite is considered to be unreactive until the first thirty hours. For the simulations in this thesis “ExternallyDefinedKinetics” were used by which the user can define hydration degree profile to match experimentally measured values by isothermal calorimetry.

Further assumptions and features of the hydration model can be found elsewhere (see also section 2.9 *mic* modeling platform) [Bishnoi and Scrivener 2009] [Bishnoi 2008] [Bishnoi 2012].

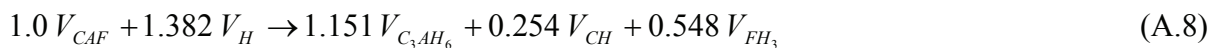
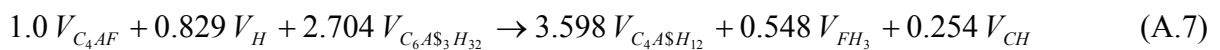
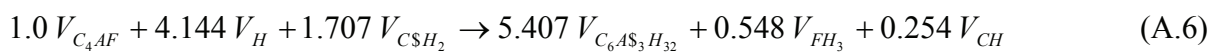
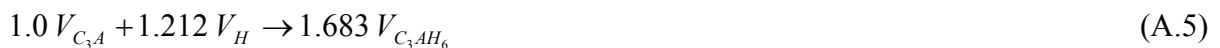
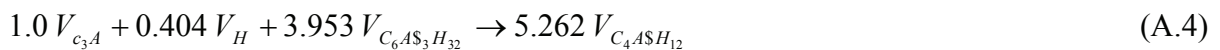
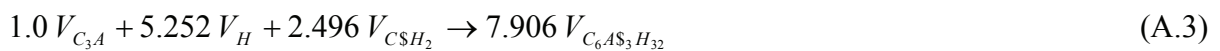
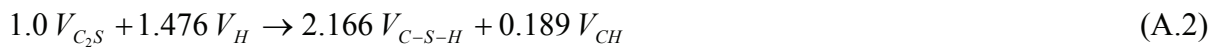


Table A.1: Bulk densities of phase are used in the simulations [Bishnoi 2008] [Bishnoi 2012].

\* As an option, C-S-H density can vary with time

Phase name	Formula	Density
Water	H	1.00
Alite	C <sub>3</sub> S	3.15
Belite	C <sub>2</sub> S	3.28
Aluminate	C <sub>3</sub> A	3.03
Ferrite	C <sub>4</sub> AF	3.73
Gypsum	C\$H <sub>2</sub>	2.80
Calcium Silicate Hydrate C-S-H	C <sub>1.7</sub> SH <sub>4</sub>	2.0*
Portlandite	CH	2.24
Ettringite	C <sub>6</sub> A\$ <sub>3</sub> H <sub>32</sub>	1.78
Monosulphate	C <sub>4</sub> A\$H <sub>12</sub>	2.00
Hydrogarnet	C <sub>3</sub> AH <sub>6</sub>	2.52
Iron Hydroxide	FH <sub>3</sub>	3.00

## B. Calculation of Cement Fineness

The simulated Blaine fineness value used in chapter 6 was fit to experimentally measured values determined by air-permeability apparatus. The specific surface  $S$  values are experimentally determined by:

$$S = \frac{k\sqrt{e^3}\sqrt{T}}{d(1-e)\sqrt{n}} \quad (\text{B.1})$$

$S$  [ $\text{m}^2/\text{kg}$ ]: specific surface of the test sample

$k$  [ $\text{m}^2/\text{kg}$ ]: specific surface of the standard sample used in calibration of the apparatus,  $k = 28.06$

$e$  [-]: porosity of cement,  $e = 0.505$

$T$  [second]: measured time interval,  $T = 86151, 9.1553$  and  $8.3893$

$n$  [ $\mu\text{Pa}\cdot\text{s}$ ]: viscosity of air according to the temperature,  $\sqrt{n} = 0.01344$

$d$  [ $\text{g}/\text{cm}^3$ ]: density of cement,  $d = 3.15$

### C. Numerical Homogenization Based on FEM

This appendix presents the numerical homogenization using FEM to calculate the effect elastic properties of the modelled microstructure (the computational volume-CV) in chapter 4.

A tri-linear shape function for brick elements was found appropriate to approximate the displacement field [Haecker *et al.* 2005, Šmilauer and Bittnar 2006]. The overall stress  $\bar{\boldsymbol{\sigma}}$  and strain  $\bar{\boldsymbol{\varepsilon}}$  tensors of CV were estimated by averaging stress  $\boldsymbol{\sigma}$  and strain  $\boldsymbol{\varepsilon}$  tensors at integration points over the entire CV as follows:

$$\bar{\boldsymbol{\sigma}} = \frac{1}{V} \int_V \boldsymbol{\sigma} dV \quad (\text{C.1})$$

$$\bar{\boldsymbol{\varepsilon}} = \frac{1}{V} \int_V \boldsymbol{\varepsilon} dV \quad (\text{C.2})$$

All elastic homogenization in this paper is considered to originate from isotropic materials and the isotropic behaviour of CV is assumed. Derived from the thermodynamic consistency and the free energy functions, the constitutive relation in a unity of linear isotropic material reads:

$$\bar{\boldsymbol{\sigma}} = \mathbf{C} \bar{\boldsymbol{\varepsilon}} \quad (\text{C.3})$$

Where

$$\bar{\boldsymbol{\sigma}} = [\sigma_{xx}, \sigma_{yy}, \sigma_{zz}, \sigma_{yz}, \sigma_{zx}, \sigma_{xy}]^T \quad (\text{C.4})$$

$$\bar{\boldsymbol{\varepsilon}} = [\varepsilon_{xx}, \varepsilon_{yy}, \varepsilon_{zz}, 2\varepsilon_{yz}, 2\varepsilon_{zx}, 2\varepsilon_{xy}]^T \quad \text{or} \quad \bar{\boldsymbol{\varepsilon}} = [\varepsilon_{xx}, \varepsilon_{yy}, \varepsilon_{zz}, \gamma_{yz}, \gamma_{zx}, \gamma_{xy}]^T \quad (\text{C.5})$$

$$\mathbf{C} = \frac{E}{(1+\nu)(1-2\nu)} \begin{bmatrix} 1-\nu & \nu & \nu & 0 & 0 & 0 \\ \nu & 1-\nu & \nu & 0 & 0 & 0 \\ \nu & \nu & 1-\nu & 0 & 0 & 0 \\ 0 & 0 & 0 & (1-2\nu)/2 & 0 & 0 \\ 0 & 0 & 0 & 0 & (1-2\nu)/2 & 0 \\ 0 & 0 & 0 & 0 & 0 & (1-2\nu)/2 \end{bmatrix} \quad (\text{C.6})$$

In equation (B.3) once  $\bar{\sigma}$  and  $\bar{\varepsilon}$  are known and  $\mathbf{C}$  is unknown, the Young's modulus and Poisson's ratio are extracted using following equations [Šmilauer 2005]:

$$\mu = \frac{\gamma_{xy} \sigma_{xy} + \gamma_{yz} \sigma_{yz} + \gamma_{zx} \sigma_{zx}}{\gamma_{xy}^2 + \gamma_{yz}^2 + \gamma_{zx}^2} \quad (\text{C.7})$$

$$a = \varepsilon_{xx}^2 + \varepsilon_{yy}^2 + \varepsilon_{zz}^2 \quad (\text{C.8})$$

$$b = 2(\varepsilon_{xx} \varepsilon_{yy} + \varepsilon_{yy} \varepsilon_{zz} + \varepsilon_{zz} \varepsilon_{xx}) \quad (\text{C.9})$$

$$W_n = \varepsilon_{xx} \sigma_{xx} + \varepsilon_{yy} \sigma_{yy} + \varepsilon_{zz} \sigma_{zz} \quad (\text{C.10})$$

$$\nu = \frac{W_n - \mu a}{\mu (b - a) + 2 W_n} \quad (\text{C.11})$$

$$E = 2\mu (1 + \nu) \quad (\text{C.12})$$

## D. Elastic Properties of Microstructural Portland cement

In this appendix, more information about the simulated elastic properties of the Portland cement paste at w/c ratio of 0.4 in chapter 6 is presented. The simulation procedures of elastic properties based on the Finite Element Method for the Portland cement are analogous to those for the alite system presented in chapter 4. Compared to alite system, The only one more step required to be carried out for the Portland cement system is that the phases (e.g. belite, aluminate, ettringite) being embedded into other phases (e.g. alite, C-S-H) are retuned with their actual volume fractions by their randomly seeding on the host phase before numerical homogenization of the Finite Element analysis. The intrinsic elastic properties of the individual phase are listed in table 5.3 (see chapter 5).

Similar to the alite paste discussed in chapter 4, the effect of boundary conditions on elastic properties for the Portland cement paste is shown in figure D.1. The similar simulated results by the static and kinematic boundary conditions indicate that the computational volume is representative. The effects of the burning algorithms on elastic properties are plotted in figure D.2a and D.2b. The sensitivity of the mesh size on the elastic results is tested using various mesh size density. It can be seen in figure D.3a and D.3b that the modelled microstructure responds softer by using a finer mesh and that the numerical solution is convergent when a mesh of 100 elements each side is used.

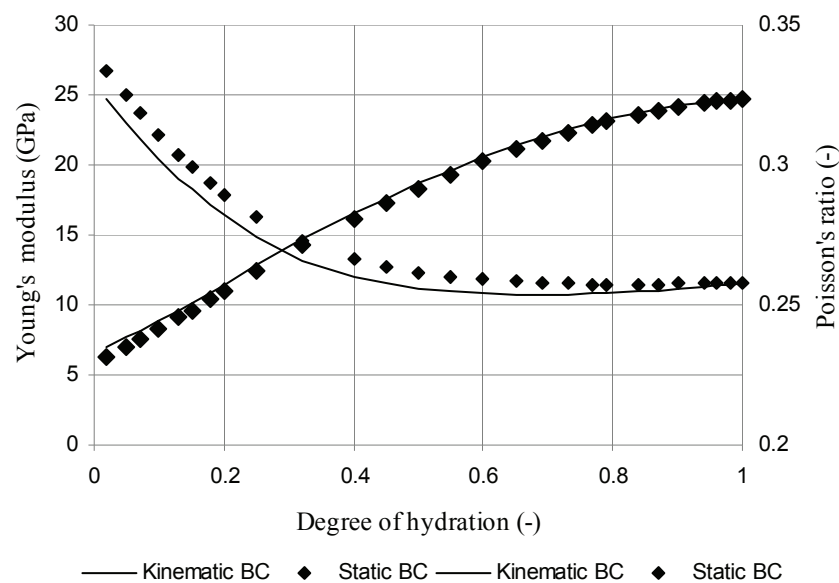


Figure D.1: The effect of boundary condition on elastic properties of no-burning microstructure

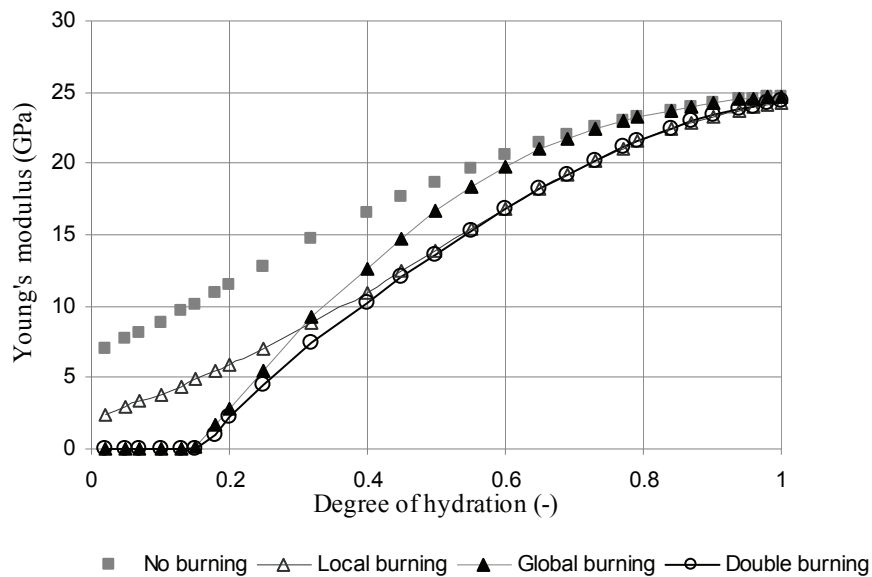


Figure D.2a: Effect of the burning algorithms on Young's modulus

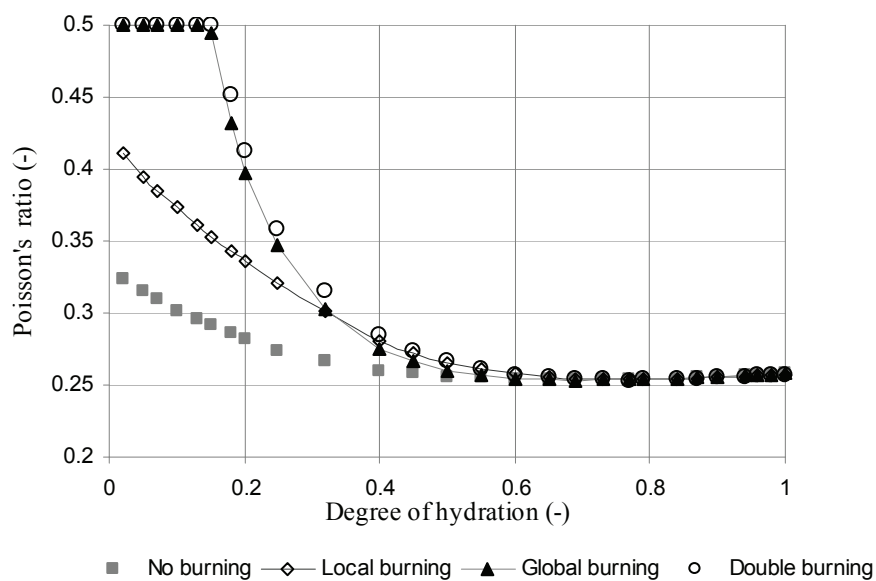


Figure D.2b: Effect of the burning algorithms on Poisson's ratio



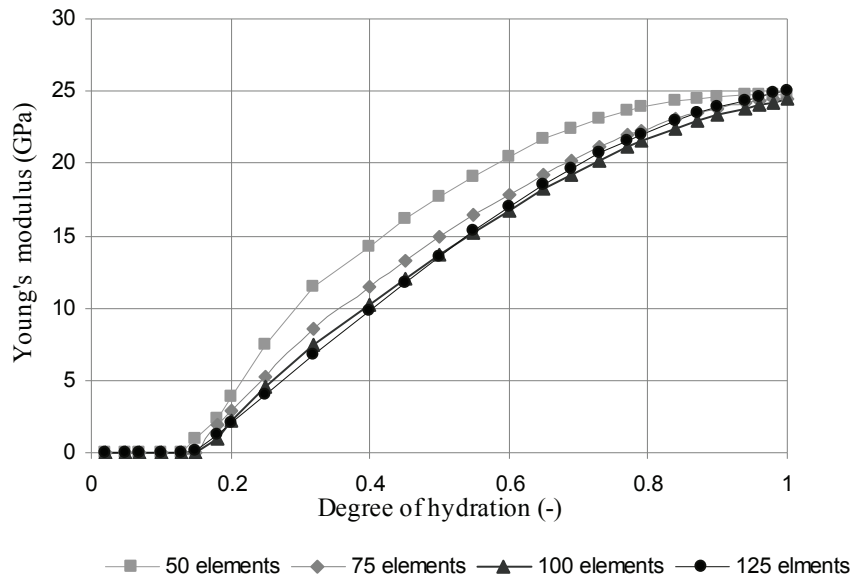


Figure D.3a: Effect of the mesh size on Young's modulus. CV of  $100 \mu\text{m}^3$  is discretized by mesh sizes of 2.0, 1.33, 1.0 and  $0.8 \mu\text{m}$  corresponding to 50, 75, 100 and 125 elements each side

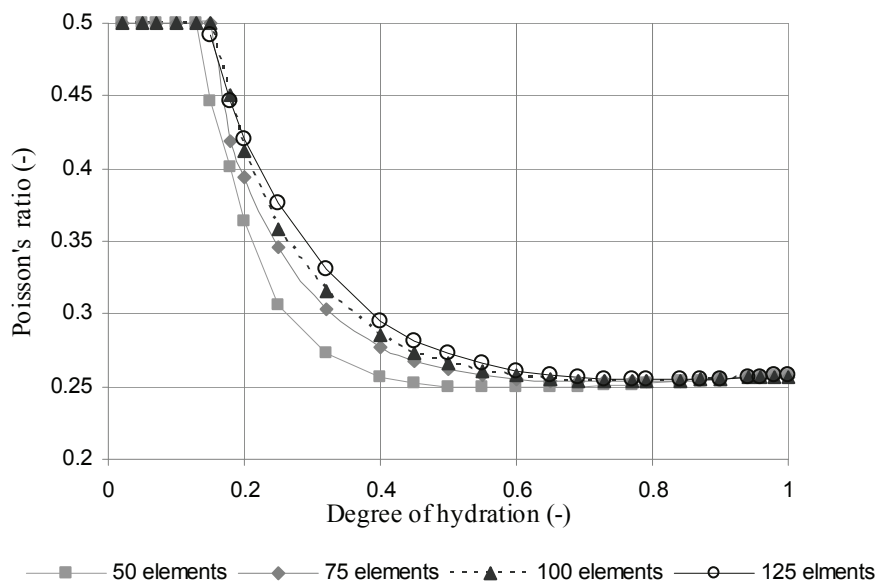


Figure D.3b: Effect of the mesh size on Poisson's ratio. CV of  $100 \mu\text{m}^3$  is discretized by mesh sizes of 2.0, 1.33, 1.0 and  $0.8 \mu\text{m}$  corresponding to 50, 75, 100 and 125 elements each side

## E. Finite Element Implementation

This appendix presents the FEM implementation of the creep simulations discussed in chapter 5. Based on the formulas presented section 5.2, a simulation of creep deformation of the modelled microstructure under given an arbitrary applied load history is carried out by two main steps: first elastic stage and then viscous stage for given time steps.

### *Elastic stage:*

The calculation procedure of the elastic deformation of the modelled microstructure is exactly the same as the FEM procedure used in chapter 4.

- Mesh the vector modelled microstructure onto a uniform mesh of  $100^3$  elements using the double burning algorithm.
- Impose boundary conditions: one side of the modelled microstructure is under an initial uniform load (external) and the opposite side is fixed with zero displacement.
- Input elastic properties of each phases ( $E, \nu$ ).
- Calculate local stiffness matrixes for each element (using tri-linear displacement shape functions [Haecker *et al.* 2005, Smilauer and Bittnar 2006, Chamrová 2010]).
- Assemble local stiffness matrixes into the global matrix.
- Solve FEM systems by using the conjugate gradient solver, which gives elastic deformation  $\mathbf{d}$  at nodes, strain  $\boldsymbol{\varepsilon}$  and stress  $\boldsymbol{\sigma}$  at Gaussian points.
- Initialize volumetric internal  $\beta_{\alpha_m}$  and deviator internal  $\beta_{\alpha_{ij}}^d$  variables to zero tensors for the *viscous stage* below.

It should be noted that only C-S-H elements have viscous behaviour as described here. For other elementary phases, the elastic constitutive materials are completely the same as discussed in chapter 4 and in Appendix C.

### *Viscous stage (at time step h):*

The calculation procedure of the incremental viscous deformation with time of the modelled microstructure is carried out under incremental external load  $\Delta \mathbf{F}_{ex}$  (in the creep simulation the external load is a constant, therefore, load increases  $\Delta \mathbf{F}_{ex}$  are set to zero tensor:  $\Delta \mathbf{F}_{ex} \equiv \mathbf{0}$ ).

- Input C-S-H viscous parameters of the Maxwell chain  $K_{\alpha=0, N}$ ,  $G_{\alpha=0, N}$  and  $\tau_{\alpha=1, N}$ , interval time step  $\Delta t_h$  (see table 5.1). In the simulations without densification, viscous parameters are identical for all C-S-H elements present in CV. However, if the C-S-H densification is considered (see section 5.3.3), once a new C-S-H element is formed at a certain age, the viscous parameters of the Maxwell chain corresponding to that age is assigned to that element's properties. By this way, the C-S-H elements formed at later age have a longer relaxation time than the ones formed at early age, and thus the densification effect is considered.

- Impose incremental external load  $\Delta F_{ex}^h$  applying on the boundary of the modelled microstructure at the time step  $h$ .

- Calculate  $\bar{K}$  according to equation (5.28),  $\bar{G}$  according to equation (5.31), then  $\bar{\mathbf{D}}$  following equation (5.37), and local stiffness matrixes  $\mathbf{K}^e$  according to equation (5.43) for each element.

- Calculate relaxation matrixes  $-\int_{\Omega^e} \mathbf{B}^T \Delta \bar{\boldsymbol{\sigma}} d\Omega$  for each element.

- Calculate  $\Delta \bar{\boldsymbol{\sigma}}_m$  according to equation (5.29), and  $\Delta \bar{\boldsymbol{\sigma}}_{ij}^d$  according to equation (5.32), and then  $\Delta \bar{\boldsymbol{\sigma}}$  according to equation (5.36) for each element.

- Assemble  $\mathbf{K}^e$  and relaxation matrixes into the global matrix.

- Solve FEM systems for equation (5.44) by using the conjugate gradient solver, which gives incremental viscous deformation  $\Delta \mathbf{d}$  at nodes, strain  $\Delta \boldsymbol{\varepsilon}$  and stress  $\Delta \boldsymbol{\sigma}$  at Gaussian points.

- Update volumetric internal variables  $\beta_{\alpha_m}$ , similar to equation (5.15), expanded into the multi-axial (3D) case as follows:

$$\beta_{\alpha_{mi}} = e^{-\frac{\Delta t_h}{\tau_\alpha}} \cdot \beta_{\alpha_{mh-1}} + \Delta \varepsilon_{mh} \left[ 1 - \frac{\tau_\alpha}{\Delta t_h} (1 - e^{-\frac{\Delta t_h}{\tau_\alpha}}) \right] + \varepsilon_{mh-1} (1 - e^{-\frac{\Delta t_h}{\tau_\alpha}}) \quad (\text{E.1})$$

- Update deviator internal variables  $\beta_{\alpha_{ij}}^d$ , similar to equation (5.15), expanded into the multi-axial (3D) case as follows:

$$\beta_{\alpha_{ijh}}^d = e^{-\frac{\Delta t_h}{\tau_\alpha}} \cdot \beta_{\alpha_{ijh-1}}^d + \Delta \varepsilon_{ijh}^d \left[ 1 - \frac{\tau_\alpha}{\Delta t_h} (1 - e^{-\frac{\Delta t_h}{\tau_\alpha}}) \right] + \varepsilon_{ijh-1}^d (1 - e^{-\frac{\Delta t_h}{\tau_\alpha}}) \quad (\text{E.2})$$

- 
- Update total deformation (elastic plus incremental viscous parts)  $\mathbf{d}_h = \mathbf{d}_{h-1} + \Delta \mathbf{d}$ , strain  $\boldsymbol{\varepsilon}_h = \boldsymbol{\varepsilon}_{h-1} + \Delta \boldsymbol{\varepsilon}$ , and stress  $\boldsymbol{\sigma}_h = \boldsymbol{\sigma}_{h-1} + \Delta \boldsymbol{\sigma}$
  - Update phase information in the same meshed microstructure.
  - Repeat the *viscous stage* for next time interval.

It is clearly seen from this description for creep simulation that the external load instantaneously charges only on hydrate elements in the initial stage (at the loading time in the *elastic stage*) of the microstructure whereas all the newly formed hydrates after this initial loading time are in a free stress state regarding to the applied external loading (if  $\Delta \mathbf{F}_{ex}^e \equiv \mathbf{0}$ ). The strain of CV increases for each time interval of the *viscous stage* due to the “internal loading” (i.e. the second term in the right hand side of equation (5.44)) coming from creep in the existing C-S-H elements.

---

## References

1. Abell A.B., Willis K.L. and Lange D.A., Mercury intrusion porosimetry and image analysis of cement-based materials, *Journal of Colloid and Interface Science*, Vol. 211, pp.39-44, 1999
2. Abrams D., *Design of Concrete Mixtures*, Structural Materials Research Laboratory, Lewis Institute, Chicago, USA, 1918
3. ACI Committee 318, *Building code requirements for structural concrete (ACI 318-08) and commentary*, American Concrete Institute, 2008
4. Acker P., Le point des connaissances sur le fluage du béton. Interpretation des mesures, modelisation pour le calcul, debouches sur la reglementation. *Annales de l'ITBTP*, No 455, pp.89-95, June 1987
5. Acker P., Micromechanical analysis of creep and shrinkage mechanisms, in: F.J. Ulm, Z.P. Bazant, F.H. Wittmann (Eds.), *creep, shrinkage and durability mechanics of concrete and other quasi-brittle materials*, Proc. of the Sixth International Conference CONCREEP 6, Elsevier, Oxford, UK, pp. 15-25, 2001
6. Argyris, J.H. and Kelsey, S., *Energy Theorems and Structural Analysis*, London, Butterworth, 1960, Part I reprinted from *Aircraft Engineering*, 26, Oct-Nov 1954 and 27, April-May 1955
7. ASTM, Standard test method for autogeneous strain of cement paste and mortar, in *ASTM International*, West Conshohocken, PA, 2009
8. Baldwin C.A., Sederman A.J., Mantle M.D., Alexander P. and Gladden L.F., Determination and Characterization of the Structure of a Pore Space from 3D Volume Images, *Journal of Colloid and Interface Science*, Vol. 181, pp.79-92, 1996
9. Bangham D.H. and Fakhoury N., Swelling of Charcoal, Part I. Preliminary experiments with water vapour, carbon dioxide, ammonia and sulphur dioxide, *Proceedings of the Royal Society of London (Series A), Containing Papers of a Mathematical and Physical Character*, Vol. 130 (812), pp.81-89, 1930
10. Barcelo L., Moranville. M and Clavaud B., Autogeneous shrinkage of concrete: a balance between autogeneous swelling and self-desiccation, *Cement and Concrete Research*, Vol. 35 (1), pp.177-183, 2005

11. Baroghel B.V. and Kheiberk A., Effect of mix-parameters on autogeneous deformations of cement pastes—microstructural interpretations. *Concrete Science and engineering*, Vol. 3, pp.23-38, 2001
12. Bary B., Ben Haha M., Adam E. and Montarnal P., Numerical and analytical effective elastic properties of degraded cement pastes, *Cement and Concrete Research*, Vol. 39, pp.902-912, 2009
13. Bažant Z.P., Mathematical models for creep and shrinkage of concrete, *Creep and shrinkage in concrete structures*, Edited by Bažant Z.P. & Wittmann F.H., Chap.7, pp.163-256, 1982
14. Bažant Z.P. *Mathematical modelling of creep and shrinkage of concrete*, John Wiley & Son Ltd, 1988
15. Bažant Z.P. and Baweja S., Creep and shrinkage prediction model for analysis and design of concrete structures: Model B3, Technical report, American Concrete Institute, pp. 1-83, 2000
16. Bažant Z.P. and Wu S.T., Rate-type creep law of aging concrete based on Maxwell chain, *Materiaux et Constructions*, Vol.7 (37), pp.45-60, 1974
17. Bell F., A survey of the engineering properties of some anhydrite and gypsum from the north and midlands of England, *Eng. Geol.* 38 (1–2), pp.1-23, 1994
18. Bentz D.P., A Three-Dimensional Cement Hydration and Microstructure Program. I. Hydration Rate, Heat of Hydration, and Chemical Shrinkage, NISTIR 5756, U.S. Department of Commerce, 1995
19. Bentz D.P., Three-dimensional computer simulation of Portland cement hydration and microstructure development, *Journal of the American Ceramic Society*, Vol. 80, pp.3-21, 1997
20. Bentz D.P., CEMHYD3D: A Three-Dimensional Cement Hydration and Microstructure Development Modelling Package. Version 2.0, NIST, April 2000
21. Bentz D.P. and Garboczi E.J., A digitized simulation model for microstructural development, *Ceramic Transactions*, Vol. 16, pp.211–226, 1991
22. Bentz D.P., Garboczi E.J., Haecker C.J. and Jensen O.M., Effects of cement particle size distribution on performance properties of Portland cement-based materials, *Cement and Concrete Research*, Vol. 29, pp.1663-1671, 1999
23. Bentz D.P., Garboczi E.J. and Quenard D.A., Modelling drying shrinkage in reconstructed porous materials: application to porous Vycor glass, *Modelling Simulation in Materials Science and Engineering*, 6, pp.211-236, 1998

24. Bentz D.P. and Jensen O.M. Mitigation strategies for autogeneous shrinkage cracking, *Cement and Concrete Composites*, Vol. 26 (6), pp.677-685, 2004
25. Bentz D.P. and Martys N.S., Hydraulic radius and transport in reconstructed model three-dimensional porous media, *Transport in Porous Media*, Vol. 17, pp.221-238, 1994
26. Bernard O., Ulm F.J. and Lemarchand E., A multiscale micromechanics-hydration model for the early-age elastic properties of cement-based materials, *Cement and Concrete Research*, Vol. 33, pp.1293-1309, 2003
27. Bezjak A. and Jelenic I., On the determination of rate constants for hydration processes in cement pastes, *Cement and Concrete Research*, Vol. 10, 1980, pp.553-563, 1980
28. Bishnoi S., Vector modelling of hydrating cement microstructure and kinetics, Doctoral thesis, École Polytechnique Fédérale de Lausanne, Switzerland, 2008
29. Bishnoi S. and Scrivener K.L., A new platform for modelling the hydration of cements, *Cement and Concrete Research*, Vol. 39 (4), pp.266-274, 2009a
30. Bishnoi S. and Scrivener K.L., Studying nucleation and growth kinetics of alite hydration using *μic*, *Cement and Concrete Research*, Vol. 39 (10), pp.849-860, 2009b
31. Bishnoi S., The user documentation for *μic*, the plugins included in *μic*, its graphical user interface and XML input file, [www.micthemodel.org](http://www.micthemodel.org), 2012
32. Bjontegaard Ø., Thermal dilation and autogeneous deformation as driving forces to self-induced stresses in high performance concrete, Ph.D. thesis, NTNU Division of Structural Engineering, Trondheim, Norway, 1999
33. Bjontegaard Ø, Hammer T.A. and Sellevold E.J., On the measurement of free deformation of early age cement paste and concrete, *Cement and Concrete Composites*, Vol. 26, pp. 427-435, 2004
34. Bolomey J., Granulation et prevision de la resistance probable des betons, *Travaux*, Vol. 30, pp.228-232, 1935
35. Boumiz A., Sorrentino D., Vernet C. and Tenoudji F.C., Modelling the development of the elastic moduli as a function of the hydration degree of cement pastes and mortars, *RILEM Proceedings*, PRO 13, Hydration and Setting: Why does Cement Set, an Interdisciplinary Approach, pp.295-316, 2000
36. Boivin S., Acker, P., Rigaud S., and Clavaud B., Experimental Assessment of Chemical Shrinkage of Hydrating Cement Paste, *Autoshrink'98 Proceedings of the International Workshop on Autogeneous Shrinkage of Concrete*, ed. E. Tazawa, pp.77-88, 1998

37. Bryant S.L., King P.R. and Mellor D.W., Network model evaluation of permeability and spatial correlation in a real random sphere packing, *Transport in porous media*, Vol. 11, 1993, pp.53-70, 1993
38. Buil M., Studies of the shrinkage of hardening cement paste, in: Doctoral thesis, Laboratoire Central des Ponts et Chaussées, Rapport de recherche LPC (92), 1979
39. Bullard J.W. and Garboczi E.J., A model investigation of the influence of particle shape on Portland cement hydration, *Cement and Concrete Research*, Vol. 36, pp.1007-1015, 2006
40. Bullard J.W., A three-dimensional microstructural model of reactions and transport in aqueous mineral systems, *Modelling and Simulations in Materials Science and Engineering* 15, pp.711–738, 2007
41. Bullard J.W., Jennings H.M., Livingston R.A., Nonat A., Scherer G.W., Schweitzer J.S., Scrivener K.L., Thomas J.J., Mechanism of cement hydration, *Cement and Concrete Research*, Vol. 41(12), pp.1208-1223, 2011
42. Castaneda P.P. and Willis J.R., The effect of spatial distribution on the effective behaviour of composite materials and cracked media, *Journal of the Mechanics and Physics of Solids*, Vol. 43, pp.1919-1951, 1995
43. Chamrová R. Modelling and measurement of elastic properties of hydrating cement paste, Doctoral thesis, École Polytechnique Fédérale de Lausanne, Switzerland, 2010
44. Chazal C. and Pitti R.M. Viscoelastic incremental formulation using creep and relaxation differential approaches, *Mechanics of Time-Dependent Materials*, Vol. 14, pp.173-190, 2010
45. Christensen R.M., Theory of viscoelastic, An introduction, Academic Press, UK, 1982
46. Chen H., Autogeneous and thermal deformations and their interaction in early age cementitious materials, Doctoral thesis, École Polytechnique Fédérale de Lausanne, Switzerland, 2013
47. Chen H., Wyrzykowski M., Scrivener L.K. and Lura. P., Prediction of self-desiccation in low water-to-cement ratio pastes based on pore structure evolution, *Cement and Concrete Research*, Vol. 49, pp. 38-47, 2013
48. Constantinides. G and Ulm F.J, The effect of two types of C-S-H on the elasticity of cement-based materials: results from nanoindentation and micromechanical modelling, *Cement and Concrete Research*, 34 (1), pp.67-80, 2004
49. Constantinides G., Invariant mechanical properties of calcium-silicate-hydrates (C-S-H) in cement-based materials: Instrumented nanoindentation and microporomechanical



- modelling, PhD thesis, Civil and Environmental Engineering Department, Massachusetts Institute of Technology, Cambridge, MA, USA, 2006
50. Constantinides G., Chandran K.S.R., Ulm F.J. and Vliet K.J.V., Grid indentation analysis of composite microstructure and mechanics: Principles and validation. *Mat Sc Eng A* 430, pp. 189-202, 2006
  51. Constantinides G. and Ulm F.J., The nanogranular nature of C-S-H, *Journal of the Mechanics and Physics of Solids*, Vol. 55, pp. 64-90, 2007
  52. Courant R., Variational methods for the solution of problems of equilibrium and vibration, *Bulletin of the American Mathematical Society*, Vol. 49, pp.1-23, 1943
  53. Coussy O., Dangla P. and Baroghel B.V., The equivalent pore pressure and the swelling and shrinkage of cement-based materials, *Materials and Structures* Vol.37, pp.15-20, 2004
  54. Cusson D., Effect of blended cements on efficiency of internal curing of HPC, ACISP 256, *Internal Curing of High-Performance Concretes: Laboratory and Field Experiences*, MI, pp.105-120, 2008
  55. Defay R., Pregogine I. and Bellemans A., *Surface tension and absorption*, Longmans London, London, 1966
  56. Diamond S., Mercury porosimetry: An inappropriate method for the measurement of pore size distributions in cement-based materials, *Cement and Concrete Research*, Vol. 30 (10), pp.1517-1525, 2000
  57. Do Q.H., Bishnoi S. and Scrivener K.L, Numerical Simulation of Porosity in Cements *Transport in Porous Media*, Vol. 99 (1), pp. 101-117, 2013
  58. Do Q.H., Bishnoi S. and Scrivener K.L, Simulating the setting time and the early age mechanical properties of tricalcium silicate pastes: Effect of flocculation and densification of calcium silicate hydrate, Submitted to *Modelling and Simulation in Materials Science and Engineering*, July 2013
  59. Dunant C.F., Bary B., Giorla A.B., Péniguel C., Sanahuja J, Toulemonde C., Tran A.B., Willot F. and Yvonnet J., A critical comparison of several numerical methods for computing effective properties of highly heterogeneous materials, *Advances in Engineering Software*, Vol. 58, pp.1-12, 2013
  60. EN 1992-1-1:2004, Eurocode 2: Design of concrete structures - Part 1-1: General rules and rules for buildings, CEN Technical Committee 250, 2004
  61. Feret R., Sur le compacité des mortiers, *Annales des Ponts et Chaussées*, Vol. 7, pp.5-164, 1892

62. Ferraris C.F., *Mecanisme du retrait de la pate de ciment durcie*, Doctoral thesis, École Polytechnique Fédérale de Lausanne, 1986
63. Fratini E., Chen S.-H. and Baglioni P., Investigation of the temporal evolution of translational dynamics of water molecules in hydrated calcium aluminate pastes, *Journal of Physical Chemistry B*, Vol. 107, pp.10057-10062, 2003
64. Eshelby J.D., The determination of the elastic field of an ellipsoidal inclusion, and related problems, *Proceedings of the Royal Society A*, Vol. 241, pp.376-396, 1957
65. Eshelby J.D., The elastic field outside an ellipsoidal inclusion, *Proceedings of the Royal Society A*, Vol. 252, pp.561-569, 1959
66. Garboczi E.J. and Bentz D.P., The effect of statistical fluctuation, finite size error, and digital resolution on the phase percolation and transport properties of the NIST cement hydration model, *Cement and Concrete Research*, Vol. 31, pp.1501-1514, 2001
67. Gartener E.M., Young J.F., Damidot D.A., Jawed I., *Hydration of Portland cement Structure and performance of cements*, Bensted and Barnes (eds.), Spon press, 2002
68. Gallucci E. and Scrivener K., Crystallisation of calcium hydroxide in early age model and ordinary cementitious systems, *Cement and Concrete Research*, Vol. 37, pp.492-501, 2007
69. Garboczi E.J. and Bentz D.P., Digitized simulation of mercury intrusion porosimetry, *Advances in Cementitious Materials*, Vol. 16, pp.365-380, 1991
70. Garboczi E.J. and Bentz D.P., The effect of statistical fluctuation, finite size error, and digital resolution on the phase percolation and transport properties of the NIST cement hydration model, *Cement and Concrete Research*, Vol. 31, pp.1501-1514, 2001
71. Gawin D., Pesavento F. and Schrefler B.A., Hygro-thermo-chemo-mechanical modelling of concrete at early ages and beyond. Part I: hydration and hygro-thermal phenomena, *International Journal for Numerical Methods in Engineering*, Vol. 67 (3), pp.299-331, 2006a
72. Gawin D., Pesavento F., and Schrefler B.A., Hygro-thermo-chemo-mechanical modelling of concrete at early ages and beyond. Part II: shrinkage and creep of concrete, *International Journal for Numerical Methods in Engineering*, Vol. 67 (3), pp.332-363, 2006b
73. Gawin D., Wyrzykowski M. and Pesavento F., Modeling Hygro-thermal performance and strains of cementitious building materials maturing in variable conditions, *Journal of Building Physics*, Vol. 31, pp.301-318, 2008

74. Grasley Z.C. and Lange D.A., Constitutive modeling of the aging viscoelastic properties of Portland cement paste, *Mech Time-Depend Mater*, Vol.11, pp. 175-198, 2007
75. Guidoum A., Simulation numérique 3D des comportements des bétons en tant que composites granulaires, Doctoral thesis No 1310, Ecole Polytechnique Federale de Lausanne, Switzerland, 1994
76. Grondin F., Dumontet H., Ben Hamida A., Mounajed G. and Boussa H., Multiscales modelling for the behaviour of damaged concrete, *Cement and Concrete Research*, Vol. 37, pp.1453-1462, 2007
77. Haecker C.-J., Garboczi E.J., Bullard J.W., Bohn R.B., Sun Z., Shah S.P. and Voigt T., Modeling the linear elastic properties of Portland cement paste, *Cement and Concrete Research*, Vol. 35, pp.1948-1960, 2005
78. Hammer T.A., Bjøntegaard, Ø. and Sellevold, E.J., Measurement methods for testing of early age autogeneous strain, early age cracking in cementitious systems, ed. Bentur A., RILEM TC 181-EAS Committee, RILEM, Cachan, France, pp.234-245, 2002
79. Hassanizadeh S.M and Gray W.G. General conservation equations for multi-phase systems: 1. Averaging procedure. *Advances in Water Resources*, Vol. 2, pp.131-144, 1979a
80. Hassanizadeh S.M. and Gray W.G. General conservation equations for multi-phase systems: 2. Mass, momenta, energy and entropy equations. *Advances in Water Resources*, Vol.2, pp.91-203, 1979b
81. Hassanizadeh S.M. and Gray W.G. General conservation equations for multi-phase systems: 3. Constitutive theory for porous media flow. *Advances in Water Resources*, Vol. 3, pp.25–40, 1980
82. He H., Guo Z., Stroeven P., Stroeven M. and Sluys L.J., Strategy on simulation of arbitrary shaped cement grains in concrete, *Image Analysis and Stereology*, Vol. 29, pp.79-84, 2010
83. Hill R., The elastic behaviour of a crystalline aggregate, *Proceedings of the Physical Society*, Vol. 65, pp.349-354, 1952
84. Hill R., A self-consistent mechanics of composite materials, *Journal of the Mechanics and Physics of Solids*, Vol. 13, pp.213–222, 1965
85. Hiller, K.H., Strength reduction and length changes in porous glass caused by vapor adsorption, *J App Phys*, Vol. 35, pp.1622-1628, 1964
86. Hrennikoff A.P., Plane stress and bending of plates by method of articulated framework, Doctoral Dissertation, MIT, Boston, 1940

87. Hua C., Acker P. and Ehrlacher A., Analyses and models of the autogeneous shrinkage of hardening cement paste. I. Modelling at macroscopic scale, *Cement and Concrete Research*, Vol.25 (7), pp.1457-1468, 1995
88. Hua C., Ehrlacher A. and Acker P., Analyses and models of the autogeneous shrinkage of hardening cement paste. II. Modelling at scale of hydrating gains, *Cement and Concrete Research*, Vol.27 (2), pp.245-258, 1997
89. Huet C., Application of variational concepts to size effects in elastic heterogeneous bodies, *Journal of the Mechanics and Physics of Solids*, Vol. 38, pp.813-841, 1990
90. Huet C., Some basis tools and pending problems in the development of constitutive equations for the delayed behaviour of concrete, *Creep and Shrinkage of concrete*, Edited by Bažant Z.P. and Carol I. Spon, pp. 189-200, 1993
91. Ishida T., Chaube R.P., Kishi T. and Maekawa K., Microphysical approach to coupled autogeneous and drying shrinkage of concrete. Proc of Intern Workshop on Autogeneous Shrinkage of Concrete, JCI, edited by Tazawa E, June 13-14, Hiroshima, Japan, pp 301-312, 1998
92. Jaouadi I. Etude numerique et experimentale de retrait endogene de la pate de ciment au jeune age, Doctoral thesis, École Polytechnique Fédérale de Lausanne, Switzerland, 2008
93. Jennings H.M. and Johnson S.K., Simulation of microstructure development during the hydration of a cement compound, *Journal of American Ceramic Society* 69, pp.790-795, 1986
94. Jennings H.M. and Parrott L.J., Microstructural analysis of hardened alite paste, part II: microscopy and reaction products, *Journal of Materials Science*, Vol. 21, pp.4053-4059, 1986
95. Jennings H.M., A model for the microstructure of calcium silicate hydrate in cement paste, *Cement and Concrete Research*, Vol. 30, 2000, pp.101-116, 2000
96. Jennings H.M., Colloid model of C-S-H and implications to the problem of creep and shrinkage, *Materials and Structures*, Vol. 37, pp.59-70, 2004
97. Jensen O.M., Autogeneous deformation and RH-change-self-desiccation and self-desiccation shrinkage, PhD thesis, Building Materials Laboratory, The Technical University of Denmark, Lyngby, Denmark, 1993, TR 284/93
98. Jensen O.M., Thermodynamic limitation of self-desiccation, *Cement and Concrete Research*. Vol.25 (1), pp.157-164, 1995
99. Jensen O.M. and Hansen P.F., A dilatometer for measuring autogeneous deformation in hardening Portland cement paste, *Materials and Structures*, Vol. 28, pp. 406-409, 1995

100. Jensen O.M. and Hansen P.F., Autogenous deformation and change of the relative humidity in silica fume-modified cement paste. *ACI Materials Journal*, Vol. 93(6), pp. 539-543, 1996
101. Jensen O.M. and Hansen P.F., Influence of temperature on autogeneous deformation and relative humidity change in hardening cement paste, *Cement and Concrete Research*, Vol. 29 pp.567-575, 1999
102. Jensen O.M., Influence of cement composition on autogeneous deformation and change of the relative humidity. *Actes du congrès RILEM Shrinkage 2000*. Edited by: Baroghel-Bouny, V. et Aïtcin, P.C., Paris : RILEM p.143-153, 2000
103. Jensen O.M. and Hansen P.F., Water-entrained cement-based materials. I. Principles and theoretical background, *Cement Concrete Research* Vol. 31(5), pp.647-654, 2001a
104. Jensen O.M. and Hansen P.F., Autogeneous deformation and RH-change in perspective, *Cement and Concrete Research*, Vol. 31(12), pp.1959-1865, 2001b
105. Juilland P., Early hydration of cementitious systems, Doctoral thesis, École Polytechnique Fédérale de Lausanne, Switzerland, 2009
106. Kamali S., Moranville M., Garboczi E., Prene S., Gerard B., Hydrate dissolution influence on the young's modulus of cement paste, in: L., et al., (Eds.), *Proc. Fracture Mechanics of Concrete Structures (FraMCoS-V)*, Routledge, Vail, pp.631-638, 2004
107. Koenders E.A.B. and van Breugel K., Numerical modelling of autogeneous shrinkage of hardening cement paste, *Cement and Concrete Research*, Vol. 27, pp.1489-1499, 1997
108. Kondo R. and Ueda S., Kinetics of hydration of cements, *Proceedings of the 5<sup>th</sup> international symposium on chemistry of cement*, Tokyo, pp.203-248, 1968
109. Kumar A. Modelling hydration kinetics of cementitious systems, Doctoral thesis, École Polytechnique Fédérale de Lausanne, 2012
110. Kumar A., Bishnoi S. and Scrivener K.L., Modelling early age hydration kinetics of alite, *Cement and Concrete Research*, Vol. 42, pp.903-918, 2012
111. L'Hermite R., Volume changes of concrete, *Proc. 4th International Symposium on the Chemistry of Cement*, Washington DC, Vol. II, pp. 659-694, 1960
112. Le Châtelier H., Sur les changements de volume qui accompagnent le durcissement des ciments, *Bulletin de la Society d' Encouragement l'Industrie Nationale V*, 5<sup>th</sup> series, pp.54-57, 1900
113. Lin C. and Cohen M.H., Quantitative methods for microgeometric modelling, *Journal of Applied Physics*, Vol. 53, pp.4152-4165, 1982

114. Lura P., Autogeneous deformation and internal curing of concrete, PhD Thesis, Delft University, the Netherlands, 2003
115. Lura P., Jensen O.M. and Van Breugel K., Autogeneous shrinkage in high-performance cement paste: An evaluation of basic mechanisms. *Cement and Concrete Research*, Vol. 33, pp.223-232, 2003
116. Lura P. and Jensen O.M., Measuring techniques for autogeneous strain of cement paste, *Materials and Structures*, Vol. 40, pp. 431-440, 2007
117. Lura P., Shrinkage mechanisms, Lecture note on: Concrete & Construction Chemistry, Empa, Dubendorf, Switzerland, 1-3 July, 2009
118. Maekawa K., Ishida T. and Kishi T., Multi-scale modeling of concrete performance integrated material and structural mechanics, *Journal of Advanced Concrete Technology* 1, pp.91-126, 2003
119. Mackenzie J.K., The elastic constants of a solid containing spherical holes *Proceedings of the Physical Society*, 683, pp.2-11, 1950
120. Marchand J., Samson E., Maltais Y., Lee R.J. and Sahu S., Predicting the performance of concrete structures exposed to chemically aggressive environment-field validation, *Materials and Structures*, Vol. 35, pp.623-631, 2002
121. Maycock J.N., Skalny J. and Kalyoncu R., Crystal defects and hydration I. Influence of lattice defects, *Cement and Concrete Research*, Vol. 4, pp.835-847, 1974
122. McDonald P.J., Mitchell J., Mulheron M., Monteilhet L. and Korb J.-P., Two-dimensional correlation relaxation studies of cement pastes, *Magnetic Resonance Imaging*, Vol. 25, pp.470-473, 2007
123. Mehta P.K. and Monteiro P.J.M., *Concrete: Microstructure, properties, and materials*, 3<sup>rd</sup> edition, Department of Civil and Environmental Engineering, University of California at Berkeley, pp.660, 2006
124. Mindess S. and Young, J.F., *Concrete*, Prentice-Hall Incorporation, 671 pp, 1981
125. Mori T. and Tanaka K., Average stress in matrix and average elastic energy of materials with misfitting inclusions, *Acta Metallurgica*, Vol. 21, pp.571-574, 1973
126. Moulinec H. and Suquet P., A fast numerical method for computing the linear and nonlinear properties of composites, *Comptes Rendus de l'Académie des Sciences Paris, II*, Vol. 318, pp.1417-1423, 1994
127. Mueller A.C.A., Scrivener K.L, Gajewicz A.M. and McDonald P.J., Densification of C–S–H Measured by <sup>1</sup>H NMR Relaxometry, *Journal of Physical Chemistry*, Vol. 117, pp. 403-412, 2012

128. Muller A.C.A, Scrivener K.L., Gajewicz A.M. and McDonald P.J., Use of bench-top NMR to measure the density, composition and desorption isotherm of C-S-H in cement paste, *Microporous and Mesoporous Materials*, In press, 2013
129. Munch B. and Holzer L., Contradicting Geometrical Concepts in Pore Size Analysis Attained with Electron Microscopy and Mercury Intrusion, *Journal of the American Ceramic Society*, Vol. 91, pp.4059-4067, 2008
130. Navi P., and Pignat C., Simulation of cement hydration and the connectivity of the capillary pore space, *Advanced Cement Based Materials*, Vol. 4, pp.58-67, 1996
131. Navi P. and Pignat C., Three-dimensional characterization of pore structure of a simulated cement paste, *Cement and Concrete Research*, Vol. 29, pp.507-514, 1999
132. Nawa T. and Horita T., Autogeneous shrinkage of high-performance concrete. *Proceeding of the international Workshop on Microstructure and Durability to Predict Service Life of Concrete Structures*, Sapporo, Japan, 2004
133. Neville A.M., *Properties of concrete*, John Wiley & Sons, New York (4th edition), 1995
134. Neville A.M., Suggestions of research areas likely to improve concrete. *Concrete International* Vol. 18 (5), pp.44–49, 1996
135. Odler I. and Schüppstuhl J., Early hydration of tricalcium silicate III. Control of the induction period, *Cement and Concrete Research*, Vol. 11, pp.765-774, 1981
136. Østergaard L., Lange D.A., Altoubat S.A. and Stang H., Tensile basic creep of early-age concrete under constant load, *Cement and Concrete Research*, 31, pp.1985-1899, 2001
137. Park K., Noguchi T. and Plawsky J., Modeling of hydration reactions using neural networks to predict the average properties of cement paste, *Cement and Concrete Research*, Vol. 35, pp.1676-1684, 2005
138. Pichler B., Hellmich C. and Eberhardsteiner J., Spherical and acicular representation of hydrates in a micromechanical model for cement paste: prediction of early-age elasticity and strength, *Acta Mechanica*, Vol. 203, pp.137-162, 2009
139. Pichler C. Lackner R. and Mang H.A., A multiscale micromechanics model for the autogeneous-shrinkage deformation of early-age cement-based materials, *Engineering Fracture Mechanics*, Vol. 74, pp.34-58, 2007
140. Pichler C. and Lackner R., A multiscale creep model as basic for simulation of early-age concrete behavior, *Computers and Concrete*, Vol. 5(4), pp.295-328, 2008

141. Pignat C., Simulation numérique de l'hydratation du silicate tricalcique, caractérisation de la structure poreuse et de la perméabilité, Doctoral thesis, École Polytechnique Fédérale de Lausanne, 2003
142. Pignat C., Navi P. and Scrivener K., Simulation of cement paste microstructure hydration, pore space characterization and permeability determination, *Materials and Structures*, Vol. 38, 459-466, 2005
143. Pommersheim J.M. and Clifton J.R., Mathematical modeling of tricalcium silicate hydration. II. Hydration sub-models and the effect of model parameters, *Cement and Concrete Research*, Vol. 12, pp.765-772, 1982
144. Powers, T.C. and Brownyard, T.L., Studies of the Physical Properties of Hardened Portland Cement Paste, *J Amer Concr Inst*, Vol. 43, Bulletin 22, Research Laboratories of the Portland Cement Association, Chicago, 1948
145. Powers T.C., Structure and Physical Properties of Hardened Portland Cement Paste, *Journal of American Ceramic Society*, Vol. 41, pp.1-6, 1958
146. Powers, T. C., Mechanisms of shrinkage and reversible creep of hardening cement paste in Proc. Int. Symp. Structure of Concrete and its behaviour under load, Cement Concrete Association, London, pp.319-344, 1965
147. Powers, T.C., Session I: The thermodynamics of volume change and creep, *Materiaux et Constructions* 1, pp. 487-507, 1968
148. Reuss A., Berechnung der Fließgrenze von Mischkristallen auf Grund der Plastizitätsbedingung für Einkristalle, *Journal of Applied Mathematics and Mechanics*, Vol. 9, pp.49-58, 1929
149. RILEM Technical Committee, Early Age Cracking in Cementitious Systems, TC 181-EAS, ed. Bentur A., Early age cracking in cementitious systems, RILEM, Cachan, pp. 388, 2002
150. Sanahuja J., Dormieux L. and Chanvillard G., Modelling elasticity of a hydrating cement paste, *Cement and Concrete Research*, Vol. 37, pp.1427-1439, 2007
151. Sanahuja J. and Toulemonde C., Numerical homogenization of concrete microstructures without explicit meshes, *Cement and Concrete Research*, 41, pp. 1320-1329, 2011
152. Sant G., The influence of temperature on autogeneous volume changes in cementitious materials containing shrinkage reducing admixtures, *Cement and Concrete Composites*, Vol. 34, pp.855-865, 2011



153. Sant G., Lothenbach B., Juilland P., Le Saout G., Weiss J. and K. Scrivener. K.L, The origin of early age expansions induced in cementitious materials containing shrinkage reducing admixtures, *Cement and Concrete Research*, Vol. 41 (3), pp.218-229, 2011
154. Sedef M. Samur E. and Basdogan C., Real-time finite element simulation of linear Viscoelastic tissue behavior based on experimental, *IEEE Computer Graphics and Applications*, pp. 28-38, 2006
155. Scheiner S. and Hellmich C., Continuum microviscoelasticity model for aging basic creep of early-age concrete, 2009
156. Scherer G.W., Crystallization in pores, *Cement and Concrete Research*, Vol. 29 (8), pp.1347-1358, 1999
157. Scherer G.W., Stress from crystallization of salt, *Cement and Concrete Research*, Vol. 34 (9), 1613-1624, 2004
158. Scherer G.W., Zhang J., Quintanilla J.A. and Torquato S., Hydration and percolation at the setting point, *Cement and Concrete Research*, Vol. 42, pp.665-672, 2012
159. Scherer G.W., Zhang J. and Thomas J.J., Nucleation and growth models for hydration of cement, *Cement and Concrete Research*, Vol. 42, pp.982-993, 2012
160. Soroka I., Portland cement paste and concrete. The Macmillan Press Ltd., London, 1979
161. Stein H. N., Thermodynamic considerations on the hydration mechanisms of  $\text{Ca}_3\text{SiO}_5$ ,  $\text{Ca}_3\text{Al}_2\text{O}$ , *Cement and Concrete Research*, Vol. 2, pp.167-177, 1972
162. Stroeven M. and Stroeven P., SPACE system for simulation of aggregated matter application to cement hydration, *Cement and Concrete Research*, Vol. 29 (8), pp 1299-1304, 1999
163. Suquet P., A simplified method for the prediction of homogeneized elastic properties of composites with a periodic structure, *Comptes Rendus de l'Académie des Sciences Paris, II*, Vol. 311, pp.769-774, 1990
164. Šmilauer V., Elastic properties of hydrating cement paste determined from hydration models, PhD thesis, Faculty of Civil Engineering, Czech Technical University in Prague, Czech, 2005
165. Šmilauer V. and Bažant Z.P., Identification of viscoelastic C-S-H behavior in mature cement paste by FFT-based homogenization method, *Cement and Concrete Research*, 40, pp. 197-207, 2010

166. Šmilauer V. and Bittnar Z., Microstructure-based micromechanical prediction of elastic properties in hydrating cement paste, *Cement and Concrete Research*, Vol. 36, pp.1708-1718, 2006
167. Tamtsia B.T., Beaudoin J.J. and Marchand J., The early age short-term creep of hardening cement paste load-induced hydration effects, *Cement and Concrete Research*, 26, pp. 481-489, 2004
168. Tao Z. and Weizu Q., Tensile creep due to restraining stresses in high-strength concrete at early ages, *Cement and Concrete Research*, 36, pp. 584-591, 2005
169. Taylor H. F. W., *Cement Chemistry*. Thomas Telford, London, U.K., 1997
170. Tazawa E.I and Miyazawa S., Experimental study on mechanism of autogenous shrinkage of concrete, *Cement and Concrete Research*, Vol. 25, pp.1633-1638, 1995a
171. Tazawa E.I. and Miyazawa S., Influence of cement and admixture on autogenous shrinkage of cement paste. *Cement and Concrete Research*, Vol. 25(2), pp.281-287, 1995b
172. Thomas J.J. and Jennings H.M., A colloidal interpretation of chemical aging of the C-S-H gel and its effects on the properties of cement paste, *Cement and Concrete Research*, Vol. 36 (1), pp. 30-38, 2006
173. Thomas J.J., Allen A.J. and Jennings H.M., Hydration kinetics and microstructure development of normal and CaCl<sub>2</sub>-Accelerated tricalcium silicate pastes, *Journal of Physical Chemistry*, Vol. 113, pp.19836-19844, 2009
174. Thomas J.J., Biernacki J.J., Bullard J.W. Bishnoi, S., Dolado J.S., Scherer G.W. Luttge, A., Modeling and simulation of cement hydration kinetics and microstructure development, *Cement Concrete Research*. Vol. 41(12), pp.1257-1278, 2011
175. Troxell G.E., Davis H.E., and Kelly J.W., *Composition and Properties of Concrete*, McGraw-Hill, New York, p. 342, 1968
176. Turner, M.J., Clough, R.W., Martin, H.C. and Topp, L.J., Stiffness and deflection analysis of complex structure, *Journal of The Aeronautical Sciences.*, Vol.23 (9), pp.805-824. 1956
177. Ulm. F.J. and Coussy O., Strength growth as chemo-plastic hardening in early age concrete, *Journal of Engineering Mechanics*, Vol. 122 (12), pp.1123-1132, 1996
178. Ulm F.J., Le Maou F. and Boulay C., Creep and shrinkage coupling: new review of some evidence. *Revue française de génie civil* 3: pp.21-37, 1999
179. Van Breugel K., Numerical simulation of hydration and microstructural development in hardening cement-based materials (I): Theory, *Cement and Concrete Research*, Vol. 25, pp.319-331, 1995a

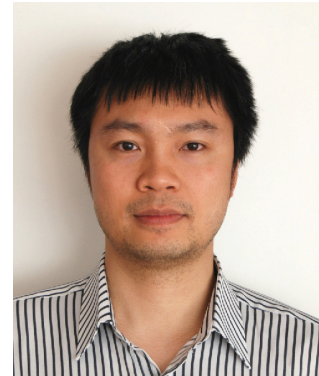
- 
180. Van Breugel K., Numerical simulation of hydration and microstructural development in hardening cement-paste (II): Applications, *Cement and Concrete Research* Vol.25, pp.522-530, 1995b
  181. Van Breugel K., Numerical modelling of volume changes at early ages - Potential, pitfalls and challenges, *Materials and Structures*, Vol. 34, pp. 293-301, 2001
  182. Vandamme M., The nanogranular origin of concrete creep: A nanoindentation investigation of microstructure and fundamental properties of calcium-silicate-hydrates, PhD thesis, Civil and Environmental Engineering Department, Massachusetts Institute of Technology, Cambridge, MA, USA, 2008
  183. Vandamme M. and Ulm F.J., Nanogranular origin of concrete creep, *Proceedings of the National Academy of Sciences of the United States of America*, Vol. 106 (26), pp. 10552-10557, 2009
  184. Velez K., Maximilien S., Damidot D., Fantozzi G. and Sorrentino F., Determination by nanoindentation of elastic modulus and hardness of pure constituents of Portland cement clinker, *Cement and Concrete Research* 31 (4), pp.555– 561, 2001
  185. Vlahinic I., Jennings H.M. and Thomas J.J., A constitutive model for drying shrinkage of a partially saturated porous materials, *Mechanics of Materials*, Vol. 41 (3), pp.319-328, 2009
  186. Visser J.H.M. Extensile hydraulic fracturing of (saturated) porous materials. PhD Thesis, Delft University, the Netherlands, 1998
  187. Voidt W., Theoretische studien über die elasticitätsverhältnisse der krystalle, *Abhandlungen der Königlichen Gesellschaft der Wissenschaften in Göttingen*, Vol. 34, pp.3-51, 1887
  188. Weiss W.J., Lura P., Rajabipour F., Sant G., Performance of shrinkage reducing admixtures at different humidities and at early ages, *American Concrete Institute Materials Journal*, Vol. 105 (5), pp.478-486, 2008
  189. Wittmann F.H., Surface tension, shrinkage and strength of hardened cement paste. *Materials and Structures* Vol. 1(6), pp.547–552, 1968
  190. Wittmann F.H., Creep and shrinkage mechanisms. Part II in creep and shrinkage in concrete structures, edited by Bažant Z.P, Wittmann F.H., John Wiley & Sons, pp 129-163, 1982
  191. Wittmann F.H., Mechanisms and mechanics of shrinkage, *Proc. 6<sup>th</sup> Int. Conf. Creep, Shrinkage and durability mechanics of concrete and other quasi-brittle materials*, eds. Ulm

- 
- F.J., Bažant Z.P. & Wittmann F.H., Cambridge, MA, August 20-22, Elsevier Science Ltd, pp. 312, 2001
192. Yamazaki Y., Monji, T., and Sugiura K., Early age expanding behavior of mortars and concretes using expansive additives of  $\text{CaO-CaSO}_4\text{-4CaO}\cdot\text{3Al}_2\text{O}_3\cdot\text{SO}_3$  system, 6<sup>th</sup> International Congress on the Chemistry of Cement, Moscow, September 1974, Stroyizdat, Moscow III-5, pp.192-195, 1976
193. Ye, G., van Breugel K. and Fraaij, A.L.A., Three-dimensional microstructure analysis of numerically simulated cementitious materials, *Cement and Concrete Research*, Vol. 33, 215-222, 2003
194. Ye G., Lura P. and van Breugel K., Modelling water permeability in cementitious materials, *Materials and Structures*, Vol. 39 (293), pp. 877-885, 2006
195. Zhou J., Ye G. and van Breugel K., Characterization of pore structure in cement-based materials using pressurization–depressurization cycling mercury intrusion porosimetry (PDC-MIP), *Cement and Concrete Research*, Vol. 40, pp.1120-1128, 2010
196. Zienkiewicz O.C., Watson M. and King I.P., A numerical method of visco-elastic stress analysis, *International Journal of Mechanical Sciences*, Vol.10 (10), pp. 807-827, 1968
197. Zienkiewicz O.C. and Taylor R.L., *The finite element method*, Solid Mechanics, fifth edition, Vol. 2, Butterworth-Heinemann, UK, 2000

## Quang-Huy Do

18<sup>th</sup> November 1978  
Nationality: Vietnamese

Rue Georges-Jordil 3  
CH – 1700 Fribourg  
Tel: +41 26 321 33 88  
Email: doquanghuy2002@yahoo.com



## Fields of expertise

Computational structural mechanics, computational material modelling, analytical and numerical homogenization methods, finite element analysis, finite element code development, structural analysis and design, lecturing on finite element software and on computer programming

## Work experience

- 2009 – 8/2013      Ecole Polytechnique Federale de Lausanne, Switzerland  
**Doctoral research assistant** at Laboratory of Construction Materials
- Develop FE code (Java) to simulate elastic and viscoelastic behaviours of ageing cement microstructures
  - Develop 3D numerical algorithms (Java) to characterize pore structures
- 2008 – 2009      Institute of Geotechnics, University of Stuttgart, Germany  
**Research assistant**
- Implement finite element code in Plaxis, a commercial software of geotechnical professionals
- 2003 – 2007      Applied Informatics Center, Hanoi Architectural University, Vietnam  
**Lecturer**
- Teach a computer aided engineering course (undergraduate level)
  - Guide the Hanoi Architectural University's selected team (undergraduate students) for the National Student Olympiad in Informatics

- 2001 – 2002      Construction consultancy Company, Hanoi Architectural University, Vietnam  
**Structural engineer**
- Structural design and analysis calculations using governing codes and standards
  - Provide drawing for own designs and produce sketches to incorporate in drawings by designers/drafters

## Education

- 2009 – 2013      **Ph.D.** in Structural Mechanics,  
Ecole Polytechnique Federale de Lausanne, Switzerland  
Thesis “Modelling properties of cement paste from microstructure:  
Porosity, mechanical properties, creep and shrinkage”
- 2007 – 2009      **M.Sc.** in Computational Mechanics of Materials and Structures,  
University of Stuttgart, Germany  
Thesis: “Implementation of Low-order tetrahedral element with strain  
enhancement”
- 2001 – 2004      **B.Sc.** in Computer Sciences, Hanoi University of Technology, Vietnam
- 1996 – 2001      **B.Sc.** in Civil Engineering, Hanoi Architectural University, Vietnam

## Distinctions and Honors

- 2001              - **Second prize**, Technical Creation Award, Vietnam Fund for Technical Creation  
                      - **Second prize**, The National Scientific research competition  
                      - Certificate of Merit, **Outstanding students award**
- 1999              - Hanoi Architectural University’s **best student of the year**
- 1998              - **Second prize**, Theoretical Mechanics competition, Hanoi Architectural University
- 1997              - **First prize**, The National Olympiad of Informatics for University Students

## Languages

- |            |                                       |
|------------|---------------------------------------|
| Vietnamese | Native                                |
| English    | C1 - European standard language level |
| German     | A2 - European standard language level |

## Computer skills

Programming languages: Delphi, C, C++, Java, Fortran, Visual Basic

Frameworks: Windows, Linux

Engineering packages: Sap, Plaxis, Abaqus, Autocad

## Publications

- **Q. H. Do**, S. Bishnoi, K. L. Scrivener, H. Chen, “*Numerical simulation and experiment of autogenous shrinkage of cement pastes at early ages*”, to be submitted to Computational Materials Science
- **Q. H. Do**, S. Bishnoi, K. L. Scrivener, “*Finite Element modelling of ageing creep behaviour of cement paste at early age*”, to be submitted to Modelling and Simulation in Materials Science and Engineering
- **Q. H. Do**, S. Bishnoi, K. L. Scrivener, “*Simulating the setting time and the early age mechanical properties of tricalcium silicate pastes: Effect of flocculation and densification of calcium silicate hydrate*”. Submitted to Modelling and Simulation in Materials Science and Engineering, July 2013
- **Q. H. Do**, S. Bishnoi, K. L. Scrivener, “Numerical simulation of porosity in cements”, *Transport in Porous Media*, Vol. 99 (1), pp. 101-117, 2013
- **Q. H. Do**, “*Integrated analysis and design of slab systems*” Reference Books, Scientific Research Department, Hanoi Architectural University, Vietnam, 2006
- **Q. H. Do**, Q. A. Vu, “*Finite element method applied in the stability and vibration puzzles of frame systems*”, Collections of Student’s Research, Scientific Research Department, Hanoi Architectural University, Vietnam, 2001

## Conferences

- Talk: “*Finite element modelling of elastic properties of hydrating cement paste at early age*” Cementitious Materials, Experiments and Modelling Across the Scales, University of Notre Dame, US, 2012
- Talk: “*Numerical analysis of porosity of hydrating cement microstructure*” Cement and Concrete Science Conference, University of Birmingham, UK, 2010